Peter Puschnig

Excitonic Effects in Organic Semi-Conductors

An Ab-initio Study within the LAPW Method

Dissertation

written at the Institute of Theoretical Physics
submitted to the Faculty of Natural Sciences
Karl–Franzens–Universität Graz

under supervision of
ao. Univ.–Prof. Dr. Dr. h.c. C. Ambrosch–Draxl

Graz, January 2002

To Sandra

"In cases of major discrepancy it's
always reality that's got it wrong."
Douglas Adams
The Hitchhiker's Guide to the Galaxy

Contents

1 Introduction **1**

2 Density Functional Theory **5**
2.1 Introductory Remarks 5
2.2 The Density as the Basic Variable 6
2.3 The Hohenberg-Kohn Theorem 7
2.4 The Kohn-Sham Equations 8
2.5 Approximations for E_{xc} 10
2.5.1 The Local Density Approximation 10
2.5.2 An Exact Expression for E_{xc} 10
2.5.3 Generalized Gradient Approximations 12
2.6 Interpretation of the Kohn-Sham Energies 12
2.6.1 The Band-Gap Problem 12
2.6.2 Possible Ways Out 14

3 Many Body Perturbation Theory **15**
3.1 Motivation 15
3.2 Theory of Green's Functions 16
3.2.1 Second Quantization 16
3.2.2 One Electron Green's Function 18
3.2.3 Equation of Motion for G 19
3.3 The Hedin Equations 20
3.3.1 The Functional-Derivative Method 20
3.3.2 Dyson's Equation 20
3.3.3 Hedin Equations and GW Approximation 22
3.4 The Bethe Salpeter Equation 23
3.4.1 Derivation of the BSE 24
3.4.2 The Hartree Approximation 26
3.4.3 The Screened Interaction Approximation 26

4 Linear Optical Response **29**
4.1 Maxwell Equations 30
4.1.1 Microscopic Maxwell Equations 30

4.1.2 Longitudinal and Transverse Dielectric Tensor 31
4.1.3 Macroscopic Quantities 31
4.2 The Self-Consistent Field Method 32
4.2.1 Linearization of the Liouville Equation 32
4.2.2 Inclusion of Local Fields 34
4.2.3 Neglecting Local Fields 36
4.2.4 The Long Wavelength Limit 37
4.2.5 The Independent Quasi-Particle Approximation 38
4.2.6 Dielectric Response within DFT 40
4.3 Inclusion of Excitonic Effects 41
4.3.1 Dielectric Response from the BSE 41
4.3.2 The Long-Range Part of the Coulomb Potential 43
4.3.3 The Dielectric Matrix in the RPA 43
4.3.4 Reformulation of the BSE 45
4.3.5 Structure of the Effective Electron-Hole Hamiltonian . . . 47
4.3.6 The Macroscopic Dielectric Function 49
4.3.7 The Electron-Hole Interaction Kernel 51
4.3.8 The Spin Structure of the Electron-Hole Interaction Kernel 52
4.3.9 The Exciton Wave Function 53
4.4 Summary 54

5 The LAPW Method 57
5.1 General Remarks 57
5.2 The Basis Set of the Variational Problem 58
5.2.1 The LAPW Basis 58
5.2.2 Local Orbitals 60
5.2.3 The APW+lo Basis 60
5.2.4 A Basis for Core Electrons 61
5.3 Electron Density and Crystal Potential 61
5.4 Physical Properties in the LAPW Method 62
5.4.1 Total Energy 62
5.4.2 Atomic Forces 62
5.4.3 Dielectric Function 63

6 Implementation 65
6.1 The Matrix Elements $M_{nm}^{\mathbf{G}}(\mathbf{k}, \mathbf{q})$ 66
6.1.1 Symmetry Properties 66
6.1.2 Expansion in a Basis 67
6.1.3 Contribution from the Interstitial 68
6.1.4 Contribution from the Spheres 69
6.1.5 Local Orbitals and APW+lo 70
6.2 The Dielectric Matrix 72
6.2.1 The Independent Particle Polarizability 72

6.2.2 Symmetry of $\hat{P}^0_{\mathbf{GG'}}(\mathbf{q})$ . . . 73
6.2.3 Diagonal Elements and the Head of $\hat{P}^0$ . . . 74
6.2.4 Static Dielectric Matrix and Screened Interaction . . . 74
6.3 Evaluation of the BSE . . . 75
6.3.1 The Exchange Interaction Kernel . . . 75
6.3.2 The Direct Interaction Kernel . . . 76
6.3.3 Symmetry Properties of the Interaction Kernel . . . 77
6.3.4 Symmetrized Basis Functions . . . 78
6.3.5 Block-diagonal Form of $\hat{H}$ . . . 79
6.3.6 Interpolation of Electron-Hole Matrix Elements . . . 80
6.4 Convergence Tests and Numerical Results . . . 82
6.4.1 The Integrals $M^{\mathbf{G}}_{nm}(\mathbf{k},\mathbf{q})$ . . . 82
6.4.2 The Dielectric Matrix . . . 85
6.4.3 Electron-Hole Interaction Kernel . . . 88
6.4.4 The Macroscopic Dielectric Function . . . 89

7 Excitonic Spectra **95**
7.1 Introduction . . . 95
7.2 Inorganic Semi-Conductors and Insulators . . . 95
7.2.1 The RPA spectrum of Silicon . . . 95
7.2.2 Correlated DF of Silicon . . . 97
7.2.3 The RPA spectrum of LiF . . . 101
7.2.4 Correlated DF of LiF . . . 102
7.3 Conjugated Polymers . . . 105
7.3.1 Isolated Poly-acetylene . . . 105
7.3.2 Crystalline Poly-acetylene . . . 108

8 Pressure Studies **115**
8.1 Motivation and Methodology . . . 115
8.2 Structural Properties . . . 116
8.2.1 Lattice Constants . . . 116
8.2.2 Molecular Arrangement and Bond Lengths . . . 120
8.2.3 Total Energies and Bulk Moduli . . . 124
8.3 The Electronic Structure . . . 125
8.4 Optical Properties . . . 128
8.5 Discussion and Outlook . . . 130

A Mathematical Tools **133**
A.1 Fourier Series Conventions of Lattice Periodic Functions . . . 133
A.1.1 Local Functions . . . 133
A.1.2 Nonlocal Functions . . . 134
A.2 Crystal Lattice Integrals and Summations . . . 134
A.3 Inversion of a Block Matrix . . . 134

B Computational Details **137**
B.1 Convergence of Electron-Hole Matrix Elements 137
B.2 Convergence of the Macroscopic DF 140
B.3 Interpolation of the e-h-Kernel 142

Acknowledgments **147**

List of Figures **149**

List of Tables **151**

Mathematical Symbols and Abbreviations **153**

Bibliography **155**

List of Papers **161**

Chapter 1

Introduction

The development of new materials and the understanding of their physical properties is at the heart of technological as well as scientific progress. It is now almost twenty-five years since doped poly-acetylene has been shown to reach electrical conductivities comparable to conventional metals [1]. These findings marked the birth of a whole new field of research focusing on the electronic and optical properties of conjugated polymers.[1] These novel materials combine the mechanical flexibility, the low molecular weight, and the low-cost processibility which is typical for "plastic" materials, with the electro-optical properties known from in-organic semi-conductors and metals. Moreover, they are low-dimensional systems, which opens new possibilities for applications, and which is also interesting from a purely scientific point of view. To date, the range of applications covers light emitting diodes [2–6], photo-diodes and photo-voltaic cells [7, 8], and also fully organic transistors [9–11]. Recently, outstanding electronic and optical properties have been observed in molecular crystals consisting of conjugated molecules. Devices based on polyacene single crystals are efficient photo-voltaic cells [12], ambipolar field effect transistors [13], super-conducting below 4 Kelvin [14, 15], show electrically driven laser emission [16], and exhibit the integral as well as the fractional Quantum Hall effect [17].

Applied scientific research depends on the existence of accurate theoretical models. In particular, highly reliable *ab-initio* methods are in-dispensable for designing novel materials as well as for a detailed understanding of their properties. The development of such theories describing the electronic structure of atoms, molecules, and solids has been one of the success stories of physics in the 20^{th} century. Among these, density functional theory (DFT) [18–21] has proven to yield ground state properties for a vast number of systems in a very precise manner.[2]

[1] The Nobel Prize in Chemistry 2000 was awarded to Alan J. Heeger, Alan G. MacDiarmid and Hideki Shirakawa for the discovery and development of conductive polymers.

[2] The Nobel Prize in Chemistry 1998 was awarded to Walter Kohn for his development of the density-functional theory.

Indeed, DFT forms the basis of all electronic *ground state* calculations carried out in the present work.

Excited states, on the other hand, are not contained within the framework of DFT, and are – generally speaking – much more demanding. However, it is these properties that are probed in spectroscopic methods, and that are utilized for technological applications. Therefore, it is necessary to develop and test *ab-initio* techniques that are capable of predicting excited state quantities equally reliable as, for instance, DFT does for the ground state properties. In this work, we are mainly interested in optical properties, thus we are concerned with the interaction of external electro-magnetic waves with electron-hole excitations in the system.[3] This can be treated rigorously within many-body perturbation theory, expressed in terms of the equation of motion for the electron-hole two-particle Green's function, the so-called Bethe-Salpeter equation (BSE) [22–28]. The interaction between the electron and the hole is characterized by an effective interaction kernel, which has to be approximated in an appropriate manner. To zeroth order, the electron and the hole can be treated as *independent* particles, which results in the random phase approximation (RPA) for the optical properties. However, solutions of the BSE in an *ab-initio* framework, appearing in the literature in the past few years, have shown that electron-hole interactions are indeed important in order to correctly describe quantitative (oscillator strengths) as well as qualitative (bound excitons) features of optical spectra of semi-conductors and insulators [29–35].

The purpose of this work is therefore (i) to develop the necessary tools in order to solve the BSE for crystalline systems, and (ii) to apply these techniques to conjugated polymers and molecular crystals. The first point again consists of two steps: All wave-functions entering the calculations are commonly expressed in terms of given basis functions. In the present work, we choose linearized augmented plane waves (LAPW). They form the basis of the full-potential LAPW method [36], which is one of the most accurate and successful band structure methods available.[4] The BSE is adopted for this basis set by deriving the appropriate formulae, and a computer program is implemented which is performing the required computational steps. The calculations focus on the influence of *inter-molecular interactions* on the electronic and optical properties of conjugated polymers and molecular crystals consisting of oligomers. This problem appears particularly interesting since technological applications are restricted to the solid state in which interactions between neighboring polymer chains or molecules are inherently present. Moreover, it is an open question whether conclusions that have been drawn from *isolated* polymer or molecule calculations, for instance

[3] We limit ourselves to weak external perturbations which can be treated within the *linear response* regime.

[4] We utilize the WIEN97 code [37], which is an implementation of the full-potential LAPW method, for all computations presented in this thesis.

the size of the exciton binding energy, have to be revised if solid state interactions are taken into account. So far, the size of the exciton binding energy has been discussed for *isolated* chains, and it has been found to be in the order of 0.5 eV or more for poly-acetylene [33], poly-(*para*-phenylene-vinylene) [33, 38], as well as for poly-thiophene [34, 39]. However, it has been pointed out that inter-chain screening considerably reduces the exciton binding energy in poly-thiophene [34, 39]. The actual size of the exciton binding energies in real 3D polymer materials remains a matter of hot debate, and will be one of the main objectives of this work.

This work is organized as follows. In Chapter 2 we give a short description of density functional theory (DFT) which provides the framework for treating ground state properties of systems of interacting electrons. After a short historical review we recall the basic theorems and equations that form the foundations of DFT [18, 19], and discuss relevant approximations entering the theory. In the final section of Chapter 2, we discuss the limitations of DFT when we are interested in *excited* state properties. This motivates the presentation of the Green's function techniques in Chapter 3. There, we introduce the concept of the one-particle Green's function which contains all information about single-particle excitations, as they occur when single electrons are added or removed to the system. In order to solve the equation of motion for the Green's function, it is necessary to know the electron self-energy operator, which describes all exchange and correlation effects among the electrons. We discuss a specific approximation to the self energy first introduced by Hedin, the so-called GW approximation [40, 41]. In the last section of Chapter 3, a short derivation of the Bethe-Salpeter equation (BSE) is given. It is the equation of motion for the *two*-particle Green's function which describes the motion of coupled electron-hole excitations that are formed from the quasi-particles due to two-particle correlations. It is these electron-hole excitations which are relevant for the optical properties and are of central interest in this work. This will be the subject of Chapter 4. After recalling Maxwell's equations in the presence of matter, we derive the macroscopic dielectric function (DF) in the random phase approximation by using the self-consistent field method following the presentation of Adler [42] and Wiser [43]. The remaining part of the chapter contains the derivation of the macroscopic DF from the Bethe-Salpeter equation. This is achieved by expanding the correlation functions in terms of quasi-particle wave functions and solving the resulting eigenvalue equation for the excitation energies.

In Chapter 5 we give a short account of the LAPW method. Then in Chapter 6, we discuss the implementation of the solution to the BSE in terms of the LAPW method. The actual formulae required for the coding are derived and numerical tests are presented. In Appendix B more detailed information about convergence tests of the results are compiled. Chapter 7 contains the main outcome of the theoretical developments attained within this work. The macroscopic DF including

electron-hole interactions is discussed for three types of systems. Bulk Si and LiF serve as test cases for our computations since they have already been discussed in the literature. The last section of Chapter 7 is concerned with the excitonic structure of isolated as well as crystalline trans-polyacetylene. By comparing the respective results we investigate the influence of inter-molecular interactions on the optical properties in that conjugated polymer.

The application of external pressure reduces the inter-molecular distances and thereby *increases* the magnitude of the inter-molecular interactions. Thus, one can study their effects by investigating the pressure dependence of relevant properties. This is the idea of a joint research project with the Institute for Solid State Physics of the University of Technology Graz. The goal of the combined experimental and theoretical study is to investigate the role of inter-molecular interactions in molecular semi-conductors by applying external pressure. Thus, in the final Chapter 8, we discuss the *pressure*-dependent electronic, optical and structural properties of biphenyl and *para*-terphenyl molecular crystals. These materials can be viewed as prototypes for conjugated molecular crystals. In a first step, we optimize their internal structural parameters, such as the bond lengths and the molecular orientation, as a function of pressure, where the lattice parameters are taken from experiment. We obtain the bulk modulus both experimentally as well as theoretically allowing for a direct comparison. The electronic band structures are calculated for the optimized structures and are debated as a function of pressure. In the present work, optical properties are treated within the independent particle approximation due to computational limitations. For the future, however, we plan to include electron-hole correlations in the calculation of the dielectric function. This way, we will be able to directly study the influence of inter-molecular interactions on the excitonic structure by applying external pressure. Moreover, experimental studies of the optical properties will supplement our work. Finally, we point out that the collaborations within this joint "pressure project" have already led to a number of publications. A list of papers dealing with oligo-phenylenes under pressure can be found on page 161, the articles are added as an appendix to this thesis.

Chapter 2

Density Functional Theory

2.1 Introductory Remarks

If we wish to discuss the properties of a system of interacting electrons, such as a molecule or a solid, it is natural to study the many-electron wave function $\Psi(\mathbf{r}_1, \mathbf{r}_2, \ldots, \mathbf{r}_N)$. Here, $\mathbf{r}_i$ denotes the spatial and spin coordinates of the i–th electron, and the number of electrons is given by N.[1] One of the earliest and most simple approximations to the many-electron wave function Ψ is due to HARTREE, who approximated Ψ as a product of single particle wave functions $\psi_i(\mathbf{r}_i)$. Then, each of the single-particle orbitals $\psi_i(\mathbf{r}_i)$ satisfies a one-electron Schrödinger equation with a local potential term arising from the average field of all other electrons, the so-called Hartree potential. It is, however, clear that such an ansatz is not in accordance with the Fermi statistics that the total wave function Ψ should obey. This can be achieved by writing the many electron wave function as a so-called Slater determinant, which leads to the Hartree-Fock approximation with a *non-local* exchange term in the single-particle Schrödinger equation. It should be emphasized that a *single* Slater determinant is only a crude approximation, and commonly leads to a poor description of the system. A better approximation results from taking into account a linear combination of Slater determinants describing also excited configurations. This method – known as *configuration interaction* (CI) – leads, in principle, to the exact many-particle wave function from which most properties of interest can be obtained. We should, however, keep in mind that the number of necessary configurations increases very drastically with the number of electrons. Indeed, it can be demonstrated that the CI scheme is not size consistent when going to extended systems. Therefore,

[1] Note that we assume throughout this work that the electronic and nuclear degrees of freedom are separable (Born-Oppenheimer approximation), therefore the nuclear coordinates enter the electronic wave function Ψ only as parameters via the dependence on the Coulomb potential of the nuclear charges.

only systems with a limited electron number can be treated accurately enough by using the CI scheme.

A different approach was taken by Thomas and Fermi, who proposed a scheme based on the *density* of electrons in the system. They assumed that the motions of the electrons are un-correlated, and the kinetic energy can be described by a local approximation based on the free electron result. Although the Thomas-Fermi approximation has only limited success in treating real materials, it is the basis of the *density functional* formalism to be described in the remaining part of this chapter. The promising aspect of using the electron density instead of the many-particle wave function as basic variable is of course, that it is much easier to obtain than the precise details of the wave function Ψ, and also the scaling with system size is much better for methods based on the density of the system.

2.2 The Density as the Basic Variable

The basic lemma of HOHENBERG and KOHN states that the ground state density $n(\mathbf{r})$ of a bound system of interacting electrons in some external potential $v_{ext}(\mathbf{r})$ determines this potential uniquely (up to an additive constant) [18]. The proof is very simple: Let $n(\mathbf{r})$ be the non-degenerate ground-state density of N electrons in the external potential $v_1(\mathbf{r})$, corresponding to the ground state characterized by the many-electron wave function Ψ_1 and its total energy E_1. Then, we can write

$$\begin{aligned} E_1 &= \langle\Psi_1|\hat{H}_1|\Psi_1\rangle \\ &= \int \mathrm{d}^3r\, v_1(\mathbf{r})n(\mathbf{r}) + \langle\Psi_1|\hat{T}+\hat{U}|\Psi_1\rangle, \end{aligned} \tag{2.1}$$

where $\hat{H}_1$ is the total Hamiltonian corresponding to the external potential $v_1(\mathbf{r})$, and $\hat{T}$ and $\hat{U}$ are the kinetic and electro-static interaction energy operators, respectively. Now suppose that there exists a second external potential $v_2(\mathbf{r})$, which differs from $v_1(\mathbf{r})$ not just by a constant, leading to the *same* density $n(\mathbf{r})$. If we denote its ground state wave function and energy with Ψ_2 and E_2, respectively, we obtain

$$E_2 = \int \mathrm{d}^3r\, v_2(\mathbf{r})n(\mathbf{r}) + \langle\Psi_2|\hat{T}+\hat{U}|\Psi_2\rangle. \tag{2.2}$$

The Rayleigh-Ritz minimal principle for Ψ_1 gives the following inequality

$$\begin{aligned} E_1 &< \langle\Psi_2|\hat{H}_1|\Psi_2\rangle \\ &= \int \mathrm{d}^3r\, v_1(\mathbf{r})n(\mathbf{r}) + \langle\Psi_2|\hat{T}+\hat{U}|\Psi_2\rangle \\ &= E_2 + \int [v_1(\mathbf{r}) - v_2(\mathbf{r})]n(\mathbf{r})\mathrm{d}^3r. \end{aligned} \tag{2.3}$$

On the other hand, the analogous argument for the ground state of Ψ_2 leads to the expression

$$E_2 < \langle \Psi_1 | \hat{H}_2 | \Psi_1 \rangle = E_1 + \int [v_2(\mathbf{r}) - v_1(\mathbf{r})] n(\mathbf{r}) \mathrm{d}^3 r. \tag{2.4}$$

Adding Eqs. (2.3) and (2.4) leads to the contradiction

$$E_1 + E_2 < E_1 + E_2. \tag{2.5}$$

Thus, our initial assumption of the existence of a second external potential $v_2(\mathbf{r})$ leading to the identical density $n(\mathbf{r})$ must be wrong, and the Hohenberg-Kohn lemma is proven. We note that the proof presented above is based on the assumption of the non-degeneracy of the ground state. This requirement, however, can be lifted as shown by KOHN [44]. Moreover, we have assumed that *any* well-behaved positive function $n(\mathbf{r})$, which integrates to the number of electrons N, is a possible ground-state density corresponding to *some* $v(\mathbf{r})$ (v-representability). LEVY [45] and LIEB have shown that there are indeed examples of well-behaved densities that are not v-representable, but these cases do not appear to limit the practical application of DFT. Thus, the important message of this section is, that the total electron density $n(\mathbf{r})$ of a system of interacting electrons determines both, the number of electrons N and the external potential $v(\mathbf{r})$. Moreover, the many-body wave function Ψ is also a functional of the electron density $n(\mathbf{r})$ [18]. Consequently, the density gives us the full Hamiltonian $\hat{H}$ for the electronic system, and $n(\mathbf{r})$ implicitly contains all properties derivable from $\hat{H}$ through solution of the Schrödinger equation.

2.3 The Hohenberg-Kohn Theorem

The ground state energy E of a system of interacting electrons can be obtained from the solution of the many-body Schrödinger equation $\hat{H}\Psi = E\Psi$. Another approach is provided by the Rayleigh-Ritz minimal principle

$$E = \min_{\tilde{\Psi}} \langle \tilde{\Psi} | \hat{H} | \tilde{\Psi} \rangle, \tag{2.6}$$

where $\tilde{\Psi}$ is a normalized trial function for the N electron system. Equivalently, the minimal principle can be formulated in terms of trial densities $\tilde{n}(\mathbf{r})$, rather than trial wave functions $\tilde{\Psi}$, as was first shown by HOHENBERG and KOHN [18], and later in the form of the *constrained search method* by LEVY [45]. By integrating the trial wave function $\tilde{\Psi}$ over all space variables except the first, one obtains the corresponding density $\tilde{n}(\mathbf{r})$. Thus, the minimization of Eq. (2.6) may be achieved in two steps: First, fix a trial density $\tilde{n}(\mathbf{r})$, where we denote all wave functions

resulting in this density by $\tilde{\Psi}^{\alpha}_{\tilde{n}}$. We define an energy functional of the density in the way

$$\begin{aligned} E_v[\tilde{n}(\mathbf{r})] &= \min_{\alpha} \langle \tilde{\Psi}^{\alpha}_{\tilde{n}} | \hat{H} | \tilde{\Psi}^{\alpha}_{\tilde{n}} \rangle \\ &= \int v(\mathbf{r}) \tilde{n}(\mathbf{r}) \mathrm{d}^3 r + F[\tilde{n}(\mathbf{r})], \end{aligned} \tag{2.7}$$

where the functional $F[\tilde{n}(\mathbf{r})]$ is independent of the external potential $v(\mathbf{r})$ and given by

$$F[\tilde{n}(\mathbf{r})] = \min_{\alpha} \langle \tilde{\Psi}^{\alpha}_{\tilde{n}} | \hat{T} + \hat{U} | \tilde{\Psi}^{\alpha}_{\tilde{n}} \rangle. \tag{2.8}$$

In a second step, minimize Eq. (2.7) over all densities $\tilde{n}(\mathbf{r})$ resulting in the ground state energy E

$$\begin{aligned} E &= \min_{\tilde{n}(\mathbf{r})} E_v[\tilde{n}(\mathbf{r})] \\ &= \min_{\tilde{n}(\mathbf{r})} \left\{ \int v(\mathbf{r}) \tilde{n}(\mathbf{r}) \mathrm{d}^3 r + F[\tilde{n}(\mathbf{r})] \right\}. \end{aligned} \tag{2.9}$$

This is the Hohenberg-Kohn minimum principle [18] stating that the total energy is a functional of the density, and that the ground state density $n(\mathbf{r})$ minimizes this functional resulting in the ground state energy $E = E[n(\mathbf{r})]$.

2.4 The Kohn-Sham Equations

Formally, the Hohenberg-Kohn principle provides a strict formulation of the ground-state energy entirely in terms of the density distribution. However, practical applications require the knowledge of the functional $F[\tilde{n}(\mathbf{r})]$ defined in Eq. (2.8). Kohn and Sham [19] suggested to write this functional in the form

$$F[\tilde{n}(\mathbf{r})] = T_s[\tilde{n}(\mathbf{r})] + \frac{1}{2} \int \frac{\tilde{n}(\mathbf{r}) \tilde{n}(\mathbf{r}')}{|\mathbf{r} - \mathbf{r}'|} \mathrm{d}^3 r \mathrm{d}^3 r' + E_{xc}[\tilde{n}(\mathbf{r})], \tag{2.10}$$

where $T_s[\tilde{n}(\mathbf{r})]$ is the kinetic energy functional for *non-interacting* electrons, and the second term is the electro-static Hartree energy. The so-called exchange-correlation energy functional $E_{xc}[\tilde{n}(\mathbf{r})]$ is then *defined* by Eqs. (2.10) and (2.8). Next, we apply the Hohenberg-Kohn minimum principle in order to obtain the corresponding Euler-Lagrange equations with the functional $F[\tilde{n}(\mathbf{r})]$ defined in (2.10). Variations of the total energy $E_v[\tilde{n}(\mathbf{r})]$ in (2.7) with respect to the density $\tilde{n}(\mathbf{r})$, that leave the total number of electrons unchanged, yield

$$\delta E_v[\tilde{n}(\mathbf{r})] = \int \delta \tilde{n}(\mathbf{r}) \left\{ v_{\mathrm{eff}}(\mathbf{r}) + \frac{\delta}{\delta \tilde{n}(\mathbf{r})} T_s[\tilde{n}(\mathbf{r})] \Big|_{\tilde{n}(\mathbf{r}) = n(\mathbf{r})} - \varepsilon \right\} \mathrm{d}^3 r = 0. \tag{2.11}$$

Here, we have defined the effective potential (Kohn-Sham potential) $v_{\text{eff}}(\mathbf{r})$ as the sum of the external, the Hartree, and the exchange-correlation potential,

$$v_{\text{eff}}(\mathbf{r}) = v_{ext}(\mathbf{r}) + \int \frac{n(\mathbf{r}')}{|\mathbf{r}-\mathbf{r}'|}\mathrm{d}^3r' + v_{xc}(\mathbf{r}). \tag{2.12}$$

The exchange-correlation potential $v_{xc}(\mathbf{r})$ is obtained as the functional derivative of the exchange-correlation energy with respect to the electron density,

$$v_{xc}(\mathbf{r}) = \frac{\delta}{\delta\tilde{n}(\mathbf{r})} E_{xc}[\tilde{n}(\mathbf{r})]\bigg|_{\tilde{n}(\mathbf{r})=n(\mathbf{r})}. \tag{2.13}$$

The Lagrange multiplier ε in Eq. (2.11) ensures the conservation of the electron number in the variational procedure. The structure of (2.11) is the same as resulting for *non-interacting* particles in an effective one-particle potential $v_{\text{eff}}(\mathbf{r})$. Thus, Kohn and Sham concluded [19] that the minimizing density $n(\mathbf{r})$ can be obtained by solving the single-particle Schrödinger equations

$$\left[-\frac{1}{2}\nabla^2 + v_{\text{eff}}(\mathbf{r}) - \varepsilon_j\right]\varphi_j(\mathbf{r}) = 0, \tag{2.14}$$

with the density $n(\mathbf{r})$ constructed from the single particle orbitals $\varphi_j(\mathbf{r})$

$$n(\mathbf{r}) = \sum_{j=1}^{N} |\varphi_j(\mathbf{r})|^2. \tag{2.15}$$

The equations (2.14) and (2.15) with the definitions of the effective potential (2.12) with the local exchange-correlation potential (2.13) are called Kohn-Sham equations. These equations have to be solved self-consistently: starting from an initial guess for the Kohn-Sham potential v_{eff}, the Kohn-Sham equations (2.14) are diagonalized yielding the Kohn-Sham energies ε_j, and orbitals φ_j, respectively, which give the density n via Eq. (2.15). The density, in turn, determines a new effective potential by applying relations (2.12) and (2.13). This cycle is repeated until a converged ground state density is obtained. The ground state energy E may then be calculated from the ground state density as

$$E = \sum_{j=1}^{N} \varepsilon_j + E_{xc}[n(\mathbf{r})] - \int v_{xc}(\mathbf{r})n(\mathbf{r})\mathrm{d}^3r - \frac{1}{2}\int \frac{n(\mathbf{r})n(\mathbf{r}')}{|\mathbf{r}-\mathbf{r}'|}\mathrm{d}^3r\mathrm{d}^3r'. \tag{2.16}$$

Note that with the *exact* E_{xc} and v_{xc} all many-body effects are included in principle in the calculation of the ground state properties.[2] Clearly, the usefulness of the Kohn-Sham equations depend entirely on whether approximations for the functional $E_{xc}[n(\mathbf{r})]$ can be found which are at the same time sufficiently simple and accurate. The next section deals with such approximations for the exchange-correlation energy functional $E_{xc}[n(\mathbf{r})]$.

[2] A discussion about the *local* character of the exchange-correlation potential v_{xc} will be given in Section 2.6.2.

2.5 Approximations for E_{xc}

2.5.1 The Local Density Approximation

The simplest approximation for $E_{xc}[n(\mathbf{r})]$ is the so-called local-density approximation (LDA),

$$E_{xc}^{LDA}[n(\mathbf{r})] = \int e_{xc}\left(n(\mathbf{r})\right) n(\mathbf{r}) \mathrm{d}^3 r, \tag{2.17}$$

where $e_{xc}(n)$ is the exchange-correlation (XC) energy per particle of a *uniform* electron gas of density n [19]. Thus, the local contribution to the XC energy of the non-uniform system is taken to be identical to the XC energy of the uniform electron gas of the same density. The exchange part $e_x(n)$ can be calculated analytically and is given by

$$e_x(n) = -\frac{0.458}{r_s}, \tag{2.18}$$

where r_s is the radius of a sphere containing one electron and is given by setting the sphere volume $(4\pi/3)r_s^3$ equal to the inverse density. The correlation part was first calculated by Ceperly [46] and Ceperly and Alder [47] using Quantum Monte Carlo methods. The LDA is obviously exact for the homogeneous electron gas. Moreover, it was expected that for non-uniform cases it is only valid for densities that are slowly varying on the scale of the local Fermi wavelength λ_F. However, it turned out that the LDA gives reasonable results not only for free-electron like metals but also for atoms and molecules where the condition of slowly varying densities is not satisfied. Indeed, a great number of calculations have shown that the LDA gives ionization energies of atoms, dissociation energies of molecules with an accuracy of typically 10–20%. Structural properties such as bond lengths or vibrational frequencies even agree within 1–5% when compared to experimental values. This remarkable success of the LDA can at least partially be explained by an exact sum rule that is satisfied by the LDA (see next subsection). Moreover, the self-consistent solution of the Kohn-Sham equations using the LDA for the exchange-correlation energy is a conceptually very easy task as it is not more difficult than the solution of the Hartree equations. Particularly, it is much easier than the solution of the Hartree-Fock equations.

2.5.2 An Exact Expression for E_{xc}

In the following, it will be useful to introduce the concept of an exchange-correlation hole $n_{xc}(\mathbf{r}, \mathbf{r}')$, defined as

$$n_{xc}(\mathbf{r}, \mathbf{r}') = g(\mathbf{r}, \mathbf{r}') - n(\mathbf{r}'). \tag{2.19}$$

The pair correlation function $g(\mathbf{r}, \mathbf{r}')$ describes the conditional density at $\mathbf{r}'$ given that one electron is at $\mathbf{r}$. Thus, $n_{xc}(\mathbf{r}, \mathbf{r}')$ can be visualized as the *hole* dug into the average density $n(\mathbf{r}')$ in the presence of an electron at $\mathbf{r}$. It can be shown that this hole is normalized reflecting a total screening of the electron

$$\int n_{xc}(\mathbf{r}, \mathbf{r}')\mathrm{d}^3r' = -1. \tag{2.20}$$

Next it will be necessary to introduce a Hamiltonian H_λ for the many body system, in which the electron-electron interaction is multiplied by $\lambda \in [0, 1]$ and the external potential $v(\mathbf{r})$ is replaced by a λ-dependent potential $v_\lambda(\mathbf{r})$

$$\frac{1}{|\mathbf{r}_i - \mathbf{r}'_j|} \longrightarrow \frac{\lambda}{|\mathbf{r}_i - \mathbf{r}'_j|} \tag{2.21}$$

$$v(\mathbf{r}) \longrightarrow v_\lambda(\mathbf{r}). \tag{2.22}$$

The potential $v_\lambda(\mathbf{r})$ is chosen such that for all λ in the interval $[0, 1]$ the corresponding density equals the physical density $n(\mathbf{r})$:

$$n_\lambda(\mathbf{r}) = n_{\lambda=1}(\mathbf{r}) = n(\mathbf{r}). \tag{2.23}$$

The procedure (2.21) and (2.22) corresponds to a transition from the Kohn-Sham system of non-interacting electrons, where $\lambda = 0$ and $v_{\lambda=0}(\mathbf{r})$ equals the Kohn-Sham potential of Eq. (2.12), to the physical system with $\lambda = 1$ with $v_{\lambda=1}(\mathbf{r})$ given by the external potential. Now we can define the *average* exchange correlation hole $\bar{n}_{xc}(\mathbf{r}, \mathbf{r}')$ as a coupling strength integration over the *physical* exchange correlation hole $n_{xc}(\mathbf{r}, \mathbf{r}'; \lambda)$ corresponding to the coupling strength λ

$$\bar{n}_{xc}(\mathbf{r}, \mathbf{r}') = \int_0^1 \mathrm{d}\lambda\, n_{xc}(\mathbf{r}, \mathbf{r}'; \lambda). \tag{2.24}$$

The significance of (2.24) for the definition of the exchange correlation energy E_{xc} in the Kohn-Sham theory was shown, independently of each other, by Harris and Jones [48], Langreth and Perdew [49], and Gunnarsson and Lundqvist [50]. They derived the following *exact* expression for E_{xc}

$$E_{xc}[n(\mathbf{r})] = \frac{1}{2}\int \mathrm{d}^3r\mathrm{d}^3r' \frac{n(\mathbf{r})\bar{n}_{xc}(\mathbf{r}, \mathbf{r}')}{|\mathbf{r} - \mathbf{r}'|}. \tag{2.25}$$

The importance of this result stems from the fact that it guides the construction of approximate functionals for E_{xc} by using the exact sum rules, scaling properties or the asymptotic behavior obeyed by the exact E_{xc} of Eq. (2.25).

2.5.3 Generalized Gradient Approximations

Expression (2.25) can be used to derive the so-called generalized gradient approximation (GGA) to the exchange correlation energy E_{xc}. It has the form

$$E_{xc}^{GGA}[n(\mathbf{r})] = \int f\left(n(\mathbf{r}), |\nabla n(\mathbf{r})|\right) n(\mathbf{r}) \mathrm{d}^3 r, \tag{2.26}$$

where f is a function of the electron density n and its gradient $|\nabla n|$. In particular, we would like to mention the work of Perdew, Burke, and Enzerhof [51], who presented a simple derivation of a GGA potential by using the properties of the exact exchange-correlation energy. The GGA has been shown to improve the description of structural properties for systems which considerably differ from the free-electron gas, such as molecules.

2.6 Interpretation of the Kohn-Sham Energies

The density functional formalism as presented so far has been designed in order to describe the *ground state* properties of systems of interacting electrons. In many cases, however, we are also interested in *excited* state properties of the system, for instance, if we consider the electronic band structure or optical properties. The question remains whether or not DFT is able to provide such excited state quantities. The Kohn-Sham energies ε_i enter the formalism as Lagrange multipliers, due to the requirement that the Kohn-Sham orbitals are orthogonal (compare Eq. 2.11). Therefore, there is no evident physical interpretation of the energies ε_i. Nevertheless, it is a common practice to interpret the Kohn-Sham energies, for instance in a crystalline material, as electronic band structure of the system. While this works remarkably well in many situations, there are also important limitations of this *empirical* rule. One of these is the well-known fact that the Kohn-Sham band gap of insulators or semi-conductors is roughly 50% smaller than the actual band gap. In the next two sections we discuss possible reasons for this failure, and also attempt to show ways how to overcome these difficulties.

2.6.1 The Band-Gap Problem

The band gap $E_g(N)$ of a system containing N electrons can be defined as the difference between the ionization potential $I(N)$, and the electron affinity $A(N)$

$$E_g(N) = I(N) - A(N). \tag{2.27}$$

The ionization potential and the electron affinity for the N electron system, in turn, are defined as differences between ground state energies E involving N

electrons on the one hand, and $N-1$ and $N+1$ electrons, respectively, on the other. Thus we can write

$$I(N) = E(N-1) - E(N), \tag{2.28}$$
$$A(N) = E(N) - E(N+1). \tag{2.29}$$

The definition of the E_g given above involves only ground state energies but no Kohn-Sham energies ε. The connection to the latter is provided with help of a theorem due to Janak [52], who has extended the density functional formalism to systems containing a non-integral number of electrons. Janak proved the following identity

$$\frac{\partial E}{\partial f_N} = \varepsilon_N, \tag{2.30}$$

which says that the energy ε_N of the highest occupied Kohn-Sham orbital is equal to the derivative of the total energy with respect to the occupation number f_N of the highest occupied orbital. This theorem can be used in order to relate the ionization potential and the electron affinity to the orbital energies. Integrating the occupation number from 0 to 1 results in

$$I(N) = -\varepsilon_N(N-\delta), \tag{2.31}$$
$$A(N) = -\varepsilon_{N+1}(N+\delta). \tag{2.32}$$

Here, $\varepsilon_N(N-\delta)$, for instance, denotes the N–th Kohn-Sham energy of a system containing $N-\delta$ electrons, where δ is a real number strictly larger than 0 and smaller than 1, which is changing the occupation of the highest occupied orbital. It has been shown by Perdew and co-workers that the above expressions are independent of δ [53, 54]. We can therefore write the band gap of the N electron system in the following way [54, 55]

$$E_g(N) = \varepsilon_{N+1}(N+\delta) - \varepsilon_N(N-\delta) = \Delta\varepsilon + \Delta, \tag{2.33}$$

where $\Delta\varepsilon$ is the Kohn-Sham gap of the N electron system, and Δ is related to a discontinuity of the exchange-correlation potential when increasing the electron number by an integer value

$$\Delta = \left.\frac{\delta E_{xc}}{\delta n(\mathbf{r})}\right|_{N+\delta} - \left.\frac{\delta E_{xc}}{\delta n(\mathbf{r})}\right|_{N-\delta}. \tag{2.34}$$

The above equation states that the Kohn-Sham gap $\Delta\varepsilon$ is smaller than the true band gap E_g by the amount of the discontinuity Δ in the exchange-correlation potential. It is a well known fact that the LDA to the exchange-correlation energy underestimates the physical band gap of semi-conductors or insulators by as much as 50%. However, it is an interesting question whether the *exact* exchange-correlation energy would considerably improve upon the LDA result

for $\Delta\varepsilon$, or the error in the gap is largely due to the discontinuity itself. In the next section we will show two ways how we attempt to answer this question. An excellent discussion on the discontinuity and its size in different systems can be found in the review article by JONES and GUNNARSSON [20].

2.6.2 Possible Ways Out

The band gap problem arises because, within the Kohn-Sham scheme, there is no rigorous justification to interpret the single-particle energies as excitation energies. This is not the case if we calculate the quasi-particle spectrum by solving the Dyson equation

$$\left[-\frac{1}{2}\nabla^2 + V(\mathbf{r})\right]\phi_j(\mathbf{r}) + \int \mathrm{d}^3r'\,\Sigma(\mathbf{r},\mathbf{r}',E_j)\phi_j(\mathbf{r}') = E_j\phi_j(\mathbf{r}). \tag{2.35}$$

Here, $V(\mathbf{r})$ is the sum of the Hartree and the external potential, E_j and $\phi_j(\mathbf{r})$ are the quasi-particle energies and wave functions, respectively, and $\Sigma(\mathbf{r},\mathbf{r}',E_j)$ is the non-local and energy-dependent self-energy operator.[3] Comparison with the Kohn-Sham equations shows that the self-energy Σ replaces the *local* and *static* exchange-correlation energy of the density-functional formalism. A number of authors have calculated the self-energy of semi-conductors and insulators in the so-called GW approximation (see next chapter) and found excellent agreement of the so-obtained quasi-particle band gaps with the experimental values [56–59]. Moreover, GODBY and co-workers concluded that the local density approximation gives an excellent approximation to the exchange-correlation potential of the DF formalism, and that the poor band gap in the LDA is due to the discontinuity [58, 59]. In the present work, we will follow the approach outlined above in order to obtain the excitation spectrum from the Kohn-Sham energies. Note that these self-energy methods are no longer part of the density functional formalism. There is, however, another approach which tries to overcome the band-gap problem of DFT by extending the density functional formalism itself, the so-called time-dependent density functional theory (TD-DFT) [60, 61]. Unfortunately, the discussion of this theory falls outside the scope of this thesis. We just mention the fact, that excited state calculations for atoms and molecules give results in good agreement with experiment, whereas it is not yet fully understood if TD-DFT can be employed for extended systems [62]. An overview of TD-DFT can be found in [63, 64].

[3] The derivation of the Dyson equation and definition of the self-energy operator by using many-body techniques will be the subject of the next chapter.

Chapter 3

Many Body Perturbation Theory

3.1 Motivation

In the previous chapter, we have learned how ground state properties of electronic systems can be obtained within the framework of density functional theory. Excited states, however, are not rigorously accounted for by that approach. For that purpose we will make use of many-body perturbation theory. One main feature of many-body perturbation theory is that it reduces the many-particle problem to an effective few-particle problem. All many-body effects are included in an effective interaction kernel. We have already mentioned the fact that the solution of the Dyson equation, the equation of motion for the *one*-particle propagator, can provide the *single*-particle excitation spectrum of the system. As the effective interaction kernel, it includes the electron self energy, which takes into account all exchange and correlation effects on the one-electron level, and which is a non-local and energy-dependent operator. In this chapter, we will review the steps that lead to the derivation of the Dyson equation. Moreover, we will discuss an important approximation of the self-energy operator introduced by Hedin, namely the so-called GW approximation [40].

The calculation of optical properties, however, requires the knowledge of *two*-particle excitations, which are described by the two-particle Green's function. Therefore, we will introduce the equation of motion for the two-particle correlation function, the Bethe-Salpeter equation (BSE) in the last part of this chapter. The electron-hole interaction is contained in an effective interaction kernel, which is defined as the functional derivative of the self energy with respect to the one-particle propagator. In the last section, we derive the form of this interaction kernel by using the GW approximation for the self energy. In particular, it involves an attractive, screened electron-hole interaction, which is responsible for the formation of bound exciton states.

An overview of the many-body techniques used in this chapter can, for instance,

be found in the book by FETTER and WALECKA [65] and in the articles by BAYM and KADANOFF [66, 67]. The GW approximation is described by HEDIN [40] and HEDIN and LUNDQUIST [41].

3.2 Theory of Green's Functions

We start the discussion with the Hamiltonian describing a system of N interacting electrons in an electrostatic potential due to the positive charges of the nuclei (assumed to be at fixed positions $\mathbf{R}_n$)

$$\hat{H} = \sum_{i=1}^{N} \hat{h}(\mathbf{r}_i) + \frac{1}{2}\sum_{i\neq j} v(\mathbf{r}_i, \mathbf{r}_j) \tag{3.1}$$

$$\hat{h}(\mathbf{r}) = -\frac{1}{2}\nabla^2 + \sum_n Z_n v(\mathbf{r}, \mathbf{R}_n) \tag{3.2}$$

$$v(\mathbf{r}, \mathbf{r}') = \frac{1}{|\mathbf{r} - \mathbf{r}'|}. \tag{3.3}$$

The one-particle term $\hat{h}(\mathbf{r})$ accounts for the kinetic energy of the electrons and the electro-static interaction of the electrons with the nuclei with charges Z_n. The second term containing the electron-electron interaction via the Coulomb potential $v(\mathbf{r}, \mathbf{r}')$ makes the solution of the Schrödinger equation

$$+i\partial_t \psi(\mathbf{r}_1, \ldots, \mathbf{r}_N; t) = \hat{H}\psi(\mathbf{r}_1, \ldots, \mathbf{r}_N; t) \tag{3.4}$$

an extremely difficult task. It will be convenient to continue the discussion in the language of second quantization.

3.2.1 Second Quantization

In this section, we give a very brief review of the concept of second quantization in order to define the notation needed in the sections to come. Let $u_k(\mathbf{r})$ denote a complete set of one-particle wave functions, then we can write the many-body wave function as a Slater determinant

$$|k_1 \cdots k_N\rangle = \frac{1}{\sqrt{N!}} \det\{u_k(\mathbf{r}_l)\}, \tag{3.5}$$

where k denotes a set of quantum numbers, for instance, the Bloch vector $\mathbf{k}$ and the band index n for crystalline systems. The action of a creation operator $\hat{a}_k^\dagger$, and an annihilation operator $\hat{a}_k$, respectively, is defined by the following equations.

$$\hat{a}_k^\dagger |k_1 \cdots k_N\rangle = \begin{cases} |k, k_1 \cdots k_N\rangle & k \neq k_i \quad \forall i \\ 0 & \exists i, \quad k = k_i \end{cases}, \tag{3.6}$$

and

$$\hat{a}_k|k_1\cdots k_N\rangle = \begin{cases} |k_1\cdots k_{i-1}\,0\,k_{i+1}\cdots k_N\rangle & k=k_i \\ 0 & k\neq k_i \quad \forall i \end{cases} . \tag{3.7}$$

From Eqs. (3.6) and (3.7) the anti-commutation rules for $\hat{a}_k^\dagger$ and $\hat{a}_k$ follow

$$\{\hat{a}_k, \hat{a}_{k'}^\dagger\} = \delta_{k,k'} \tag{3.8}$$

$$\{\hat{a}_k, \hat{a}_{k'}\} = \{\hat{a}_k^\dagger, \hat{a}_{k'}^\dagger\} = 0, \tag{3.9}$$

reflecting the Fermion character of the electrons. With the definition of the field operators $\hat{\psi}(\mathbf{r})$ and $\hat{\psi}^\dagger(\mathbf{r})$

$$\hat{\psi}(\mathbf{r}) = \sum_k \hat{a}_k u_k(\mathbf{r}) \tag{3.10}$$

$$\hat{\psi}^\dagger(\mathbf{r}) = \sum_k \hat{a}_k^\dagger u_k^*(\mathbf{r}), \tag{3.11}$$

we can verify the anti-commutation relations

$$\{\hat{\psi}(\mathbf{r}), \hat{\psi}^\dagger(\mathbf{r}')\} = \delta(\mathbf{r}-\mathbf{r}') \tag{3.12}$$

$$\{\hat{\psi}(\mathbf{r}), \hat{\psi}(\mathbf{r}')\} = \{\hat{\psi}^\dagger(\mathbf{r}), \hat{\psi}^\dagger(\mathbf{r}')\} = 0. \tag{3.13}$$

The operators $\hat{\psi}$ and $\hat{\psi}^\dagger$ can be used to express the Hamiltonian $\hat{H}$ in terms of the field operators

$$\hat{H} = \int \mathrm{d}^3 r \hat{\psi}^\dagger(\mathbf{r})\hat{h}(\mathbf{r})\hat{\psi}(\mathbf{r}) + \frac{1}{2}\int \mathrm{d}^3 r \mathrm{d}^3 r' \hat{\psi}^\dagger(\mathbf{r})\hat{\psi}^\dagger(\mathbf{r}')v(\mathbf{r},\mathbf{r}')\hat{\psi}(\mathbf{r}')\hat{\psi}(\mathbf{r}). \tag{3.14}$$

The first term contains the single particle part of the Hamiltonian, that is the kinetic energy and the electro-static interaction energy due the positive nuclei, whereas the second term describes the electron-electron interactions. Equation (3.14) together with the time evolution of the field operators in the Heisenberg representation

$$\hat{\psi}(\mathbf{r},t) = e^{i\hat{H}t}\hat{\psi}(\mathbf{r})e^{-i\hat{H}t} \tag{3.15}$$

determines the equation of motion of the field operator $\hat{\psi}(\mathbf{r},t)$. Accounting for the anti-commutation relations (3.12) and (3.13) we obtain the equation of motion for the field operator

$$\begin{aligned} i\partial_t\hat{\psi}(\mathbf{r},t) &= [\hat{\psi}(\mathbf{r},t), \hat{H}] \\ &= \left[\hat{h}(\mathbf{r}) + \int \mathrm{d}^3 r' v(\mathbf{r},\mathbf{r}')\hat{\psi}^\dagger(\mathbf{r}',t)\hat{\psi}(\mathbf{r}',t)\right]\hat{\psi}(\mathbf{r},t). \end{aligned} \tag{3.16}$$

Note that the time evolution of $\hat{\psi}$ is due to the one-particle term $\hat{h}$ plus a term involving the electron-electron interaction. It is this latter term that makes the solution of (3.16) an extremely difficult task, because the desired operator $\hat{\psi}$ also appears in the definition of the two-particle potential. It will be the objective of the following sections to derive a perturbative method that allows for an appropriate treatment of the electron-electron interaction to all orders of perturbation theory.

3.2.2 One Electron Green's Function

The field operators $\hat{\psi}$ and $\hat{\psi}^\dagger$ can be utilized to introduce the one-particle Green's function G. It measures the probability of finding an electron at position $\mathbf{r}$ and time t if it was injected at position $\mathbf{r}'$ and at time t'. It can be calculated from the following expression [65]

$$G(\mathbf{r}, t, \mathbf{r}', t') = -i\langle N|\hat{T}[\hat{\psi}(\mathbf{r}, t)\hat{\psi}^\dagger(\mathbf{r}', t')]|N\rangle, \tag{3.17}$$

where $|N\rangle$ is the many-body ground state of the N electron system and $\hat{T}$ is Dyson's time ordering operator. The operator $\hat{T}$ is defined such that field operators at later times are ordered from left to right. If Θ denotes Heaviesides' step function, then the definition of $\hat{T}$ gives

$$\begin{aligned} G(\mathbf{r}, t, \mathbf{r}', t') &= -i\langle N|\hat{\psi}(\mathbf{r}, t)\hat{\psi}^\dagger(\mathbf{r}', t')|N\rangle\Theta(t - t') \\ &\quad +i\langle N|\hat{\psi}^\dagger(\mathbf{r}', t')\hat{\psi}(\mathbf{r}, t)|N\rangle\Theta(t' - t). \end{aligned} \tag{3.18}$$

In order to gain some intuition of the properties of the Green's function defined above, and a meaning of how to interpret it, we introduce the eigenvectors $|N, S\rangle$ and eigenvalues $E(N, S)$ of the Hamiltonian $\hat{H}$ as

$$\hat{H}|N, S\rangle = E(N, S)|N, S\rangle. \tag{3.19}$$

Here, N denotes the fact that the system contains N electrons, and S is used to number the excited states of the system, so $S = 0$ is the ground state, $|N, S = 0\rangle \equiv |N\rangle$. We also define the energy difference

$$\varepsilon_S(N + 1) = E(N + 1, S) - E(N, 0). \tag{3.20}$$

Thus, $\varepsilon_S(N + 1)$ can be interpreted as an excitation energy of the system: the energy that is needed to add an electron to the ground state into the excited state S of the $N + 1$ electron system. Inserting into the first (second) term of G in Eq. (3.18) a complete set of eigenvectors for an $N+1$ ($N-1$) electron system by using the closure relation of the states $|N + 1, S\rangle$ ($|N - 1, S\rangle$) results in

$$\begin{aligned} G(\mathbf{r}, t, \mathbf{r}', t') &= -i\sum_S f_S(\mathbf{r})f_S^*(\mathbf{r}')e^{-i\varepsilon_S(t-t')} \\ &\quad \times \left[\Theta(t - t')\Theta(\varepsilon_S - \mu) - \Theta(t' - t)\Theta(\mu - \varepsilon_S)\right], \end{aligned} \tag{3.21}$$

with the definition

$$f_S(\mathbf{r}) = \begin{cases} \langle N|\hat{\psi}(\mathbf{r})|N + 1, S\rangle & \varepsilon_S = \varepsilon_S(N + 1) \quad \text{if} \quad \varepsilon_S(N + 1) > \mu \\ \langle N - 1, S|\hat{\psi}(\mathbf{r})|N\rangle & \varepsilon_S = -\varepsilon_S(N - 1) \quad \text{if} \quad -\varepsilon_S(N - 1) < \mu \end{cases}. \tag{3.22}$$

Here, we have introduced the chemical potential μ. This is the so-called Lehmann representation of the one-particle Green's function [65]. From expressions (3.21) and (3.22) it is seen that the one-particle Green's function contains all the information about the single-particle excitations of the system. We will show in the next section how to obtain the equation of motion for the Green's function.

3.2.3 Equation of Motion for G

We are interested in the response of the system due to a small external perturbation causing the system in the ground state to be transformed into some excited state. To this end, we introduce in addition to the Hamiltonian $\hat{H}$ from the previous sections which we will denote from now on $\hat{H}_0$, a Hamiltonian $\hat{H}_1$ stemming from an external time dependent potential $\phi(\mathbf{r},t)$, thus

$$\begin{aligned}
\hat{H} &= \hat{H}_0 + \hat{H}_1, \\
\hat{H}_0 &= \int \mathrm{d}^3 r \hat{\psi}^\dagger(\mathbf{r})\hat{h}(\mathbf{r})\hat{\psi}(\mathbf{r}) + \frac{1}{2}\int \mathrm{d}^3 r \mathrm{d}^3 r' \hat{\psi}^\dagger(\mathbf{r})\hat{\psi}^\dagger(\mathbf{r}')v(\mathbf{r},\mathbf{r}')\hat{\psi}(\mathbf{r}')\hat{\psi}(\mathbf{r}), \\
\hat{H}_1 &= \int \mathrm{d}^3 r \hat{\psi}^\dagger(\mathbf{r})\phi(\mathbf{r},t)\hat{\psi}(\mathbf{r}).
\end{aligned}$$

The equation of motion for the field operator $\hat{\psi}(\mathbf{r})$ is again given by Eq. (3.16) just replacing $\hat{h}(\mathbf{r})$ by $\hat{h}(\mathbf{r}) + \phi(\mathbf{r},t)$. Using the equation of motion for the field operators and their anti-commutation relations (3.12) and (3.13) one can derive the following equation of motion for the Green's function

$$\Big[i\partial_{t_1} - \hat{h}(1) - \phi(1)\Big] G(1,1') = \delta(1,1') - i\int \mathrm{d}(2) v(1,2) G_2(1,2;1',2^+). \quad (3.23)$$

In the last result we have introduced the following abbreviations which considerably simplify the notation

$$\begin{aligned}
1 &\rightarrow \{\mathbf{r}_1, t_1\}, \\
1^+ &\rightarrow \{\mathbf{r}_1, t_1 + 0^+\}, \\
\mathrm{d}(1) &= \mathrm{d}^3 r \mathrm{d}t, \\
v(1,2) &= v(\mathbf{r}_1,\mathbf{r}_2)\delta(t_1 - t_2), \\
\delta(1,2) &= \delta(\mathbf{r}_1 - \mathbf{r}_2)\delta(t_1 - t_2).
\end{aligned}$$

Moreover, we used the definition of the two-particle Green's function $G_2(1,2;1,2')$ (see for instance [65])

$$G_2(1,2;1,2') = -\langle N|\hat{T}[\psi(1)\psi(2)\psi^\dagger(2')\psi^\dagger(1')]|N\rangle. \quad (3.24)$$

It is important to note from Eq. (3.23) that in order to know the time evolution of the one-particle Green's function one has to know the time evolution of the two-particle Green's function. Moreover, the equation of motion for G_2 would already involve a term containing six field operators and so on. One technique that is a way out of this circle is the functional-derivative method to be described in the next section.

3.3 The Hedin Equations

3.3.1 The Functional-Derivative Method

In the following we will make use of the functional-derivative technique due to Schwinger [68], Martin and Schwinger [69], and Kadanoff and Baym [66, 67]. It allows for a replacement of the two-particle Green's function G_2 in the equation of motion (3.23) by an expression only including one-particle Green's functions. Let $\phi(1)$ be a function of space and time (the external perturbation), and the operator $\hat{S}$ be defined as

$$\hat{S} = \exp\left\{-i\int_{-\infty}^{\infty} \mathrm{d}(2)\phi(2)\psi^\dagger(2)\psi(2)\right\}. \tag{3.25}$$

Then we can write the one-particle Green's function describing the perturbed system as

$$G(1,1';\phi) = -i\frac{\langle N|\hat{T}[\hat{S}\psi(1)\psi^\dagger(1')]|N\rangle}{\langle N|\hat{T}[\hat{S}]|N\rangle}. \tag{3.26}$$

It is clear that the above form of G agrees with the previous one if $\phi = 0$, that is $G(1,1';0) \equiv G(1,1')$. By taking the derivative of G with respect to t_1 and using the equation of motion for the field operators again, we can show that $G(1,1';\phi)$ fulfills an equation of motion equivalent to that of $G(1,1')$ from Eq. (3.23). Thus, we have

$$\left[i\partial_{t_1} - \hat{h}(1) - \phi(1)\right] G(1,1';\phi) = \delta(1,1') - i\int \mathrm{d}(2)v(1,2)G_2(1,2;1',2^+). \tag{3.27}$$

So far, we did not gain anything new, but let us now evaluate the variation of $G(1,1';\phi)$ with respect to the function $\phi(2)$. One obtains:

$$\frac{\delta G(1,1';\phi)}{\delta\phi(2)} = -G_2(1,2;1',2^+) + G(2,2^+;\phi)G(1,1';\phi), \tag{3.28}$$

which can be used to replace G_2 in Eq. (3.27) by a term involving the product of two single-particle Green's functions and a term describing the variational change of G with respect to a function ϕ.

3.3.2 Dyson's Equation

From now on we drop the explicit functional dependence of the Green's function on the external perturbation ϕ in order to simplify the notation. Moreover, we replace $1'$ by 2. Then, the insertion of (3.28) into (3.27) directly leads to

$$\left[i\partial_{t_1} - \hat{h}(1) - V(1)\right] G(1,2) = \delta(1,2) + i\int \mathrm{d}(3)v(1,3)\frac{\delta G(1,2)}{\delta\phi(3)}. \tag{3.29}$$

where we have introduced the potential $V(1)$ as

$$V(1) = \phi(1) - i \int \mathrm{d}(2) v(1,2) G(2,2^+). \tag{3.30}$$

Note that $-iG(2,2^+)$ is the density $n(2)$ of the system, so the second term in Eq. (3.30) is just the Hartree potential. It describes the electro-static energy of an electron in the average field of all other electrons. In order to evaluate (3.29) further we define the inverse of the Green's function G^{-1} in the way

$$\int G(1,4) G^{-1}(4,5) \mathrm{d}(4) = \delta(1,5). \tag{3.31}$$

Variation of (3.31) with respect to the perturbation $\phi(3)$, multiplication with the Green's function $G(5,2)$, and integration over the variable 5 leads to

$$\frac{\delta G(1,2)}{\delta \phi(3)} = -\int G(1,4) \frac{\delta G^{-1}(4,5)}{\delta \phi(3)} G(5,2) \mathrm{d}(4,5). \tag{3.32}$$

This expression can be used to replace the functional derivative in the equation of motion (3.29) giving Dyson's equation of motion for the single particle Green's function G.

$$\left[i\partial_{t_1} - \hat{h}(1) - V(1) \right] G(1,2) = \delta(1,2) + \int \Sigma(1,5) G(5,2) \mathrm{d}(5). \tag{3.33}$$

Here, the self-energy Σ has been introduced via the definition

$$\Sigma(1,5) = -i \int v(1,3) G(1,4) \frac{\delta G^{-1}(4,5)}{\delta \phi(3)} \mathrm{d}(3,4). \tag{3.34}$$

The self-energy Σ appearing in Eq. (3.33) can be viewed as a non-local and energy-dependent function describing all exchange and correlation effects on the one-particle level. We will shortly see how the self energy completely determines the one-particle Green's function from which in turn the one-particle excitation spectrum can be obtained. To this end, we transform (3.33) into a more familiar form. Let us introduce the *non-interacting* Green's function G_0 in the way

$$\left[i\partial_{t_1} - \hat{h}(1) - V(1) \right] G_0(1,2) = \delta(1,2). \tag{3.35}$$

Consequently, G_0 is the Green's function on the Hartree level describing the motion of free electrons in the electro-static Hartree potential included in the potential $V(1)$. Moreover, we can define the inverse of G_0 in a similar way as in Eq. (3.31). Then we can combine expressions (3.33) and (3.35) to obtain

$$\int G_0^{-1}(1,3) G(3,2) \mathrm{d}(3) = \delta(1,2) + \int \Sigma(1,5) G(5,2) \mathrm{d}(5). \tag{3.36}$$

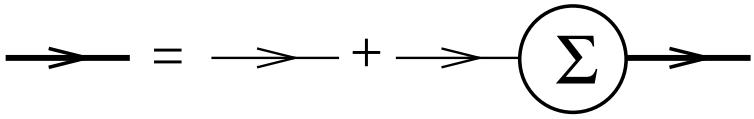

Figure 3.1: Diagrammatic form of Dyson's equation (3.38). The thin line denotes the non-interacting Green's function G_0, whereas the thick line corresponds to the interacting Green's function G, and Σ is the self energy.

By multiplying the above expression from the right by G^{-1}, or alternatively by G_0 from the left, and integrating over one set of variables in order to use the definition of the inverse of the Green's function, leads to the important relations – the Dyson's equations – which are also illustrated in Fig. (3.1)

$$G_0^{-1}(1,2) = G^{-1}(1,2) + \Sigma(1,2) \tag{3.37}$$

$$G(1,2) = G_0(1,2) + \int G_0(1,3)\Sigma(3,4)G(4,2)\mathrm{d}(3,4). \tag{3.38}$$

The propagation of an electron can be viewed as the independent propagation of an electron in the average electro-static potential, plus a term accounting for the exchange and correlation effects, which is described by the self-energy operator Σ.

3.3.3 Hedin Equations and GW Approximation

The central quantity in the previous section is the self-energy operator Σ. By means of equations (3.37) or (3.38) it determines the Green's function, which in turn contains all the information about the one-particle excitations in the system. By using similar techniques as in the previous subsection Hedin and Lundquist [40, 41] derived the following set of self-consistent equations from which the self-energy Σ can be calculated.

$$\Sigma(1,5) = i\int W(1,2)G(1,4)\Gamma(4,5;2)\mathrm{d}(2,4) \tag{3.39}$$

$$W(1,2) = v(1,2) + \int W(1,6)\hat{P}(6,7)v(7,2)\mathrm{d}(6,7) \tag{3.40}$$

$$\hat{P}(6,7) = -i\int G(7,4)G(5,7)\Gamma(4,5;6)\mathrm{d}(4,5) \tag{3.41}$$

$$\Gamma(1,2;3) = \delta(1,2)\delta(1,3) + \frac{\delta\Sigma(1,2)}{\delta V(3)} \tag{3.42}$$

Here, W denotes the screened interaction, $\hat{P}$ the irreducible polarization and Γ the vertex function. The set of equations (3.39–3.42) has to be solved iteratively,

where it is important to note that at any step in the iterative procedure the approximations are *conserving*. That means that the number of particles, the total energy, the momentum, and the angular momentum are conserved quantities in all iterative steps [66, 67]. A first approximation of HEDIN's equations (3.39–3.42) is obtained by neglecting the second term in (3.42) for the vertex function. This is the so-called GW-approximation, named after the resulting expression for the self-energy Σ

$$\begin{aligned} \Sigma(1,2) &= iG(1,2)W(1,2) && (3.43)\\ W(1,2) &= v(1,2) + \int W(1,6)\hat{P}(6,7)v(7,2)\mathrm{d}(6,7) && (3.44)\\ \hat{P}(1,2) &= -iG(2,1)G(1,2) && (3.45)\\ \Gamma(1,2;3) &= \delta(1,2)\delta(1,3). && (3.46) \end{aligned}$$

In the GW approximation the vertex function Γ is given by a product of two delta functions. Consequently, the irreducible polarization is simply the product of two Green's functions. This gives rise to the so-called random phase approximation (RPA) for the polarization. Alternatively, this approximation is called the independent particle approximation, because it results from the two-particle correlation function, if the motion of the individual particles is assumed to be independent of each other. This statement will become clear in the next chapter. The integral equation for the screened interaction W can be solved by introducing the dielectric matrix ϵ in the way

$$\epsilon(1,2) = \delta(1,2) - \int v(1,3)\hat{P}(3,2)\mathrm{d}(3). \tag{3.47}$$

Then, we can obtain the screened interaction from the inverse of the dielectric matrix ϵ^{-1} as

$$W(1,2) = \int \epsilon^{-1}(1,3)v(3,2)\mathrm{d}(3). \tag{3.48}$$

Finally, the self energy in the GW approximation is calculated simply as the product of the Green's function G and the screened interaction W.

3.4 The Bethe Salpeter Equation

Up to now, we have developed methods in order to describe the *one*-particle excitation energies of electronic systems. These quantities are, for instance, relevant in photo-electron emission and inverse photo-emission experiments since a single electron is removed or added to the system. Our interest, however, is the description of optical properties of solids, in which the incident photons create electron-hole pairs. This information is contained in the two-particle Green's function G_2

which we have already defined in Eq. (3.24). In this section, we will derive the equation of motion for the two-particle correlation function, the so-called Bethe-Salpeter equation (BSE). Moreover, we will discuss two relevant approximations, namely, the Hartree, and the screened interaction approximation. We will make use of the latter result in the second part of the next chapter in order to obtain the optical properties of semi-conductors and insulators including electron-hole correlation effects beyond the RPA.

3.4.1 Derivation of the BSE

We start by a generalization of expression (3.28) by evaluating the variation of the one-particle Green's function with respect to $u(1', 2')$ which is a function of the two independent variables $1'$ and $2'$ (see for example [66])

$$\frac{\delta G(1,2)}{\delta u(1',2')} = -G_2(1,1';2,2') + G(1',2')G(1,2). \tag{3.49}$$

Here the Green's functions are defined in an analogous way to the definition (3.27) with the generalization that the operator $\hat{S}$ is now defined as

$$\hat{S} = \exp\left\{-i\int_{-\infty}^{\infty} \mathrm{d}(1',2')u(1',2')\psi^\dagger(1')\psi(2')\right\}. \tag{3.50}$$

It is convenient to introduce the two-particle correlation function L defined as

$$L(1,1';2,2') = G_2(1,1';2,2') - G(1',2')G(1,2). \tag{3.51}$$

Thus, L is the part of the two-particle Green's function G_2 which excludes the disconnected term $G(1',2')G(1,2)$, and the functional derivative of $G(1,2)$ with respect to $u(1',2')$ in Eq. (3.49) is simply $-L(1,1';2,2')$. In order to derive the equation of motion for the correlation function L, we observe that the functional derivative of $GG^{-1} = 1$ with respect to $u(1',2')$ leads to

$$\frac{\delta G(1,2)}{\delta u(1',2')} = -\int \mathrm{d}(3,4)G(1,3)\frac{\delta G^{-1}(3,4)}{\delta u(1',2')}G(4,2). \tag{3.52}$$

We can eliminate the functional derivative of G^{-1} by using Dyson's Equation (3.37). Here, we use the fact that the functional derivative of the *non-interacting* Green's function is just a product of delta functions. This follows from the definition of G_0 given by Eq. (3.35). Hence, we get from (3.52)

$$-L(1,1';2,2') = G(1,1')G(2',2) + \int \mathrm{d}(3,4)G(1,3)\frac{\delta\Sigma(3,4)}{\delta u(1',2')}G(4,2). \tag{3.53}$$

The term involving the functional derivative of the self energy Σ is rewritten by applying the chain rule, and noting that the self energy depends on u only through its dependence on G

$$\frac{\delta\Sigma(3,4)}{\delta u(1',2')} = \int \mathrm{d}(5,6)\frac{\delta\Sigma(3,4)}{\delta G(6,5)}\frac{\delta G(6,5)}{\delta u(1',2')}. \tag{3.54}$$

As a result, we obtain the Bethe-Salpeter equation for the correlation function L in the form

$$\begin{aligned} L(1,1',2,2') &= L_0(1,1',2,2') \\ &+ \int \mathrm{d}(3,3',4,4')L_0(1,1',3,3')\Xi(3,3',4,4')L(4,4',2,2'). \end{aligned} \tag{3.55}$$

Note that we have introduced the function L_0 describing the *independent* motion of two particles as

$$L_0(1,1',2,2') = G(1',2')G(2,1), \tag{3.56}$$

and the kernel Ξ is an effective two-particle interaction expressed as the functional derivative of the self-energy operator with respect to the single-particle Green's function [66]

$$\Xi(3,3',4,4') = \frac{\delta[V_H(4,4') + \Sigma(4,4')]}{\delta G(3,3')}. \tag{3.57}$$

Because we have subtracted the Hartree part V_H from the self energy in the derivations leading to the self energy (compare Eq. 3.29), we have to add the Hartree potential here explicitly

$$V_H(4,4') = -i\,\delta(4,4')\int G(5,5^+)v(5,4)d(5). \tag{3.58}$$

A diagrammatic representation of the Bethe-Salpeter equation (3.55) can be seen in Fig. (3.2). We want to point out that the correlation function L is a conserving quantity due to the property

$$L(1,1',2,2') = L(1',1,2',2), \tag{3.59}$$

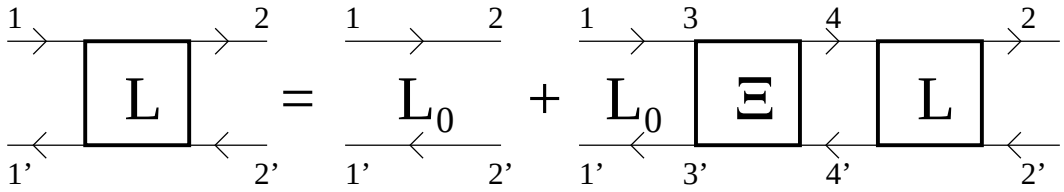

Figure 3.2: Diagrammatic form of the Bethe-Salpeter equation (3.55). The two-particle correlation function L is given by by the independent propagation L_0 of an electron and the hole, plus a term involving the electron-hole interaction Ξ.

which is guaranteed by the symmetry of the interaction kernel Ξ

$$\Xi(3,3',4,4') = \Xi(3',3,4',4). \tag{3.60}$$

The construction of the correlation function L, and the interaction kernel Ξ as functional derivatives ensures the conservation of energy, momentum and the number of particles not only for the exact L, but also for any approximate solution to the Bethe-Salpeter equation [66, 67]. In the next subsections we will discuss two specific approximations of the kernel Ξ. First, we want to treat the electron and hole as independent particles leading to the random phase approximation for the polarization function. Finally, we will approximate the interaction kernel by the functional derivative of the self energy in the GW approximation. This leads to the screened interaction approximation which will be used in the next chapter to obtain the optical response of semi-conductors and insulators including electron-hole correlations beyond the independent particle approximation.

3.4.2 The Hartree Approximation

The Hartree approximation, which describes the motion of particles in the system as that of free particles in a self-consistent potential field, is the simplest non-perturbative approximation for G. We obtain the Hartree approximation by setting the self-energy operator in equation (3.57) equal to zero. Then, the interaction kernel Ξ is simply the functional derivative of the Hartree potential V_H, which is given by the bare Coulomb potential v

$$\Xi(3,3',4,4') = -\delta(3,3')\delta(4,4')v(3,4). \tag{3.61}$$

Equivalently, the Hartree approximation is characterized by the fact that the two-particle Green's function G_2 is just the product of two one-particle Green's functions. We note that the interaction kernel in Eq. (3.61) obviously satisfies the symmetry condition (3.60). Therefore, the corresponding solutions fulfill all relevant conservation laws. We will see in Sec. (4.3.3) how the Hartree approximation leads to the polarization function in the random phase approximation.

3.4.3 The Screened Interaction Approximation

In this section, we consider a better approximation to the interaction kernel Ξ that already includes correlation effects between the two excited particles. We evaluate Ξ by choosing the GW approximation for the self energy as given in Eq. (3.43), and take the functional derivative with respect to G. Additionally, accounting for the Hartree potential as in the previous section, we obtain

$$\begin{aligned}\Xi(3,3',4,4') &= -i\,\delta(3,3')\delta(4,4')v(3,4) + i\,\delta(3,4)\delta(3',4')W(3,3') \\ &+ i\,G(4,4')\frac{\delta W(4,4')}{\delta G(3,3')}.\end{aligned} \tag{3.62}$$

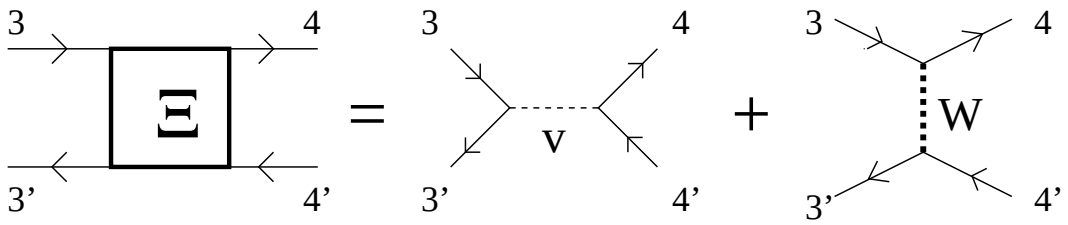

Figure 3.3: The electron-hole interaction kernel in the GW approximation. The first term accounts for a repulsive exchange interaction, whereas the second screened interaction term is responsible for the attractive nature of the electron-hole correlations.

The first term in (3.62) describes the repulsive and unscreened exchange interaction, whereas the second term is responsible for the electron-hole attraction. This term contains the screened interaction W defined in Eq. (3.44). These two diagrams are also depicted in Fig (3.3). The third term contains information about the change in screening due to the excitation, and is very difficult to evaluate. It is generally believed, however, that this latter term is small compared to the other two terms [27, 28]. Therefore, it will be neglected in the numerical evaluation of the Bethe-Salpeter equation as described in Sec. 4.3. Moreover, Ξ satisfies the symmetry relation (3.60) which shows that the approximation is again conserving.

Chapter 4

Linear Optical Response

The aim of this chapter is to set up methods that will enable us to calculate the linear optical response of periodic solids from first principles. As a prerequisite, we discuss the microscopic Maxwell equations in the first section. There, we introduce the concept of the dielectric matrix and discuss some of its general properties.

Following the work of Ehrenreich [70], Adler [42], and Wiser [43], we then describe the linear optical properties of solids in terms of the self-consistent field method. Ehrenreich and Cohen [70] derived an expression for the dielectric function of solids by assuming that electrons and holes move *independently* of each other in a self-consistent potential arising from the externally applied electric field plus a screening field. This is the widely-used random phase approximation (RPA) or equivalently the time-dependent Hartree-approximation. Adler [42] and Wiser [43] generalized the RPA description by allowing the screening field to vary on an atomic scale, giving rise to the so-called *local field* corrections. A presentation of the optical properties of solids on the RPA level can, for instance, be found in a book by Wooten [71].

In the last section, we go beyond the RPA by including excitonic effects. These electron-hole interactions have important consequences in the description of the optical properties of semiconductors and insulators. In order to include these electron-hole correlation effects we make use of the Green's function techniques presented in the previous chapter. We show how the Bethe-Salpeter equation for the two-particle correlation function can be utilized in order to obtain optical spectra of solids including both, local-field as well as excitonic effects. This is achieved by expanding the electron-hole correlation function in terms of quasi-particle wave functions, which leads to an eigenvalue equation for the excitation energies and wave functions [27, 28].

4.1 Maxwell Equations

4.1.1 Microscopic Maxwell Equations

We start the discussion by reviewing the basic equations of electrodynamics in the presence of matter and on a microscopic (atomic) scale. They can be written in the form

$$\nabla \mathbf{D} = 4\pi\rho_{ex} \tag{4.1}$$

$$\nabla \times \mathbf{E} = -\frac{\partial \mathbf{B}}{\partial t} \tag{4.2}$$

$$\nabla \mathbf{B} = 0 \tag{4.3}$$

$$\nabla \times \mathbf{B} = \mathbf{j}_{ex} + \frac{\partial \mathbf{D}}{\partial t}, \tag{4.4}$$

where the electric displacement $\mathbf{D}$ is connected to the electric field $\mathbf{E}$ via the polarization $\mathbf{P}$, as $\mathbf{D} = \mathbf{E} + \mathbf{P}$. The Maxwell equations in the form (4.1–4.4) correspond to systems which are described by the external charge density ρ_{ex} with the current density $\mathbf{j}_{ex}$. Thus, the fields entering the Maxwell equations are *difference* fields between the perturbed and the unperturbed system. Moreover, we assume that magnetic effects are not important in the systems under study. Therefore, we have set the magnetic permeability $\mu = 1$. The most general form of the dielectric tensor ϵ is defined by *linearly* relating the electric displacement $\mathbf{D}$ to the electric field $\mathbf{E}$

$$D_i(\mathbf{r}, t) = \int \mathrm{d}^3 r' \mathrm{d}t' \epsilon_{ij}(\mathbf{r}, \mathbf{r}'; t - t') E_j(\mathbf{r}', t'). \tag{4.5}$$

Note that ϵ_{ij} is a tensor of second rank for crystals other than cubic symmetry, and we have used the summation convention for double appearing indices j in the above equation. In a perfect crystal, we have translational symmetry, and the dielectric tensor remains unchanged when both coordinates, $\mathbf{r}$ and $\mathbf{r}'$, are shifted by a lattice vector $\mathbf{R}$. Hence,

$$\epsilon_{ij}(\mathbf{r} + \mathbf{R}, \mathbf{r}' + \mathbf{R}; t - t') = \epsilon_{ij}(\mathbf{r}, \mathbf{r}'; t - t'), \tag{4.6}$$

and the dielectric tensor can be Fourier analyzed with the following convention to be used for all lattice-periodic two-point functions in this thesis (see also Appendix A.1)

$$\epsilon_{ij}(\mathbf{r}, \mathbf{r}'; t - t') = \frac{1}{\Omega} \sum_{\mathbf{q}} \sum_{\mathbf{G}\mathbf{G}'} e^{-i[(\mathbf{q}+\mathbf{G})\mathbf{r} - \omega t]} \epsilon_{ij}(\mathbf{q} + \mathbf{G}, \mathbf{q} + \mathbf{G}'; \omega) e^{i[(\mathbf{q}+\mathbf{G}')\mathbf{r}' - \omega t]}. \tag{4.7}$$

Here, $\mathbf{q}$ is a vector within the first Brillouin zone, $\mathbf{G}$ and $\mathbf{G}'$ are reciprocal lattice vectors, and Ω denotes the crystal volume. By transforming $\mathbf{D}$ and $\mathbf{E}$ to reciprocal space and to the frequency domain, and using the Fourier expansion for ϵ,

expression (4.5) can be written as

$$D_i(\mathbf{q}+\mathbf{G};\omega) = \sum_{\mathbf{G}'} \epsilon_{ij}(\mathbf{q}+\mathbf{G},\mathbf{q}+\mathbf{G}';\omega) E_j(\mathbf{q}+\mathbf{G}';\omega). \tag{4.8}$$

Eq. (4.8) can be interpreted in the following intuitive way: The $(\mathbf{q},\omega)$ Fourier component of the dielectric displacement $\mathbf{D}$ is a vector in the reciprocal lattice vectors $\mathbf{G}$, and the same is true for the electric field. Then, the $(\mathbf{q},\omega)$ component of the dielectric displacement $\mathbf{D}$ is related to the $(\mathbf{q},\omega)$ component of the electric field via a matrix multiplication with the dielectric matrix corresponding to $(\mathbf{q},\omega)$, and having the matrix indices $\mathbf{G}\mathbf{G}'$.

4.1.2 Longitudinal and Transverse Dielectric Tensor

In this section, we follow a practice introduced by Lindhard [72] and describe the dielectric response in terms of the longitudinal and the transverse dielectric tensor describing the response to a longitudinal and transverse electric field, respectively. In the case of a homogeneous system, for instance the free-electron gas, a longitudinal (transverse) current can not be induced by a transverse (longitudinal) electric field. Consequently, the longitudinal and transverse dielectric tensors give a complete description of the linear dielectric properties of the homogeneous electron gas. In *inhomogeneous* systems, such as periodic solids, however, a purely transverse or purely longitudinal electric field induces both transverse and longitudinal currents. We are interested in the response to an optical perturbation, which is a transverse electro-magnetic field. Therefore, the optical properties have to be calculated using the transverse-response formalism, with a term $\mathbf{A}\cdot\mathbf{p}$ as perturbation. Here, $\mathbf{A}$ denotes the vector potential, and $\mathbf{p}$ is the momentum operator. In the *limit of vanishing* $\mathbf{q}$ vectors, however, it can be shown that a longitudinal perturbation described by a scalar potential leads to the same result. This property is referred to as the gauge invariance of optical properties and was shown by Ambegaokar and Kohn [73] for cubic crystals, and by Del Sole and Fiorino [74] for systems with lower than cubic symmetry. For this reason, it is sufficient to consider the longitudinal dielectric tensor, if one is interested only in the limit $\mathbf{q}\to\mathbf{0}$. Therefore, we will restrict the discussion in the following sections to the description of the longitudinal dielectric function only.

4.1.3 Macroscopic Quantities

When we are interested in the response to an optical perturbation, we are interested in the *average* response of the system due to the large wave length of light in the visible region as compared to an atomic scale. We define the macroscopic

quantity f_M corresponding to its microscopic counterpart f by averaging the microscopic quantity over one unit cell. We can express f in terms of the Fourier representation such that

$$f(\mathbf{r}) = \frac{1}{\Omega} \sum_{\mathbf{qG}} f_{\mathbf{G}}(\mathbf{q}) e^{-i(\mathbf{q}+\mathbf{G})\mathbf{r}}. \tag{4.9}$$

The average over one unit cell with volume Ω_0 at the position $\mathbf{R}$ defines the macroscopic quantity in the following way

$$f_M(\mathbf{R}) = \frac{1}{\Omega_0} \int_{\Omega_0} \mathrm{d}^3 r f(\mathbf{r}+\mathbf{R}). \tag{4.10}$$

Taking into account the definition (4.9) and using the fact that $|\mathbf{q}|$ is assumed to be much smaller than $|\mathbf{G}|$, the term $e^{-i\mathbf{qr}}$ is approximately 1, which leads to the result

$$f_M(\mathbf{R}) = \sum_{\mathbf{q}} f_{\mathbf{0}}(\mathbf{q}) e^{-i\mathbf{qR}}. \tag{4.11}$$

The above relation simply says that the $\mathbf{q}$ Fourier component of any macroscopic quantity is just the $\{\mathbf{q}, \mathbf{G} = \mathbf{0}\}$ component of the corresponding microscopic quantity. We will make use of this result in the next sections, when we derive an expression for the macroscopic dielectric function.

4.2 The Self-Consistent Field Method

4.2.1 Linearization of the Liouville Equation

In this section, we want to describe the longitudinal dielectric response of solids. As a motivation, we discuss the optical response first within the *independent* particle approximation, before we include electron-hole correlations in Section 4.3. We follow the derivation of the the longitudinal dielectric matrix for periodic crystals in the random phase approximation as given by Adler and Wiser [42, 43]. An alternative description using field theoretical techniques is due to Nozieres and Pines [75–77]. The starting point for the discussion is the single particle Liouville–von-Neumann equation

$$i\frac{\partial \hat{\rho}}{\partial t} = [\hat{H}, \hat{\rho}]. \tag{4.12}$$

Here, $\hat{\rho}$ denotes the density operator of the system and the Hamiltonian $\hat{H}$ consists of a time-independent part $\hat{H}_0$ describing the unperturbed system plus the self-consistent potential $V(\mathbf{r}, t)$

$$\hat{H} = \hat{H}_0 + V(\mathbf{r}, t). \tag{4.13}$$

The self-consistent potential $V(\mathbf{r}, t)$ in turn is the sum of the externally applied potential V_{ext} and the screening potential V_s due to the rearrangement of the electrons in response to the external perturbation

$$V(\mathbf{r}, t) = V_{ext}(\mathbf{r}, t) + V_s(\mathbf{r}, t). \tag{4.14}$$

Note that we have assumed the response V_s to be a classical electro-static screening potential, and we did not allow for exchange and correlation effects here. This approximation accounts for the fact that we treat electrons and holes as independent particles. It is assumed that the motion of the electrons in the unperturbed case can be described by an effective single-particle potential such as the Kohn-Sham potential of density functional theory, which we write in the form[1]

$$\hat{H}_0|n\mathbf{k}\rangle = \varepsilon_{n\mathbf{k}}|n\mathbf{k}\rangle. \tag{4.15}$$

Here, $|n\mathbf{k}\rangle$ denotes the Bloch state of band number n and wave vector $\mathbf{k}$ with the single-particle energy $\varepsilon_{n\mathbf{k}}$. The action of the density operator of the unperturbed system $\hat{\rho}_0$ on the eigenstates $|n\mathbf{k}\rangle$ is given by

$$\hat{\rho}_0|n\mathbf{k}\rangle = f_0(\varepsilon_{n\mathbf{k}})|n\mathbf{k}\rangle, \tag{4.16}$$

where f_0 is the Fermi-Dirac distribution function. We now assume that the density operator of the perturbed system can be written as

$$\hat{\rho} = \hat{\rho}_0 + \hat{\rho}_1, \tag{4.17}$$

where $\hat{\rho}_1$ denotes the density change due the perturbation. By neglecting a term $[V, \hat{\rho}_1]$, containing products of the density change and the self-consistent perturbing potential, we obtain – per definitionem – the linear response regime, and arrive at the linearized form of the Liouville equation for the density change $\hat{\rho}_1$

$$i\frac{\partial \hat{\rho}_1}{\partial t} = [\hat{H}_0, \hat{\rho}_1] + [V, \hat{\rho}_0]. \tag{4.18}$$

Moreover, we assume that the time dependence of the external potential V_{ext} is given by

$$V_{ext} \sim e^{-i\omega' t} e^{\delta t} = e^{-i\omega t}, \tag{4.19}$$

where δ is an infinitesimal positive number producing an adiabatic switching on of the perturbation. In the following it is understood that ω contains the appropriate infinitesimal δ. In the linear response regime all quantities exhibit the same time dependence as the external perturbation. Taking the matrix elements

[1] We will discuss the modifications of the present theory due to the exchange-correlation term of density functional theory in Section 4.2.6.

of Eq. (4.18) between the states $\langle l\mathbf{k}|$ and $|m\mathbf{k}+\mathbf{q}\rangle$, using the relations (4.15) and (4.16), and taking into account the $e^{-i\omega t}$ time dependence leads to

$$\langle l\mathbf{k}|\hat{\rho}_1|m\mathbf{k}+\mathbf{q}\rangle = \frac{f_0(\varepsilon_{m\mathbf{k}+\mathbf{q}}) - f_0(\varepsilon_{l\mathbf{k}})}{\varepsilon_{m\mathbf{k}+\mathbf{q}} - \varepsilon_{l\mathbf{k}} - \omega}\langle l\mathbf{k}|V|m\mathbf{k}+\mathbf{q}\rangle. \tag{4.20}$$

Hence, we have found a relation between the induced density and the self-consistent potential from which we will get the polarizability of the system.

4.2.2 Inclusion of Local Fields

In order to evaluate expression (4.20) further, we represent the potential V as a Fourier series. The external potential V_{ext} is expected to spatially vary only on a macroscopic scale, whereas we must allow the total perturbing potential V to vary on a microscopic scale. This is due to the fact that the screening fields of an inhomogeneous electron system due to a macroscopic external electric field vary on an atomic scale. These are the so-called local fields. For this reason, the spatial Fourier transform of the self-consistent potential must be written in the form

$$V(\mathbf{r}) = \frac{1}{\Omega}\sum_{\mathbf{q}}\sum_{\mathbf{G}} V_{\mathbf{G}}(\mathbf{q})e^{-i(\mathbf{q}+\mathbf{G})\mathbf{r}}, \tag{4.21}$$

including a sum over reciprocal lattice vectors $\mathbf{G}$ accounting for the variation of $V(\mathbf{r})$ on an atomic scale. Insertion of (4.21) into the right hand side of (4.20) gives

$$\langle l\mathbf{k}|\hat{\rho}_1|m\mathbf{k}+\mathbf{q}\rangle = \frac{f_0(\varepsilon_{m\mathbf{k}+\mathbf{q}}) - f_0(\varepsilon_{l\mathbf{k}})}{\varepsilon_{m\mathbf{k}+\mathbf{q}} - \varepsilon_{l\mathbf{k}} - \omega}\sum_{\mathbf{G}} V_{\mathbf{G}}(\mathbf{q})M_{lm}^{\mathbf{G}}(\mathbf{k},\mathbf{q}), \tag{4.22}$$

where we have introduced the abbreviation $M_{lm}^{\mathbf{G}}(\mathbf{k},\mathbf{q})$ for the matrix elements

$$M_{lm}^{\mathbf{G}}(\mathbf{k},\mathbf{q}) = \langle l\mathbf{k}|e^{-i(\mathbf{q}+\mathbf{G})\mathbf{r}}|m\mathbf{k}+\mathbf{q}\rangle. \tag{4.23}$$

Note that the sum over $\mathbf{q}$ in equation (4.21) has dropped out in expression (4.22) due to the conservation of crystal momentum. The induced charge density denoted by n can be obtained by using the relation

$$\begin{aligned} n(\mathbf{r}) &= \mathrm{Tr}[\delta(\mathbf{r}-\mathbf{r}_e)\hat{\rho}_1] \\ &= \sum_{\mathbf{q}}\sum_{lm\mathbf{k}} \psi^*_{m\mathbf{k}+\mathbf{q}}(\mathbf{r})\psi_{l\mathbf{k}}(\mathbf{r})\langle l\mathbf{k}|\hat{\rho}_1|m\mathbf{k}+\mathbf{q}\rangle. \end{aligned} \tag{4.24}$$

Transforming n to reciprocal space gives

$$n_{\mathbf{G}}(\mathbf{q}) = \sum_{lm\mathbf{k}} \left[M_{lm}^{\mathbf{G}}(\mathbf{k},\mathbf{q})\right]^* \langle l\mathbf{k}|\hat{\rho}_1|m\mathbf{k}+\mathbf{q}\rangle, \tag{4.25}$$

where we have again made use of the definition of the matrix elements $M_{lm}^{\mathbf{G}}(\mathbf{k},\mathbf{q})$ in Eq. (4.23). Finally we insert (4.22) into the right hand side of Eq. (4.25) to obtain a relation between the induced charge density n and the total perturbing potential V

$$n_{\mathbf{G}}(\mathbf{q},\omega) = \sum_{\mathbf{G}'} \hat{P}^0_{\mathbf{G}\mathbf{G}'}(\mathbf{q},\omega) V_{\mathbf{G}'}(\mathbf{q},\omega) \tag{4.26}$$

$$\hat{P}^0_{\mathbf{G}\mathbf{G}'}(\mathbf{q},\omega) = \frac{1}{\Omega}\sum_{lm\mathbf{k}} \frac{f_0(\varepsilon_{m\mathbf{k}+\mathbf{q}}) - f_0(\varepsilon_{l\mathbf{k}})}{\varepsilon_{m\mathbf{k}+\mathbf{q}} - \varepsilon_{l\mathbf{k}} - \omega} \left[M_{lm}^{\mathbf{G}}(\mathbf{k},\mathbf{q})\right]^* M_{lm}^{\mathbf{G}'}(\mathbf{k},\mathbf{q}). \tag{4.27}$$

Here, the summation over states is understood to include both spin directions. The polarization $\hat{P}^0$ can be interpreted as a matrix with indices $(\mathbf{G},\mathbf{G}')$ that relates the self-consistent potential, expressed as a vector in $\mathbf{G}'$, to the induced density via a matrix multiplication. Due to the translational symmetry of the crystal, perturbations with wave vector $\mathbf{q}$ couple only to density changes belonging to the same vector $\mathbf{q}$. The definition of the irreducible polarization $\hat{P}$ is given as the variation of the density with respect to the total potential, whereas the complete polarization P is defined as the variation of the density with respect to the external potential. Consequently, P is the density-density correlation function.

$$\hat{P} = \frac{\delta n}{\delta V} \tag{4.28}$$

$$P = \frac{\delta n}{\delta V_{ext}} \tag{4.29}$$

Thus, we identify $\hat{P}^0$ from Eq. (4.27) as the irreducible polarization in the independent particle approximation. The approximation of *independent* particles can be traced back to Eq. (4.14). There, we assumed the response to the external potential to consist of an electro-static screening field only. This corresponds to the time-dependent Hartree approximation. In order to obtain an expression for the longitudinal dielectric tensor we use an alternative definition of ϵ which is equivalent to that of Eq. (4.8). The dielectric function is defined by relating the external potential V_{ext} to the total potential V in the way

$$V_{ext} = \epsilon V. \tag{4.30}$$

The screening potential V_s is related to the density change n via Poisson's equation which reads in reciprocal space

$$V^s_{\mathbf{G}}(\mathbf{q}) = v(\mathbf{q}+\mathbf{G}) n_{\mathbf{G}}(\mathbf{q}), \tag{4.31}$$

v denoting the Coulomb potential. Inserting (4.31) into (4.26) and using the fact that the total potential is the sum of the external and the screening potential leads to

$$V^{ext}_{\mathbf{G}}(\mathbf{q}) = \sum_{\mathbf{G}'} \left[\delta_{\mathbf{G}\mathbf{G}'} - v(\mathbf{q}+\mathbf{G}')\hat{P}^0_{\mathbf{G}\mathbf{G}'}(\mathbf{q},\omega)\right] V_{\mathbf{G}}(\mathbf{q}). \tag{4.32}$$

Comparison with Eq. (4.30) shows that the microscopic dielectric matrix is given by

$$\epsilon_{\mathbf{G}\mathbf{G}'}(\mathbf{q},\omega) = \delta_{\mathbf{G}\mathbf{G}'} - v(\mathbf{q}+\mathbf{G}')\hat{P}^0_{\mathbf{G}\mathbf{G}'}(\mathbf{q},\omega). \tag{4.33}$$

In order to obtain the macroscopic dielectric function ϵ_M we have to take the average of equation (4.32) over one unit cell as described in Sec. 4.1.3. Note that the external potential is assumed to have a long wave length compared to the unit cell dimensions, and therefore

$$V^{ext}_{\mathbf{G}}(\mathbf{q}) = \delta_{\mathbf{G},\mathbf{0}} V^{ext}(\mathbf{q}). \tag{4.34}$$

In order to use the above relation we introduce the inverse of the dielectric matrix as

$$\sum_{\mathbf{G}''} \epsilon_{\mathbf{G}\mathbf{G}''}(\mathbf{q},\omega)\epsilon^{-1}_{\mathbf{G}''\mathbf{G}'}(\mathbf{q},\omega) = \delta_{\mathbf{G}\mathbf{G}'}. \tag{4.35}$$

We can invert Eq. (4.32) with the above definition, and set $\mathbf{G} = \mathbf{0}$

$$V_{\mathbf{0}}(\mathbf{q}) = \epsilon^{-1}_{\mathbf{0}\mathbf{0}}(\mathbf{q},\omega) V^{ext}_{\mathbf{0}}(\mathbf{q}). \tag{4.36}$$

Remembering that the $\mathbf{G} = \mathbf{0}$ components of the microscopic fields are just the corresponding macroscopic quantities, and using the definition of the dielectric function as given in Eq. (4.30) shows that the macroscopic dielectric function is given by the $\{\mathbf{G} = \mathbf{0}, \mathbf{G}' = \mathbf{0}\}$ component of the *inverse* dielectric matrix, thus

$$\epsilon_M(\mathbf{q},\omega) = \frac{1}{\epsilon^{-1}_{\mathbf{0}\mathbf{0}}(\mathbf{q},\omega)}. \tag{4.37}$$

Summing up we have seen that the computation of the microscopic dielectric matrix in the random phase approximation involves the calculation of the irreducible polarization in the independent particle approximation as given by Eq. (4.27). In order to obtain the macroscopic dielectric function the dielectric matrix has to be inverted for the reasons stated above. The computation of the whole dielectric matrix together with its inversion is a major computational effort. Therefore, the next subsection is devoted to a simplified description of the linear optical response where local field effects are neglected.

4.2.3 Neglecting Local Fields

The approximation that will be used in this section and which greatly simplifies the computation of the macroscopic dielectric function is the following: The macroscopic external perturbation which is described by the scalar potential V_{ext} only produces a screening potential V_s on a macroscopic scale. Therefore, both V_{ext} and V_s as well as the total perturbing potential V can be expressed in a Fourier series

$$V(\mathbf{r},t) = \sum_{\mathbf{q}} V(\mathbf{q},t) e^{-i\mathbf{q}\mathbf{r}}. \tag{4.38}$$

Here, no summation over rapidly varying $\mathbf{G}$ Fourier components are necessary. In analogy to the procedure of the previous subsection we can derive an expression for the polarization $\hat{P}^0$ that is relating the change in the density n to the total potential V. Instead of Eqs. (4.26) and (4.27) we derive the simpler expressions

$$n(\mathbf{q},\omega) = \hat{P}^0(\mathbf{q},\omega)V(\mathbf{q},\omega) \tag{4.39}$$

$$\hat{P}^0(\mathbf{q},\omega) = \frac{1}{\Omega}\sum_{lm\mathbf{k}} \frac{f_0(\varepsilon_{m\mathbf{k}+\mathbf{q}}) - f_0(\varepsilon_{l\mathbf{k}})}{\varepsilon_{m\mathbf{k}+\mathbf{q}} - \varepsilon_{l\mathbf{k}} - \omega} \left[M^{\mathbf{0}}_{lm}(\mathbf{k},\mathbf{q})\right]^* M^{\mathbf{0}}_{lm}(\mathbf{k},\mathbf{q}). \tag{4.40}$$

Application of Poisson's equation and using the definition (4.30) directly leads to the macroscopic dielectric function

$$\epsilon_M(\mathbf{q},\omega) = 1 + v(\mathbf{q})\hat{P}^0(\mathbf{q},\omega). \tag{4.41}$$

Compared to the corresponding expression (4.37) where local field effects have been taken into account, the above expression is considerably easier to evaluate, because only the $\mathbf{G} = \mathbf{G}' = \mathbf{0}$ component of the irreducible polarization $\hat{P}^0$ has to be computed, and moreover no matrix inversion is involved.

4.2.4 The Long Wavelength Limit

Our main interest in this chapter is to describe the linear response of solids to *optical* perturbations. Since the wave length of electro-magnetic waves at optical frequencies is much larger than the characteristic momenta in solids, optical perturbations can be described by taking the limit of vanishing $\mathbf{q}$ vectors. On account of the Coulomb potential appearing for instance in Eq. (4.41) this limit has to be taken analytically, because simply setting $\mathbf{q} = \mathbf{0}$ would result in an indeterminate expression for the dielectric function. This follows from the fact that the matrix elements $M^{\mathbf{0}}_{lm}(\mathbf{k},\mathbf{q})$ entering Eq. (4.40) are given by Kronecker deltas, when $\mathbf{q}$ is identically $\mathbf{0}$

$$M^{\mathbf{0}}_{lm}(\mathbf{k},\mathbf{q}=\mathbf{0}) = \delta_{lm}. \tag{4.42}$$

The reason is of course the fact that the normalized Bloch states belonging to different bands are orthogonal to each other. We can, however, derive an expression for the matrix elements $M^{\mathbf{0}}_{lm}(\mathbf{k},\mathbf{q})$ in the limit of vanishing wave vector $\mathbf{q}$ by using $\mathbf{k}\cdot\mathbf{p}$ perturbation theory. One obtains

$$M^{\mathbf{0}}_{lm}(\mathbf{k},\mathbf{q}\to\mathbf{0}) = \delta_{lm} + \frac{\langle l\mathbf{k}|\mathbf{q}\mathbf{p}|m\mathbf{k}\rangle}{\varepsilon_{m\mathbf{k}} - \varepsilon_{l\mathbf{k}}}(1-\delta_{lm}), \tag{4.43}$$

where $\mathbf{p}$ denotes the momentum operator. Before, we insert this relation into expression (4.40), we want to adjust our description to the special case of semiconducting or insulating crystals. In that case, the Fermi-Dirac distributions

function f_0 are either 0 or 1, and the summation over bands runs over occupied valence bands (v) and unoccupied conduction bands (c) separately. Rewriting the summations in such a way produces a factor of 2, when compared to Eq. (4.40). Moreover, we assume that the materials under study are spin-degenerate which is taken into account by an additional factor of 2. Thus, making use of the relation (4.43) we get an expression for the polarization in the limit of small $\mathbf{q}$

$$\hat{P}^0(\mathbf{q} \to \mathbf{0}, \omega) = 4q^2 \sum_{vc\mathbf{k}} \frac{\langle v\mathbf{k}|p_i|c\mathbf{k}\rangle\langle c\mathbf{k}|p_j|v\mathbf{k}\rangle}{(\varepsilon_{c\mathbf{k}} - \varepsilon_{v\mathbf{k}} - \omega)(\varepsilon_{c\mathbf{k}} - \varepsilon_{v\mathbf{k}})^2}. \tag{4.44}$$

Remembering that the frequency ω contains the infinitesimal imaginary number $i\delta$, we can use the identity

$$\mathrm{Im}\frac{1}{\varepsilon_{c\mathbf{k}} - \varepsilon_{v\mathbf{k}} - \omega + i\delta} = -\pi\,\delta(\varepsilon_{c\mathbf{k}} - \varepsilon_{v\mathbf{k}} - \omega). \tag{4.45}$$

We finally arrive at an expression for the imaginary part of the macroscopic dielectric function in the independent particle approximation where local field effects are neglected

$$\mathrm{Im}\epsilon_M(\mathbf{q} \to \mathbf{0}, \omega) = \frac{16\pi^2}{\Omega\omega^2} \sum_{vc\mathbf{k}} \langle v\mathbf{k}|p_i|c\mathbf{k}\rangle\langle c\mathbf{k}|p_j|v\mathbf{k}\rangle\delta(\varepsilon_{c\mathbf{k}} - \varepsilon_{v\mathbf{k}} - \omega). \tag{4.46}$$

Note that the prefactor $1/\omega^2$ is a consequence of the square of the energy difference in the denominator of Eq. (4.44) and the delta function due to the replacement (4.45). It is important to note that the quantity in the above expression is actually a tensor, on account of the momentum operators p_i and p_j. This is somewhat surprising because we started our derivation with the aim to obtain the longitudinal dielectric function. In fact, it has been shown that in the limit of vanishing $\mathbf{q}$, the response to a transverse perturbation is equivalent to that of a longitudinal perturbation, as has already been discussed in Sec. 4.1.2. This is not only true for cubic systems [73] but also for crystals with lower symmetry [74]. For that reason, Eq. (4.46) describes the response to an optical perturbation, where the tensor character of $\epsilon_M(\mathbf{q} \to \mathbf{0}, \omega)$ takes into account the anisotropy of crystals with symmetries lower than cubic. We note that the real part of ϵ_M can be obtained by using the well-known Kramers-Kronig relations.

4.2.5 The Independent Quasi-Particle Approximation

So far we did not specify the single-particle wave functions $|n\mathbf{k}\rangle$ and energies $\varepsilon_{n\mathbf{k}}$ to be used in the evaluation of the dielectric response outlined in the preceding sections. An obvious – but at the same time little justified – choice is to use Kohn-Sham orbitals and energies for $|n\mathbf{k}\rangle$ and $\varepsilon_{n\mathbf{k}}$. The problem is of course that the Kohn-Sham energies can not be interpreted as the excitation spectrum of the

system under study. For instance, it is a well known fact that the Kohn-Sham band gap of semi-conductors and insulators underestimates the physical gap by roughly 50% (see discussion in Sec. 2.6). On the other hand, a great number of electron self-energy calculations on the GW level have shown that

(i) the quasi-particle wave functions as obtained from GW calculations have almost perfect overlap with the corresponding Kohn-Sham orbitals [57, 78, 79], and

(ii) in many cases the corrections to the Kohn-Sham energies obtained by evaluating the self-energy operator, result in a rigid upward shift of the conduction bands (*scissors operator*) [59].

This suggests to use scissors-operator corrected Kohn-Sham energies, and Kohn-Sham orbitals in the evaluation of the dielectric function. However, care must be taken due to the non-locality of the self-energy operator even when approximated as a simple rigid shift of the conduction bands. Levine and Allen [78, 79], and Del Sole and Girlanda [80] have shown that one has to carefully define the velocity operator in the way

$$\mathbf{v} = i[H, \mathbf{r}] \tag{4.47}$$

to get results that are invariant with respect to the chosen gauge. The above definition of the velocity operator will differ from the usual choice $\mathbf{v} = \mathbf{p}/m$ if the Hamiltonian H contains a *non-local* potential as is the case when H includes the non-local self-energy. Then it can be shown that the corresponding relation to (4.46) for the transverse macroscopic dielectric tensor $\epsilon_{ij}(\omega)$ in the independent *quasi-particle* approximation is given by [80]

$$\mathrm{Im}\epsilon_{ij}(\omega) = \frac{16\pi^2}{\Omega\omega^2} \sum_{vc\mathbf{k}} \langle v\mathbf{k}|p_i|c\mathbf{k}\rangle\langle c\mathbf{k}|p_j|v\mathbf{k}\rangle \times \left(\frac{E_{c\mathbf{k}} - E_{v\mathbf{k}}}{\varepsilon_{c\mathbf{k}} - \varepsilon_{v\mathbf{k}}}\right)^2 \times \delta(E_{c\mathbf{k}} - E_{v\mathbf{k}} - \omega). \tag{4.48}$$

Here $|v\mathbf{k}\rangle$ and $|c\mathbf{k}\rangle$ denote quasi-particle wave functions which are very well approximated by Kohn-Sham orbitals. The Kohn-Sham valence and conduction band energies are given by $\varepsilon_{v\mathbf{k}}$ and $\varepsilon_{c\mathbf{k}}$, respectively, whereas $E_{v\mathbf{k}}$ and $E_{c\mathbf{k}}$ denote the corresponding quasi-particle energies.[2] The above result can be interpreted in terms of a renormalized transition matrix element which is corrected for the non-locality in the self-energy operator

$$\langle v\mathbf{k}|\mathbf{p}|c\mathbf{k}\rangle^{\mathrm{QP}} = \frac{E_{c\mathbf{k}} - E_{v\mathbf{k}}}{\varepsilon_{c\mathbf{k}} - \varepsilon_{v\mathbf{k}}} \langle v\mathbf{k}|\mathbf{p}|c\mathbf{k}\rangle. \tag{4.49}$$

We point out that a naive approach, not concerned about non-locality and gauge invariance, where *only* the Kohn-Sham energies are replaced by corresponding

[2]The quasi-particle energies $E_{v\mathbf{k}}$ and $E_{c\mathbf{k}}$ are not necessarily connected to the Kohn-Sham energies by a simple scissors shift, but are in general the solutions of the Dyson equation.

quasi-particle ones *without* the re-normalization (4.49) would, for instance, give systematically to small results for the static dielectric constant. We obtain a particularly simple result when we can approximate the self-energy corrections to the Kohn-Sham energies by a rigid, **k**-independent upward shift Δ of the conduction bands (scissors operator approximation). Then we obtain from Eq. (4.48) the result

$$\mathrm{Im}\epsilon_{ij}(\omega) = \frac{16\pi^2}{\Omega(\omega-\Delta)^2}\sum_{vc\mathbf{k}}\langle v\mathbf{k}|p_i|c\mathbf{k}\rangle\langle c\mathbf{k}|p_j|v\mathbf{k}\rangle \times \delta(\varepsilon_{c\mathbf{k}} - \varepsilon_{v\mathbf{k}} + \Delta - \omega). \quad (4.50)$$

This demonstrates the simple, but not at all trivial result, that the dielectric function in the independent quasi-particle approximation using a scissors operator can be obtained from the LDA dielectric function by simply shifting the imaginary part of ϵ by the band gap correction Δ to higher energies. Thus, we can write

$$\mathrm{Im}\epsilon_{ij}^{\mathrm{QP}}(\omega) = \mathrm{Im}\epsilon_{ij}^{\mathrm{LDA}}(\omega - \Delta). \quad (4.51)$$

So far, we have treated electrons and holes as *independent* particles during the excitation process, thereby neglecting exchange-correlation effects.

4.2.6 Dielectric Response within DFT

In this section, we want to consider exchange-correlation (XC) effects in the response function resulting from the XC energy appearing in density functional theory. To this end, we have to add to the classical, electro-static screening potential V_s a term V_{xc} stemming from the *change* in the exchange-correlation potential (2.13) due to the external perturbation given by the scalar potential V_{ext}. Thus, we can write for the self-consistent potential V

$$V = V_{ext} + V_s + V_{xc}, \quad (4.52)$$

where V_s is just the Hartree potential due to the density change n, as discussed in the previous sections,

$$V_s(\mathbf{r}) = \int \mathrm{d}^3r' \frac{n(\mathbf{r}')}{|\mathbf{r}-\mathbf{r}'|}. \quad (4.53)$$

The variation of the XC potential with the density, V_{xc}, is obtained from

$$V_{xc} = \int \mathrm{d}^3r' K_{xc}(\mathbf{r},\mathbf{r}')n(\mathbf{r}'), \quad (4.54)$$

where the exchange-correlation kernel K_{xc} is defined as the functional derivative of the XC potential with respect to the density, or equivalently, as second functional derivative of the exchange-correlation *energy*,

$$K_{xc}(\mathbf{r},\mathbf{r}') = \frac{\delta^2 E_{xc}}{\delta n(\mathbf{r})\delta n(\mathbf{r}')}. \quad (4.55)$$

Taking into account the definition of the independent particle polarizability $\hat{P}^0$ as the response to the *total* change in the effective potential, and the full polarizability P as the response to the *external* potential (compare Eqs. 4.28 and 4.29), we obtain in matrix notation [78, 79, 81]

$$P = (1 - v\hat{P}^0 - K_{xc}\hat{P}^0)^{-1}\hat{P}^0. \tag{4.56}$$

This expression differs from the corresponding RPA expression used in the previous section, by the additional term $K_{xc}\hat{P}^0$ involving the exchange-correlation kernel. If the exchange-correlation energy E_{xc} is a *local* function, as is the case in the framework of density functional theory, then also the kernel K_{xc} is a local function and given by

$$K_{xc}(\mathbf{r}, \mathbf{r}') = \left.\frac{dV_{xc}}{dn}\right|_{n(\mathbf{r})} \delta(\mathbf{r} - \mathbf{r}'). \tag{4.57}$$

As a consequence of the delta function in the above equation, the reciprocal-space expression of K_{xc} is independent of $\mathbf{q}$,

$$K^{xc}_{\mathbf{G}\mathbf{G}'} = K^{xc}(\mathbf{G} - \mathbf{G}'). \tag{4.58}$$

This is an artifact of the LDA in particular, and *not* of the density-functional approach in general [81]. The LDA description of K^{xc} gives rise to an incorrect behavior, for instance, in the electron gas where K^{xc} is strongly dependent on $\mathbf{q}$ [81]. On the other hand, forms of K_{xc} that go beyond the LDA and show the correct asymptotic behavior have been shown to bring the product $K_{xc}\hat{P}^0$ to vanish for small wave vectors [24]. It is this limit, however, which is relevant for the description of optical properties. Therefore, we neglect the exchange-correlation term appearing in the polarization function in Eq. (4.56) and work with the RPA expressions when calculating the dielectric function in the framework of density functional theory. In the remaining part of the chapter, however, we develop a method to go beyond the RPA which allows us to incorporate electron-hole interactions into the description of the optical response of semi-conductors and insulators. Thereby, we will leave the density functional approach and make use of the many-body perturbation techniques presented in the previous chapter.

4.3 Inclusion of Excitonic Effects

4.3.1 Dielectric Response from the BSE

In Chapter 3 we have seen how Green's function techniques can be used to describe the single-particle excitations of a system of interacting particles. Moreover, the equation of motion for the two-particle Green's function – the Bethe-Salpeter equation – in principle contains all the information about the two particle

excitations of the system. In this and the following sections we will describe how the macroscopic optical properties can be obtained from a solution of the BSE. In particular, we will take into account electron-hole correlations that have been neglected in the description of the optical response so far. In addition, we will re-derive expressions equivalent to the RPA as presented in the previous sections starting from the Bethe-Salpeter equation by treating electrons and holes as independent particles.

We start by reviewing some basic relations well known from field theory. We have already learned in Sec. 4.2.2 that the definition of the *irreducible* polarization $\hat{P}$ in Eq. (4.28), and the *complete* polarization P in Eq. (4.29), can be given as variations of the density with respect to the self-consistent and the external potentials, respectively. The connection of $\hat{P}$ and P to the dielectric matrix ϵ is given by the following relations where matrix notation is understood

$$\epsilon = 1 - v\hat{P} \tag{4.59}$$

$$\epsilon^{-1} = 1 + vP. \tag{4.60}$$

Again, v denotes the Coulomb potential as usual and ϵ^{-1} is the inverse of the dielectric matrix. In fact, we already made use of Eq. (4.59) in the previous section when we obtained the dielectric matrix in the RPA (compare with Eq. 4.33). Equations (4.59) and (4.60) can be combined to yield a generalized Dyson's equation for the complete polarization

$$P = \hat{P} + \hat{P}vP. \tag{4.61}$$

From that expression we see that the polarization P is the sum of two contributions termed *proper* and *improper* polarization parts, respectively. The proper polarization part, which is equal to the irreducible polarization $\hat{P}$, describes just the electron-hole polarizations which are due directly to the excitations by the external applied field. The improper part, $\hat{P}vP$, contains the polarization part due to the induced field coming from the polarization of all other electron-hole pairs. On the other hand we know that the polarization P is connected to the two-particle correlation function in the way that [65]

$$P(1,2) = -iL(1,1,2,2). \tag{4.62}$$

Consequently, solving the BSE (3.55) and using (4.62) leads to the inverse of the dielectric matrix as can be seen from Eq. (4.60). Remembering that the macroscopic dielectric function is connected to the inverse dielectric matrix (see Eq. 4.37) we obtain the macroscopic optical properties without having to invert ϵ as is done in the Adler-Wiser formulation. In the next sections we will describe the steps leading from the BSE to the macroscopic dielectric function.

4.3.2 The Long-Range Part of the Coulomb Potential

For the calculation of the optical response we are interested in the long wavelength limit, thus $|\mathbf{q}| \to 0$. In this case, the term $\hat{P}vP$ in Eq. (4.61) contains divergent Coulomb factors. These divergent factors can, however, be isolated following a procedure due to AMBEGAOKAR and KOHN [73], which has also been described by HANKE [24]. We define the new polarization function $\bar{P}$ as the sum of all polarization processes *not* involving the long-range part of the Coulomb interaction. In analogy to (4.61) we obtain a generalized Dyson equation for $\bar{P}$

$$\bar{P} = \hat{P} + \hat{P}\bar{v}\bar{P}, \tag{4.63}$$

where $\bar{v}$ denotes a modified Coulomb potential defined in the way

$$\bar{v}(\mathbf{q}+\mathbf{G}) = \begin{cases} \mathbf{0} & \text{for} \quad \mathbf{G} = \mathbf{0} \\ v(\mathbf{q}+\mathbf{G}) & \text{for} \quad \mathbf{G} \neq \mathbf{0} \end{cases} . \tag{4.64}$$

It has been shown by KOHN [82] that, for insulating crystals, the irreducible polarization $\hat{P}$ is proportional to q^2 for small $\mathbf{q}$ vectors. Moreover, due to the "cut-off" Coulomb potential $\bar{v}$ the polarization function $\bar{P}$ defined above shows the same behavior as $\hat{P}$ for small $\mathbf{q}$. Thus, we can combine Eqs. (4.61) and (4.63) in order to derive the following relation between the $\mathbf{G} = \mathbf{G}' = \mathbf{0}$ components of P and $\bar{P}$ in the limit of vanishing $\mathbf{q}$

$$P_{\mathbf{00}}(\mathbf{q},\omega) = \frac{\bar{P}_{\mathbf{00}}(\mathbf{q},\omega)}{1 - v(\mathbf{q})\bar{P}_{\mathbf{00}}(\mathbf{q},\omega)}. \tag{4.65}$$

By using the above expression we can now rewrite Eq. (4.60) in the form

$$\begin{aligned} \epsilon^{-1}_{\mathbf{00}}(\mathbf{q},\omega) &= 1 + v(\mathbf{q})P_{\mathbf{00}}(\mathbf{q},\omega) \\ &= \frac{1}{1 - v(\mathbf{q})\bar{P}_{\mathbf{00}}(\mathbf{q},\omega)}. \end{aligned} \tag{4.66}$$

By the definition of the macroscopic dielectric function via the $\mathbf{G} = \mathbf{G}' = \mathbf{0}$ element of the inverse of the dielectric matrix (see Eq. 4.37), we finally obtain

$$\epsilon_M(\mathbf{q},\omega) = 1 - v(\mathbf{q})\bar{P}_{\mathbf{00}}(\mathbf{q},\omega). \tag{4.67}$$

Expression (4.67) can be evaluated by solving the Bethe-Salpeter equation (3.55) for the two-particle correlation function L and then setting the polarization P equal to L using Eq. (4.62).

4.3.3 The Dielectric Matrix in the RPA

In order to get a connection to the macroscopic dielectric function derived according to the Adler-Wiser scheme (see Sec. 4.2.2), we approximate the electron-hole

kernel Ξ by the exchange part only, and neglect for the moment the direct, attractive electron-hole term. This is the Hartree – or equivalently – the independent particle approximation. From the analysis in Sec. 3.4.2 we have obtained for the interaction kernel

$$\Xi^x(3,3',4,4') = -i\,\delta(3,3')\delta(4,4')\bar{v}(3,4). \tag{4.68}$$

Note that a Coulomb potential $\bar{v}$, where the long range has been cut off, enters the exchange interaction for the reasons that have been outlined in the previous section. When (4.68) is substituted into the Bethe-Salpeter equation (3.55), we obtain the following integral equation

$$L(1,1',2,2') = L_0(1,1',2,2') - i\int \mathrm{d}(3,4)L_0(1,1',3,3)\bar{v}(3,4)L(4,4,2,2'). \tag{4.69}$$

In order to use the connection between the correlation function L and the polarization P of Eq. (4.62), we set $1 = 1'$ and $2 = 2'$. We recall that L_0, describing the independent propagation of an electron and a hole, is given by a product of two Green's functions in the way (compare Eq. 3.56)

$$L_0(1,1',2,2') = G(1',2')G(2,1),$$

and Eq. (4.69) reduces to

$$\bar{P}(1,2) = \hat{P}^0(1,2) + \int \mathrm{d}(3,4)\hat{P}^0(1,3)\bar{v}(3,4)\bar{P}(4,2). \tag{4.70}$$

We identify the above expression as the generalized Dyson equation (4.63) for the polarization $\bar{P}$. In order to distinguish the *exact* irreducible polarization $\hat{P}$, from the irreducible polarization in the independent particle approximation, we have added a superscript 0. It is given simply as the product of two single-particle Green's functions

$$\hat{P}^0(1,2) = -iG(1,2)G(2,1). \tag{4.71}$$

We have derived the following important result: Solving the Bethe-Salpeter equation with the exchange interaction (4.68) only, and computing the macroscopic dielectric function according to (4.67) is completely equivalent to Adler-Wiser scheme with inclusion of local fields using expressions (4.27), (4.33) and (4.37). In the Adler-Wiser formulation one calculates the irreducible polarization (in the RPA), $\hat{P}^0$ according to (4.27) and obtains the dielectric matrix ϵ (see also Eq. 4.59). In this case, the inversion of the dielectric matrix is needed in order to obtain the macroscopic dielectric function. On the other hand, the solution of the BSE with the exchange term only directly yields the complete polarization and via (4.60) the inverse of ϵ, so that no matrix inversion is involved. The solution of the integral equation (4.61) for the complete polarization P is equivalent to the inversion of the dielectric matrix.

4.3.4 Reformulation of the BSE

So far we have just demonstrated a method that is equivalent to the Adler-Wiser formulation in order to obtain the macroscopic DF on the RPA level. But now we want to go a step further and include the direct electron-hole interaction term in the kernel of the BSE (see second term in Eq. 3.62). In order to simplify the numerical evaluation, we demonstrate in the discussion to follow how the BSE can be transformed from an integral equation to a matrix eigenvalue equation [28, 30, 83]. A similar derivation has also been given by ARNAUD [84]. We start by noting that we can set $t_1 = t_{1'}$ and $t_2 = t_{2'}$, because we are only interested in electron-hole excitations. So the functions L and L_0 only depend on the time difference $t_1 - t_2$, which we Fourier transform to frequency space ω. Moreover, we neglect the dynamical properties of the screened Coulomb interaction W, because it has been pointed out by BECHSTEDT [85] that dynamical effects in the electron-hole screening and in the one-particle Green's function tend to cancel each other. This suggests to neglect both of them as will be done in the subsequent discussion. Consequently, we can write the BSE symbolically as

$$L(\omega) = L_0(\omega) + L_0(\omega)\Xi L(\omega). \tag{4.72}$$

We observe that the 4-point functions L, L_0 and Ξ must obey the translational symmetry of the crystal, for instance

$$L(\mathbf{r}_1 + \mathbf{R}, \mathbf{r}'_1 + \mathbf{R}, \mathbf{r}_2 + \mathbf{R}, \mathbf{r}'_2 + \mathbf{R}; \omega) = L(\mathbf{r}_1, \mathbf{r}'_1, \mathbf{r}_2, \mathbf{r}'_2; \omega), \tag{4.73}$$

where $\mathbf{R}$ denotes a direct lattice vector. Therefore, one can express the functions L, L_0 and Ξ as a sum over functions $L_\mathbf{q}$, where $\mathbf{q}$ is a vector from the first Brillouin zone, defined in the way

$$L(\mathbf{r}_1, \mathbf{r}'_1, \mathbf{r}_2, \mathbf{r}'_2) = \sum_\mathbf{q} L_\mathbf{q}(\mathbf{r}_1, \mathbf{r}'_1, \mathbf{r}_2, \mathbf{r}'_2). \tag{4.74}$$

The function $L_\mathbf{q}$ has the lattice periodicity in each variable separately, therefore, it can be expanded in any complete set of Bloch functions. In particular, we can choose as basis functions the quasi-particle wave functions which we approximate by the Kohn-Sham orbitals $\psi_{n\mathbf{k}}$. This is suggested by the physical picture of interacting electron-hole pairs. In order to achieve a more compact notation, we abbreviate the quantum numbers $n\mathbf{k}$ with one single index i in the discussion below. We use the following convention for the expansion of $L_\mathbf{q}$ in terms of Kohn-Sham orbitals

$$L_\mathbf{q}(\mathbf{r}_1, \mathbf{r}'_1, \mathbf{r}_2, \mathbf{r}'_2) = \sum_{i_1 i_2 i_3 i_4} \psi^*_{i_1}(\mathbf{r}_1)\psi_{i_2}(\mathbf{r}'_1)\psi_{i_3}(\mathbf{r}_2)\psi^*_{i_4}(\mathbf{r}'_2)L_{(i_1 i_2),(i_3 i_4)} \tag{4.75}$$

with the abbreviations

$$(i_1 i_2) = (n_1\mathbf{k}_1, n_2\mathbf{k}_1 - \mathbf{q}) \tag{4.76}$$

$$(i_3 i_4) = (n_3\mathbf{k}_3, n_4\mathbf{k}_3 - \mathbf{q}). \tag{4.77}$$

Using expressions (4.74)–(4.77) we can rewrite the Bethe-Salpeter equation (4.72) for a fixed $\mathbf{q}$ vector in the form

$$L_{\mathbf{q}}(\omega) = L^0_{\mathbf{q}}(\omega) + L^0_{\mathbf{q}}(\omega)\Xi_{\mathbf{q}}L_{\mathbf{q}}(\omega). \tag{4.78}$$

We can identify $\mathbf{q}$ as the momentum of the external perturbation. As we are interested in optical transitions only, having approximately zero momentum transfer, we set $\mathbf{q} = \mathbf{0}$ in the following analysis.

The function L_0 describes the independent propagation of an electron and a hole, and it is given by the product of two one-particle Green's functions (see Eq. 3.56). We approximate the one-particle Green's function by its quasi-particle approximation on the GW level, given by [56, 57]

$$G(\mathbf{r}, \mathbf{r}', \omega) = \lim_{\delta\to 0^+} \sum_{n\mathbf{k}} \frac{\psi_{n\mathbf{k}}(\mathbf{r})\psi^*_{n\mathbf{k}}(\mathbf{r}')}{\omega - E_{n\mathbf{k}} + i\,\delta\,\mathrm{sgn}(E_{n\mathbf{k}} - \mu)}. \tag{4.79}$$

Here $\psi_{n\mathbf{k}}(\mathbf{r})$ are the quasi-particle wave functions (approximated by the Kohn-Sham orbitals), $E_{n\mathbf{k}}$ denote the quasi-particle energies, and μ is the chemical potential. Using the representation of the Green's function (4.79) and the Fourier transform of (3.56)

$$L_0(\mathbf{r}_1, \mathbf{r}'_1, \mathbf{r}_2, \mathbf{r}'_2, \omega) = \frac{1}{2\pi} \lim_{\delta\to 0^+} \int \mathrm{d}\omega' e^{i\delta\omega'} G(\mathbf{r}'_1, \mathbf{r}'_2, \omega')G(\mathbf{r}_2, \mathbf{r}_1, \omega' - \omega), \tag{4.80}$$

we can derive an expression for L_0 using the analytic properties of the Green's function for the integration over the frequency ω'

$$L_0(\mathbf{r}_1, \mathbf{r}'_1, \mathbf{r}_2, \mathbf{r}'_2, \omega) = i \sum_{i_1 i_2 i_3 i_4} \frac{\psi^*_{i_1}(\mathbf{r}_1)\psi_{i_2}(\mathbf{r}'_1)\psi_{i_3}(\mathbf{r}_2)\psi^*_{i_4}(\mathbf{r}'_2)}{E_{i_2} - E_{i_1} - \omega - i\delta} \times (f_{i_2} - f_{i_1})\delta_{i_1 i_3}\delta_{i_2 i_4}. \tag{4.81}$$

In the above expression we have introduced the Fermi-Dirac distribution functions f. It is interesting to note that the irreducible polarization

$$\hat{P}^0(\mathbf{r}, \mathbf{r}', \omega) = L_0(\mathbf{r}, \mathbf{r}, \mathbf{r}', \mathbf{r}', \omega) \tag{4.82}$$

calculated from Eq. (4.81) is equivalent to the polarization function within the random phase approximation as obtained from the Adler-Wiser formulation. This is clear because the correlation function L_0 is the product of two single-particle Green's functions, and therefore describes the independent motion of an electron and a hole just as in the RPA. Comparison of (4.81) with the expansion convention (4.75) gives the result

$$L^0_{(i_1 i_2),(i_3 i_4)} = -i\frac{(f_{i_2} - f_{i_1})\delta_{i_1 i_3}\delta_{i_2 i_4}}{E_{i_2} - E_{i_1} - \omega - i\delta}. \tag{4.83}$$

We can now use this result in order to reformulate the BSE in the form (4.78). In a first step, we can write

$$L_{(i_1 i_2),(i_3 i_4)}(\omega) = \sum_{j_3 j_4} \Pi_{(i_1 i_2),(j_3 j_4)}(\omega) L^0_{(j_3 j_4),(i_3 i_4)}, \tag{4.84}$$

where the matrix Π is defined as

$$\Pi(\omega) = \left[1 - L^0(\omega)\Xi\right]^{-1}. \tag{4.85}$$

In this last equation we have adopted a simplified notation by leaving out the matrix indices and summations, in order to get more compact expressions. For instance, the 1 appearing in Eq. (4.85) is actually given by the unit matrix

$$1_{(i_1 i_2),(i_3 i_4)} = \delta_{i_1 i_3}\delta_{i_2 i_4}. \tag{4.86}$$

By factoring out the diagonal terms from the matrix inversion in (4.85) and using relation (4.83) for L_0, we can write for Π

$$\begin{aligned} \Pi_{(i_1 i_2),(i_3 i_4)}(\omega) &= \left[(E_{j_2} - E_{j_1} - \omega)1 - i(f_{j_2} - f_{j_1})\Xi_{(j_1 j_2),(j_3 j_4)}\right]^{-1}_{(i_1 i_2),(i_3 i_4)} \\ &\times \quad (E_{i_4} - E_{i_2} - \omega - i\delta). \end{aligned} \tag{4.87}$$

Finally we introduce an excitonic Hamiltonian H^e defined as

$$H^e_{(j_1 j_2),(j_3 j_4)} = (E_{j_2} - E_{j_1})\delta_{j_1 j_3}\delta_{j_2 j_4} - i(f_{j_2} - f_{j_1})\Xi_{(j_1 j_2),(j_3 j_4)}, \tag{4.88}$$

and we can write L in the compact form

$$L_{(i_1 i_2),(i_3 i_4)}(\omega) = i\left[H^e - \omega\right]^{-1}_{(i_1 i_2),(i_3 i_4)} \times (f_{j_4} - f_{j_3}). \tag{4.89}$$

At this stage, the two-particle correlation function L is obtained by an inversion of an excitonic Hamiltonian for each frequency ω. We will see in the next sections how we can avoid this inversion by computing the eigenvalues of the Hamiltonian H^e. But before we do so, we have to analyze the structure of H^e for systems containing a gap in the excitation spectrum (semi-conductors or insulators).

4.3.5 Structure of the Effective Electron-Hole Hamiltonian

If we explicitly specify the indices $i_1 \dots i_4$ by band indices (v for valence, and c for conduction states) and Bloch vectors, we obtain the following block-structure of the Hamiltonian H^e

$$H^e = \begin{pmatrix} H & P \\ Q & R \end{pmatrix}, \tag{4.90}$$

where H, P, Q and R are defined via the relation (4.88) as

$$H = \begin{pmatrix} H^e_{v_1c_1\mathbf{k}_1,v_2c_2\mathbf{k}_2} & H^e_{v_1c_1\mathbf{k}_1,c_2v_2\mathbf{k}_2} \\ H^e_{c_1v_1\mathbf{k}_1,v_2c_2\mathbf{k}_2} & H^e_{c_1v_1\mathbf{k}_1,c_2v_2\mathbf{k}_2} \end{pmatrix} \tag{4.91}$$

$$P = \begin{pmatrix} H^e_{v_1c_1\mathbf{k}_1,v_2v'_2\mathbf{k}_1} & H^e_{v_1c_1\mathbf{k}_1,c_2c'_2\mathbf{k}_1} \\ H^e_{c_1v_1\mathbf{k}_1,v_2v'_2\mathbf{k}_1} & H^e_{c_1v_1\mathbf{k}_1,c_2c'_2\mathbf{k}_1} \end{pmatrix} \tag{4.92}$$

$$Q = \begin{pmatrix} H^e_{v_1v'_1\mathbf{k}_2,v_2c_2\mathbf{k}_2} & H^e_{v_1v'_1\mathbf{k}_2,c_2v_2\mathbf{k}_2} \\ H^e_{c_1c'_1\mathbf{k}_2,v_2c_2\mathbf{k}_2} & H^e_{c_1c'_1\mathbf{k}_2,c_2v_2\mathbf{k}_2} \end{pmatrix} \tag{4.93}$$

$$R = \begin{pmatrix} H^e_{v_1v'_1\mathbf{k}_2,v_2v'_2\mathbf{k}_1} & H^e_{v_1v'_1\mathbf{k}_2,c_2c'_2\mathbf{k}_1} \\ H^e_{c_1c'_1\mathbf{k}_2,v_2v'_2\mathbf{k}_1} & H^e_{c_1c'_1\mathbf{k}_2,c_2c'_2\mathbf{k}_1} \end{pmatrix}. \tag{4.94}$$

By looking at the definition of H^e in Eq. (4.88) we notice that the block Q is identically zero. This is because the product of the Kronecker delta's $\delta_{j_1j_3}\delta_{j_2j_4}$ as well as the difference in occupation numbers $f_{j_2} - f_{j_1}$ are zero in that case. Hence, we have to invert a matrix with the block structure

$$H^e = \begin{pmatrix} H & P \\ 0 & R \end{pmatrix}, \tag{4.95}$$

which according to (A.18) can be achieved by

$$[H^e - \omega\,1]^{-1} = \begin{pmatrix} [H - \omega\,1]^{-1} & -[H - \omega\,1]^{-1}P[R - \omega\,1]^{-1} \\ 0 & [R - \omega\,1]^{-1} \end{pmatrix}. \tag{4.96}$$

Due to the occupation factors $(f_{j_4} - f_{j_3})$ in Eq. (4.89) we finally obtain the simplified matrix structure for the correlation function $L(\omega)$

$$L_{(i_1i_2),(i_3i_4)}(\omega) = \begin{pmatrix} [H - \omega\,1]^{-1}_{(i_1i_2),(i_3i_4)} \times (f_{i_4} - f_{j_3}) & 0 \\ 0 & 0 \end{pmatrix}. \tag{4.97}$$

The remaining block of the Hamiltonian has the structure shown in Eq. (4.91). We can further simplify the structure of H by noting that the interaction kernel Ξ remains unchanged if the primed and unprimed coordinates are interchanged (compare Sec. 3.4.1)

$$\Xi(\mathbf{r}_1, \mathbf{r}'_1, \mathbf{r}_2, \mathbf{r}'_2) = \Xi(\mathbf{r}'_1, \mathbf{r}_1, \mathbf{r}'_2, \mathbf{r}_2). \tag{4.98}$$

In terms of the matrix $\Xi_{(i_1i_2),(i_3i_4)}$ we deduce from the expansion convention (4.75) the corresponding property

$$\Xi_{(i_1i_2),(i_3i_4)} = -\left[\Xi_{(i_2i_1),(i_4i_3)}\right]^*. \tag{4.99}$$

This relation can be used in order to write the four blocks in the matrix H of Eq. (4.91) in the form

$$\begin{aligned} H^e_{v_1c_1\mathbf{k}_1,v_2c_2\mathbf{k}_2} &= (E_{c_1\mathbf{k}_1} - E_{v_1\mathbf{k}_1})\delta_{v_1v_2}\delta_{c_1c_2}\delta_{\mathbf{k}_1\mathbf{k}_2} + i\Xi_{v_1c_1\mathbf{k}_1,v_2c_2\mathbf{k}_2} && (4.100)\\ H^e_{v_1c_1\mathbf{k}_1,c_2v_2\mathbf{k}_2} &= +i\Xi_{v_1c_1\mathbf{k}_1,c_2v_2\mathbf{k}_2} && (4.101)\\ H^e_{c_1v_1\mathbf{k}_1,v_2c_2\mathbf{k}_2} &= -\left[H^e_{v_1c_1\mathbf{k}_1,c_2v_2\mathbf{k}_2}\right]^* && (4.102)\\ H^e_{c_1v_1\mathbf{k}_1,c_2v_2\mathbf{k}_2} &= -\left[H^e_{v_1c_1\mathbf{k}_1,v_2c_2\mathbf{k}_2}\right]^*. && (4.103) \end{aligned}$$

The off-diagonal coupling matrices $H^e_{v_1c_1\mathbf{k}_1,c_2v_2\mathbf{k}_2}$ and $H^e_{c_1v_1\mathbf{k}_1,v_2c_2\mathbf{k}_2}$ do not contain the quasi-particle energy differences but only the electron-hole interaction kernel Ξ. We can neglect these off-diagonal parts provided that the band gap is much larger than the electron-hole interaction strength. This requirement is for instance well satisfied in bulk silicon, whereas for systems where the exciton binding energies are of the order of 1 eV, this approximation is only justified by the success of numerical results. If, however, these off-diagonal coupling matrices are set equal to zero, the Hamiltonian H splits into two block-diagonal parts: the resonant contributions, which are active for positive frequencies, and the anti-resonant ones, only contributing to negative frequencies. It is important to note, that the matrix of the resonant part $H^e_{v_1c_1\mathbf{k}_1,v_2c_2\mathbf{k}_2}$ by its own is Hermitian, and can therefore be diagonalized. We can write down the matrix eigenvalue equation of H^e with the real eigenenergies E^λ, and eigenvectors $A^\lambda_{vc\mathbf{k}}$ as

$$\sum_{v'c'\mathbf{k}'} H^e_{vc\mathbf{k},v'c'\mathbf{k}'} A^\lambda_{v'c'\mathbf{k}'} = E^\lambda A^\lambda_{vc\mathbf{k}}. \tag{4.104}$$

4.3.6 The Macroscopic Dielectric Function

In order to obtain the function L and in turn the macroscopic dielectric function, we have to invert the matrix $(H^e - \omega)$ according to (4.89). Knowing the solution to the eigenvalue problem of H^e, this can be achieved very easily by using the spectral theorem, and we obtain L in terms of the eigenvalues and eigenfunctions of H^e as

$$L_{v_1c_1\mathbf{k}_1,v_2c_2\mathbf{k}_2}(\omega) = -i\sum_\lambda \frac{A^\lambda_{v_1c_1\mathbf{k}_1}\left[A^\lambda_{v_2c_2\mathbf{k}_2}\right]^*}{E^\lambda - \omega}. \tag{4.105}$$

We can now express the correlation function L in its real space representation according to Eq. (4.75), and relate L to the polarization function $\bar{P}$ utilizing (4.62). The Fourier transform of $\bar{P}$ is given by

$$\bar{P}_{\mathbf{00}}(\mathbf{q},\omega) = -\frac{1}{\Omega}\sum_\lambda \left|\sum_{vc\mathbf{k}} A^\lambda_{vc\mathbf{k}}\langle v\mathbf{k}|e^{-i\mathbf{qr}}|c\mathbf{k}\rangle\right|^2 \times \left(\frac{1}{E^\lambda - \omega} + \frac{1}{E^\lambda + \omega}\right). \tag{4.106}$$

Taking into account Eq. (4.67), we can finally derive an expression for the macroscopic dielectric function including local-field as well as electron-hole correlation effects

$$\begin{aligned}\epsilon_M(\omega) &= 1 - \lim_{\mathbf{q}\to\mathbf{0}} v(\mathbf{q})\bar{P}_{\mathbf{00}}(\mathbf{q},\omega) \\ &= 1 + 2\lim_{\mathbf{q}\to\mathbf{0}} \frac{4\pi}{\Omega}\frac{1}{\mathbf{q}^2}\sum_\lambda \left|\sum_{vc\mathbf{k}} A^\lambda_{vc\mathbf{k}}\langle v\mathbf{k}|e^{-i\mathbf{qr}}|c\mathbf{k}\rangle\right|^2 \\ &\times \left(\frac{1}{E^\lambda - \omega - i\delta} + \frac{1}{E^\lambda + \omega + i\delta}\right). \end{aligned} \tag{4.107}$$

Here, we have assumed that the one-particle states are spin-degenerate, therefore we have included a factor of 2 to account for the spin-degrees of freedom. As discussed in Chapter 3, it is the *time-ordered* Green's functions that can be treated in many-body perturbation theory. In order to obtain the *causal* dielectric function from the time-ordered correlation function L, we have to add the appropriate infinitesimals δ in the energy denominators of Eq. (4.107) [65]. By using the identity

$$\lim_{\delta\to 0}\frac{\delta}{(E^\lambda-\omega)^2+\delta^2} = \pi\delta(E^\lambda-\omega), \tag{4.108}$$

we get for the imaginary part of the macroscopic dielectric function

$$\mathrm{Im}\epsilon_M(\omega) = \lim_{\mathbf{q}\to\mathbf{0}}\frac{8\pi^2}{\Omega}\frac{1}{\mathbf{q}^2}\sum_\lambda\left|\sum_{vc\mathbf{k}} A^\lambda_{vc\mathbf{k}}\langle v\mathbf{k}|e^{-i\mathbf{qr}}|c\mathbf{k}\rangle\right|^2 \times \delta(E^\lambda-\omega). \tag{4.109}$$

Expression (4.109) involves a *coherent* sum of transition matrix elements. In order to obtain the correct interference of matrix elements in the sum over $vc\mathbf{k}$ in (4.109) it is therefore crucial to treat the *phases* consistently in the wave functions, in the electron-hole interaction, in the coupling coefficients $A^\lambda_{vc\mathbf{k}}$, as well as in the computation of the optical matrix elements. In order to take the limit of vanishing $\mathbf{q}$ analytically, we make use of the identity (4.43) leading to an expression for $\mathrm{Im}\epsilon_M$ containing the optical transition matrix elements $\langle v\mathbf{k}|p_i|c\mathbf{k}\rangle$ instead of the matrix elements $\langle v\mathbf{k}|e^{-i\mathbf{qr}}|c\mathbf{k}\rangle$. However, an additional complication arises if we want to use quasi-particle wave functions and energies in the calculation of the optical matrix elements. Even if the quasi-particle shifts are the same for all empty states (scissors operator approximation), the non-locality of the self-energy operator leads to a re-normalization of the optical matrix elements as was shown by Levine and Allan [78, 79] as well as by Del Sole and Girlanda [80]. The re-normalization of the optical transition matrix element has already been discussed in Sec. 4.2.5

$$\langle v\mathbf{k}|\mathbf{p}|c\mathbf{k}\rangle^{\mathrm{QP}} = \frac{E_{c\mathbf{k}}-E_{v\mathbf{k}}}{\varepsilon_{c\mathbf{k}}-\varepsilon_{v\mathbf{k}}}\langle v\mathbf{k}|\mathbf{p}|c\mathbf{k}\rangle^{\mathrm{LDA}}.$$

Here, the superscripts QP and LDA denote the optical matrix elements to be used with the quasi-particle approximation, and the local density approximation, respectively. The energies E are the quasi-particle energies, whereas ε denotes the Kohn-Sham energies. By applying $\mathbf{k}\cdot\mathbf{p}$ perturbation theory as described in Sec. 4.2.4 we obtain

$$\langle v\mathbf{k}|e^{-i\mathbf{qr}}|c\mathbf{k}\rangle = \frac{\mathbf{q}}{E_{c\mathbf{k}} - E_{v\mathbf{k}}}\langle v\mathbf{k}|\mathbf{p}|c\mathbf{k}\rangle^{\mathrm{QP}}, \tag{4.110}$$

which enables us to express the macroscopic dielectric function in terms of the optical matrix elements

$$\mathrm{Im}\epsilon_M(\omega) = \frac{8\pi^2}{\Omega}\sum_{\lambda}\left|\sum_{vc\mathbf{k}} A^{\lambda}_{vc\mathbf{k}}\frac{\langle v\mathbf{k}|p_i|c\mathbf{k}\rangle^{\mathrm{LDA}}}{\varepsilon_{c\mathbf{k}} - \varepsilon_{v\mathbf{k}}}\right|^2 \times \delta(E^{\lambda} - \omega). \tag{4.111}$$

Thus, the effect of the re-normalization is that the weight of a transition in (4.111) remains unchanged when the transition is shifted to higher energies due to the quasi-particle correction.

4.3.7 The Electron-Hole Interaction Kernel

In order to compute the dielectric function according to (4.109) or (4.111), we have to diagonalize the Hamiltonian matrix given by Eq. (4.100). If we approximate the electron-hole kernel as a sum of an exchange interaction, and a direct screened interaction as discussed in Sec. 3.4,

$$\Xi(3,3',4,4') = -i\,\delta(3,3')\delta(4,4')v(3,4) + i\,\delta(3,4)\delta(3',4')W(3,3'), \tag{4.112}$$

the Hamiltonian consists of three terms

$$H = H^{diag} + H^{dir} + H^{x}. \tag{4.113}$$

Using the form of the kernel (4.112) in the definition of the Hamiltonian H in (4.100), we can calculate the two terms H^{dir} and H^{x} from the inverse of (4.75), which is

$$\Xi_{(i_1i_2),(i_3i_4)} = \int \mathrm{d}^3r_1\mathrm{d}^3r_1'\mathrm{d}^3r_2\mathrm{d}^3r_2'\psi_{i_1}(\mathbf{r}_1)\psi^*_{i_2}(\mathbf{r}_1')\psi^*_{i_3}(\mathbf{r}_2)\psi_{i_4}(\mathbf{r}_2')\Xi(\mathbf{r}_1,\mathbf{r}_1',\mathbf{r}_2,\mathbf{r}_2'). \tag{4.114}$$

Using the above relations we can derive the following expressions for the contributions of the Hamiltonian

$$H^{diag}_{vc\mathbf{k},v'c'\mathbf{k}'} = (E_{c\mathbf{k}} - E_{v\mathbf{k}})\delta_{vv'}\delta_{cc'}\delta_{\mathbf{k}\mathbf{k}'} \tag{4.115}$$

$$H^{dir}_{vc\mathbf{k},v'c'\mathbf{k}'} = -\int \mathrm{d}^3r\mathrm{d}^3r'\psi_{v\mathbf{k}}(\mathbf{r})\psi^*_{c\mathbf{k}}(\mathbf{r}')W(\mathbf{r},\mathbf{r}')\psi^*_{v'\mathbf{k}'}(\mathbf{r})\psi_{c'\mathbf{k}'}(\mathbf{r}') \tag{4.116}$$

$$H^{x}_{vc\mathbf{k},v'c'\mathbf{k}'} = \int \mathrm{d}^3r\mathrm{d}^3r'\psi_{v\mathbf{k}}(\mathbf{r})\psi^*_{c\mathbf{k}}(\mathbf{r})\bar{v}(\mathbf{r},\mathbf{r}')\psi^*_{v'\mathbf{k}'}(\mathbf{r}')\psi_{c'\mathbf{k}'}(\mathbf{r}') \tag{4.117}$$

The direct interaction term H^{dir} is responsible for the attractive nature of the electron-hole interaction and for the formation of bound electron-hole states (excitons). The exchange term H^x, on the other hand, controls details of the excitation spectrum, such as the splitting between spin-singlet and spin-triplet excitations as will become clear in the next section. Note that the direct interaction term involves the *screened* Coulomb interaction W, whereas the exchange term contains the bare Coulomb interaction $\bar{v}$ without the long-range part as described in Sec. 4.3.2. The diagonal elements of H contain the differences in quasi-particle energies of the electron and the hole and is therefore usually much larger than the off-diagonal elements.

At this stage it is interesting to see how we can re-derive the macroscopic dielectric function in the independent-particle approximation neglecting local field effects, from Eq. (4.111). To this end, we simply set H^{dir} and H^x equal to zero. Then the Hamiltonian H is diagonal already, and we can write the eigenvectors and eigenvalues of Eq. (4.104) in the form

$$A^{\lambda}_{vc\mathbf{k}} = \delta_{\lambda,vc\mathbf{k}} \tag{4.118}$$

$$E^{\lambda} = (E_{c\mathbf{k}} - E_{v\mathbf{k}}), \tag{4.119}$$

which can be inserted into Eq. (4.111). Due to the simple form of the coupling coefficients $A^{\lambda}_{vc\mathbf{k}}$ only one term in the sum over states $vc\mathbf{k}$ survives. The summation over exciton states λ reduces to a sum over single-particle states which we denote by $vc\mathbf{k}$ again. Moreover, we use the re-normalization of the optical transition matrix elements (4.49) which is necessary in the quasi-particle picture, and obtain

$$\mathrm{Im}\epsilon_M(\omega) = \frac{8\pi^2}{\Omega}\frac{1}{\omega^2}\sum_{vc\mathbf{k}} \left|\langle v\mathbf{k}|p_i|c\mathbf{k}\rangle^{\mathrm{QP}}\right|^2 \times \delta(E_{c\mathbf{k}} - E_{v\mathbf{k}} - \omega). \tag{4.120}$$

This expression is identical to that derived in Sec. (4.2.5), where we treated the electron and the hole as independent quasi-particles neglecting local-field effects. Thus, we see that the expressions deduced from the solution of the Bethe-Salpeter equation reduce to the previously obtained results, if we neglect electron-hole correlation effects in the kernel of the BSE altogether.

4.3.8 The Spin Structure of the Electron-Hole Interaction Kernel

An important issue concerns the spin structure of the solutions of the BSE [83]. Depending on the strength of the spin-orbit interaction in the system, two situations can occur: If the spin-orbit interaction is negligible compared to the electron-hole interaction, the single particle states $|v\mathbf{k}\rangle$ and $|c\mathbf{k}\rangle$ can be classified as spin-up $\uparrow$ or spin-down $\downarrow$ states. The Hilbert space of the electron-hole

pairs now consists of the four subspaces: $|v_\uparrow c_\uparrow \mathbf{k}\rangle$, $|v_\uparrow c_\downarrow \mathbf{k}\rangle$, $|v_\downarrow c_\uparrow \mathbf{k}\rangle$, and $|v_\downarrow c_\downarrow \mathbf{k}\rangle$. Between these subspaces most of the matrix elements of Eqs. (4.115)–(4.117) are zero; in the notation of these subspaces the Hamiltonian obtains the form

$$H = \begin{pmatrix} H^{diag} + H^{dir} + H^x & 0 & 0 & H^x \\ 0 & H^{diag} + H^{dir} & 0 & 0 \\ 0 & 0 & H^{diag} + H^{dir} & 0 \\ H^x & 0 & 0 & H^{diag} + H^{dir} + H^x \end{pmatrix}.$$

This Hamiltonian decouples into a spin-triplet class of solutions, and a spin-singlet class of solutions. The singlet solutions correspond to the subspace

$$\Phi^S = \frac{1}{\sqrt{2}} \left(|v_\uparrow c_\uparrow \mathbf{k}\rangle - |v_\downarrow c_\downarrow \mathbf{k}\rangle \right),$$

with the Hamiltonian $H^{diag}+H^{dir}+2H^x$, whereas the spin-triplet class of solutions belong to the subspace

$$\begin{aligned} \Phi_1^T &= |v_\uparrow c_\downarrow \mathbf{k}\rangle \\ \Phi_2^T &= \frac{1}{\sqrt{2}} \left(|v_\uparrow c_\uparrow \mathbf{k}\rangle + |v_\downarrow c_\downarrow \mathbf{k}\rangle \right) \\ \Phi_3^T &= |v_\downarrow c_\uparrow \mathbf{k}\rangle, \end{aligned}$$

having the Hamiltonian $H^{diag}+H^{dir}$. Therefore, the BSE can be solved for singlet and triplet configurations separately. The spin degrees of freedom have been completely eliminated from the remaining problem. If, however, the spin-orbit interaction is of the same order of magnitude as the electron-hole interaction, the single particle states can not be classified as spin-up or spin-down states. In such cases, singlet and triplet configurations would be mixed, and the Bethe-Salpeter equation must be discussed including the full spin structure, thereby increasing the size of the matrix-problem by a factor of 4. In this work, we will only study systems, where it is a safe approximation to neglect spin-orbit couplings, and we can therefore work with the decoupled Hamiltonian discussed above. The difference between singlet and triplet excitations, respectively, stems from the exchange term $2H^x$ only present in the case of spin-singlet excitations.

4.3.9 The Exciton Wave Function

The diagonalization of the Hamiltonian according to Eq.(4.104) not only allows for the calculation of the excitation energies E^λ, but also yields the coupling coefficient $A^\lambda_{vc\mathbf{k}}$. These can be used to construct the exciton wave function Φ as sum over single particle configurations weighted by the coupling coefficients

$$\Phi^\lambda(\mathbf{r}_e, \mathbf{r}_h) = \sum_{vc\mathbf{k}} A^\lambda_{vc\mathbf{k}} \psi^*_{v\mathbf{k}}(\mathbf{r}_h) \psi_{c\mathbf{k}}(\mathbf{r}_e). \tag{4.121}$$

Here, $\mathbf{r}_e$ and $\mathbf{r}_h$, respectively, denote the electron and hole coordinates, whereas $\psi_{v\mathbf{k}}$ and $\psi_{c\mathbf{k}}$ are the single-particle wave functions for valence and conduction states with momentum $\mathbf{k}$ as usual. The interpretation of Φ^λ as an electron-hole wave function follows from the representation of the two-particle correlation function L in terms of the coupling coefficients as given in Eq. (4.105). We can discuss the exciton wave function Φ in order to investigate the structure of the exciton, which is, however, not easily possible due to the high dimensionality of the function $\Phi^\lambda(\mathbf{r}_e, \mathbf{r}_h)$. To get the best insight into the real-space correlation between the electron and the hole in the excited state, and to observe the attractive nature of this correlation, we keep the position of *one* of the particles fixed and analyze Φ in terms of the coordinates of the other particle. This results in a correlation function including all details of the microscopic excitonic structure.

In the case of a simplified isotropic effective-mass model, this correlation function would correspond to the envelope function of an exciton. It means that the real space electron-hole function is given by a Hydrogen-like $1s$ wave function. Thus, it is very easy to evaluate the structure of such an isotropic exciton state in terms of the envelope coefficients $A^\lambda_{vc\mathbf{k}}$ which are just the Fourier coefficients of the real space wave function. The hydrogen-like result has the form

$$\frac{A_{vc\mathbf{k}}}{A_{vc\mathbf{k}=\mathbf{0}}} = \frac{1}{\left[1 + k^2 a_{ex}^2\right]^2}, \tag{4.122}$$

where, a_{ex} defines an approximate value for the binding radius of the exciton. Thus, we can extract the extension of the exciton a_{ex} by fitting the coupling coefficients $A_{vc\mathbf{k}}$ to the above form.

4.4 Summary

At this stage it is instructive to give a brief summary of the main results derived in this section. In particular, we will review the steps leading to the macroscopic dielectric response including electron-hole correlations and discuss the relevant approximations that have been made.

The computation of the dielectric function within the independent quasi-particle approximation (RPA) and neglecting local field effects involves the following steps:

(i) The Kohn-Sham energies and orbitals are determined from a standard DFT calculation.

(ii) The momentum matrix elements between the valence and conduction Kohn-Sham orbitals are calculated.

(iii) The correction of the Kohn-Sham band gap by shifting the conduction bands rigidly by Δ has the consequence that the transition matrix elements have to be normalized according to Eq. (4.49).

(iv) The dielectric function is given by a sum over the Brillouin zone, and over all valence and conduction states according to Eq. (4.50).

If we want to include local field effects as well as electron-hole correlations we have to solve the Bethe-Salpeter equation, following the prescription:

(i) Calculate the Kohn-Sham orbitals and energies from a standard density functional calculation.

(ii) Determine the *static* dielectric matrix ϵ in the independent particle approximation according to Eqs. (4.27) and (4.33).

(iii) Invert the dielectric matrix in order to obtain the screened Coulomb interaction W using expression (3.48).

(iv) Construct the direct and the exchange interaction kernel entering the Bethe-Salpeter equation utilizing Eqs. (4.116) and (4.117). Note that the Kohn-Sham orbitals serve as approximate quasi-particle wave functions in this step. The diagonal part of the effective electron-hole Hamiltonian (see Eq. 4.115) contains the quasi-particle energies that are approximated by Kohn-Sham energies shifted according to the scissors operator.

(v) Diagonalize the effective Hamiltonian in order to obtain the excitation energies and the electron-hole coupling coefficients. The spectrum is computed according to Eq. (4.111). It is given as a sum over all excitonic states λ, and the oscillator strength of a given excitonic state is given as a *coherent* sum of transition matrix elements weighted by the electron-hole coupling coefficients $A^{\lambda}_{vc\mathbf{k}}$.

Before we end this chapter, we want to review the relevant approximations which have led to the macroscopic dielectric function, Eq. (4.111), and discuss the physical arguments that have allowed us to make these simplifications. The electron-hole kernel Ξ is given as the functional derivative of the self-energy with respect to the one-particle Green's function (Eq. 3.57). If the self-energy is evaluated in the GW approximation, the kernel Ξ consists of three parts of which we neglected the term $G\frac{\delta W}{\delta G}$. This term contains information about the *change* in screening due to the excitation process. It is generally believed that this term is negligible compared to the other two terms [27, 28]. Another simplification arises from the fact that the screened interaction is taken to be *static*. Therefore, the whole kernel Ξ becomes independent of frequency as can be seen in Eq. (4.72). However, it has

been pointed out by Bechstedt and co-workers [85], that dynamical effects in the electron-hole screening and in the one-particle Green's function tend to cancel each other. Therefore, it seems natural to neglect dynamical effects in both terms. Finally, we have dropped the off-diagonal matrices in the derivation of the effective Schrödinger equation for the electron-hole pairs (see Eq. 4.104). For the systems studied in this work, however, these off-diagonal blocks are expected to be small. Rohlfing and Louie have calculated the excitation energies of the SiH_4 molecule with and without taking into account the off-diagonal blocks and found that the excitation energies agree within 0.03 eV [83]. Moreover, Albrecht and co-workers found almost no effect of the off-diagonal blocks on the absorption spectrum of bulk Si, and only a slight change in the macroscopic dielectric constant [29].

Chapter 5

The LAPW Method

5.1 General Remarks

The aim of this chapter is to describe the method that has been used throughout this work in order to solve the Kohn-Sham equations for periodic crystals. For such systems plane waves $e^{i(\mathbf{k}+\mathbf{K})\mathbf{r}}$ would be a natural choice of basis functions compatible with the periodic boundary conditions. Here, $\mathbf{k}$ denotes a vector from the first Brillouin zone, and $\mathbf{K}$ is a reciprocal lattice vector. However, an unrealistically large number of plane waves would be necessary to achieve an appropriate description of the wave functions near the atomic nuclei. It was the idea of SLATER [86] to *augment* the plane waves by atomic-like functions in the vicinity of the atomic nuclei. Since SLATER first proposed the method in 1937, the augmented plane wave (APW) method and its descendents has been among the most popular schemes for solving the electronic structure using density-functional theory. In part, this popularity arose from the fact that the APW method in its modern general potential, and linearized forms combines a conceptual simplicity with high accuracy for a general system. The method uses a smaller basis set than soft pseudo-potential plane-wave basis approaches, but still substantially larger than local function methods like the linear-muffin-tin-orbital (LMTO) method or Gaussian-orbital techniques. During the years, there have been important developments of the original APW method, for instance the full-potential implementation and of course the linearization of the secular problem as proposed by ANDERSEN [36].

The full-potential Linearized Augmented Plane Wave (FP-LAPW) method is one of the most accurate methods used for the solution of the Kohn-Sham equations for crystalline systems. This chapter gives a short introduction into the LAPW formalism, where the main intention is to provide a collection of formulae, which are referenced in the following chapters. A more detailed description of the LAPW method can be found elsewhere [87, 88]. The code that has been used for

all calculations in this work (WIEN97) is a full-potential LAPW code developed by Blaha and co-workers [37].

The idea of the LAPW method is to divide the unit cell into two different regions: non-overlapping *spheres* around the positions of the nuclei, and the remaining *interstitial* region, schematically depicted in Fig. (5.1). In the two regions, different sets of basis functions are used for the wave functions as well as for the electron density and the crystal potential. The choice of these basis functions is guided by the observation that near the nuclei the wave functions remain atomic-like even in a crystalline environment, whereas they are more plane-wave like between the atoms. The same argument also applies for the density as well as for the potential.

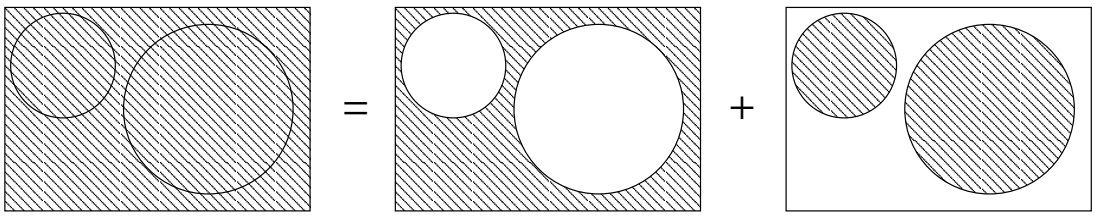

Figure 5.1: Splitting of the unit cell volume into the interstitial and the spheres region, which is also often referred to as the muffin–tin region.

5.2 The Basis Set of the Variational Problem

5.2.1 The LAPW Basis

By expanding the wave function ψ in terms of a given basis set ϕ_i with expansion coefficients C_i, the Kohn-Sham equation (2.14) is transformed into a generalized matrix eigenvalue problem (Ritz's variational principle), where ε denotes the Kohn-Sham energy

$$H_{ij}C_j = \varepsilon S_{ij}C_j. \tag{5.1}$$

Here, H_{ij} are the matrix elements of the single-particle Kohn-Sham Hamiltonian $h(\mathbf{r})$ with the basis functions ϕ

$$H_{ij} = \int \mathrm{d}^3 r \phi_i^*(\mathbf{r}) h(\mathbf{r}) \phi_j(\mathbf{r}), \tag{5.2}$$

and S_{ij} denotes the overlap matrix

$$S_{ij} = \int \mathrm{d}^3 r \phi_i^*(\mathbf{r}) \phi_j(\mathbf{r}). \tag{5.3}$$

In the LAPW method, normalized plane waves are used as trial functions ϕ within the interstitial region, given by

$$\phi_{\mathbf{k}+\mathbf{G}}(\mathbf{r}) = \frac{1}{\sqrt{\Omega}} e^{i(\mathbf{k}+\mathbf{G})\mathbf{r}} \qquad \mathbf{r} \in I, \tag{5.4}$$

where $\mathbf{k}$ and $\mathbf{G}$ denote a vector within the first Brillouin zone and a reciprocal lattice vector, respectively, and Ω is the crystal volume. On the other hand, atomic radial functions and spherical harmonics are used to represent the wave function inside the sphere α

$$\phi_{\mathbf{k}+\mathbf{G}}(\mathbf{r}) = \sum_{l=0}^{l_{max}} \sum_{m=-l}^{+l} [A_{lm}^{\alpha}(\mathbf{k}+\mathbf{G}) u_l(r_\alpha, E_l) + B_{lm}^{\alpha}(\mathbf{k}+\mathbf{G}) \dot{u}_l(r_\alpha, E_l)] Y_{lm}(\hat{r}_\alpha). \tag{5.5}$$

Here, $\mathbf{r}_\alpha$ denotes the position vector shifted by the position $\mathbf{R}_\alpha$ of atom α with the sphere radius R_α

$$\mathbf{r}_\alpha = \mathbf{r} - \mathbf{R}_\alpha, \qquad |\mathbf{r}_\alpha| \leq R_\alpha. \tag{5.6}$$

The radial wave functions $u_l(r_\alpha, E_l)$ and their *energy* derivatives $\dot{u}_l(r_\alpha, E_l)$ are determined from a numerical integration of the radial part of the Schrödinger equation (5.7) and its energy derivative (5.8)

$$[\hat{T} + v_{\text{eff}}(r_\alpha)] u_l(r_\alpha, E_l) Y_{lm}(\hat{r}_\alpha) = E_l u_l(r_\alpha, E_l) Y_{lm}(\hat{r}_\alpha), \tag{5.7}$$

$$[\hat{T} + v_{\text{eff}}(r_\alpha)] \dot{u}_l(r_\alpha, E_l) Y_{lm}(\hat{r}_\alpha) = [E_l \dot{u}_l(r_\alpha, E_l) + u_l(r_\alpha, E_l)] Y_{lm}(\hat{r}_\alpha). \tag{5.8}$$

In this context, the energies E_l are not eigenvalues, but chosen, fixed expansion energies, the *linearization* energies. The radial functions fulfill the following normalization conditions

$$\int_0^{R_\alpha} r^2 u_l^2(r) \mathrm{d}r = 1, \tag{5.9}$$

$$\int_0^{R_\alpha} r^2 u_l(r) \dot{u}_l(r) \mathrm{d}r = 0. \tag{5.10}$$

In addition we define the following integral

$$N_l \equiv \int_0^{R_\alpha} r^2 \dot{u}_l(r) \mathrm{d}r. \tag{5.11}$$

The coefficients $A_{lm}^{\alpha}(\mathbf{k}+\mathbf{G})$ and $B_{lm}^{\alpha}(\mathbf{k}+\mathbf{G})$ entering the expression (5.5) are chosen such, that the basis functions are continuous up to the first derivative at the sphere boundaries. These two conditions determine the coefficients A_{lm} and B_{lm}

$$A_{lm}^{\alpha}(\mathbf{k}+\mathbf{G}) = \frac{4\pi}{\sqrt{\Omega}} i^l Y_{lm}^*(\widehat{\mathbf{k}+\mathbf{G}}) c_l^{\alpha}(\mathbf{k}+\mathbf{G}) R_\alpha^2 e^{i(\mathbf{k}+\mathbf{G})\mathbf{R}_\alpha}, \tag{5.12}$$

$$B_{lm}^{\alpha}(\mathbf{k}+\mathbf{G}) = \frac{4\pi}{\sqrt{\Omega}} i^l Y_{lm}^*(\widehat{\mathbf{k}+\mathbf{G}}) d_l^{\alpha}(\mathbf{k}+\mathbf{G}) R_\alpha^2 e^{i(\mathbf{k}+\mathbf{G})\mathbf{R}_\alpha}, \tag{5.13}$$

with the abbreviations

$$c_l^\alpha(\mathbf{k}+\mathbf{G}) = j_l'(|\mathbf{k}+\mathbf{G}|R_\alpha)\dot{u}_l(R_\alpha) - j_l(|\mathbf{k}+\mathbf{G}|R_\alpha)\dot{u}_l'(R_\alpha), \quad (5.14)$$

$$d_l^\alpha(\mathbf{k}+\mathbf{G}) = j_l(|\mathbf{k}+\mathbf{G}|R_\alpha)u_l'(R_\alpha) - j_l'(|\mathbf{k}+\mathbf{G}|R_\alpha)u_l(R_\alpha). \quad (5.15)$$

Here, j_l is the spherical Bessel function, and the primes (dots) denote partial derivatives with respect to the radius r (expansion energy E_l). Thus, the basis functions and their first derivatives are continuous in the whole unit cell. The second derivative, however, is discontinuous at the sphere boundary.

5.2.2 Local Orbitals

Local orbitals were first introduced to the LAPW method by SINGH [88] in order to treat semi-core states, but they are also used to improve the flexibility of the basis set. Local orbitals (lo's) are simply added to the usual LAPW basis set described in the previous subsection, and correspond to a given angular quantum number l_{lo}. They are local in the sense that they are completely confined with the MT spheres:

$$\phi_{l_{lo}}(\mathbf{r}) = \begin{cases} 0 & \mathbf{r} \in I \\ \sum_m [A_{l_{lo}m}u_{l_{lo}}(r) + B_{l_{lo}m}\dot{u}_{l_{lo}}(r) + C_{l_{lo}m}u_{l_{lo}}(r, E_{l_{lo}})]Y_{l_{lo}m}(\hat{r}) & \mathbf{r} \in S \end{cases} \quad (5.16)$$

Here, the third radial function in the above expression with the coefficient $C_{l_{lo}m}$ is evaluated at a different linearization energy $E_{l_{lo}}$, which can, for instance, be set energetically close to a semi-core state. The coefficient $C_{l_{lo}m}$ is chosen such that the function $\phi_{l_{lo}}(\mathbf{r})$ vanishes at the sphere boundary. Further details about local orbitals can be found in [88, 89].

5.2.3 The APW+lo Basis

There are two important distinctions between the LAPW method described in Sec. 5.2.1 and its predecessor, the APW method which was first introduced by SLATER [86]. First, only the basis functions themselves but not their first derivatives are continuous at the sphere boundaries, and second, no linearization of the eigenvalue problem is possible in the traditional APW method. The first point actually turns out to be an advantage of the APW over the LAPW scheme, because usually a smaller plane-wave cut-off can be used to describe the wave functions appropriately. The second difference, however, is really a major disadvantage: instead of obtaining all eigenvalues in one step by diagonalizing the Hamiltonian as in the LAPW method, one has to find the zeroes of the determinant of the Hamilton matrix as a function of energy due to the energy dependence

of the basis functions. This is a computationally troublesome task. Fortunately, it has been shown recently [90] that it is possible to combine the advantages of the APW and LAPW method, that is to find an energy-independent basis that does not demand a noticeable higher plane-wave cut-off than the original APW basis functions. By adding local orbitals, as described in the previous subsection, the variational freedom of the basis is improved and it is possible to linearize the basis. Thus, the so-called APW+lo consists of APW functions with fixed linearization energies

$$\phi^{\mathrm{APW}}_{\mathbf{k}+\mathbf{G}}(\mathbf{r}) = \begin{cases} \frac{1}{\sqrt{\Omega}} e^{i(\mathbf{k}+\mathbf{G})\mathbf{r}} & \mathbf{r} \in I \\ \sum_{l=0}^{l_{max}} \sum_{m=-l}^{+l} A_{lm}(\mathbf{k}+\mathbf{G}) u_l(r, E_l) Y_{lm}(\hat{r}) & \mathbf{r} \in S \end{cases}, \tag{5.17}$$

plus local orbitals $\phi_{l_{lo}}(\mathbf{r})$ as defined in (5.16). Indeed, it has been shown in [90] that, for instance, total energies of bulk Cu or molecular O_2 converge faster with respect to the plane-wave cut-off when using an APW+lo basis rather than an LAPW basis. We have made a similar observation for the materials studied in this work, and will return to that point in a later chapter.

5.2.4 A Basis for Core Electrons

So far, we have given a description of the *valence* electrons only. These are defined such, that their wave function is de-localized over the whole unit cell, in particular there is a non-vanishing probability for them to be located in the interstitial region. Energetically, valence electron states lie close to the Fermi level. On the other hand, *core* electrons are energetically much deeper an can therefore be assumed to be confined within one atomic sphere. In the LAPW method, which is an *all*-electron method, core electrons are thus treated only inside the muffin-tin spheres, by solving the Schrödinger equation, or indeed the relativistic Dirac equation, inside the spheres [88].

5.3 Electron Density and Crystal Potential

Similar to the treatment of wave functions in the full-potential LAPW method, also the valence electron density is expanded in a dual representation in the full-potential LAPW method: spherical harmonics are used inside the muffin-tin spheres and plane waves are taken in the interstitial. Thus, we may write for the

valence electron density

$$\rho_{val}(\mathbf{r}) = \begin{cases} \sum_{\mathbf{G}} \rho^v(\mathbf{G}) e^{i\mathbf{G}\mathbf{r}} & \mathbf{r} \in I \\ \sum_{LM} \rho^v_{LM}(\mathbf{G}) Y_{LM}(\hat{\mathbf{r}}) & \mathbf{r} \in S \end{cases} . \tag{5.18}$$

The electron density of the core electrons is assumed to be spherically symmetric and to be confined within the muffin-tin sphere

$$\rho_c(\mathbf{r}) = \begin{cases} 0 & \mathbf{r} \in I \\ \rho^c_{00}(\mathbf{G}) Y_{00} & \mathbf{r} \in S \end{cases} . \tag{5.19}$$

The total electron density is simply the sum of the valence and the core contributions. In analogy to the representation of the electron density described in the previous section, the Kohn-Sham potential is given by

$$V(\mathbf{r}) = \begin{cases} \sum_{\mathbf{G}} V(\mathbf{G}) e^{i\mathbf{G}\mathbf{r}} & \mathbf{r} \in I \\ \sum_{LM} V_{LM}(\mathbf{G}) Y_{LM}(\hat{\mathbf{r}}) & \mathbf{r} \in S \end{cases} . \tag{5.20}$$

5.4 Physical Properties in the LAPW Method

5.4.1 Total Energy

The central quantity obtained from a density functional calculation is the ground state energy E of the system. It can be constructed from the ground state density n and the Kohn-Sham energies ε_i according to Eq. (2.16). Assuming the validity of the Born-Oppenheimer approximation, total energy calculations for slightly changed geometric arrangements of the atoms can be used to compute the total energy as a function of lattice constants or atomic positions: the first giving rise to elastic constants, the latter leading to the equilibrium atomic positions and vibrational frequencies. It is, however, quite cumbersome to determine the complete energy surface in such a manner, if the number of degrees of freedom in the atomic coordinates is large. Fortunately, it is possible to directly calculate the gradient of the energy surface – the atomic forces – which speeds up both the optimization of the structure as well as the calculation of vibrational frequencies.

5.4.2 Atomic Forces

A variation of the total energy with respect to the nuclear coordinates shows that the force acting on a nucleus is equal to the total Coulomb force exerted on a point

charge that is embedded in the static field of electrons and other nuclei. This fact is known as the Hellmann-Feynman theorem and the corresponding force is usually called Hellmann-Feynman force. In the LAPW basis two additional corrections to that force have to be considered. The site-dependence of the basis functions in combination with the finite number of basis functions leads to the so-called incomplete-basis-set (IBS) force. The other correction – the "core" correction – results from the fact that within the LAPW method core electrons are treated in the radial symmetric part of the potential only. The computation of the atomic forces including these two corrections have been implemented into the WIEN97 code by KOUBA [91], and by KOHLER and co-workers [92].

5.4.3 Dielectric Function

The WIEN97 code [37] allows for the calculation of the dielectric function within the independent quasi-particle approximation according to Eq. (4.50). It involves the computation of the transition matrix elements $\langle n\mathbf{k}|p_i|m\mathbf{k}\rangle$, which has been implemented into the WIEN97 code by ABT and co-workers [93]. The summation over the Brillouin required for the calculation of the imaginary part of the DF is realized utilizing the tetrahedron method [94, 95]. The real part of the DF is obtained from a Kramers-Kronig analysis of the imaginary part. Thus, the full dielectric tensor is available, which can be used to calculate the absorption spectra of bulk materials as well as of layered structures commonly used in experiments [96].

Chapter 6

Implementation

In Chapter 4, we have derived expressions for the macroscopic dielectric functions beyond the random phase approximation by including electron-hole correlation effects. For that purpose, we have seen that it is necessary to solve the Bethe-Salpeter equation involving an exchange interaction as well as a *screened* direct interaction term. This in turn requires the microscopic dielectric matrix to be computed in order to construct the screened interaction W. The aim of this chapter is to derive the actual expressions needed for the evaluation of the Bethe-Salpeter equation within the LAPW scheme. We choose a plane wave representation of the dielectric matrix, consequently we will encounter the following integrals

$$M^{\mathbf{G}}_{nm}(\mathbf{k},\mathbf{q}) = \langle n\mathbf{k}|e^{-i(\mathbf{q}+\mathbf{G})\mathbf{r}}|m\mathbf{k}'\rangle. \tag{6.1}$$

Here, $|n\mathbf{k}\rangle$ and $|m\mathbf{k}'\rangle$ denote the Kohn-Sham orbitals at wave vectors $\mathbf{k}$ and $\mathbf{k}'$ and with band indices m and n, respectively. As will become evident in the following section, the vector $\mathbf{q}$ connects $\mathbf{k}$ and $\mathbf{k}'$, that is

$$\mathbf{k}' = \mathbf{k} + \mathbf{q}, \tag{6.2}$$

and as usual $\mathbf{G}$ denotes a reciprocal lattice vector. In the first part of this chapter we will concentrate on the matrix element $M^{\mathbf{G}}_{nm}(\mathbf{k},\mathbf{q})$. First, we will discuss some of its general properties, independent of the choice of basis functions in which the wave functions are expanded, before we derive the explicit expressions needed for an LAPW basis set. With these tools in hand, we will be able to evaluate the dielectric matrix in the independent particle approximation, as well as the interaction kernel needed for the solution of the BSE. Finally, we will discuss the solution of the BSE itself leading to the macroscopic dielectric function including excitonic effects. In the last sections of this chapter, we show some selected results for the dielectric matrix of Si, LiF and poly-acetylene (PA), including convergence tests of relevant parameters entering the numerical evaluation, and comparison with previous calculations from the literature.

6.1 The Matrix Elements $M^{\mathbf{G}}_{nm}(\mathbf{k},\mathbf{q})$

6.1.1 Symmetry Properties

For the evaluation of the dielectric matrix as well as for the electron-hole kernel, it will be beneficial to make use of the symmetry of the crystal in order to reduce the computational time. Therefore, we investigate the symmetry properties of the matrix elements $M^{\mathbf{G}}_{nm}(\mathbf{k},\mathbf{q})$. Because the effective potential in the Kohn-Sham equations has the full symmetry of the crystal, the action of a symmetry operation $\{\alpha|\mathbf{t}\}$ on the Kohn-Sham orbitals is given by (omitting the band indices for a second)

$$\hat{S}_{\{\alpha|\mathbf{t}\}}\psi_{\mathbf{k}}(\mathbf{r}) \equiv \psi_{\mathbf{k}}[\alpha^{-1}(\mathbf{r}-\mathbf{t})] = \psi_{\alpha\mathbf{k}}(\mathbf{r}), \tag{6.3}$$

where α and $\mathbf{t}$ denote the rotational and translational parts of the space group element, respectively.[1] Equation (6.3) can be used to derive a relation for the matrix element $M^{\mathbf{G}}(\alpha\mathbf{k},\mathbf{q})$ at the rotated vector $\alpha\mathbf{k}$. Provided that the symmetry operation belongs to the small group of $\mathbf{q}$, insertion of (6.3) into (6.1) and changing the variable of integration leads to

$$M^{\mathbf{G}}(\alpha\mathbf{k},\mathbf{q}) = e^{-i(\mathbf{q}+\mathbf{G})\mathbf{t}} M^{\alpha^{-1}\mathbf{G}}(\mathbf{k},\mathbf{q}) \qquad \text{for} \quad \mathbf{q} = \alpha\mathbf{q}. \tag{6.4}$$

The above relation can be used in order to reduce the summation over the Brillouin zone to an irreducible wedge of the BZ constructed from those symmetry operations that leave the vector $\mathbf{q}$ unaltered. As a special case of interest we consider the situation, where inversion symmetry is present. Equation (6.3) gives for spatial inversion symmetry

$$\psi_{\mathbf{k}}(-\mathbf{r}) = \psi_{-\mathbf{k}}(\mathbf{r}). \tag{6.5}$$

Together with Kramer's theorem for systems with time reversal symmetry

$$\psi_{\mathbf{k}}(\mathbf{r}) = \psi^*_{-\mathbf{k}}(\mathbf{r}), \tag{6.6}$$

we obtain the important relation

$$\psi_{\mathbf{k}}(\mathbf{r}) = \psi^*_{\mathbf{k}}(-\mathbf{r}). \tag{6.7}$$

The above result can be used to show that the matrix elements $M^{\mathbf{G}}(\mathbf{k},\mathbf{q})$ are real numbers. By taking the complex conjugate of (6.1) and using the symmetry property (6.7) one obtains for systems having inversion symmetry

$$[M^{\mathbf{G}}(\mathbf{k},\mathbf{q})]^* = M^{\mathbf{G}}(\mathbf{k},\mathbf{q}). \tag{6.8}$$

[1] The simple form of Eq. (6.3) is only valid in the case of non-degenerate states.

6.1.2 Expansion in a Basis

Next, we will prove a statement from the introduction, namely that the matrix elements $M^{\mathbf{G}}_{nm}(\mathbf{k},\mathbf{q})$ are only non-zero if $\mathbf{k}' = \mathbf{k}+\mathbf{q}$. To this end, we switch to an integral notation for $M^{\mathbf{G}}_{nm}(\mathbf{k},\mathbf{q})$

$$M^{\mathbf{G}}_{nm}(\mathbf{k},\mathbf{q}) = \int_{\Omega} \mathrm{d}^3 r\, \psi^*_{n\mathbf{k}}(\mathbf{r}) e^{-i(\mathbf{q}+\mathbf{G})\mathbf{r}} \psi_{m\mathbf{k}'}(\mathbf{r}), \tag{6.9}$$

where the integral is taken over the entire *crystal* volume Ω. However, the integration may be restricted to one *unit* cell volume Ω_0, by using the Bloch wave property of the wave functions

$$\psi_{n\mathbf{k}}(\mathbf{r}+\mathbf{R}) = e^{i\mathbf{k}\mathbf{R}} \psi_{n\mathbf{k}}(\mathbf{r}). \tag{6.10}$$

Taking into account the identity (see App. A.2)

$$\sum_{\mathbf{R}} e^{-i(\mathbf{k}-\mathbf{k}'+\mathbf{q})\mathbf{R}} = \frac{\Omega}{\Omega_0} \delta_{\mathbf{q},\mathbf{k}'-\mathbf{k}}, \tag{6.11}$$

shows that $\mathbf{k}' = \mathbf{k}+\mathbf{q}$, and that the integral has to be taken only over one unit cell volume

$$M^{\mathbf{G}}_{nm}(\mathbf{k},\mathbf{q}) = \frac{\Omega}{\Omega_0} \int_{\Omega_0} \mathrm{d}^3 r\, \psi^*_{n\mathbf{k}}(\mathbf{r}) e^{-i(\mathbf{q}+\mathbf{G})\mathbf{r}} \psi_{m,\mathbf{k}+\mathbf{q}}(\mathbf{r}). \tag{6.12}$$

The relation (6.2) resulting from the Kronecker delta in (6.11) ensures the conservation of the crystal momentum. In actual computations, the wave functions $\psi_{n\mathbf{k}}(\mathbf{r})$ are expanded in a basis set $\phi_{\mathbf{k}_i}(\mathbf{r})$

$$\psi_{n\mathbf{k}}(\mathbf{r}) = \sum_i c_{n\mathbf{k}_i} \phi_{\mathbf{k}_i}(\mathbf{r}). \tag{6.13}$$

Then, insertion of (6.13) into expression (6.12) gives

$$M^{\mathbf{G}}_{nm}(\mathbf{k},\mathbf{q}) = \sum_{ij} c^*_{n\mathbf{k}_i} c_{m\mathbf{k}'_j} m^{\mathbf{G}}_{ij}(\mathbf{k},\mathbf{q}), \tag{6.14}$$

with the abbreviation

$$m^{\mathbf{G}}_{ij}(\mathbf{k},\mathbf{q}) = \frac{\Omega}{\Omega_0} \int_{\Omega_0} \mathrm{d}^3 r\, \phi^*_{\mathbf{k}_i}(\mathbf{r}) e^{-i(\mathbf{q}+\mathbf{G})\mathbf{r}} \phi_{\mathbf{k}'_j}(\mathbf{r}). \tag{6.15}$$

Expression (6.15) will be used in the next section, when we insert an LAPW basis set for $\phi_{\mathbf{k}_i}(\mathbf{r})$. The aim of the next subsections will be the computation of the matrix $m^{\mathbf{G}}_{ij}(\mathbf{k},\mathbf{q})$ using the LAPW basis set.

6.1.3 Contribution from the Interstitial

We proceed with the calculation of the integral (6.15) by inserting the explicit form of the LAPW basis set defined in equations (5.4) and (5.5). Due to the separation of the unit cell into non-overlapping spheres (S) and the remaining interstitial (I) we can split the integral into two parts

$$m_{ij}^{\mathbf{G}}(\mathbf{k},\mathbf{q}) = I_{ij}^{\mathbf{G}}(\mathbf{k},\mathbf{q}) + S_{ij}^{\mathbf{G}}(\mathbf{k},\mathbf{q}), \tag{6.16}$$

where $I_{ij}^{\mathbf{G}}(\mathbf{k},\mathbf{q})$ and $S_{ij}^{\mathbf{G}}(\mathbf{k},\mathbf{q})$ denote the interstitial and the sphere part, respectively. In the following it will be useful to define a step function

$$\Theta(\mathbf{r}) = \begin{cases} 1 & \mathbf{r} \in I \\ 0 & \mathbf{r} \notin I \end{cases}, \tag{6.17}$$

which is defined to be 1 in the interstitial region (I) and 0 inside the spheres (S). By inserting the plane wave form of the basis functions in the interstitial, we obtain for the interstitial contribution

$$I_{ij}^{\mathbf{G}}(\mathbf{k},\mathbf{q}) = \frac{1}{\Omega_0}\int_{\Omega_0} \mathrm{d}^3 r\, \Theta(\mathbf{r}) e^{-i(\mathbf{K}_i - \mathbf{K}_j + \mathbf{G})\mathbf{r}}, \tag{6.18}$$

where the integral can be taken over the whole unit cell on account of the property (6.17) of the step function. Since the step function $\Theta(\mathbf{r})$ has the periodicity of the lattice we may expand it in a Fourier series with the Fourier coefficients $\tilde{\Theta}_{\mathbf{G}}$

$$\Theta(\mathbf{r}) = \sum_{\mathbf{G}} \tilde{\Theta}_{\mathbf{G}} e^{i\mathbf{G}\mathbf{r}}, \tag{6.19}$$

where $\tilde{\Theta}_{\mathbf{G}}$ can be calculated analytically, giving [87]

$$\tilde{\Theta}_{\mathbf{G}} = \begin{cases} 1 - \sum\limits_{\alpha} \dfrac{4\pi R_\alpha^3}{3\Omega_0} & \mathbf{G} = \mathbf{0} \\ -\dfrac{4\pi}{\Omega_0 |\mathbf{G}|} \sum\limits_{\alpha} j_1(|\mathbf{G}|R_\alpha) R_\alpha^2 e^{i\mathbf{G}\mathbf{R}_\alpha} & \mathbf{G} \neq \mathbf{0} \end{cases}. \tag{6.20}$$

By inserting (6.19) into (6.18), we eventually obtain

$$I_{ij}^{\mathbf{G}}(\mathbf{k},\mathbf{q}) = I_{ij}^{\mathbf{G}} = \tilde{\Theta}_{\mathbf{K}_i - \mathbf{K}_j + \mathbf{G}}, \tag{6.21}$$

where we have made use of the identity (see Appendix A.2)

$$\int_{\Omega_0} \mathrm{d}^3 r\, e^{-i(\mathbf{K}_i - \mathbf{K}_j + \mathbf{G})\mathbf{r}} = \Omega_0 \delta_{\mathbf{K}_i - \mathbf{K}_j + \mathbf{G}}. \tag{6.22}$$

Thus, the interstitial contribution to the desired integrals $m_{ij}^{\mathbf{G}}(\mathbf{k},\mathbf{q})$ are simply obtained from the analytic expressions of the Fourier transformed step function.

6.1.4 Contribution from the Spheres

The integral over sphere part of the unit cell can again be divided into a sum of integrations over one sphere MT_α each

$$S^{\mathbf{G}}_{ij}(\mathbf{k},\mathbf{q}) = \frac{1}{\Omega_0}\sum_\alpha e^{-i(\mathbf{q}+\mathbf{G})\mathbf{R}_\alpha} s^{\mathbf{G}}_{ij}(\mathbf{k},\mathbf{q}), \tag{6.23}$$

with

$$s^{\mathbf{G}}_{ij}(\mathbf{k},\mathbf{q}) = \int_{MT_\alpha} \mathrm{d}^3 r\, \phi^*_{\mathbf{k}_i}(\mathbf{r}) e^{-i(\mathbf{q}+\mathbf{G})\mathbf{r}} \phi_{\mathbf{k}'_j}(\mathbf{r}). \tag{6.24}$$

The phase factor in (6.23) reflects the fact that the origin has to be shifted into the center of the sphere α at position $\mathbf{R}_\alpha$. Note that we have omitted the explicit dependence on the atom number α in the notation of $s^{\mathbf{G}}_{ij}(\mathbf{k},\mathbf{q})$. In order to further evaluate the integral in (6.24) we expand the plane wave $e^{-i(\mathbf{q}+\mathbf{G})\mathbf{r}}$ in spherical harmonics and spherical Bessel functions using the Rayleigh expansion

$$e^{i\mathbf{g}\mathbf{r}} = 4\pi \sum_{L=0}^{\infty}\sum_{M=-L}^{+L} i^L j_L(gr) Y^*_{LM}(\hat{g}) Y_{LM}(\hat{r}), \tag{6.25}$$

where we have set $\mathbf{g} = -(\mathbf{q}+\mathbf{G})$. Expression (6.25) together with the form of the basis functions inside the spheres (5.5) splits the integral (6.24) into a radial and an angular part. After reordering terms one obtains

$$\begin{aligned} s^{\mathbf{G}}_{ij}(\mathbf{k},\mathbf{q}) \;=\; & \sum_{l'm'} \Bigg\{ A_{l'm'}(\mathbf{k}'_j) \sum_{lm} [A^*_{lm}(\mathbf{k}_i) T^{\mathbf{g}}_{uu} + B^*_{lm}(\mathbf{k}_i) T^{\mathbf{g}}_{\dot{u}u}] \\ & + B_{l'm'}(\mathbf{k}'_j) \sum_{lm} [A^*_{lm}(\mathbf{k}_i) T^{\mathbf{g}}_{u\dot{u}} + B^*_{lm}(\mathbf{k}_i) T^{\mathbf{g}}_{\dot{u}\dot{u}}] \Bigg\}. \end{aligned} \tag{6.26}$$

To give a more compact notation, we have introduced the following set of abbreviations

$$T^{\mathbf{g}}_{uu} = 4\pi \sum_{LM} i^L Y^*_{LM}(\hat{g}) G(l,m,L,M,l',m') F^g_{uu}(l,L,l'), \tag{6.27}$$

$$T^{\mathbf{g}}_{\dot{u}u} = 4\pi \sum_{LM} i^L Y^*_{LM}(\hat{g}) G(l,m,L,M,l',m') F^g_{\dot{u}u}(l,L,l'), \tag{6.28}$$

$$T^{\mathbf{g}}_{u\dot{u}} = 4\pi \sum_{LM} i^L Y^*_{LM}(\hat{g}) G(l,m,L,M,l',m') F^g_{u\dot{u}}(l,L,l'), \tag{6.29}$$

$$T^{\mathbf{g}}_{\dot{u}\dot{u}} = 4\pi \sum_{LM} i^L Y^*_{LM}(\hat{g}) G(l,m,L,M,l',m') F^g_{\dot{u}\dot{u}}(l,L,l'). \tag{6.30}$$

Moreover, the Gaunt coefficients $G(l,m,L,M,l',m')$ and the set of radial integrals $F^g(l,L,l')$ have been defined as

$$G(l,m,L,M,l',m') = \int \mathrm{d}\Omega\, Y^*_{lm}(\hat{r}) Y_{LM}(\hat{r}) Y_{l'm'}(\hat{r}) \tag{6.31}$$

$$F^g_{uu}(l,L,l') = \int_0^R r^2 \mathrm{d}r\, u_l(r) j_L(Gr) u_{l'}(r), \tag{6.32}$$

$$F^g_{u\dot{u}}(l,L,l') = \int_0^R r^2 \mathrm{d}r\, u_l(r) j_L(Gr) \dot{u}_{l'}(r), \tag{6.33}$$

$$F^g_{\dot{u}u}(l,L,l') = \int_0^R r^2 \mathrm{d}r\, \dot{u}_l(r) j_L(Gr) u_{l'}(r), \tag{6.34}$$

$$F^g_{\dot{u}\dot{u}}(l,L,l') = \int_0^R r^2 \mathrm{d}r\, \dot{u}_l(r) j_L(Gr) \dot{u}_{l'}(r). \tag{6.35}$$

Equations (6.23) and (6.26) for the sphere contributions and relation (6.21) taking account of the interstitial part completely determine the matrix elements $m^{\mathbf{G}}_{ij}(\mathbf{k},\mathbf{q})$ between two ordinary LAPW basis functions. What is still missing are the corresponding expressions for local orbitals and the APW+lo basis set introduced in Sec. 5.2.2 and 5.2.3, respectively. These integrals will be described in the next subsection.

6.1.5 Local Orbitals and APW+lo

Since local orbitals are defined to be completely confined within the muffin-tin spheres there is no interstitial contribution to the desired integrals. Two types of integrals are required: matrix elements between an ordinary LAPW basis function and a local orbital, $m^{\mathbf{G}}_{i,lo}(\mathbf{k},\mathbf{q})$, and between two local orbitals, $m^{\mathbf{G}}_{lo1,lo2}(\mathbf{k},\mathbf{q})$. Knowing that there is no interstitial contribution we can write in analogy to (6.23)

$$m^{\mathbf{G}}_{i,lo}(\mathbf{k},\mathbf{q}) = \frac{1}{\Omega_0} \sum_\alpha e^{-i(\mathbf{q}+\mathbf{G})\mathbf{R}_\alpha} s^{\mathbf{G}}_{i,lo}(\mathbf{k},\mathbf{q}), \tag{6.36}$$

$$m^{\mathbf{G}}_{lo1,lo2}(\mathbf{k},\mathbf{q}) = \frac{1}{\Omega_0} \sum_\alpha e^{-i(\mathbf{q}+\mathbf{G})\mathbf{R}_\alpha} s^{\mathbf{G}}_{lo1,lo2}(\mathbf{k},\mathbf{q}), \tag{6.37}$$

where the integrals $s^{\mathbf{G}}_{i,lo}(\mathbf{k},\mathbf{q})$ and $s^{\mathbf{G}}_{lo1,lo2}(\mathbf{k},\mathbf{q})$ are defined as

$$s^{\mathbf{G}}_{i,lo}(\mathbf{k},\mathbf{q}) = \int_{MT_\alpha} \mathrm{d}^3 r\, \phi^*_{\mathbf{k}_i}(\mathbf{r}) e^{-i(\mathbf{q}+\mathbf{G})\mathbf{r}} \phi_{l_{lo}}(\mathbf{r}), \tag{6.38}$$

$$s^{\mathbf{G}}_{lo1,lo2}(\mathbf{k},\mathbf{q}) = \int_{MT_\alpha} \mathrm{d}^3 r\, \phi^*_{l_{lo1}}(\mathbf{r}) e^{-i(\mathbf{q}+\mathbf{G})\mathbf{r}} \phi_{l_{lo2}}(\mathbf{r}). \tag{6.39}$$

Inserting the expressions (5.5) and (5.16) for the LAPW and local orbital functions, respectively, and using the Rayleigh expansion (6.25) for the plane wave again, one finally obtains the following expressions

$$\begin{aligned} s^{\mathbf{G}}_{i,lo}(\mathbf{k},\mathbf{q}) &= \sum_{m'}\Bigg\{ A_{l_o m'}\sum_{lm}[A^*_{lm}(\mathbf{k}_i)T^{\mathbf{g}}_{uu} + B^*_{lm}(\mathbf{k}_i)T^{\mathbf{g}}_{\dot{u}u}] \\ &\quad + B_{l_o m'}\sum_{lm}[A^*_{lm}(\mathbf{k}_i)T^{\mathbf{g}}_{u\dot{u}} + B^*_{lm}(\mathbf{k}_i)T^{\mathbf{g}}_{\dot{u}\dot{u}}] \\ &\quad + C_{l_o m'}\sum_{lm}[A^*_{lm}(\mathbf{k}_i)T12^{\mathbf{g}}_{uu} + B^*_{lm}(\mathbf{k}_i)T12^{\mathbf{g}}_{\dot{u}u}]\Bigg\}, \end{aligned} \tag{6.40}$$

and

$$\begin{aligned} s^{\mathbf{G}}_{lo1,lo2}(\mathbf{k},\mathbf{q}) &= \sum_{m'}\Bigg\{ A_{l_{o2} m'}\sum_{m}[A^*_{l_{o1}m}T^{\mathbf{g}}_{uu} + B^*_{l_{o1}m}T^{\mathbf{g}}_{\dot{u}u} + C^*_{l_{o1}m}T21^{\mathbf{g}}_{uu}] \\ &\quad + B_{l_{o2} m'}\sum_{m}[A^*_{l_{o1}m}T^{\mathbf{g}}_{u\dot{u}} + B^*_{l_{o1}m}T^{\mathbf{g}}_{\dot{u}\dot{u}} + C^*_{l_{o1}m}T21^{\mathbf{g}}_{u\dot{u}}] \\ &\quad + C_{l_{o2} m'}\sum_{m}[A^*_{l_{o1}m}T12^{\mathbf{g}}_{uu} + B^*_{l_{o1}m}T12^{\mathbf{g}}_{\dot{u}u} + C^*_{l_{o1}m}T22^{\mathbf{g}}_{uu}]\Bigg\}. \end{aligned} \tag{6.41}$$

Unfortunately, these rather bulky expressions still have to be completed with some more definitions used as abbreviations in the formulae given above.

$$\begin{aligned} T12^{\mathbf{g}}_{uu} &= 4\pi\sum_{LM} i^L Y^*_{LM}(\hat{g})G(l,m,L,M,l_{lo},m')F12^g_{uu}(l,L,l_{lo}), \\ T12^{\mathbf{g}}_{\dot{u}u} &= 4\pi\sum_{LM} i^L Y^*_{LM}(\hat{g})G(l,m,L,M,l_{lo},m')F12^g_{\dot{u}u}(l,L,l_{lo}), \\ F12^g_{uu}(l,L,l_{lo}) &= \int_0^R r^2 \mathrm{d}r\, u_l(r) j_L(Gr) u_{l_{lo}}(r,E_{l_{lo}}), \\ F12^g_{\dot{u}u}(l,L,l_{lo}) &= \int_0^R r^2 \mathrm{d}r\, \dot{u}_l(r) j_L(Gr) u_{l_{lo}}(r,E_{l_{lo}}). \end{aligned}$$

And still some more ...

$$\begin{aligned} T21^{\mathbf{g}}_{uu} &= 4\pi\sum_{LM} i^L Y^*_{LM}(\hat{g})G(l_{lo1},m,L,M,l_{lo2},m')F21^g_{uu}(l_{lo1},L,l_{lo2}), \\ T21^{\mathbf{g}}_{u\dot{u}} &= 4\pi\sum_{LM} i^L Y^*_{LM}(\hat{g})G(l_{lo1},m,L,M,l_{lo2},m')F21^g_{u\dot{u}}(l_{lo1},L,l_{lo2}), \\ T22^{\mathbf{g}}_{uu} &= 4\pi\sum_{LM} i^L Y^*_{LM}(\hat{g})G(l_{lo1},m,L,M,l_{lo2},m')F22^g_{uu}(l_{lo1},L,l_{lo2}), \end{aligned}$$

with

$$\begin{aligned} F21^g_{uu}(l_{lo1}, L, l_{lo2}) &= \int_0^R r^2 \mathrm{d}r\, u_{l_{lo1}}(r, E_{l_{lo1}}) j_L(Gr) u_{l_{lo2}}(r), \\ F21^g_{u\dot{u}}(l_{lo1}, L, l_{lo2}) &= \int_0^R r^2 \mathrm{d}r\, u_{l_{lo1}}(r, E_{l_{lo1}}) j_L(Gr) \dot{u}_{l_{lo2}}(r), \\ F22^g_{uu}(l_{lo1}, L, l_{lo2}) &= \int_0^R r^2 \mathrm{d}r\, u_{l_{lo1}}(r, E_{l_{lo1}}) j_L(Gr) u_{l_{lo2}}(r, E_{l_{lo2}}). \end{aligned}$$

In all equations given above we have used the convention that radial wave functions *without* explicitly specifying the linearization energy are evaluated at the conventional E_l. On the other hand, radial wave functions *with* an energy argument are meant to be evaluated at the extra linearization energy used for local orbitals as described in Sec. 5.2.2. What is missing up to now, are expressions for the APW+lo basis set which has been outlined in Sec. 5.2.3. But fortunately, this is accomplished very easily as can be seen by looking at Eq. (5.17): simply set $B^*_{lm}(\mathbf{k}_i) = 0$ in all expressions given above in order to obtain the corresponding matrix elements in the APW+lo basis. Concluding this section, we have given all necessary details to evaluate the matrix elements $M^{\mathbf{G}}_{nm}(\mathbf{k}, \mathbf{q})$ within the LAPW scheme.

6.2 The Dielectric Matrix

6.2.1 The Independent Particle Polarizability

In order to evaluate the microscopic dielectric matrix in the random phase approximation we require the irreducible polarization $\hat{P}^0$ in the independent-particle approximation. We have already derived an expression for $\hat{P}^0$ in Sec. 4.2.2 leading to Eq. (4.27). Here, we are only interested in the *static* dielectric function, therefore we simply set $\omega = 0$ in Eq. (4.27). Moreover, we specialize the notation to systems having a gap in the spectrum, and denote valence states by v and conduction states by the letter c, respectively. Consequently, we obtain instead of the more general formula (4.27)

$$\hat{P}^0_{\mathbf{G}\mathbf{G}'}(\mathbf{q}) = \frac{4}{\Omega} \sum_{cv\mathbf{k}}^{\mathrm{BZ}} \frac{M^{\mathbf{G}}_{vc}(\mathbf{k}, \mathbf{q}) [M^{\mathbf{G}'}_{vc}(\mathbf{k}, \mathbf{q})]^*}{\varepsilon_{v\mathbf{k}} - \varepsilon_{c,\mathbf{k}+\mathbf{q}}}, \tag{6.42}$$

where Ω denotes the crystal volume $\Omega = \Omega_0 \times N_{\mathbf{k}}$, and $\varepsilon_{v\mathbf{k}}$ and $\varepsilon_{c,\mathbf{k}+\mathbf{q}}$ are Kohn-Sham valence (v) and conduction (c) states at wave vectors $\mathbf{k}$ and $\mathbf{k}+\mathbf{q}$, respectively. The summations in (6.42) run over all occupied (v) and all unoccupied (c) states, which gives a factor of 2 as compared to expression (4.27). In addition, spin degeneracy is supposed and included in (6.42) by an additional factor of 2.

Here, the $\mathbf{k}$ summation runs over the full Brillouin zone (BZ). It should be noted, that whereas the phases of $M_{vc}^{\mathbf{G}}(\mathbf{k},\mathbf{q})$ are not determined unambiguously due to the arbitrary choice of phases in the wave functions, this ambiguity is removed in expression (6.42). There, the wave functions enter with their complex conjugates and an arbitrary phase drops out as it should be the case for any physically observable quantity.

6.2.2 Symmetry of $\hat{P}^0_{\mathbf{G}\mathbf{G}'}(\mathbf{q})$

From its real space representation it is clear that the polarization function P fulfills the following relations because it has the full symmetry of the crystal

$$\hat{P}(\mathbf{r}+\mathbf{R},\mathbf{r}'+\mathbf{R}) = \hat{P}(\mathbf{r},\mathbf{r}'), \tag{6.43}$$
$$\hat{P}[\alpha^{-1}(\mathbf{r}-\mathbf{t}),\alpha^{-1}(\mathbf{r}'-\mathbf{t})] = \hat{P}(\mathbf{r},\mathbf{r}'). \tag{6.44}$$

Here, $\mathbf{R}$ denotes a lattice vector, and α and $\mathbf{t}$ are the rotational and translational part of a symmetry operation included in the space group of the crystal. The response of the system remains unaltered if both the position of the perturbation $\mathbf{r}'$ and the probing position $\mathbf{r}$ are translated by a direct lattice vector. Moreover, if both $\mathbf{r}$ and $\mathbf{r}'$ are rotated by a symmetry operation of the crystal, the response function should be unchanged as well. In fact, relation (6.43) is used to write $\hat{P}$ in a matrix notation in reciprocal space. In addition, Eq. (6.44) can be used to show the corresponding symmetry relations in the plane wave representation [81]

$$\hat{P}^0_{\mathbf{G}\mathbf{G}'}(\mathbf{q}_1) = e^{i(\mathbf{G}'-\mathbf{G})\mathbf{t}}\hat{P}^0_{\mathbf{G}_1\mathbf{G}'_1}(\mathbf{q}), \tag{6.45}$$
$$\mathbf{q}_1 = \alpha\mathbf{q}+\mathbf{G}_\alpha, \tag{6.46}$$
$$\mathbf{G}_1 = \alpha^{-1}(\mathbf{G}+\mathbf{G}_\alpha). \tag{6.47}$$

Here, $\mathbf{q}$ and $\mathbf{q}_1$ are vectors inside the first Brillouin zone, and $\mathbf{G}_\alpha$ is a reciprocal lattice vector that might only be nonzero for $\mathbf{q}$ vectors at the boundary of the Brillouin zone. These symmetry relations have several consequences that considerably reduce the computational effort in the construction of the dielectric matrix. Most important, only $\mathbf{q}$'s from the irreducible wedge of the BZ, constructed by all symmetry operations of the crystal need to be computed. In addition, the number of independent $\mathbf{G}$ vectors for which the response function has to be calculated is reduced, and finally equation (6.45) together with the symmetry properties of the matrix elements $M^{\mathbf{G}}(\mathbf{k},\mathbf{q})$ described in Eq. (6.4) can be used to reduce the sum over the full BZ in (6.42). The symmetry operations that leave the $\mathbf{q}$ vector under consideration unaltered, that is $\mathbf{q}=\alpha\mathbf{q}+\mathbf{G}_\alpha$, define an irreducible wedge

of the Brillouin zone which we denote by $\mathrm{BZ}_{\mathbf{q}}$. Then we obtain for $\hat{P}^0_{\mathbf{GG'}}(\mathbf{q})$

$$\begin{aligned}\hat{P}^0_{\mathbf{GG'}}(\mathbf{q}) &= \frac{4}{\Omega}\sum_{vc}\sum_{\mathbf{k}}^{\mathrm{BZ}_{\mathbf{q}}}\frac{1}{\varepsilon_{v\mathbf{k}}-\varepsilon_{c,\mathbf{k}+\mathbf{q}}}\times \\ &\quad \sum_{\alpha}^{\mathrm{star}(\mathbf{k})} e^{i\alpha(\mathbf{G}-\mathbf{G'})\mathbf{t}} M_{vc}^{\alpha\mathbf{G}+\mathbf{G}_\alpha}(\mathbf{k},\mathbf{q})[M_{vc}^{\alpha\mathbf{G'}+\mathbf{G}_\alpha}(\mathbf{k},\mathbf{q})]^*. \qquad (6.48)\end{aligned}$$

6.2.3 Diagonal Elements and the Head of $\hat{P}^0$

In cases where only the diagonal elements of $\hat{P}^0$ are required, we can work with simplified expressions, which will be presented here to complete the record

$$\hat{P}^0_{\mathbf{GG}}(\mathbf{q}) = \frac{4}{\Omega}\sum_{vc}\sum_{\mathbf{k}}^{\mathrm{BZ}_{\mathbf{q}}}\frac{1}{\varepsilon_{v\mathbf{k}}-\varepsilon_{c,\mathbf{k}+\mathbf{q}}}\sum_{\alpha}^{\mathrm{star}(\mathbf{k})}|M_{vc}^{\alpha\mathbf{G}+\mathbf{G}_\alpha}(\mathbf{k},\mathbf{q})|^2. \qquad (6.49)$$

Moreover, a special treatment is required for the so-called head of $\hat{P}^0$, meaning the element for which $\mathbf{q}=\mathbf{0}$ and $\mathbf{G}=\mathbf{G'}=\mathbf{0}$. It is clear from the definition of $M^{\mathbf{G}}(\mathbf{k},\mathbf{q})$ in (6.1) that it gives a Kronecker δ_{nm} in this case. Consequently, $\hat{P}_{\mathbf{00}}(\mathbf{q}=\mathbf{0})$ is identically zero which would lead to a divergent dielectric matrix element $\varepsilon_{\mathbf{00}}(\mathbf{q}=\mathbf{0})$ due to the $4\pi/|\mathbf{q}+\mathbf{G}|^2$ factor from the Coulomb potential as can be seen for instance from expression (4.33). In order to overcome these difficulties one has to take the limit $\mathbf{q}\to\mathbf{0}$ instead of setting $\mathbf{q}$ identically zero. From $\mathbf{k}\cdot\mathbf{p}$ perturbation theory one obtains the following expression valid in the limit of small $\mathbf{q}$ (compare Sec. 4.2.4)

$$\langle v\mathbf{k}|e^{-i\mathbf{qr}}|c,\mathbf{k}+\mathbf{q}\rangle = \mathbf{q}\frac{\langle v\mathbf{k}|\mathbf{p}|c\mathbf{k}\rangle}{\varepsilon_{c\mathbf{k}}-\varepsilon_{v\mathbf{k}}}. \qquad (6.50)$$

Insertion of (6.50) into (6.42) directly leads to

$$\hat{P}_{\mathbf{00}}(\mathbf{q}\to\mathbf{0}) = \frac{4q^2}{\Omega}\sum_{cv\mathbf{k}}\frac{|\langle v\mathbf{k}|p|c\mathbf{k}\rangle|^2}{(\varepsilon_{v\mathbf{k}}-\varepsilon_{c\mathbf{k}})^3}, \qquad (6.51)$$

which gives a finite value for the head of the dielectric matrix $\varepsilon_{\mathbf{00}}(\mathbf{q}=\mathbf{0})$ due to the cancellation of the $1/q^2$ factor arising from the Coulomb potential.

6.2.4 Static Dielectric Matrix and Screened Interaction

We have already seen that the dielectric matrix in the RPA is obtained from the polarization function $\hat{P}^0$ as

$$\varepsilon_{\mathbf{GG'}}(\mathbf{q}) = \delta_{\mathbf{GG'}} - \frac{4\pi}{|\mathbf{q}+\mathbf{G}||\mathbf{q}+\mathbf{G'}|}\hat{P}^0_{\mathbf{GG'}}(\mathbf{q}). \qquad (6.52)$$

Moreover, in Section 3.3.3 we have defined the screened interaction W in terms of the *inverse* dielectric matrix ϵ^{-1} according to Eq. (3.48)

$$W_{\mathbf{GG'}}(\mathbf{q}) = \frac{4\pi\varepsilon^{-1}_{\mathbf{GG'}}(\mathbf{q})}{|\mathbf{q}+\mathbf{G}||\mathbf{q}+\mathbf{G'}|}. \tag{6.53}$$

We obtain a particularly simple result for the screened interaction W if we neglect local field effects. Then, the off-diagonal elements of the dielectric matrix ϵ are identically zero and the matrix inversion in Eq. (6.53) is trivial

$$W_{\mathbf{GG'}}(\mathbf{q}) = \frac{4\pi\delta_{\mathbf{GG'}}}{\varepsilon_{\mathbf{GG}}(\mathbf{q})|\mathbf{q}+\mathbf{G}|^2}. \tag{6.54}$$

6.3 Evaluation of the BSE

6.3.1 The Exchange Interaction Kernel

The formulae derived in the previous sections represent all the ingredients needed for the evaluation of the electron-hole kernel of the Bethe-Salpeter equation. The exchange interaction kernel entering the BSE has been derived in Sec. 4.3.7. It is given by (compare Eq. 4.117)

$$H^x_{vc\mathbf{k},v'c'\mathbf{k'}} = \int\int \mathrm{d}^3r\mathrm{d}^3r' \frac{\psi^*_{v'\mathbf{k'}}(\mathbf{r'})\psi^*_{c\mathbf{k}}(\mathbf{r})\psi_{v\mathbf{k}}(\mathbf{r})\psi_{c'\mathbf{k'}}(\mathbf{r'})}{|\mathbf{r}-\mathbf{r'}|}. \tag{6.55}$$

This expression is evaluated most easily by inserting the reciprocal space representation of the Coulomb potential

$$\frac{1}{|\mathbf{r}-\mathbf{r'}|} = \frac{1}{\Omega}\sum_{\mathbf{qG}} \frac{4\pi}{|\mathbf{q}+\mathbf{G}|^2} e^{-i(\mathbf{q}+\mathbf{G})(\mathbf{r}-\mathbf{r'})} \tag{6.56}$$

into Eq. (6.55). The double space integration can now be split into a product of two space integrations and with the definition of $M^{\mathbf{G}}_{nm}(\mathbf{k},\mathbf{q})$ in (6.1) we get

$$H^x_{vc\mathbf{k},v'c'\mathbf{k'}} = \frac{4\pi}{\Omega}\sum_{\mathbf{G}\neq\mathbf{0}} \frac{1}{|\mathbf{G}|^2} M^{\mathbf{G}}_{v'c'}(\mathbf{k'},\mathbf{q}=\mathbf{0})[M^{\mathbf{G}}_{vc}(\mathbf{k},\mathbf{q}=\mathbf{0})]^*. \tag{6.57}$$

When compared to (6.56) the summation over $\mathbf{q}$ has dropped out due to conservation of crystal momentum as has been pointed out in the Sec. 6.1.2: The matrix element $\langle n\mathbf{k}|e^{-i(\mathbf{q}+\mathbf{G})\mathbf{r}}|m\mathbf{k'}\rangle$ is only non-zero provided $\mathbf{k'} = \mathbf{k}+\mathbf{q}$. On account of the exchange character of the interaction only matrix elements for $\mathbf{q}=\mathbf{0}$ enter (6.57). Moreover, the $\mathbf{G}=\mathbf{0}$ term can be excluded from the summation, since it has been shown to yield no contribution (compare with Sec. 4.3.2). There we have seen that it is possible to exclude the long-range part $\mathbf{G}=\mathbf{0}$ in constructing the macroscopic dielectric function in the limit of vanishing $\mathbf{q}$ vector.

6.3.2 The Direct Interaction Kernel

The direct interaction term, which is responsible for the attraction between the electron-hole pairs described by the Bethe-Salpeter equation is given by (compare Eq. 4.116)

$$H^{dir}_{vc\mathbf{k},v'c'\mathbf{k}'} = -\int\int \mathrm{d}^3r\mathrm{d}^3r' \frac{\psi_{v\mathbf{k}}(\mathbf{r})\psi^*_{c\mathbf{k}}(\mathbf{r}')\varepsilon^{-1}(\mathbf{r},\mathbf{r}')\psi^*_{v'\mathbf{k}'}(\mathbf{r})\psi_{c'\mathbf{k}'}(\mathbf{r}')}{|\mathbf{r}-\mathbf{r}'|}. \tag{6.58}$$

Here, we have used the definition of the screened interaction W in terms of the inverse dielectric matrix as discussed in the previous section. In analogy to the procedure for the exchange kernel H^x, we express the screened interaction in reciprocal space using its Fourier representation according to the convention (A.7)

$$\frac{\varepsilon^{-1}(\mathbf{r},\mathbf{r}')}{|\mathbf{r}-\mathbf{r}'|} = \frac{1}{\Omega}\sum_{\mathbf{qGG}'} e^{-i(\mathbf{q}+\mathbf{G})\mathbf{r}} \frac{4\pi\varepsilon^{-1}_{\mathbf{GG}'}(\mathbf{q})}{|\mathbf{q}+\mathbf{G}||\mathbf{q}+\mathbf{G}'|} e^{i(\mathbf{q}+\mathbf{G}')\mathbf{r}'}, \tag{6.59}$$

and insert it into the integral (6.58). As before, the double space integrals split into two products and with help of the matrix elements $M^{\mathbf{G}}_{nm}(\mathbf{k},\mathbf{q})$ we obtain the following expression

$$H^{dir}_{vc\mathbf{k},v'c'\mathbf{k}'} = -\frac{1}{\Omega}\sum_{\mathbf{GG}'} W_{\mathbf{GG}'}(\mathbf{k}'-\mathbf{k}) M^{\mathbf{G}}_{cc'}(\mathbf{k},\mathbf{q})[M^{\mathbf{G}'}_{vv'}(\mathbf{k},\mathbf{q})]^*, \tag{6.60}$$

with the screened Coulomb interaction $W_{\mathbf{GG}'}(\mathbf{q})$ given by Eq. (6.53). Again the summation over $\mathbf{q}$ in (6.59) drops out due to conservation of momentum. Special care has to be taken in the leading $\mathbf{G}=\mathbf{G}'=\mathbf{0}$ term for the diagonal elements of $H^{dir}_{vc\mathbf{k},v'c'\mathbf{k}'}$, where $\mathbf{k}=\mathbf{k}'$, that is $\mathbf{q}=\mathbf{0}$. If we denote this term by $h^0_{vc\mathbf{k},v'c'\mathbf{k}}$, we have

$$h^0_{vc\mathbf{k},v'c'\mathbf{k}} = -\frac{1}{\Omega} W_{\mathbf{00}}(\mathbf{q}\to\mathbf{0}) M^{\mathbf{0}}_{cc'}(\mathbf{k},\mathbf{q}\to\mathbf{0})[M^{\mathbf{0}}_{vv'}(\mathbf{k},\mathbf{q}\to\mathbf{0})]^*. \tag{6.61}$$

This term is divergent for the diagonal components $v=v'$ and $c=c'$, because the matrix elements $M^{\mathbf{0}}_{cc'}(\mathbf{k},\mathbf{q}\to\mathbf{0})$ are one in that case, and the screened interaction diverges for $\mathbf{q}$ approaching zero. However, this divergence can be integrated out when the electron-hole kernel $H_{vc\mathbf{k},v'c'\mathbf{k}'}$ is diagonalized according to Eq. (4.104) [83]. If we re-write the summation over the vector $\mathbf{k}'$ as an integration over $\mathbf{k}'$, we obtain for the leading term $h^0_{vc\mathbf{k},v'c'\mathbf{k}'}$ of the direct interaction kernel

$$\sum_{v'c'\mathbf{k}'} h^0_{vc\mathbf{k},v'c'\mathbf{k}'} A^{\lambda}_{v'c'\mathbf{k}'} = \sum_{v'c'}\left[\frac{\Omega}{(2\pi)^3}\int_{S_{\mathbf{q}}} \mathrm{d}^3q\, h^0_{vc\mathbf{k},v'c'\mathbf{k}+\mathbf{q}}\right] A^{\lambda}_{v'c'\mathbf{k}+\mathbf{q}}. \tag{6.62}$$

Here, the integration over $\mathbf{q}$ runs over a region around $\mathbf{q}=\mathbf{0}$ having a volume given by the discretization of the $\mathbf{k}$ mesh. Thus, the reciprocal volume $S_{\mathbf{q}}$ is

given by the volume of the Brillouin zone Ω_{BZ} divided by the number of discrete $\mathbf{k}$ points $N_{\mathbf{k}}$ in the Brillouin zone,

$$S_{\mathbf{q}} = \frac{\Omega_{BZ}}{N_{\mathbf{k}}}. \tag{6.63}$$

We can now evaluate the quantity in square brackets of Eq. (6.62). Choosing for the integration volume $S_{\mathbf{q}}$ a sphere having the same volume as defined by Eq. (6.63), and by assuming that the dielectric matrix is constant over the small region $S_{\mathbf{q}}$, yields for the leading term in the diagonal components of the direct interaction term

$$h^0_{vc\mathbf{k},v'c'\mathbf{k}} = -\frac{2}{(2\pi)^2}\left(\frac{6\pi^2}{\Omega}\right)^{\frac{1}{3}}\frac{4\pi}{\epsilon(\mathbf{q}=\mathbf{0})}\delta_{cc'}\delta_{vv'}. \tag{6.64}$$

This term is a constant for all diagonal elements of $H^{dir}_{vc\mathbf{k},v'c'\mathbf{k}'}$, thereby producing a rigid shift of the exciton energies given by the size of $h^0_{vc\mathbf{k},v'c'\mathbf{k}}$. It can be viewed as the zeroth order approximation to the electron-hole attraction, only changing the excitation energies but not the oscillator strengths of the transitions. In the numerical evaluation of expression (6.60) it is understood that the summation excludes the $\mathbf{G} = \mathbf{G}' = \mathbf{0}$ term for the diagonal $\mathbf{k} = \mathbf{k}'$ components. Instead, a term given by Eq. (6.64) has to be added. Finally, if we employ the diagonal approximation for the screened interaction W as given by Eq. (6.54), only one summation over reciprocal lattice vectors in Eq. (6.60) survives, and we obtain the particularly simple result

$$\begin{aligned} H^{dir}_{vc\mathbf{k},v'c'\mathbf{k}'} &= -\left(\frac{6\pi^2}{\Omega}\right)^{\frac{1}{3}}\frac{4\pi}{\epsilon(\mathbf{q}=\mathbf{0})}\delta_{cc'}\delta_{vv'}\delta_{\mathbf{k}\mathbf{k}'} \\ &- \frac{1}{\Omega}{\sum_{\mathbf{G}}}' W_{\mathbf{G}\mathbf{G}}(\mathbf{k}'-\mathbf{k})M^{\mathbf{G}}_{cc'}(\mathbf{k},\mathbf{q})[M^{\mathbf{G}}_{vv'}(\mathbf{k},\mathbf{q})]^*. \end{aligned} \tag{6.65}$$

Note that $\sum'$ denotes a summation where the $\mathbf{G} = \mathbf{0}$ term has to be omitted for the diagonal components $\mathbf{k} = \mathbf{k}'$.

6.3.3 Symmetry Properties of the Interaction Kernel

Symmetry can be used to block-diagonalize the interaction kernel of the Bethe-Salpeter equation. This can be seen by using the transformation property of the wave function under the action of the symmetry element $\{\alpha|\mathbf{t}\}$ as given in Eq. (6.3). For instance, if we consider the exchange kernel H^x at the rotated wave vectors $\alpha\mathbf{k}$ and $\alpha\mathbf{k}'$

$$H^x_{vc\alpha\mathbf{k},v'c'\alpha\mathbf{k}'} = \int\int \mathrm{d}^3r\mathrm{d}^3r' \frac{\psi^*_{v'\alpha\mathbf{k}'}(\mathbf{r}')\psi^*_{c\alpha\mathbf{k}}(\mathbf{r})\psi_{v\alpha\mathbf{k}}(\mathbf{r})\psi_{c'\alpha\mathbf{k}'}(\mathbf{r}')}{|\mathbf{r}-\mathbf{r}'|}, \tag{6.66}$$

and apply the relation (6.3), a change of variables inside the integral leads to the identity[2]

$$H^x_{vc\alpha\mathbf{k},v'c'\alpha\mathbf{k}'} = H^x_{vc\mathbf{k},v'c'\mathbf{k}'}. \tag{6.67}$$

The corresponding expression for the direct interaction kernel can be derived in a similar manner, if additionally the symmetry properties of the screened interaction is taken into account. For the inverse of the dielectric matrix an analogous result as given in Eq. (6.44) for the polarizability holds. Thus, we also find

$$H^{dir}_{vc\alpha\mathbf{k},v'c'\alpha\mathbf{k}'} = H^{dir}_{vc\mathbf{k},v'c'\mathbf{k}'}, \tag{6.68}$$

which together with (6.67) and the symmetry of the band energies states that the total interaction kernel, that we denote with $H^e_{vc\mathbf{k},v'c'\mathbf{k}'}$, has the symmetry property (6.68).

6.3.4 Symmetrized Basis Functions

In this section, we want to show how the symmetry property of the interaction kernel derived in the previous section can be utilized in order to reduce the eigenvalue problem of the BSE to a set of smaller eigenvalue problems. We introduce basis functions Φ for the electron hole wave function given as the product of two Kohn-Sham orbitals

$$\Phi_{vc\mathbf{k}}(\mathbf{r}_e, \mathbf{r}_h) = \psi_{c\mathbf{k}}(\mathbf{r}_e)\psi^*_{v\mathbf{k}}(\mathbf{r}_h), \tag{6.69}$$

where $\mathbf{r}_e$ and $\mathbf{r}_h$ denote electron and hole coordinates, respectively. In the following we will drop the dependence of Φ on $\mathbf{r}_e$ and $\mathbf{r}_h$ in the notation in order to get more compact formulae. We define the symmetrized basis function for the electron-hole wave function in the following way [97]

$$\Phi^{\mu i}_{vc\mathbf{k},j} = \sum_R [\Gamma^{(\mu)}_{ji}(R)]^*(R : \Phi_{vc\mathbf{k}}). \tag{6.70}$$

Here R denotes a symmetry operation and is just a short cut for our previous notation $\{\alpha|\mathbf{t}\}$, and $\Gamma^{(\mu)}_{ji}(R)$ is the μ–th irreducible representation matrix with matrix indices ji belonging to the symmetry element R. These symmetrized basis functions are now used to expand the electron-hole wave function Ψ

$$\Psi^{\nu i}_j = \sum_{\mathbf{k}'}^{\mathrm{IBZ}} \sum_{v'c'} A^{\nu i}_{v'c'\mathbf{k}',j} \Phi^{\nu i}_{v'c'\mathbf{k}',j}, \tag{6.71}$$

which fulfills the eigenvalue equation (4.104) that we write in the form

$$\hat{H}\Psi^{\nu i'}_{j'} = E^{\nu i'}_{j'} \Psi^{\nu i'}_{j'}, \tag{6.72}$$

[2]Note that these expressions are only valid for non-degenerate states!

with $\hat{H}$ and $E^{\nu,i'}_{j'}$ denoting the interaction Kernel and the exciton energy, respectively. Operating on (6.72) from the left with $\int\int \mathrm{d}^3r_e \mathrm{d}^3r_h \Phi^*_{vc\mathbf{k}}$ results in the following matrix equation

$$\sum_{v'c'\mathbf{k}'}^{\mathrm{IBZ}} H^{\mu i,\nu i'}_{(vc\mathbf{k},j),(v'c'\mathbf{k}',j')} A^{\nu i}_{v'c'\mathbf{k}',j'} = E^{\nu i'}_{j'} \sum_{v'c'\mathbf{k}'}^{\mathrm{IBZ}} S^{\mu i,\nu i'}_{(vc\mathbf{k},j),(v'c'\mathbf{k}',j')} A^{\nu i}_{v'c'\mathbf{k}',j'}, \tag{6.73}$$

with

$$H^{\mu i,\nu i'}_{(vc\mathbf{k},j),(v'c'\mathbf{k}',j')} = \langle \Phi^{\mu i}_{vc\mathbf{k},j} | \hat{H} | \Phi^{\nu i'}_{v'c'\mathbf{k}',j'} \rangle, \tag{6.74}$$

$$S^{\mu i,\nu i'}_{(vc\mathbf{k},j),(v'c'\mathbf{k}',j')} = \langle \Phi^{\mu i}_{vc\mathbf{k},j} | \Phi^{\nu i'}_{v'c'\mathbf{k}',j'} \rangle. \tag{6.75}$$

6.3.5 Block-diagonal Form of $\hat{H}$

The transformation of the symmetrized basis function $\Phi^{\mu i}_{vc\mathbf{k},j}$ upon the action of the symmetry operation R is given by

$$R : \Phi^{\mu i}_{vc\mathbf{k},j} = \sum_{l=1}^{d_\mu} \Gamma^{(\mu)}_{lj}(R) \Phi^{\mu i}_{vc\mathbf{k},l}, \tag{6.76}$$

where d_μ is the dimension of the irreducible representation μ. Using the invariance of the scalar product

$$\langle \Phi^{\mu i}_{vc\mathbf{k},j} | \Phi^{\nu i'}_{v'c'\mathbf{k}',j'} \rangle = \langle R : \Phi^{\mu i}_{vc\mathbf{k},j} | R : \Phi^{\nu i'}_{v'c'\mathbf{k}',j'} \rangle \tag{6.77}$$

and the transformation rule (6.76) finally leads to

$$S^{\mu i,\nu i'}_{(vc\mathbf{k},j),(v'c'\mathbf{k}',j')} = \frac{1}{d_\mu} \delta_{\mu\nu} \delta_{jj'} \sum_{l=1}^{d_\mu} \langle \Phi^{\mu i}_{vc\mathbf{k},l} | \Phi^{\mu i'}_{v'c'\mathbf{k}',l} \rangle. \tag{6.78}$$

In order to derive (6.78) the grand orthogonality theorem of group theory has been utilized [97]

$$\sum_R [\Gamma^{(\mu)}_{lj}(R)]^* \Gamma^{(\nu)}_{l'j'}(R) = \frac{g}{d_\mu} \delta_{\mu\nu} \delta_{ll'} \delta_{jj'}, \tag{6.79}$$

where g is the order of the group. Most importantly, Eq. (6.78) says that the scalar product of two symmetrized basis functions belonging to *different* irreducible representations μ and ν vanishes. A similar result also holds for the Hamilton matrix $H^{\mu i,\nu i'}_{(vc\mathbf{k},j),(v'c'\mathbf{k}',j')}$ on account of

$$\langle \Phi^{\mu i}_{vc\mathbf{k},j} | \hat{H} | \Phi^{\nu i'}_{v'c'\mathbf{k}',j'} \rangle = \langle R : \Phi^{\mu i}_{vc\mathbf{k},j} | \hat{H} | R : \Phi^{\nu i'}_{v'c'\mathbf{k}',j'} \rangle, \tag{6.80}$$

which is a consequence of the commutivity of R and $\hat{H}$. Insertion of (6.76) into (6.80) via (6.79) then leads to the desired expression

$$H^{\mu i,\nu i'}_{(vc\mathbf{k},j),(v'c'\mathbf{k}',j')} = \frac{1}{d_\mu}\delta_{\mu\nu}\delta_{jj'}\sum_{l=1}^{d_\mu}\langle\Phi^{\mu i}_{vc\mathbf{k},l}|\hat{H}|\Phi^{\mu i'}_{v'c'\mathbf{k}',l}\rangle. \tag{6.81}$$

The Kronecker $\delta_{\mu\nu}$ in the above result constitutes the block-diagonal form of the Hamilton matrix. Thus, the eigenvalue equation (6.72) can be solved for each irreducible representation separately.

6.3.6 Interpolation of Electron-Hole Matrix Elements

The calculation of the direct electron-hole matrix elements $H^{dir}_{vc\mathbf{k},v'c'\mathbf{k}'}$ according to Eq. (6.65) represents the bottleneck of the calculation. For instance, if we choose a moderately dense $\mathbf{k}$ mesh of $8\times8\times8$ points in the BZ, we have to evaluate expression (6.65) already $512\times512 = 262144$ times. This number may be reduced by taking into account the Hermiticity of the matrix or by making use of symmetry as described in the previous section. Still, it may be desirable to seek for an interpolation scheme which allows us to calculate the electron-hole interaction first on a coarse grid, $\{\tilde{\mathbf{k}},\tilde{\mathbf{k}}'\}$, and then compute the matrix elements on a denser grid, $\{\mathbf{k},\mathbf{k}'\}$, by using an efficient interpolation method. Such a procedure has already been described by Rohlfing and Louie [83]. It relies on the fact that the Bloch-periodic part $u_{n\mathbf{k}}(\mathbf{r})$ of a wave function at a given $\mathbf{k}$ point and band index n might be expressed as a linear combination of functions $u_{\tilde{n}\tilde{\mathbf{k}}}(\mathbf{r})$ on a different Bloch vector $\tilde{\mathbf{k}}$, thus

$$u_{n\mathbf{k}}(\mathbf{r}) = \sum_{\tilde{n}} d^{\tilde{n}\tilde{\mathbf{k}}}_{n\mathbf{k}} u_{\tilde{n}\tilde{\mathbf{k}}}(\mathbf{r}). \tag{6.82}$$

By applying the operation $\int \mathrm{d}^3r\, u^*_{\tilde{m}\tilde{\mathbf{k}}}(\mathbf{r})$ to the above expansion and using the ortho-normality of the Bloch-periodic functions at $\tilde{\mathbf{k}}$, one obtains for the expansion coefficients $d^{\tilde{n}\tilde{\mathbf{k}}}_{n\mathbf{k}}$ the overlap between the Bloch-periodic parts of the wave functions

$$d^{\tilde{n}\tilde{\mathbf{k}}}_{n\mathbf{k}} = M^{\mathbf{0}}_{\tilde{n}n}(\tilde{\mathbf{k}},\mathbf{k}-\tilde{\mathbf{k}}) = \int_\Omega \mathrm{d}^3r\, u^*_{\tilde{n}\tilde{\mathbf{k}}}(\mathbf{r}) u_{n\mathbf{k}}(\mathbf{r}). \tag{6.83}$$

The identification of $d^{\tilde{n}\tilde{\mathbf{k}}}_{n\mathbf{k}}$ with the previously defined matrix element $M^{\mathbf{0}}_{\tilde{n}n}(\tilde{\mathbf{k}},\mathbf{k}-\tilde{\mathbf{k}})$ can be easily seen from the definition (6.9) by inserting the Bloch wave property of the wave functions. In order to make use of the expansion given above, we insert it into Eq. (6.58) for the direct electron-hole kernel $H^{dir}_{vc\mathbf{k},v'c'\mathbf{k}'}$, which we write in the form

$$H^{dir}_{vc\mathbf{k},v'c'\mathbf{k}'} = \frac{1}{|\mathbf{k}'-\mathbf{k}|^2}A_{vc\mathbf{k},v'c'\mathbf{k}'} + C_{vc\mathbf{k},v'c'\mathbf{k}'}. \tag{6.84}$$

The matrices A and C are obtained by inserting the Fourier transform of the screened Coulomb interaction W into the integral (6.58), thus

$$A_{vc\mathbf{k},v'c'\mathbf{k}'} = \frac{1}{\Omega}\frac{4\pi}{\epsilon_{\mathbf{00}}(\mathbf{q})}M^{\mathbf{0}}_{cc'}(\mathbf{k},\mathbf{q})\left[M^{\mathbf{0}}_{vv'}(\mathbf{k},\mathbf{q})\right]^* \tag{6.85}$$

$$C_{vc\mathbf{k},v'c'\mathbf{k}'} = \frac{1}{\Omega}\sum_{\mathbf{G}\neq\mathbf{0}}\frac{4\pi}{\epsilon_{\mathbf{GG}}(\mathbf{q})|\mathbf{q}+\mathbf{G}|^2}M^{\mathbf{G}}_{cc'}(\mathbf{k},\mathbf{q})\left[M^{\mathbf{G}}_{vv'}(\mathbf{k},\mathbf{q})\right]^*, \tag{6.86}$$

where we have used the abbreviation $\mathbf{q} = \mathbf{k}' - \mathbf{k}$. The partitioning of the kernel into a term A containing the $\mathbf{G} = \mathbf{0}$ portion, and one comprising all $\mathbf{G} \neq \mathbf{0}$ contributions is crucial for a successful interpolation scheme. This is because, the $\mathbf{G} = \mathbf{0}$ term of H^{dir} behaves as $1/q^2$ as can be seen from Eq. (6.84). Therefore, the matrix elements $H^{dir}_{vc\mathbf{k},v'c'\mathbf{k}'}$ depend very sensitively on the reciprocal distance $\mathbf{q}$, and an interpolation scheme would converge very slowly. On the other hand, the functions A and C defined above depend fairly weakly on $\mathbf{q}$ enabling an effective interpolation. This is demonstrated by inserting the expansion (6.82) into the definition of the matrix elements M entering Eqs. (6.85) and (6.86). If we expand the wave functions at the vectors $\mathbf{k}$ and $\mathbf{k}'$ in terms of Bloch-periodic functions at wave vectors $\tilde{\mathbf{k}}$ and $\tilde{\mathbf{k}}'$, respectively, we obtain, for instance, for A

$$\begin{aligned} A_{vc\mathbf{k},v'c'\mathbf{k}'} = & \sum_{\tilde{n}_1\tilde{n}_2\tilde{n}_3\tilde{n}_4}\left[M^{\mathbf{0}}_{\tilde{n}_1 c}(\tilde{\mathbf{k}},\mathbf{q}_1)\right]^* M^{\mathbf{0}}_{\tilde{n}_2 c'}(\tilde{\mathbf{k}}',\mathbf{q}_2)M^{\mathbf{0}}_{\tilde{n}_3 v}(\tilde{\mathbf{k}},\mathbf{q}_1)\left[M^{\mathbf{0}}_{\tilde{n}_4 v'}(\tilde{\mathbf{k}}',\mathbf{q}_2)\right]^* \\ & \times \frac{1}{\Omega}\frac{4\pi}{\epsilon_{\mathbf{00}}(\mathbf{q})}M^{\mathbf{0}}_{\tilde{n}_1\tilde{n}_2}(\tilde{\mathbf{k}},\tilde{\mathbf{q}})\left[M^{\mathbf{0}}_{\tilde{n}_3\tilde{n}_4}(\tilde{\mathbf{k}},\tilde{\mathbf{q}})\right]^*. \end{aligned} \tag{6.87}$$

Here, we have introduced the following abbreviations: $\mathbf{q} = \mathbf{k}' - \mathbf{k}$, $\tilde{\mathbf{q}} = \tilde{\mathbf{k}}' - \tilde{\mathbf{k}}$, $\mathbf{q}_1 = \mathbf{k} - \tilde{\mathbf{k}}$, and $\mathbf{q}_2 = \mathbf{k}' - \tilde{\mathbf{k}}'$. In order to gain something from the above result instead of complicating the situation as it might seem, we have to make two approximations at this stage. First, we assume that we can replace the vector $\mathbf{q}$ in the argument of the dielectric matrix by $\tilde{\mathbf{q}}$. Then, the second line in Eq. (6.87) is simply $A_{\tilde{n}_3\tilde{n}_1\tilde{\mathbf{k}},\tilde{n}_4\tilde{n}_2\tilde{\mathbf{k}}'}$ as can be seen from comparison with the definition (6.85). This approximation is valid as long as the head of the dielectric matrix does not strongly depend on the reciprocal distance. As a second approximation, we limit the summations in Eq. (6.87), which should run over *all* states, to a very small subset of states. This is a valid approximation provided the functions $u_{n\mathbf{k}}(\mathbf{r})$ vary only fairly weakly with respect to the Bloch vector $\mathbf{k}$. In the actual calculations we will restrict the summations over $\tilde{n}_1$ and $\tilde{n}_2$ ($\tilde{n}_3$ and $\tilde{n}_4$) to the same set of conduction (valence) states as are used in the treatment of the electron-hole interaction. With these two simplifications, we can write Eq. (6.87) now in the form

$$\begin{aligned} A_{vc\mathbf{k},v'c'\mathbf{k}'} = & \sum_{\tilde{v}\tilde{c}\tilde{v}'\tilde{c}'}\left[M^{\mathbf{0}}_{\tilde{c}c}(\tilde{\mathbf{k}},\mathbf{q}_1)\right]^* M^{\mathbf{0}}_{\tilde{c}'c'}(\tilde{\mathbf{k}}',\mathbf{q}_2)M^{\mathbf{0}}_{\tilde{v}v}(\tilde{\mathbf{k}},\mathbf{q}_1)\left[M^{\mathbf{0}}_{\tilde{v}'v'}(\tilde{\mathbf{k}}',\mathbf{q}_2)\right]^* \\ & \times A_{\tilde{v}\tilde{c}\tilde{\mathbf{k}},\tilde{v}'\tilde{c}'\tilde{\mathbf{k}}'}. \end{aligned} \tag{6.88}$$

Thus, we have arrived at the desired result: Once we have computed the matrix elements on the coarse mesh $\{\tilde{\mathbf{k}}, \tilde{\mathbf{k}}'\}$, we acquire the interaction kernel on a dense grid $\{\mathbf{k}, \mathbf{k}'\}$ very efficiently by applying Eq. (6.88). Of course, we have to test the validity of the approximations we have made by direct computation. This is demonstrated in Appendix B.3. But before we do so, we present the analogous results for the matrix C defined above, and also for the exchange-kernel H^x given by Eq. (6.55). The $\mathbf{G} \neq \mathbf{0}$ part of the direct interaction kernel C can be interpolated in complete analogy to the scheme already shown for the $\mathbf{G} = \mathbf{0}$ part. Assuming that the dielectric matrix for $\mathbf{G} \neq \mathbf{0}$ is not strongly dependent on the reciprocal distance $\mathbf{q}$, which is generally well satisfied, and restricting the summations over states as described above, leads to

$$\begin{aligned} C_{vc\mathbf{k},v'c'\mathbf{k}'} &= \sum_{\tilde{v}\tilde{c}\tilde{v}'\tilde{c}'} \left[M^{\mathbf{0}}_{\tilde{c}c}(\tilde{\mathbf{k}}, \mathbf{q}_1)\right]^* M^{\mathbf{0}}_{\tilde{c}'c'}(\tilde{\mathbf{k}}', \mathbf{q}_2) M^{\mathbf{0}}_{\tilde{v}v}(\tilde{\mathbf{k}}, \mathbf{q}_1) \left[M^{\mathbf{0}}_{\tilde{v}'v'}(\tilde{\mathbf{k}}', \mathbf{q}_2)\right]^* \\ &\times C_{\tilde{v}\tilde{c}\tilde{\mathbf{k}},\tilde{v}'\tilde{c}'\tilde{\mathbf{k}}'}. \end{aligned} \tag{6.89}$$

The exchange kernel matrix elements H^x do not suffer from the divergent behavior of the Coulomb interaction. Therefore, the interpolation procedure applies directly to H^x. Moreover, the kernel of H^x does not depend on the reciprocal distance and the only approximation entering in this case is the truncation of the summation over states to the subset used for the electron-hole treatment. The interpolated exchange matrix elements are given by

$$\begin{aligned} H^x_{vc\mathbf{k},v'c'\mathbf{k}'} &= \sum_{\tilde{v}\tilde{c}\tilde{v}'\tilde{c}'} \left[M^{\mathbf{0}}_{\tilde{c}c}(\tilde{\mathbf{k}}, \mathbf{q}_1)\right]^* M^{\mathbf{0}}_{\tilde{c}'c'}(\tilde{\mathbf{k}}', \mathbf{q}_2) M^{\mathbf{0}}_{\tilde{v}v}(\tilde{\mathbf{k}}, \mathbf{q}_1) \left[M^{\mathbf{0}}_{\tilde{v}'v'}(\tilde{\mathbf{k}}', \mathbf{q}_2)\right]^* \\ &\times H^x_{\tilde{v}\tilde{c}\tilde{\mathbf{k}},\tilde{v}'\tilde{c}'\tilde{\mathbf{k}}'}. \end{aligned} \tag{6.90}$$

6.4 Convergence Tests and Numerical Results

In this section, we will present some numerical results for the matrix elements $M^{\mathbf{G}}_{nm}(\mathbf{k}, \mathbf{q})$, for the dielectric matrix as well as for the electron-hole interaction kernel. In particular, we will investigate the convergence of the results with respect to a number of cut-off parameters. The systems we have chosen are bulk Si, LiF and an isolated PA chain. Si and LiF are well-known exemplars of an inorganic semi-conductor, and a wide band-gap insulator, respectively. Undoped PA, on the other hand, can be viewed as the prototype of an organic semiconductor exhibiting strongly anisotropic properties which are typical for these organic materials.

6.4.1 The Integrals $M^{\mathbf{G}}_{nm}(\mathbf{k}, \mathbf{q})$

The matrix elements $M^{\mathbf{G}}_{nm}(\mathbf{k}, \mathbf{q})$ play the central role in the evaluation of the dielectric matrix and of the electron-hole interaction kernel. For this reason, we take

a closer look at their computational evaluation, in particular, at the convergence with respect to numerical cut-off parameters. First of all, it is clear from looking at Eq. (6.14) that the results depend on the number of basis functions used for the expansion of the wave functions. Within the LAPW method, this parameter is best described by the so-called $RK_{\max}$ parameter, which is the product of the muffin-tin radius R_{MT} and the magnitude of the largest plane wave component $\mathbf{K}_{\max}$ in the basis set. Another parameter arises from the expansion of the plane wave $e^{i(\mathbf{q}+\mathbf{G})\mathbf{r}}$ in terms of spherical Bessel functions inside the muffin-tin spheres. For instance, the summation over angular quantum numbers in Eq. (6.26) must be truncated at a finite value, which we denote by $l_{\max}$.

Instead of looking at a single matrix element $M^{\mathbf{G}}_{nm}(\mathbf{k},\mathbf{q})$, which might not be representative, we compute the imaginary part of the dielectric matrix $\epsilon_{\mathbf{G}\mathbf{G}'}(\mathbf{q},\omega)$ by using

$$\mathrm{Im}\epsilon_{\mathbf{G}\mathbf{G}'}(\mathbf{q},\omega) = \frac{16\pi^2}{|\mathbf{q}+\mathbf{G}|^2\Omega}\sum_{cv\mathbf{k}}^{\mathrm{BZ}} M^{\mathbf{G}}_{vc}(\mathbf{k},\mathbf{q})[M^{\mathbf{G}'}_{vc}(\mathbf{k},\mathbf{q})]^*\times\delta(\varepsilon_{c,\mathbf{k}+\mathbf{q}}-\varepsilon_{v\mathbf{k}}-\omega). \quad (6.91)$$

This formula can be easily derived from expressions (6.42) and (6.52) by introducing the frequency $\omega - i\delta$ in the energy denominator again and utilizing the delta function representation as given in Eq. (4.108). In Fig. (6.1), $\mathrm{Im}\epsilon_{\mathbf{G}\mathbf{G}'}(\mathbf{q},\omega)$ is depicted for Si, where we have chosen quite arbitrarily $\mathbf{q} = \{\frac{1}{5},\frac{1}{5},\frac{1}{5}\}$, and the diagonal element for $\mathbf{G} = \{-1,1,3\}$. Note that here and in the following all $\mathbf{q}$ and $\mathbf{G}$ vectors are given in units of the reciprocal lattice vectors constructed from the *conventional* unit cell vectors. The left panel shows two spectra that have been calculated with two $RK_{\max}$ values of 6.0 and 9.0, respectively. For low transition energies, the two curves lie on top of each other, whereas at higher energies there are some small deviations. This is because the energetically low lying states are already well described by an $RK_{\max}$ value of 6.0, whereas the higher lying bands need more basis functions in order to be well represented. Note that the convergence with number of basis functions is improved for smaller $\mathbf{G}$ components. In fact, the corresponding spectra for $\mathbf{G} = \{0,0,0\}$ computed for an $RK_{\max}$ of 6.0 (130 plane waves) and 9.0 (410 plane waves), respectively, are indeed indistinguishable. Keeping in mind that the computational time scales as the square of the number of basis functions, we sacrifice a possible higher accuracy for larger $\mathbf{G}$ components by reasonable computational times, and choose $RK_{\max}$ to be 6.0 in the case of Si. The right panel of Fig. (6.1) displays the same components of $\mathrm{Im}\epsilon_{\mathbf{G}\mathbf{G}'}(\mathbf{q},\omega)$ for Si computed for three different values of $l_{\max}$. Whereas there is a considerable change when going from $l_{\max} = 2$ to $l_{\max} = 4$, we find that $l_{\max} = 6$ does not improve the results further. The same observation also applies to LiF and PA. Therefore, we use $l_{\max} = 4$ in all subsequent computations, if not mentioned differently.

Another way of checking the validity of the matrix elements $M^{\mathbf{G}}_{nm}(\mathbf{k},\mathbf{q})$ is to take the limit of vanishing $\mathbf{q}$ vectors numerically. Then, by Eq. (6.50), we should

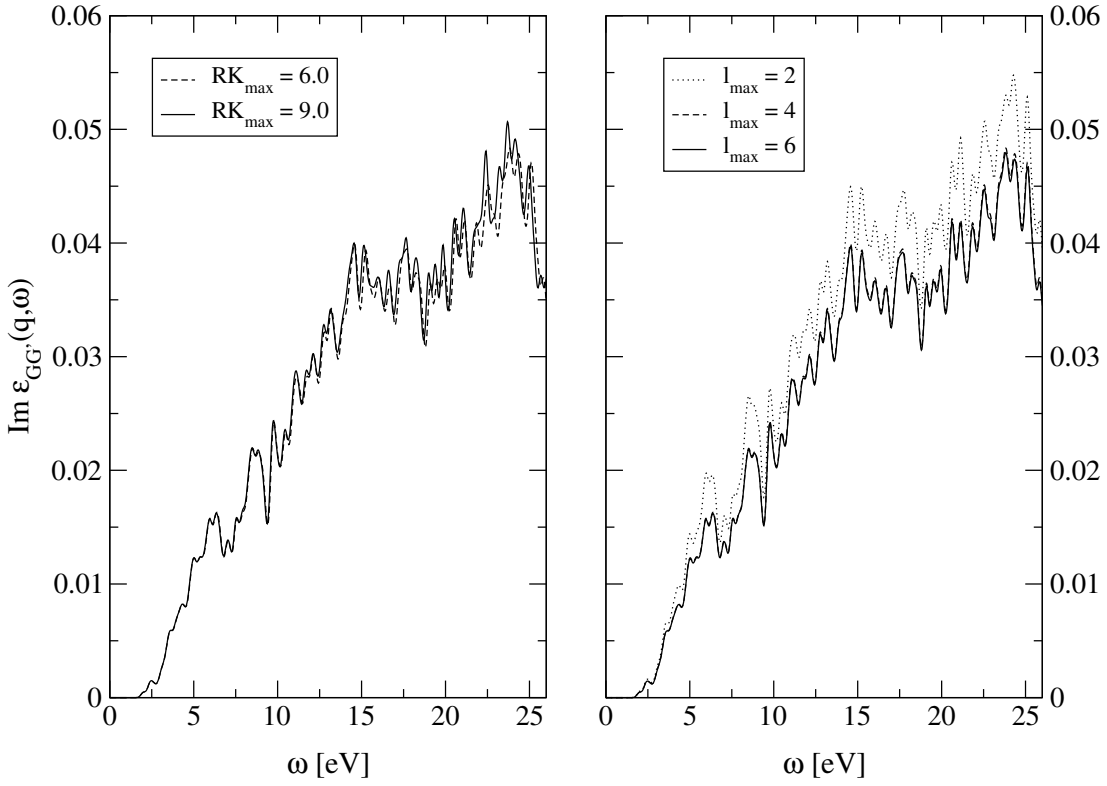

Figure 6.1: Convergence of $\mathrm{Im}\epsilon_{\mathbf{GG}'}(\mathbf{q},\omega)$ of Si with respect to $RK_{\max}$ (left panel) and $l_{\max}$ (right panel). The diagonal component for $\mathbf{G} = \{-1,1,3\}$ with $\mathbf{q} = \{\frac{1}{5},\frac{1}{5},\frac{1}{5}\}$ is shown.

obtain the optical transition matrix elements. In Fig. (6.2), we compare the imaginary part of the head of ϵ for Si, calculated for $\mathbf{q} = \{\frac{1}{80},\frac{1}{80},\frac{1}{80}\}$ according to Eq. (6.91), with the optical spectrum obtained by using momentum matrix elements utilizing Eq. (4.46). We notice the excellent agreement between the two methods. The residual differences may be attributed to the finite $\mathbf{q}$ vector, or to numerical subtleties. In order to further illustrate the equivalence of the optical matrix elements and $M^{\mathbf{G}}_{nm}(\mathbf{k},\mathbf{q})$ in the limit of vanishing $\mathbf{q}$ vectors, we have plotted the head of the dielectric matrix of PA in Fig. (6.3) for three different different directions of $\mathbf{q}$. In contrast to the cubic symmetry in Si, PA has orthorhombic symmetry and therefore exhibits quite distinct optical responses for the three principal directions. The comparison with the dielectric tensor components obtained from the momentum matrix elements shows again a reasonable agreement with the numerical $\mathbf{q} \to \mathbf{0}$ limits. There is a pronounced anisotropy in the optical properties: parallel to the polymer chain (z axis), there is a strong absorption peak at around 1 eV, whereas perpendicular to the polymer chain there are much weaker absorption bands starting at about 7 eV. We point out that the $\mathbf{k}$ space integration has been performed by using the linear tetrahedron method

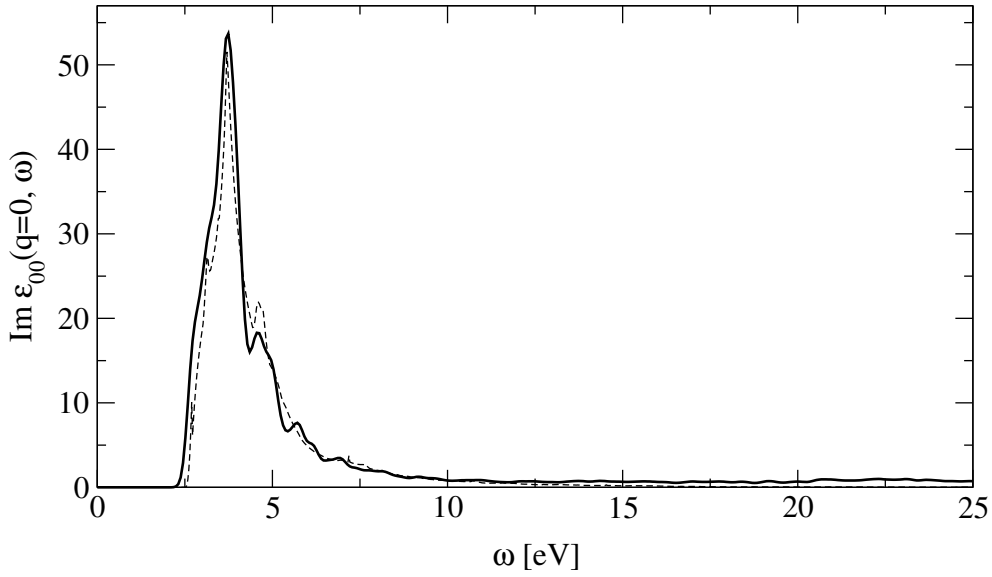

Figure 6.2: The imaginary part of $\epsilon_{\mathbf{00}}(\mathbf{q} \to \mathbf{0}, \omega)$ for Si calculated in two different ways: The dashed line results from using momentum matrix elements according to Eq. (4.46), whereas the full line is obtained by taking the limit $\mathbf{q} \to \mathbf{0}$ numerically, utilizing expression (6.91).

for the momentum matrix element method (dashed lines), whereas only a simple summation with a Lorentzian line shape has been implemented for the $\mathbf{q} \to \mathbf{0}$ limit (full lines). The difference in the two methods for the $\mathbf{k}$ space integration might be seen, for instance, in the x component of $\mathrm{Im}\,\epsilon_{\mathbf{00}}(\mathbf{q} \to \mathbf{0}, \omega)$ shown in Fig. (6.3). There it is seen that the tetrahedron method averages the oscillations appearing in the low energy part of the spectrum that are originating from the finite $\mathbf{k}$ point sampling in the simple summation method.

6.4.2 The Dielectric Matrix

The static dielectric matrix is given by Eq. (6.52) via expression (6.42) for the polarization. It involves a sum over the Brillouin zone as well as a sum over unoccupied states. In this section, we investigate the convergence of the dielectric matrix with respect to these two summations. In Figs. (6.4, 6.5, 6.6), some selected diagonal elements of the dielectric matrix $\epsilon_{\mathbf{GG}}(\mathbf{q})$ for Si, LiF and PA, respectively, are plotted as a function of the number of $\mathbf{k}$ points in the Brillouin zone. Generally speaking, the $\mathbf{k}$ mesh is not very critical in the calculation of the dielectric matrix for the systems studied in this work. For Si, we find a $\mathbf{k}$ mesh of $8 \times 8 \times 8$ to be sufficient, whereas for LiF already a $6 \times 6 \times 6$ yields converged values for $\epsilon_{\mathbf{GG}}(\mathbf{q})$. This is because LiF has a much larger band gap and also much lower band width of individual bands. Consequently, a coarser

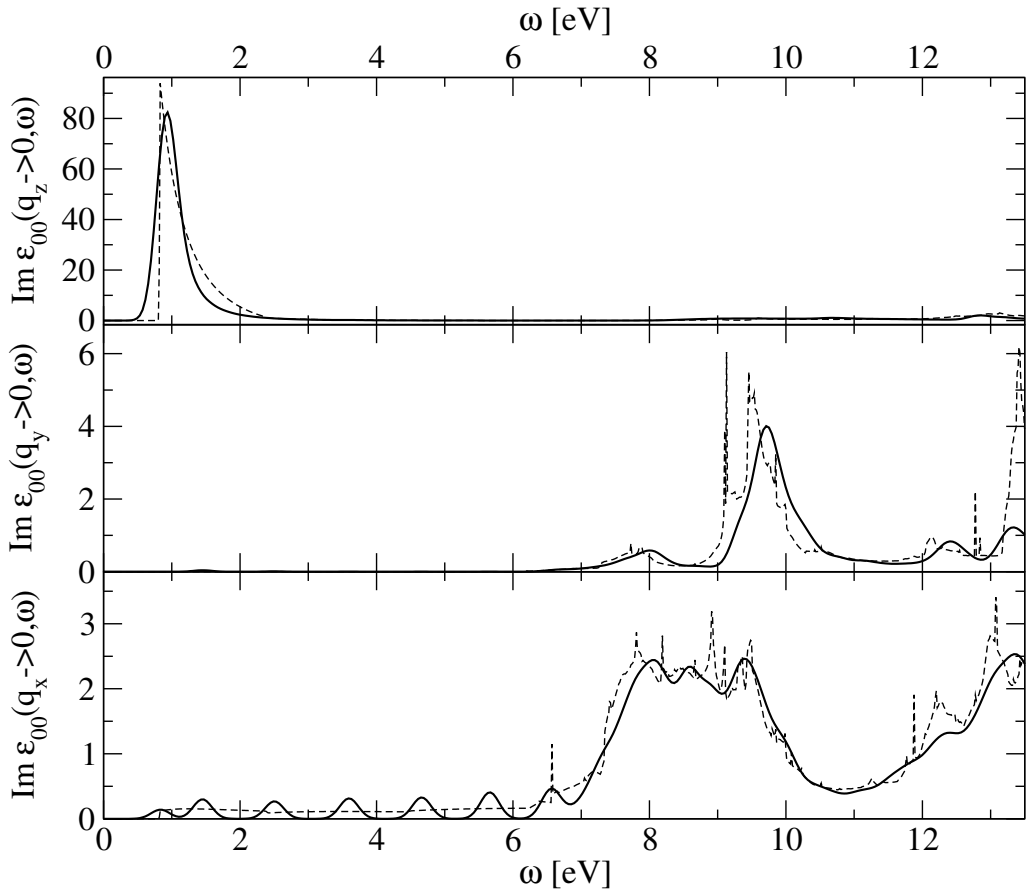

Figure 6.3: The imaginary part of $\epsilon_{\mathbf{00}}(\mathbf{q} \to \mathbf{0}, \omega)$ for PA calculated in two different ways: The dashed line results from using momentum matrix elements according to Eq. (4.46), whereas the full line is obtained by taking the limit $\mathbf{q} \to \mathbf{0}$ numerically, utilizing expression (6.91). Top, middle, and bottom panels, respectively, correspond to z, y and x polarization, where the z axis is taken to be parallel to the polymer chain.

sampling of the Brillouin zone is sufficient. For the isolated PA chain we have chosen one-dimensional $\mathbf{k}$ meshes along the chain axis due to the 1D character of PA. The convergence of the dielectric matrix with respect to the number of $\mathbf{k}$ points along the direction of the polymer is less good as, for instance, in the case of silicon on account of the smaller band gap of PA as compared to silicon. Moreover, we observe that the convergence of $\epsilon_{\mathbf{GG}}(\mathbf{q})$ with respect to the $\mathbf{k}$ point sampling of the BZ depends on the length of the vector $\mathbf{q}+\mathbf{G}$, where shorter vectors $\mathbf{q}+\mathbf{G}$ require denser meshes. This can be recognized, for instance, from the slower convergence of the head of ϵ ($\mathbf{G} = \mathbf{G}' = \mathbf{0}$) compared to the $\mathbf{G} \neq \mathbf{0}$ components as can be seen from Figs. (6.4, 6.5, 6.6).

The dependence of the dielectric matrix on the number of unoccupied states included in the summation is depicted in Figs. (6.7, 6.8, 6.9) for Si, LiF and PA,

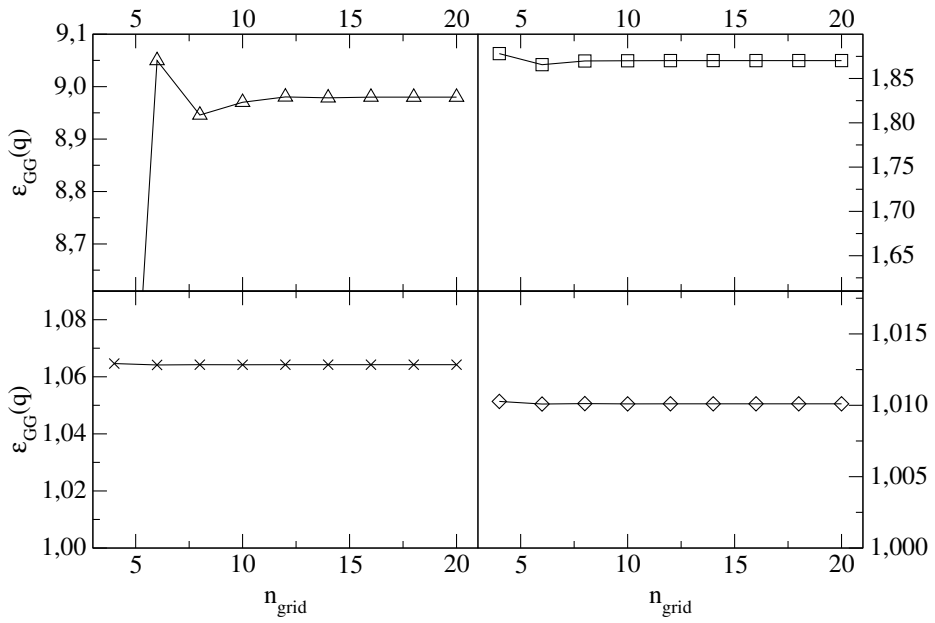

Figure 6.4: Si, convergence of the static dielectric matrix for $\mathbf{q} = \{\frac{1}{5}, \frac{1}{5}, \frac{1}{5}\}$ with respect to the number of $\mathbf{k}$ points (n^3_{grid}) in the BZ. Four diagonal elements of $\epsilon_{\mathbf{GG}}(\mathbf{q})$ are displayed: $\mathbf{G}_1 = \{0, 0, 0\}$ (top left), $\mathbf{G}_2 = \{-1, -1, -1\}$ (top right), $\mathbf{G}_3 = \{-1, 1, 3\}$ (bottom left), and $\mathbf{G}_4 = \{0, 2, 4\}$ (bottom right).

respectively. We find that empty states as high as 10 Ryd above the Fermi level have to be taken into account in order to get converged results for Si. For LiF, an energy cut-off of even 20 Ryd is necessary due to the larger band width of the unoccupied bands, whereas for PA already 10 Ryd are sufficient. For finite $\mathbf{q}$ vectors, the energy denominator in Eq. (6.42) approaches zero very slowly when going to higher lying states, whereas for $\mathbf{q} = \mathbf{0}$ we expect a faster convergence due to the third power in the energy denominator as can be seen from Eq. (6.51). Generally speaking, we notice an opposite convergence behavior compared to the $\mathbf{k}$ summation discussed before: The shorter the $\mathbf{q} + \mathbf{G}$ vector the faster the convergence with respect to the number of empty states. This can be observed from Figs. (6.7, 6.8, 6.9) where the head of ϵ clearly reaches its converged value faster than the larger $\mathbf{G}$ components.

In summary, the size of the band gap determines the number of $\mathbf{k}$ points to be used, where a larger band gap favors a smaller $\mathbf{k}$ grid size. The overall band width, on the other hand, determines the energy cut-off for the unoccupied bands. Note that the magnitude of the $\mathbf{q} + \mathbf{G}$ vector influences the convergence with respect to the $\mathbf{k}$ grid as well as with the energy cut-off E_{max} as was discussed above. Small values for $|\mathbf{q} + \mathbf{G}|$ require dense $\mathbf{k}$ meshes and a lower energy cut-off, whereas the larger $|\mathbf{q} + \mathbf{G}|$ components manage with less dense $\mathbf{k}$ meshes, but require a higher number of empty states. These findings could be employed in order to speed up

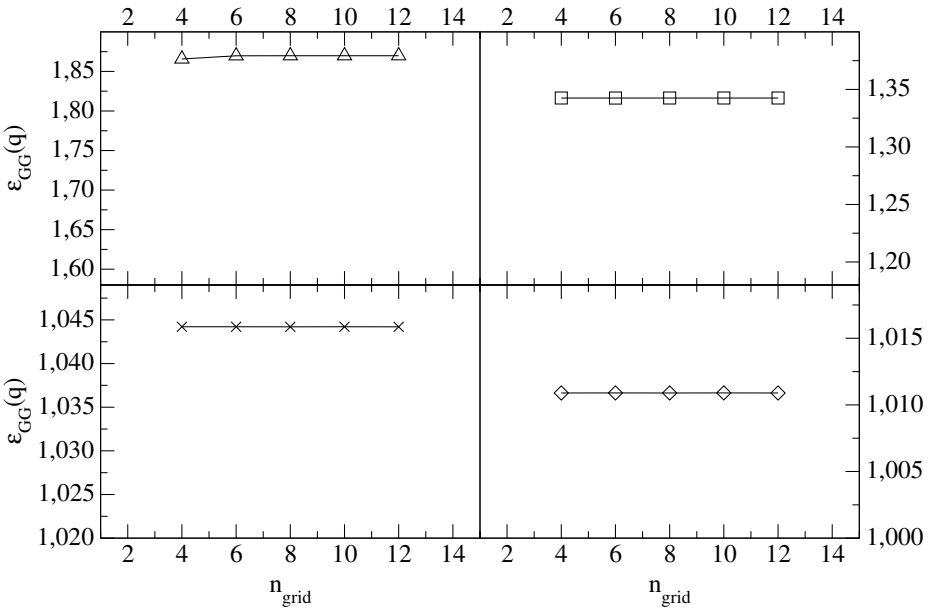

Figure 6.5: LiF, convergence of the static dielectric matrix for $\mathbf{q} = \{\frac{1}{5}, \frac{1}{5}, \frac{1}{5}\}$ with respect to the number of $\mathbf{k}$ points (n^3_{grid}) in the BZ. Four diagonal elements of $\epsilon_{\mathbf{GG}}(\mathbf{q})$ are displayed: $\mathbf{G}_1 = \{0, 0, 0\}$ (top left), $\mathbf{G}_2 = \{-1, -1, -1\}$ (top right), $\mathbf{G}_3 = \{-1, -1, 3\}$ (bottom left), and $\mathbf{G}_4 = \{2, -2, -4\}$ (bottom right).

the computations, for instance, by choosing different $\mathbf{k}$ meshes for the $\mathbf{G} = \mathbf{0}$ and $\mathbf{G} \neq \mathbf{0}$ components, respectively. However, such a scheme has not yet been implemented in the present work.

6.4.3 Electron-Hole Interaction Kernel

In order to compute the macroscopic dielectric function including electron-hole correlation effects, we have to evaluate the electron-hole kernel. The direct interaction term is given by Eq. (6.65). First of all, we notice that the calculation of a given matrix element $H^{dir}_{vc\mathbf{k},v'c'\mathbf{k}'}$ involves a sum over reciprocal lattice vectors $\mathbf{G}$. It is clear that in actual computations we have to truncate the summation, that is only $\mathbf{G}$ vectors shorter than a chosen $\mathbf{G}_{\max}$ are considered. In Fig. (6.10), we have depicted the convergence of some – arbitrarily – chosen matrix elements $H^{dir}_{vc\mathbf{k},v'c'\mathbf{k}'}$ for Si with respect to $\mathbf{G}_{\max}$. We find a cut-off value of only 3.0 Bohr^{-1} to be sufficient to yield converged results in the case of Si. We have also tested the dependence of the interaction kernel with respect to the number of basis functions, that is determined by $RK_{\max}$. We expect the convergence of $H^{dir}_{vc\mathbf{k},v'c'\mathbf{k}'}$ to be slightly faster than that of the dielectric matrix, because the former do not involve high lying empty states, which require a larger basis set. In Fig. (6.11), we show the convergence of the direct interaction elements for Si with respect

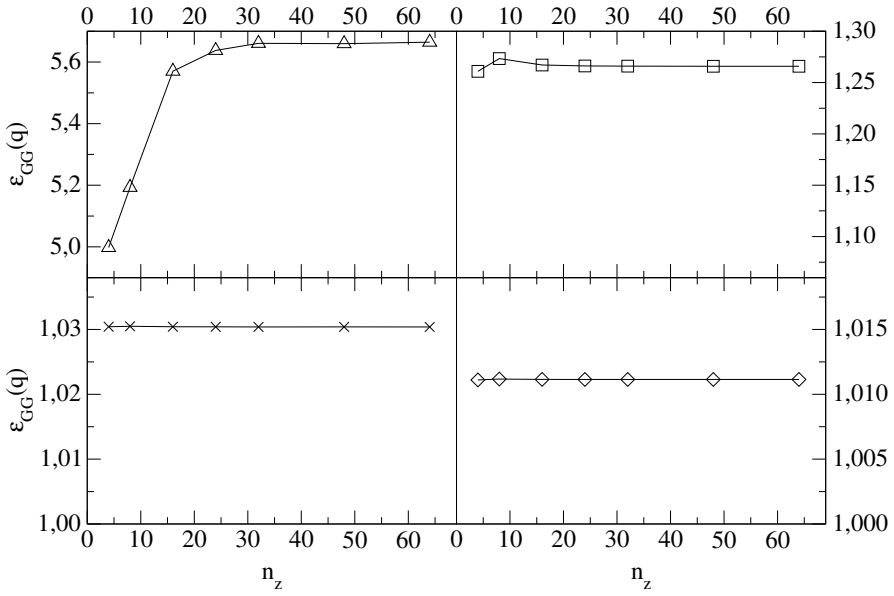

Figure 6.6: PA, convergence of the static dielectric matrix for $\mathbf{q} = \{0, 0, \frac{1}{8}\}$ with respect to the number of $\mathbf{k}$ points n_z in the BZ. Four diagonal elements of $\epsilon_{\mathbf{GG}}(\mathbf{q})$ are displayed: $\mathbf{G}_1 = \{0, 0, 0\}$ (top left), $\mathbf{G}_2 = \{0, 0, -1\}$ (top right), $\mathbf{G}_3 = \{-2, -2, 1\}$ (bottom left), and $\mathbf{G}_4 = \{1, -4, -1\}$ (bottom right).

to $RK_{\max}$. We see that above $RK_{\max} = 6.0$ there is almost no change in the electron-hole kernel suggesting that this value is sufficient for accurate results. For completeness, we have also checked the convergence for LiF and PA. The corresponding graphs are given in the Appendix B.1, Figs. (B.1) and (B.2) for LiF, and Figs. (B.3) and (B.4) for PA, respectively. It turns out that we have to work with a cut-off value $\mathbf{G}_{\max} = 4.0$ and an LAPW basis size given by $RK_{\max} = 6.0$ for LiF, whereas we can use $\mathbf{G}_{\max} = 3.0$ and $RK_{\max} = 2.5$ for PA.[3]

6.4.4 The Macroscopic Dielectric Function

The calculation of the macroscopic dielectric function according to Eq. (4.109) involves the diagonalization of the effective electron-hole interaction kernel yielding the excitation energies E^λ and the coupling coefficients $A^\lambda_{vc\mathbf{k}}$. The matrix size N of the kernel $H^e_{vc\mathbf{k},v'c'\mathbf{k}'}$ in the diagonalization (see Eq. 4.104) is given as the product of the number of $\mathbf{k}$ points $N_\mathbf{k}$ in the Brillouin zone with the number of valence N_v and conduction bands N_c

$$N = N_\mathbf{k} \times N_v \times N_c. \tag{6.92}$$

[3]We have used muffin tin radii of 2.0 for Si and F, 1.8 for Li, 1.28 for C, and 0.75 for H.

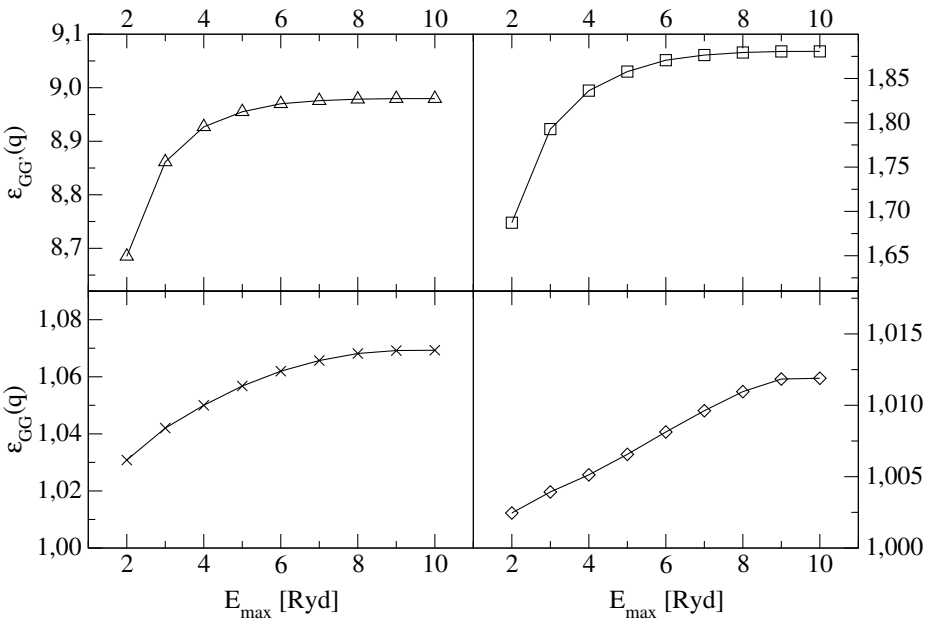

Figure 6.7: Si, convergence of the static dielectric matrix for $\mathbf{q} = \{\frac{1}{5}, \frac{1}{5}, \frac{1}{5}\}$ with respect to the energy cut-off $E_{\max}$. The same $\mathbf{G}$ vectors as in Fig. (6.4) are displayed.

Even for moderately dense $\mathbf{k}$ meshes and for a limited number of valence and conduction bands, the matrix size N soon becomes prohibitively large. Therefore, it is important to check the convergence of the dielectric function with respect to the three parameters $N_{\mathbf{k}}$, N_v and N_c. We choose LiF as a test case: Fig (6.12) shows the dielectric function of LiF computed for a $\mathbf{k}$ mesh with $N_{\mathbf{k}} = 8 \times 8 \times 8$ and for four different sets of N_v and N_c, respectively. If only 1 valence and 1 conduction band is included in the electron-hole interaction, the dielectric function does not show the strong bound exciton peak around 12 eV. The description of this excitonic state is improved if N_v and N_c are set equal to 2, but the position of the exciton peak is still not converged. The low energy parts of the spectrum computed for $N_v = 3$ and $N_c = 3$, and that for $N_c = 4$ lie almost on top of each other, and we can consider the dielectric function to be converged below 20 eV with respect to the number of bands included in the exciton description. Unfortunately, it was not possible to increase N_v or N_c further, because matrix sizes of roughly 6500 were the upper limit in the numerical diagonalization. In the Appendix B.2, we show the convergence of the dielectric function with respect to the number of bands for Si (Fig. B.5). We find a similar result as for LiF, namely, that $N_v = 3$ and $N_c = 4$ already produces sufficiently converged spectra below 8 eV. As for LiF we have used a $N_{\mathbf{k}} = 8 \times 8 \times 8$ mesh. We have also checked the dependence of $\epsilon_M(\omega)$ on N_v and N_c for PA (Fig. B.6). Here, we find that even a single valence band and a single conduction band suffices in order to describe the dominant bound exciton around 1.5 eV both in its energetic position and oscil-

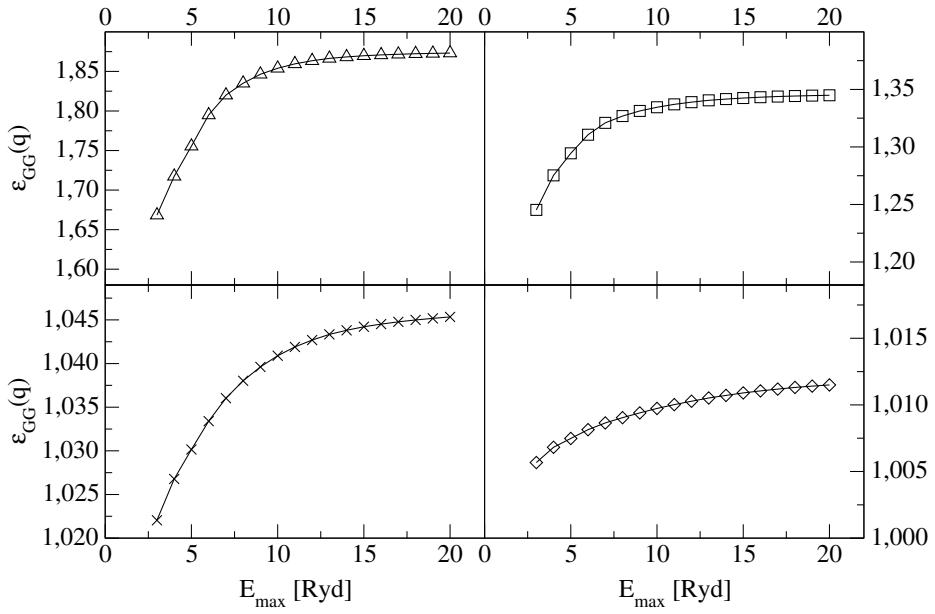

Figure 6.8: LiF, convergence of the static dielectric matrix for $\mathbf{q} = \{\frac{1}{5}, \frac{1}{5}, \frac{1}{5}\}$ with respect to the energy cut-off $E_{\max}$. The same $\mathbf{G}$ vectors as in Fig. (6.5) are displayed.

lator strength. Upon increasing the number of bands up to $N_v = 4$ and $N_c = 4$ only the spectral features around 10 eV are improved, but the main absorption peak remains almost unaltered.

It is of course also very instructive to check the dependence of the spectra with respect to the $\mathbf{k}$ grid. Fig. (6.13) shows the DF of LiF computed for $N_{\mathbf{k}} = 64$, $N_{\mathbf{k}} = 216$ and $N_{\mathbf{k}} = 512$, respectively. In all three cases three valence and four conduction bands have been included in the diagonalization of the effective electron-hole Hamiltonian. We notice that even a $4\times4\times4$ mesh gives a reasonable good description of the dominant exciton peak around 12.5 eV. However, at frequencies above 13 eV the DF does not appear to be converged. The differences between the spectra calculated for the $6\times6\times6$ and $8\times8\times8$ meshes, respectively, are less pronounced, though there are still some changes in the details of the spectra. We expect the convergence of the DF with respect to $N_{\mathbf{k}}$ to depend on the bandwidth of the valence and conduction bands. For a wide band-gap insulator, such as LiF, this band width is rather small, and a coarse $\mathbf{k}$ sampling suffices in order to yield reliable results (compare Fig. 6.13). Si on the other hand, has a much larger band width and therefore requires also more dense $\mathbf{k}$ meshes. This fact can be seen from Fig. (B.7) given in Appendix B.2. Though the $8 \times 8 \times 8$ mesh does seem to yield a completely converged DF for Si, we did not increase the density of the $\mathbf{k}$ grid further due to computational limitations. We still believe that the results are reasonably accurate because of the agreement of our results with experimental spectra as well as with computations performed

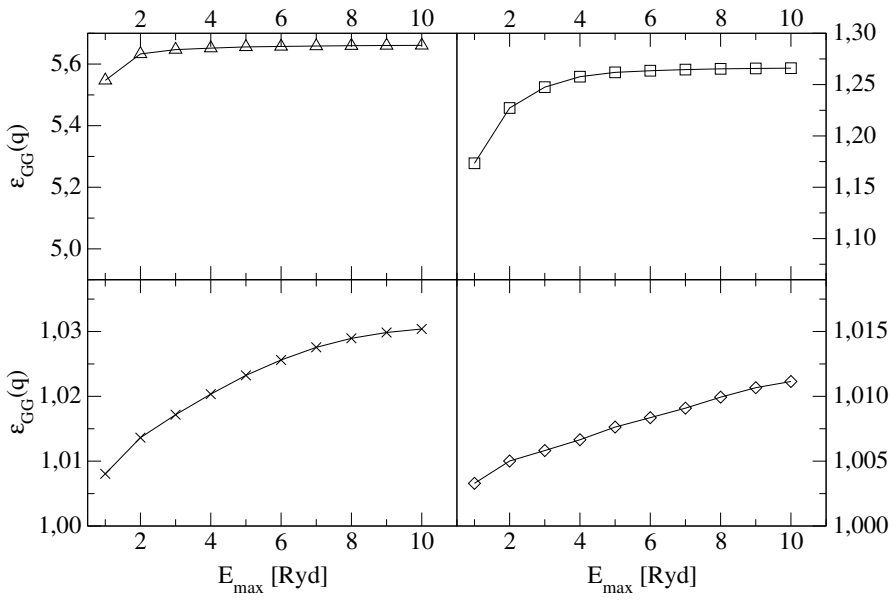

Figure 6.9: PA, convergence of the static dielectric matrix for $\mathbf{q} = \{0, 0, \frac{1}{8}\}$ with respect to the energy cut-off $E_{\max}$. The same $\mathbf{G}$ vectors as in Fig. (6.6) are displayed.

by other groups (see discussion in the next section).

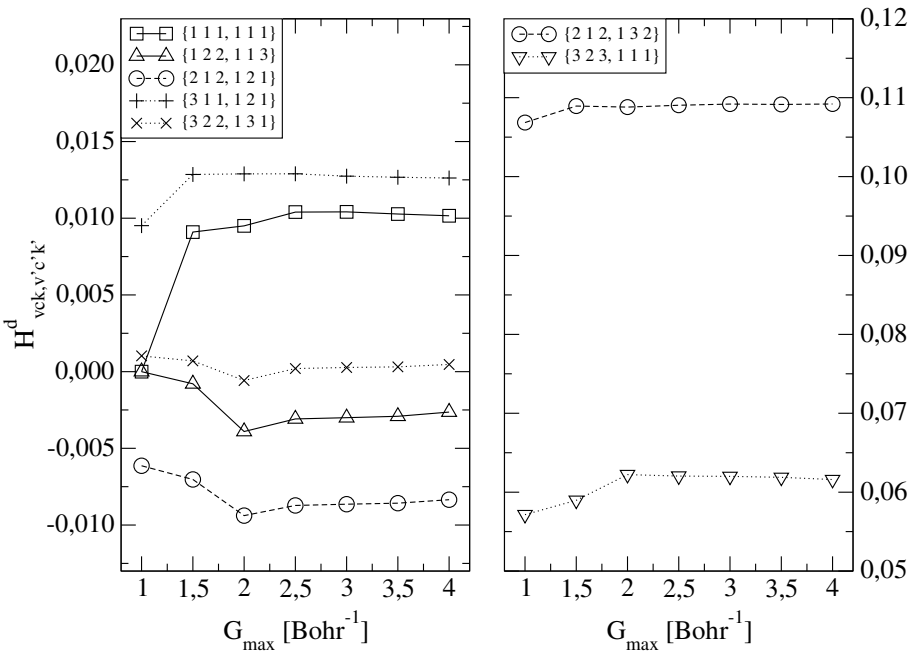

Figure 6.10: The convergence of some selected electron-hole interaction matrix elements for Si with respect to $G_{\max}$.

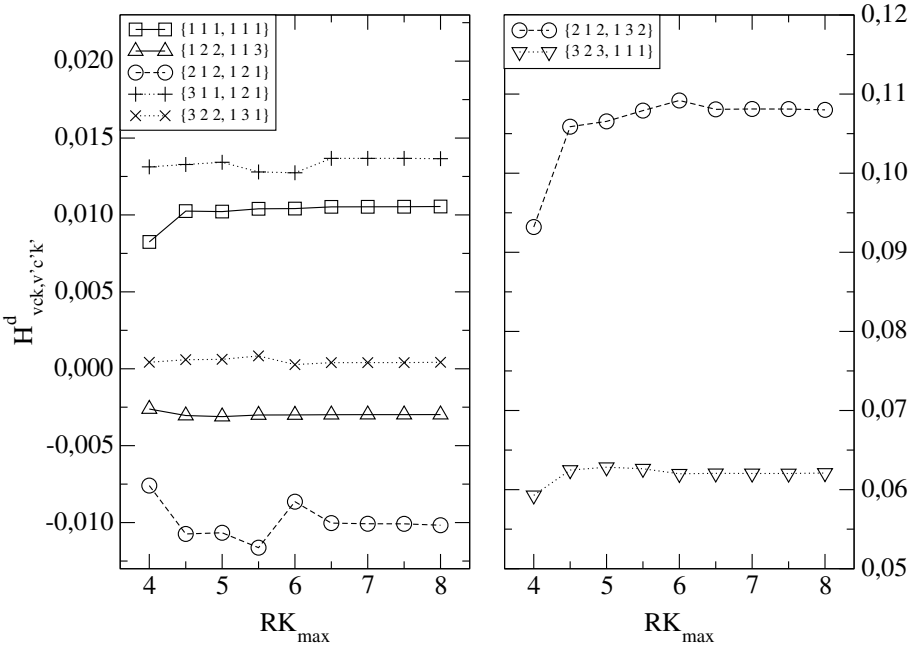

Figure 6.11: The convergence of some selected electron-hole interaction matrix elements for Si with respect to $RK_{\max}$.

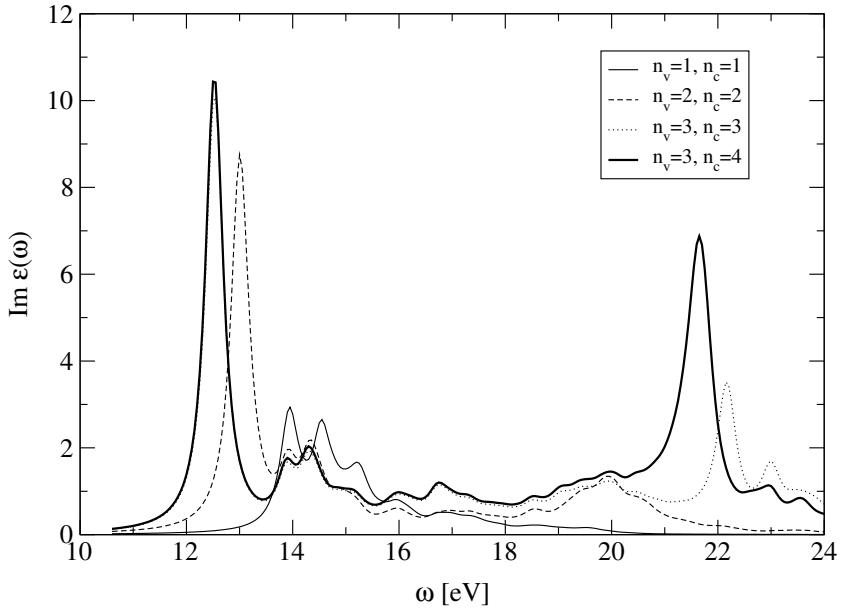

Figure 6.12: The convergence of the dielectric function of LiF with respect to the number of valence bands N_v and conduction bands N_c included in the exciton description. The number of **k** points was set to 512.

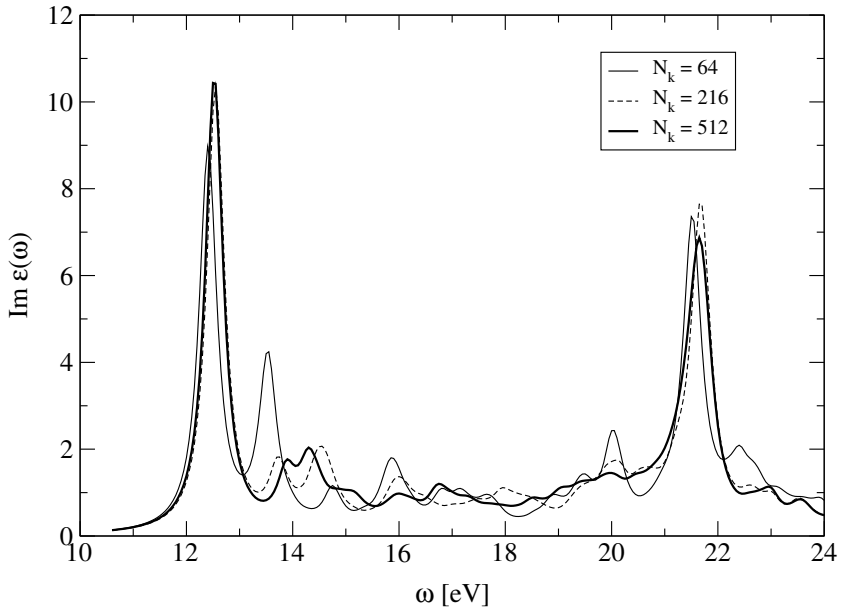

Figure 6.13: The convergence of the dielectric function of LiF with respect to the number of **k** points $N_{\mathbf{k}}$ used for the evaluation of the electron-hole interaction. The number of valence and conduction bands was set to 3 and 4, respectively.

Chapter 7

Excitonic Spectra

7.1 Introduction

This chapter comprises the main outcome of the theoretical description presented in the preceding chapters of this thesis. Numerical results for the macroscopic dielectric function $\epsilon_M(\omega)$ as obtained from the solution of the Bethe-Salpeter equation will be shown. In the first two sections, we apply our theoretical approach to bulk Si and LiF, respectively, and compare our results with experimental spectra as well as with theoretical work recently appearing in the literature. By this we intend to demonstrate the correctness of our theoretical description, and in particular, of the implementation into our LAPW code. The remaining sections then focus on the type of materials that are the subject of this thesis, namely organic conducting polymers. As a prototypical example we discuss the excitonic spectrum of an isolated poly-acetylene chain, before we investigate the modifications due to intermolecular interactions by means of a 3D crystalline structure of poly-acetylene.

7.2 Inorganic Semi-Conductors and Insulators

7.2.1 The RPA spectrum of Silicon

As a first test case we have chosen bulk silicon, because it can be viewed as prototypical representative of all group IV, III-V, and II-VI inorganic semiconductors. Moreover, a number of groups have already studied the optical response of Si including electron-hole correlations, allowing for a comparison with our results. Two experimental spectra of Si as measured by Aspenes et al. [98] and Lautenschlager et al. [99], respectively, are shown in Fig. (7.1). The optical spectrum shows two major structures in the region between 3 and 5 eV. The first peak

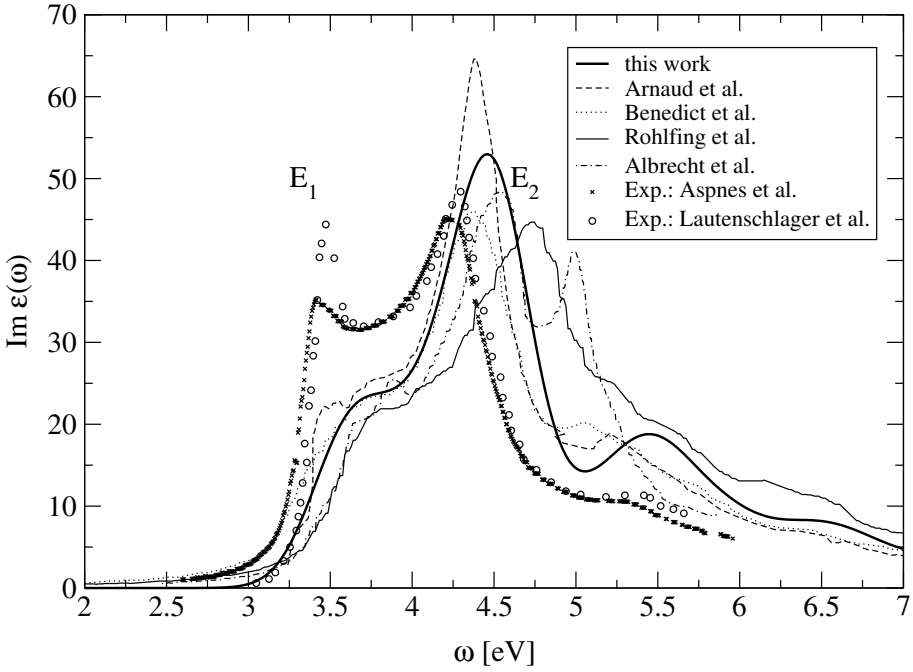

Figure 7.1: Comparison of the dielectric function in the RPA for Si with data taken from the literature.

(E_1) has been interpreted as a M_1 type critical transition, and the second peak as a M_2 type one [100]. Fig. (7.1) also displays, together with the experimental data, some recent theoretical results for the dielectric function as obtained by a number of different authors, calculated within the RPA and neglecting local field effects. ARNAUD et al. [35, 84] have used the projector augmented wave method, whereas BENEDICT et al. [101], ROHLFING et al. [83] and ALBRECHT et al. [30] have utilized pseudo-potential plane wave methods. All these authors have performed GW calculations in order to correct the Kohn-Sham energies, whereas in this work we have used a simple scissors shift of $\Delta = 0.9$ eV as described in Sec. 4.2.5. However, ARNAUD et al. have pointed out that the resulting spectra remain almost unchanged, whether the full GW quasi-particle correction or a simple scissors shift is used to correct the Kohn-Sham energies [35, 84].

Despite the differences among the RPA results of Fig. (7.1), the generic feature of all calculations within the *independent* quasi-particle approximation is to place oscillator strength too high in energy relative to experiment: The E_1 peak is underestimated by as much as 50% in intensity, whereas the E_2 peak is slightly overestimated. We further point out that an inclusion of local field effects does not improve the spectrum in the region around 4 eV as has already been observed by LOUIE et al. [102]. The same effect is also observed from our calculations as can be seen from Fig. (7.2) discussed in the next section. It was suggested that the

discrepancies between the RPA spectrum and experiment arise from neglecting electron-hole correlations.

7.2.2 Correlated DF of Silicon

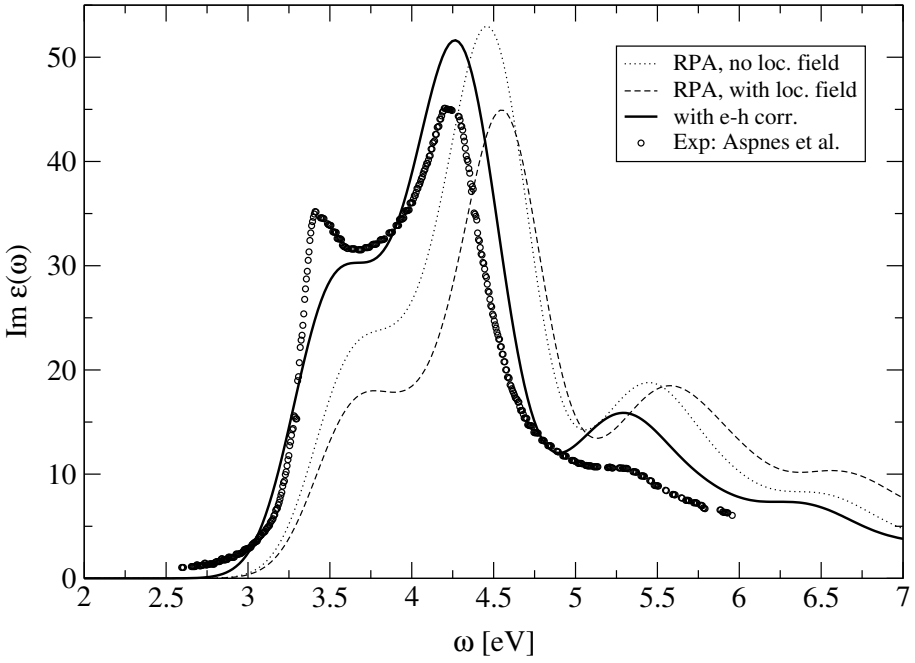

Figure 7.2: The dielectric function of Si as obtained from the solution of the BSE. The dotted line results from setting both the exchange and the direct interaction term equal to zero. The RPA result including local fields (dashed) is obtained by only including the exchange part, whereas the full line is attained by taking into account the direct as well as the exchange interaction. For comparison, experimental data as obtained by ASPENES et al. [98] is shown (circles).

The first computations including electron-hole correlations as well as local-field effects were done by HANKE and SHAM [25, 26] using semi-empirical LCAO calculations. Again, local field effects alone were shown to transfer oscillator strength to *higher* energies, thereby increasing the discrepancy with experiment. On the contrary, the electron-hole interaction shifted the position of the E_1 peak to slightly lower energies, and almost doubled its intensity, while the oscillator strength of the higher energy peaks was decreased. The overall agreement with experiment was hence improved, and clear evidence for the importance of excitonic effects was given. However, the intensity ratio between the E_1 and the E_2 peaks was reversed, in disagreement with experiment which was attributed to the semi-empirical character of the approach taken by HANKE and SHAM.

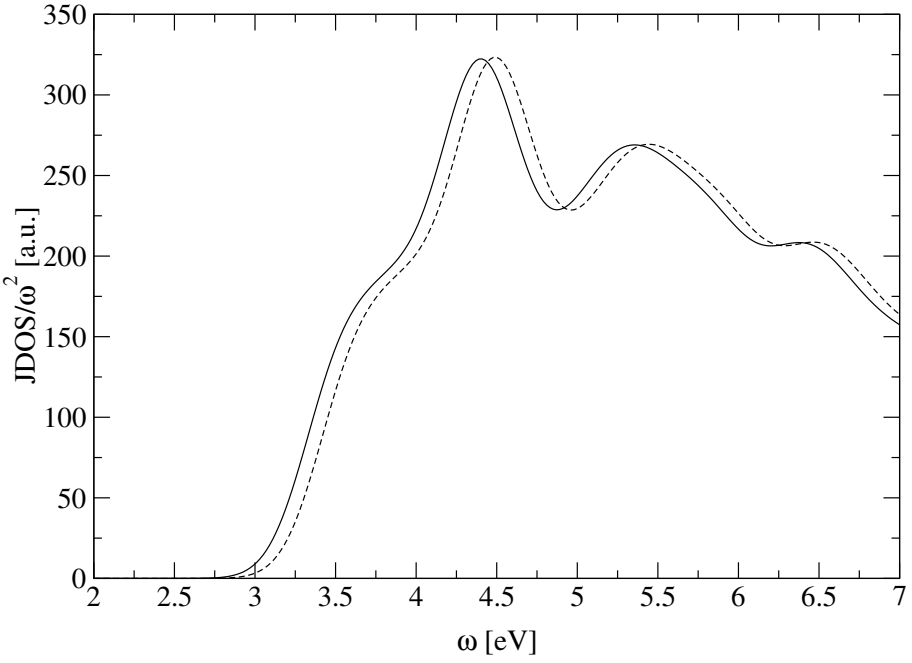

Figure 7.3: The joint density of states (JDOS) divided by ω^2 for Si. The dashed line is the JDOS of independent electron-hole pairs, whereas the full line is the density of excited states as obtained from the solution of the BSE.

We have calculated the dielectric function of Si including electron-hole correlations according to Eq. (4.109). We compute the electron-hole interaction matrix elements on an $8 \times 8 \times 8$ $\mathbf{k}$ mesh that has been shifted from the origin by a small vector $\mathbf{k}_\Delta$ which was chosen to be $\mathbf{k}_\Delta = \{\frac{1}{80}, \frac{3}{80}, \frac{5}{80}\}$, and we included 3 valence and 4 conduction bands, respectively. The non-symmetric shift of the $\mathbf{k}$ grid leads to a finer sampling of the spectrum of electron-hole pairs than a non-shifted mesh of the same size would do. This is because, the shifted mesh corresponds to 512 crystallographically different points in the BZ, whereas a non-shifted one would only yield 29 inequivalent $\mathbf{k}$ points in the BZ, which would be much too few to achieve a good spectral convergence. The calculation of the direct as well as the exchange interaction involves a sum over reciprocal lattice vectors $\mathbf{G}$ according to Eqs. (6.57) and (6.65) for which we have used a cut-off parameter of $\mathbf{G}_{\max} = 4.0$ Bohr^{-1}. Note that we have assumed the screened interaction W to be diagonal in $\mathbf{G}$ and $\mathbf{G}'$. It has been pointed out by Albrecht et al. that this approximation has no effect on the resulting DF of Si [30]. The dielectric matrix has been calculated for 29 crystallographically different $\mathbf{q}$ points with an $RK_{\max}$ of 6.0, and conduction states up to $E_{\max} = 10.0$ Ryd have been included. For the calculation of the electron-hole kernel, we use the same $RK_{\max} = 6.0$. The results are displayed in Fig. (7.2), where we have used a Lorentzian line-shape with a broadening of $\delta = 0.2$ eV.

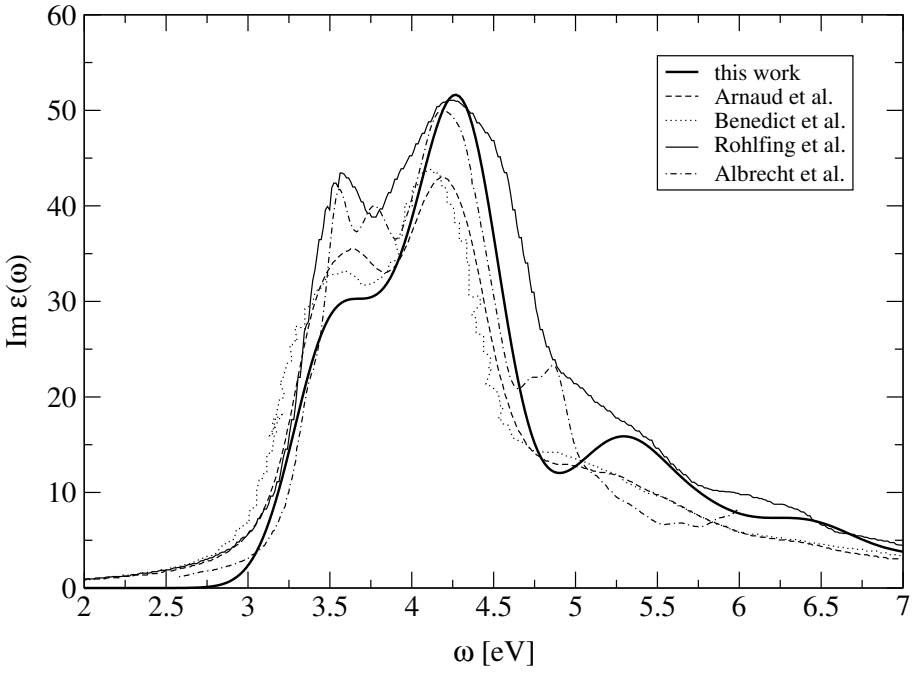

Figure 7.4: Comparison of the dielectric function including electron-hole correlations for Si with corresponding calculations taken from the literature.

Fig. (7.2) contains three theoretical results together with an experimental spectrum of Si. If both the exchange and the direct interaction term in the BSE are set equal to zero, then the description reduces to the independent quasi-particle approximation (dotted curve). This result is in fact equivalent to the RPA without taking into account local field effects, which has already been shown in Fig. (7.1). We have learned in Chapter 4 that an inclusion of the exchange term *only* is indeed equivalent to including local field effects (dashed curve). We notice that the full RPA worsens the agreement with experiment as has been found previously [102]. Only the full electron-hole interaction including the attractive direct interaction term (full line) results in the correct behavior of the DF: the E_1 peak is shifted slightly to lower energies and its intensity is increased, and the E_2 peak is also shifted to the red without a change of intensity. The resulting DF is in much better agreement with experimental data.

Two things have to be mentioned. First, the calculation does not produce *bound* exciton states that would occur in the low-energy onset of the spectra, because of the limited spectral resolution in the computation. The achievable resolution is directly related to the density of the **k** grid which in our case results in a spectral resolution of roughly 0.15 eV. This value is clearly to high to resolve the bound excitons in Si which are on the meV scale. Note that also the experimental results shown do not contain these bound exciton states due to the limited spectral

resolution of the data. It is, however, possible to obtain these bound exciton states by increasing the density of **k** points as was demonstrated by ROHLFING et al. [32, 83]. The second interesting result is that the effect of electron-hole interaction is *not* to simply shift the excitation energies to lower energies due the electron-hole attraction as one might naively expect. This fact is demonstrated in Fig. (7.3) where we show the joint density of states divided by ω^2 for both the RPA and the correlated case. We see that apart from a rigid shift of 0.09 eV given by expression (6.64) there is almost no change in the density of excited states due to the electron-hole correlation. It is the *coherent* superposition of oscillator strengths that is responsible for the modifications of the spectra presented in Fig. (7.2): a constructive superposition increases the oscillator strength at the low-energy side of the spectrum, whereas a destructive superposition decreases the oscillator strength at the high-energy parts of the DF. We point out that it is extremely important to treat the *phases* of the wave functions consistently throughout all steps of the calculation, because otherwise the results would virtually reduce to a random phase approximation spectrum. Finally, in Fig. (7.4) we compare our results to four similar calculations from the recent literature. The agreement of our results with those previously obtained [30, 32, 35, 101] is quite satisfying.

7.2.3 The RPA spectrum of LiF

In wide band-gap insulators the dielectric screening is much weaker as compared to semi-conductors. The static dielectric constant of LiF is only $\epsilon = 1.9$ compared to $\epsilon = 11.7$ in Si [32, 83]. Therefore, we expect the electron-hole interaction to be much stronger in LiF, and its effects on the dielectric function to be more pronounced. This is because at long range the screened electron-hole interaction is approximately given by $1/\epsilon r$ and therefore stronger by a factor of 6 in LiF as compared to Si. Fig. (7.5) compares experimental data for the dielectric function [103] with RPA results from the literature [31, 32, 84], and our own RPA result. All theoretical results on the independent-particle level bear almost no resemblance to the experimental spectrum over the entire energy range. In particular, the pronounced peak at 12.7 eV does not show up in the theoretical description. We can attribute the failure of the RPA to neglecting electron-hole correlations as will be proven in the next subsection. We point out that we have shifted the calculated LDA gap of 9.0 eV by a rigid shift of $\Delta = 5.7$ eV in order to obtain the quasi-particle spectrum in accordance with GW calculations by Rohlfing and Louie [32, 83] who obtained a quasi-particle gap of 14.4 eV.

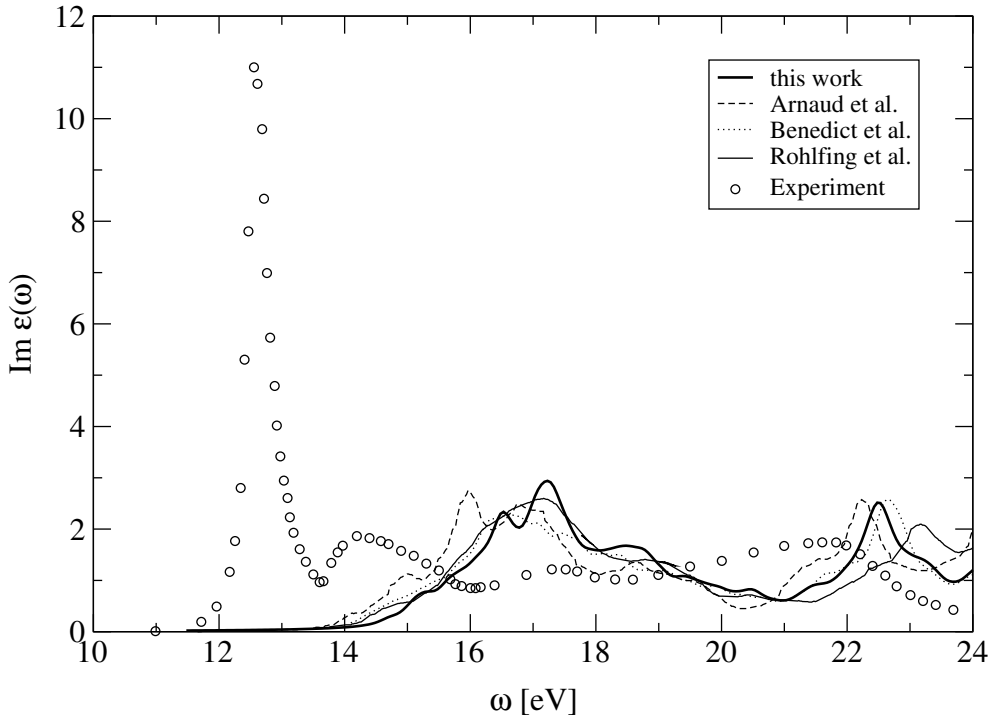

Figure 7.5: Comparison of the dielectric function in the RPA for LiF with data taken from the literature.

7.2.4 Correlated DF of LiF

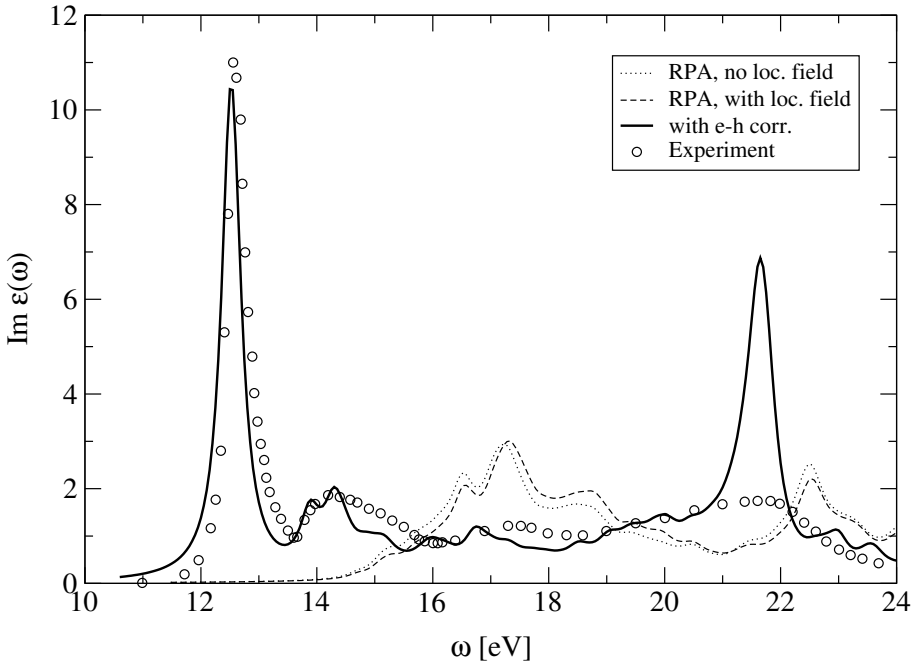

Figure 7.6: The dielectric function of LiF as obtained from the solution of the BSE. The dotted line results from setting both the exchange and the direct interaction term equal to zero. The RPA result including local fields (dashed) is obtained by only including the exchange part, whereas the full line is attained by taking into account the direct as well as the exchange interaction. For comparison, experimental data as obtained by ROESSLER et al. [103] is shown (circles).

As for Si, we have calculated the dielectric function of LiF including electron-hole correlations according to Eq. (4.109). The electron-hole interaction matrix elements were computed on a shifted $8\times8\times8$ $\mathbf{k}$ mesh, where we have chosen $\mathbf{k}_\Delta = \{\frac{1}{160}, \frac{3}{160}, \frac{5}{160}\}$, and we included 3 valence and 4 conduction bands, respectively. For the calculation of the direct as well as the exchange interaction we have used a cut-off parameter of $\mathbf{G}_{\max} = 4.0$ Bohr^{-1} (compare Fig. B.1), and we neglected off-diagonal components in the screened interaction. The dielectric matrix has been calculated for the 29 crystallographically different $\mathbf{q}$ points with an $RK_{\max}$ of 7.0, and conduction states up to $E_{\max} = 15.0$ Ryd have been included. For the calculation of the electron-hole kernel, on the other hand, it was sufficient to use an $RK_{\max} = 6.0$ (compare Fig. B.2). The resulting spectra are displayed in Fig. (7.6), where we have used a Lorentzian line-shape with a broadening of $\delta = 0.2$ eV. The dotted line results from setting both the direct interaction H^{dir} as well as the exchange term H^x equal to zero, thus it comprises the RPA result identically to that shown in Fig. (7.5). The inclusion of the exchange-term

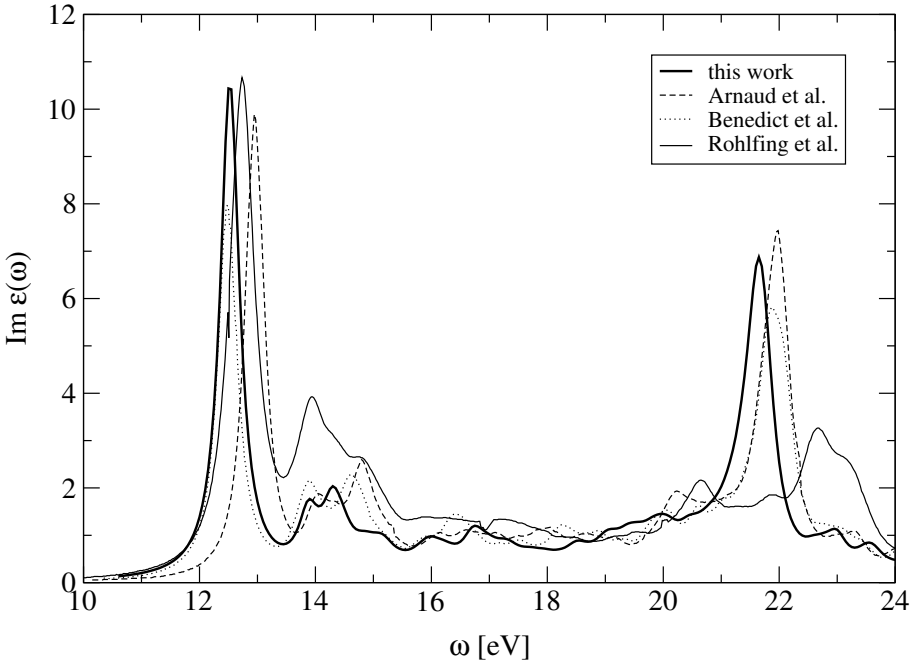

Figure 7.7: Comparison of the dielectric function including electron-hole correlations for LiF with corresponding calculations taken from the literature.

H^x *only* is equivalent to including local-field effects, i.e. to the inversion of the dielectric matrix, as was described in Sec. (4.3.3). The resulting DF, given by the dashed curve, does not improve the agreement with experiment, on the contrary, the exchange interaction places oscillator strength to higher energies and thereby slightly worsens the situation. But with the addition of the attractive direct interaction term H^{dir} the dielectric function nicely reproduces the bound exciton at an experimental value of 12.7 eV. The calculation gives three excitons at 12.5 of which only one has an appreciable oscillator strength, whereas the other two are optically inactive. Moreover, the inclusion of electron-hole correlation is also important for energies above the band gap of 14.7 eV since the spectrum is now in much better agreement with experiment than the RPA spectra. The only major discrepancy remains at roughly 21.5 eV, where the theoretical result predicts a strong peak which does not show up in experimental data. This failure might be attributed to the limited number of bands included in the solution of the BSE. Moreover, also the results of some other groups fail to produce the experimental spectra in this respect as can be seen from Fig. (7.7).

It is instructive to study the real-space electron-hole wave function $\Phi^\lambda(\mathbf{r}_e, \mathbf{r}_h)$ given by Eq. (4.121) as a sum over electron-hole pairs weighted by the coupling coefficients $A^\lambda_{vc\mathbf{k}}$. Here, $\mathbf{r}_e$ and $\mathbf{r}_h$ denote the position of the electron and the hole, respectively. As an example we discuss the electron-hole distribution of the

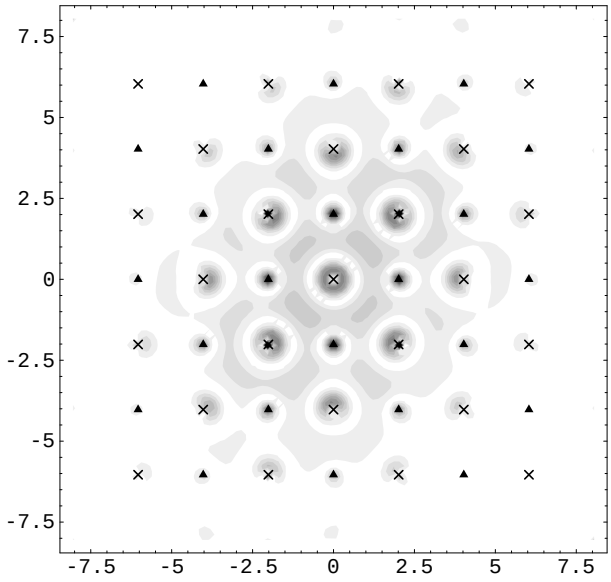

Figure 7.8: The absolute value of the exciton wave function of LiF in the (010) plane as a density plot. The position of the hole has been fixed at the central F atom (origin of the plot). Crosses (triangles) denote the positions of the F (Li) atoms.

bound exciton at 12.5 eV dominating the low energy part of the spectrum. In Fig. (7.8) we show the distribution of the electron relative to the hole in the (010) plane. We have fixed the position of the hole at the central F atom (origin of the plot), and crosses (triangles) denote the positions of the F (Li) atoms. First of all, we see that the radius of the exciton is roughly 4 Å, and the distribution function is more or less spherically symmetric. In Fig. (7.9) we show the exciton wave function along the [101] (top panel) and the [100] (lower panel) directions. From these plots we see that the highest probability to find the electron is at the F atoms along the [101] direction at a distance of 2.85 Å from the position of the hole. But there is also a considerable probability for the electron to be located at the central F atom. Similar observations have also been made by Rohlfing et al. [32]. Our results, however, differ in one aspect from the findings of Rohlfing, in that we find also a considerable probability on the nearest-neighbor Li atoms whereas Rohlfing et al. do not. This can be seen from the two peaks in a distance of 2 Å from the hole in the lower panel of Fig. (7.9).

In summary, we have seen that electron-hole correlations are necessary in order to achieve experimental agreement for the DF, both for the semi-conductor Si as well as for the insulator LiF. For Si the coherent coupling of e-h pairs only leads to a shift of oscillator strength to lower energies (Figure 7.2), whereas for LiF these correlations are vital in order to correctly describe the bound exciton state observed in experiment (Figure 7.6). Moreover, our correlated spectra compare

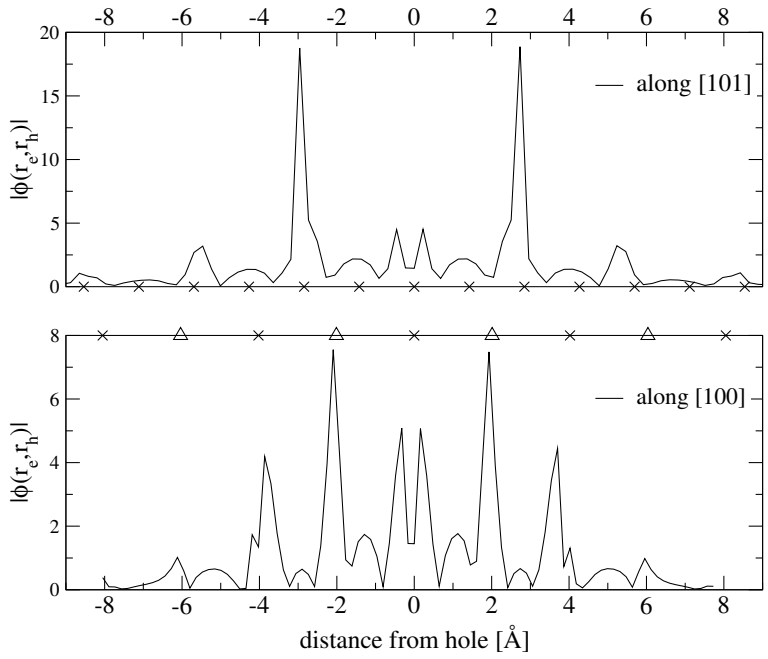

Figure 7.9: The absolute value of the exciton wave function of LiF along the [101] (top panel) and [100] (bottom panel) directions. Crosses (triangles) denote the positions of the F (Li) atoms.

well with previous *ab-initio* results thereby establishing the correctness of our approach. Thus, we can now focus on the type of materials which are the main subject of this thesis.

7.3 Conjugated Polymers

Due to its simple structure, trans-polyacetylene (PA) is an ideal candidate for studying the role of electron-hole correlations in these low-dimensional systems. We will first present the optical spectrum of an *isolated* PA chain before we discuss the modifications of the optical properties arising from a three-dimensional arrangement of the polymer chains.

7.3.1 Isolated Poly-acetylene

In order to consider an isolated PA chain within a 3D band structure calculation one has to use a unit cell which sufficiently separates one polymer chain from its periodic images. Indeed, such computations are not at all trivial since one should cross-check the results with respect to the size of the empty space. In our

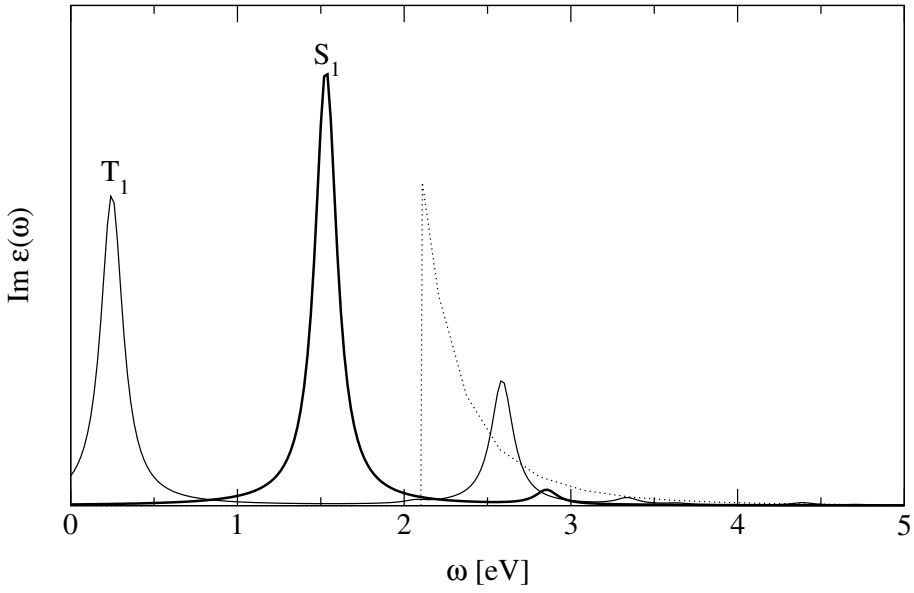

Figure 7.10: Imaginary part of the dielectric function for an isolated PA chain. The dotted line corresponds to the uncorrelated result, whereas the full (thin) continuous lines depict the correlated result for spin singlet (triplet) transitions.

study, however, we have only used one single size for the cell given by the lattice constants $a = 6.0$ Å (in the plane of the polymer backbone) and $b = 5.0$ Å (perpendicular to it). Thus, the results obtained for the *isolated* chain may be subject to some quantitative changes when increasing the empty volume around the polymer chain. The computations are, however, capable of describing some qualitative arguments which are then used in the discussion of *crystalline* PA in the final section of this chapter. Moreover, the effects of electron-hole correlations on the optical properties of an isolated PA chain have already been published by Rohlfing and Louie [33].

We have taken experimental values for the structural parameters of a PA chain as listed in [104]. We particularly want to emphasize that we have used a dimerization of $u_C = 0.052$ Å since structural optimizations using an LDA or GGA potential underestimate this dimerization considerably.[1] The LDA-DFT calculations give a direct band gap of 0.85 eV at the Z point in accordance with previous studies [104]. Rohlfing and Louie have found the quasi-particle band gap of an isolated PA chain in the GW approximation to be 2.1 eV [33]. We have therefore shifted the conduction bands rigidly upward by a $\Delta_c = 1.25$ eV. The electron-hole interaction matrix elements are computed on a shifted one-dimensional mesh with 32 $\mathbf{k}$ points along the polymer direction, where we have

[1] We have found that a geometry optimization using the PBE-GGA exchange correlation potential [51] leads to a dimerization of less than $u_C = 0.01$ Å.

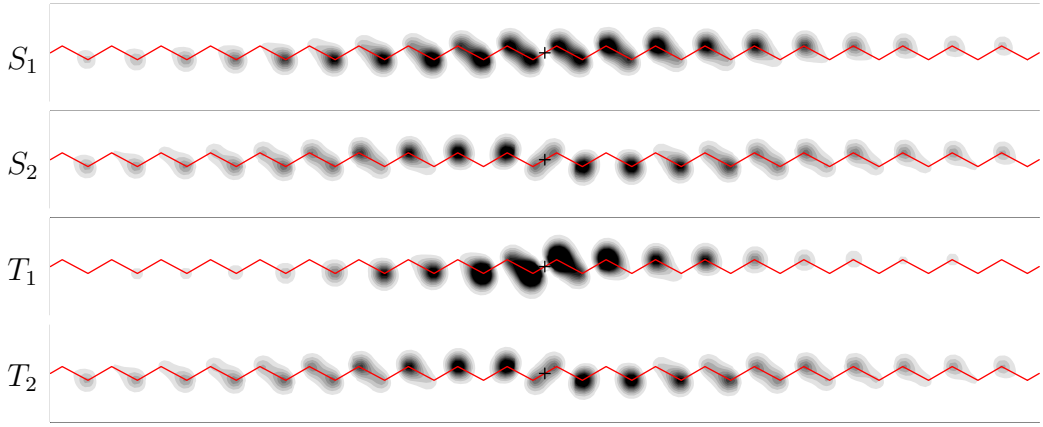

Figure 7.11: Electron-hole wave functions $|\Phi|^2$ of isolated polyacetylene chain for lowest lying singlet (S_1 and S_2) and triplet (T_1 and T_2) states in a plane parallel to the polymer backbone and shifted to account for the π character of the wave function. The position of the hole is fixed at the central C–C bond indicated by a cross. The polymer backbone is indicated through the zig-zag line.

chosen $\mathbf{k}_\Delta = \{0, 0, \frac{1}{256}\}$. We found that only 2 valence and 2 conduction bands are sufficient to yield converged spectra (Figure B.6). For the calculation of the direct as well as the exchange interaction we have used a cut-off parameter of $\mathbf{G}_{\max} = 3.0$ Bohr^{-1} (compare Figure B.3), and we neglected off-diagonal components in the screened interaction. The dielectric matrix has been calculated for the 17 crystallographically different $\mathbf{q}$ points along the polymer chain, and conduction states up to $E_{\max} = 10.0$ Ryd have been included.[2] We have used an $RK_{\max}$ of 2.5 and the APW+lo basis set for all computations. The convergence of the direct interaction term, for instance, with respect to $RK_{\max}$ is depicted in Figure (B.4).

The resulting optical spectra are depicted in Figure (7.10). The dotted line denotes the spectrum neglecting electron-hole correlations, thus it corresponds to vertical $\pi \rightarrow \pi^*$ transitions of *independent* electron-hole pairs. Due to the one-dimensional character of the transition it roughly behaves as $(\omega - E_g)^{-1/2}$ (van-Hove singularity), where E_g is the quasi-particle gap of 2.1 eV. The inclusion of electron-hole correlations produces a single *bound* exciton state at 1.55 eV inside the quasi-particle gap. This state (S_1) exhibits a strong oscillator strength for optical transitions. Rohlfing and Louie have calculated this exciton to lie at 1.7 eV [33]. Thus, our exciton binding energy of 0.55 is 30 % larger than those given in [33]. The next higher exciton state S_2, on the other hand, has virtually no oscillator strength in accordance with previous results [33]. However,

[2]Note that the dielectric matrix ϵ is computed with the *uncorrected* Kohn-Sham energies.

in our computations S_2 is roughly at the original gap energy of 2.1 eV, whereas ROHLFING reports an energy of 1.8 eV. We have have also plotted the exciton wave function $\Phi(\mathbf{r}_e, \mathbf{r}_h)$ of these two states in Figure (7.11). We consider a plane parallel to the polymer backbone and slightly shifted from the polymer backbone in order to account for the π character of the wave function, and we have fixed the position of the hole $\mathbf{r}_h$ above the center of a C–C bond in that plane. We see the distribution of the electron over several monomer units. While for S_1 the oscillator strengths of the contributing electron hole pairs add up constructively, there is a destructive superposition of oscillator strengths for S_2. This can also be seen from the different shapes of the exciton wave functions for S_1 and S_2. In Section 4.3.8, we have pointed out that spin triplet excitons do not feel the repulsive exchange interaction, thus we expect them to be more localized and have a larger exciton binding energy. This is indeed confirmed by our calculations which give the lowest two triplet states T_1 and T_2 at 0.25 and 2.05 eV, respectively. The corresponding electron-hole distribution functions are displayed in Figure (7.11), where we clearly observe the stronger localization of T_1 compared to S_1. The binding energy of T_1, however, is considerable 0.65 eV too large compared to a value reported by ROHLFING and LOUIE [33]. Moreover, they compute a $S_1 - T_1$ splitting of 0.8 eV, whereas we obtain a much higher splitting of 1.3 eV. Thus, both terms of the electron-hole kernel separately, namely the direct term entering the triplet energy T_1, as well as the exchange term responsible for the $S_1 - T_1$ splitting are overestimated. Interestingly enough, both terms differ by roughly half an eV from the corresponding values obtained by ROHLFING and LOUIE. We believe that the discrepancies stem from the fact that we did not use a sufficiently large cell in order to separate the polymer chain from its periodic images. By using a one-dimensional $\mathbf{k}$ grid along the polymer we force the exciton to be located on one chain. However, the spatial extension of the exciton in a plane perpendicular to the chain is artificially reduced due to the too small distance to neighboring chains. As a consequence, the interaction between the electron and the hole turns out to be too large resulting in an overestimated exciton binding energy. We are therefore tempted to scale both the direct and the exchange interaction by the same factor which can be interpreted as changing the volume of the unit cell. If we increase the unit cell volume by 20 % by rescaling the strength of the interaction kernel, we obtain a singlet energy S_1 of 1.70, and a triplet energy T_1 of 0.85. These two values would indeed agree very well with previously reported values [33].

7.3.2 Crystalline Poly-acetylene

Polyacetylene, as many other conjugated polymers or oligomers, crystallizes in the so called herring-bone arrangement with two polymer chains per unit cell. There are two different crystal structures belonging to the space groups $P2_1/a$ and

$P2_1/n$, respectively, differing by a modified arrangement of the second polymer chain with respect to the first one. In the following, we will abbreviate the $P2_1/a$ and $P2_1/n$ structures with a–PA and n–PA, respectively. It has been found that the total energy for a–PA is slightly smaller than for n–PA [104]. Thus, the former is expected to be more stable. In Figure (7.12), we depict the LDA-DFT band structures of a–PA (left panel) and n–PA (right panel). These band structures have already been discussed by Vogl and Campbell [104, 105]. We have used the same geometry of the polymer chain as for the one-dimensional case. The lattice constants and the other structural parameters have been taken from Table II of [104]. There are several interesting features that can be recognized from Figure (7.12). First, we notice that the band dispersions along the polymer chain

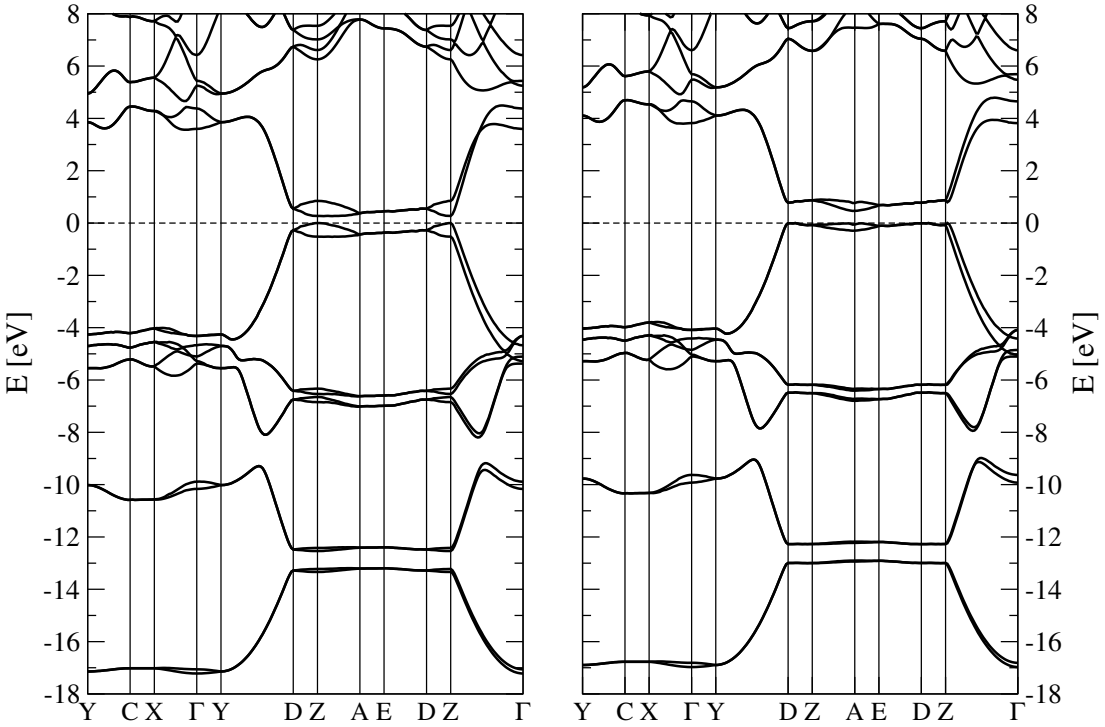

Figure 7.12: Electronic band structure of crystalline poly-acetylene along high symmetry directions in the BZ. Panels (left) and (right) correspond to the $P2_1/a$ and $P2_1/n$ crystal structures, respectively.

– compare the ΓZ and YD directions – are much higher than perpendicular to it, where the valence and conduction bands close to the Fermi level (dashed line) are comprised by states having π symmetry. Second, the fact that there are two polymer chains per unit cell doubles the number of bands when compared to an isolated-chain calculation. The splitting of these bands is a measure for the inter-chain interaction. It is of course quite weak, therefore the splittings are of the order of only 0.2 eV. The features mentioned are above are common to both

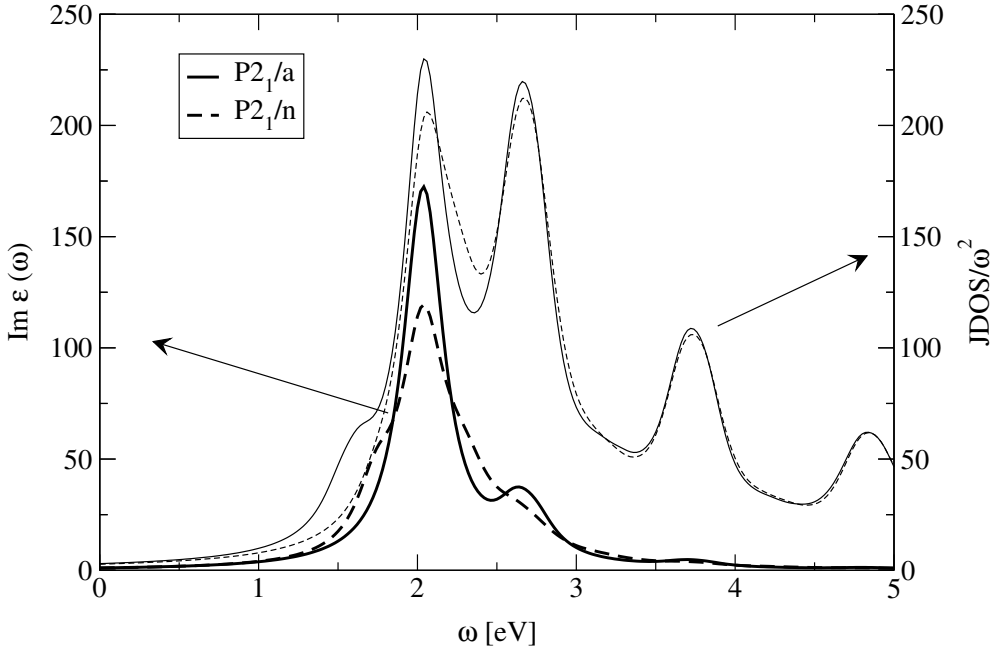

Figure 7.13: The imaginary part of the DF in the RPA (thick lines) and the joint density of states divided by ω^2 (thin lines) for a–PA (full lines) and n–PA (dashed lines).

a–PA and n–PA. There are, however, also subtle differences which are in fact the reason why we want to compare these two structures. The distinct arrangement of the two chains in a–PA and n–PA leads to different inter-chain interactions. For instance, these result in a band splitting of the top valence band at the Z (A) point of 0.50 (0.0) and 0.01 (0.25) eV for a–PA and n–PA, respectively. As a consequence, a–PA is a direct band-gap semiconductor with an LDA-DFT gap of 0.27 eV at the Z point, whereas the n–PA has a slightly in-direct band gap with a valence band maximum at D and a conduction band minimum at A, and an LDA-DFT gap of 0.49 eV.

Before we report on the excitonic structure of crystalline PA, we discuss the DF in the independent quasi-particle approximation. The results for the DF as well as for the joint density of states for optical transitions (JDOS) are depicted in Figure (7.13). We have shifted the conduction bands rigidly upward by using the scissors operator with a Δ_c of 1.25 eV. Thus, we have used the same value as we did for the one-dimensional polymer chain. There is no rigorous justification for such a treatment since it is not clear whether the quasi-particle correction is equal for three systems having quite different LDA-DFT band gaps. As a consequence, we do not expect our results to describe the absolute position of the excitations correctly. We can, however, interpret our results in terms of exciton binding energies, or discuss the differences of the RPA spectra and the ones including

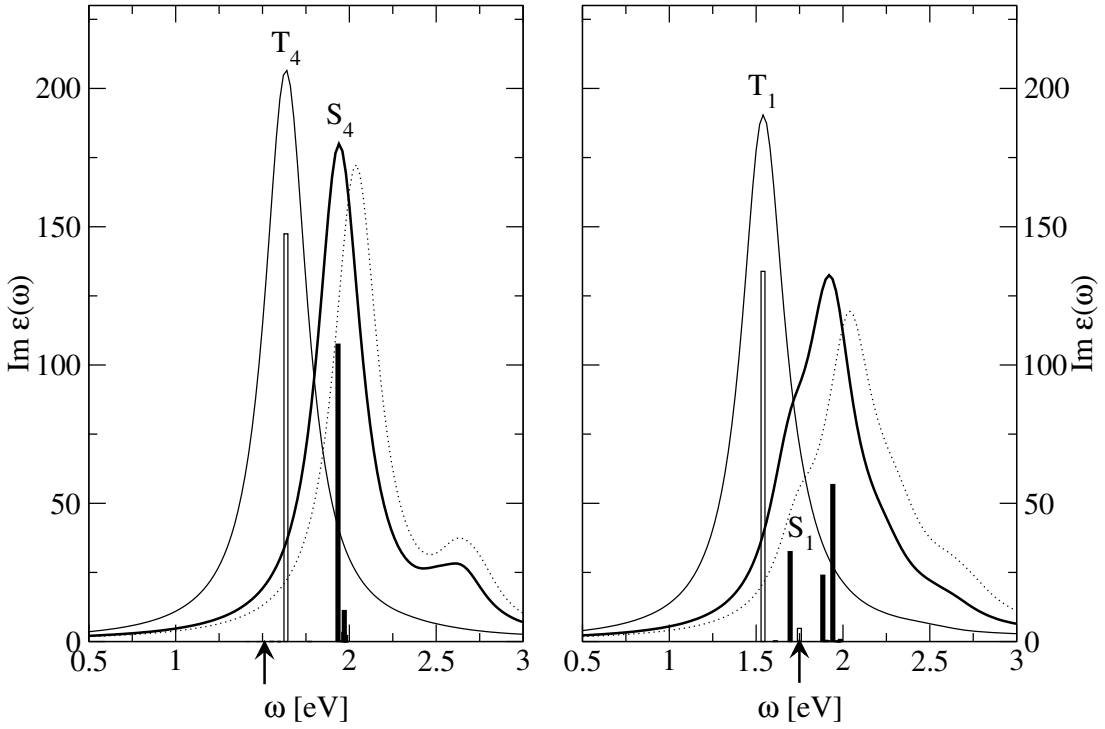

Figure 7.14: The imaginary part of the DF for *a*–PA (left panel) and *n*–PA (right panel). The dotted lines are the RPA spectra already shown in Fig. (7.13), the continuous lines correspond to the spin singlet (thick) and triplet (thin) excitations. The positions and oscillator strengths of the energetically lowest singlet and triplet states is indicated as filled and open bars, respectively. The arrows indicate the position of the band gap.

electron-hole correlations. For future studies, it will be certainly necessary to obtain the quasi-particle gap by *ab initio* methods such as GW calculations instead of treating the quasi-particle band gap as an adjustable parameter. But let us now turn to the discussion of the RPA spectra in Figure (7.13), and see what we can learn from them, despite of the fact that we have shifted the band gaps quite arbitrarily by 1.25 eV. Although *a*–PA has a *lower* band gap than *n*–PA, the DF of the former appears to be shifted to *higher* energies as compared to the DF of *n*–PA. This is because the energetically lowest electron-hole pairs in *a*–PA at an energy of 1.52 eV have no oscillator strength, whereas the energetically lowest optical transition in *n*–PA at 1.75 eV exhibits a considerable oscillator strength. This effect can also be observed by comparing the DFs of *a*–PA and *n*–PA with their corresponding JDOS.

We can now turn to the discussion of excitonic effects in the two crystalline polyacetylene structures *a*–PA and *n*–PA, respectively. The electron-hole interaction matrix elements are computed on a shifted mesh with $4 \times 2 \times 32$ **k** points, where

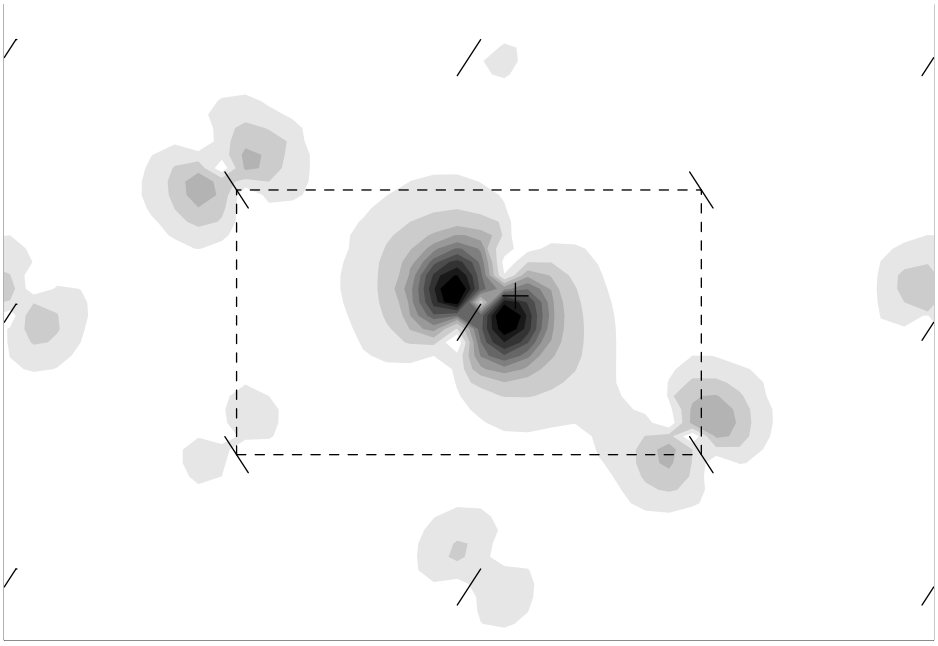

Figure 7.15: The electron distribution with respect to the hole (cross) of the S_4 state of *a*–PA in a plane perpendicular to the polymer chains and through a C atom. The unit cell axis a (vertical) and b (horizontal) are shown by dashed lines, and the projections of the C polymer-backbone are indicated by the short lines.

we have chosen $\mathbf{k}_\Delta = \{\frac{1}{512}, \frac{1}{512}, \frac{1}{512}\}$. From what was found for the isolated chain, we expect that 4 valence and 4 conduction bands are sufficient since we have to double the number of bands included due to the second polymer chain in the unit cell. For the calculation of the direct as well as the exchange interaction we have used a cut-off parameter of $\mathbf{G}_{\max} = 2.0$ Bohr^{-1}, and we neglected off-diagonal components in the screened interaction. The dielectric matrix has been calculated for the 132 crystallographically different $\mathbf{q}$ points, and conduction states up to $E_{\max} = 8.5$ Ryd have been included. We have used an $RK_{\max} = 2.3$ and the APW+lo basis set for all computations. We have reduced the cut-off parameters $RK_{\max}$ and $\mathbf{G}_{\max}$ as compared to the isolated-chain computations in order to save computer time. The convergence behavior of the electron-hole kernel in Figures (B.3) and (B.4), however, strengthens our confidence in the so obtained results.

The spectra are displayed in Figure (7.14), where the left and right panels, respectively, correspond to *a*–PA and *n*–PA. For both structures we compare the RPA result (dotted line) with the spin singlet (thick line) and triplet (thin line) solutions. In addition we have also indicated the positions and oscillator strengths of the lowest exciton states as bars, and the energetic position of the band gap is indicated by an arrow. The results for both crystalline structures *a*–PA and *n*–PA are quite different to those obtained for the isolated PA chain. For the iso-

lated chain we found a strong bound exciton peak with an exciton binding energy of 0.55 eV. In the crystalline environment, however, the electron-hole interaction is greatly reduced due to two effects. First, the screening is more effective for the crystalline material as compared to the isolated chain. This effect has already been observed by VAN DER HORST and co-workers [34, 39] who have found that for bulk polythiophene inter-chain screening drastically reduces the exciton binding energies.

The second effect, which is equally important, concerns the spatial extent of the exciton. While the exciton is obviously confined to one polymer chain for the isolated polymer, it appears to be extended over the neighboring chains in the crystalline case. We have illustrated this effect in Figure (7.15), where we have plotted the exciton wave function for the S_4 state of *a*–PA in a plane perpendicular to the polymer axis. We notice that if we fix the position of the hole on one chain, there is some probability for the electron to be found on neighboring chains. Consequently, the average distance between the electron and the hole is increased. Thus, the interaction between the electron and the hole is reduced, and the exciton binding energy is much smaller than for the isolated polymer chain. Quantitatively, the excitonic spectra are strongly influenced by the details of the inter-chain interaction, which can be seen from a comparison of the results for *a*–PA and *n*–PA. For both systems, the lowest singlet exciton S_1 has a binding energy of 0.05 eV, thus it lies at 1.47 and 1.70 eV, respectively. While it has almost no oscillator strength (OS) for optical transitions in *a*–PA, it is optically active for the *n*–PA phase. It is not until the fourth singlet state (S_4) in *a*–PA at an energy of 1.93 eV that shows a strong OS (compare Figure 7.14). The lowest triplet state T_1 lies at an energy of 0.10 and 0.20 eV in *a*–PA and *n*–PA, respectively. There is obviously no transition probability for optical transition from the singlet ground state, but we can nevertheless calculate the OS of triplet states by assuming a triplet ground state. By doing so we find that T_1 has no OS for *a*–PA, whereas we observe a very pronounced peak for *n*–PA as can be seen from Figure (7.14). Finally, we notice that the singlet-triplet splittings of lowest lying states $S_1 - T_1$ is only 0.05 eV for the *a*–PA phase, whereas it is considerably larger in *n*–PA (0.15 eV).

In summary, we have seen that inter-chain interactions crucially alter the excitonic states in trans-polyacetylene. We find strongly bound exciton states for the isolated chain with exciton binding energies in the order of 0.5 eV. On the other hand, a crystalline arrangement of the polymer chains as in the two considered phases *a*–PA and *n*–PA, respectively, drastically reduces the strength of the electron-hole interaction. This is because (i) the screening of the electron-hole interaction is more efficient in the crystalline case than it is for the isolated chain, and (ii) the electron and the hole are allowed to be spread over several neighboring polymer chains in the crystalline phase. Both effects increase the average distance between the electron and the hole and thereby reduce the ex-

citon binding energy. We calculate this binding energy to be only 0.05 eV for both *a*–PA and *n*–PA. We believe that the qualitative arguments given above do not only apply for trans-polyacetylene, but quite generally for the whole class of conducting polymers and oligomers. Moreover, the details of the inter-chain (or inter-molecular) interaction determine the actual values of the exciton binding energies as we have also seen from the comparison of the two phases *a*–PA and *n*–PA. Consequently, we believe that it is not sufficient to treat the inter-chain interactions in the screening only as has been suggested by VAN DER HORST and co-workers [34, 39]. One should also take into the modified band structure (band splittings) and wave functions. For the future, it will be highly desirable to obtain the quasi-particle spectrum in an *ab initio* manner, for instance by performing a GW calculation, instead of simply shifting the conduction bands rigidly upward. Thereby it will be possible to obtain the absolute energetic positions of the excited states, and not only the exciton binding energies.

Chapter 8

Pressure Studies

8.1 Motivation and Methodology

This chapter deals with the investigation of the electronic, optical and structural properties of molecular crystals consisting of conjugated molecules. Such systems are interesting materials both for fundamental research as well as for applications. For instance, organic solid state injection lasers [16], field effect transistors [13], super-conducting devices [15] as well as photo-voltaic cells [12] have been realized on the basis of such molecular crystals. Understanding the crystal and molecular structure of the active materials is of vital importance, since these aspects critically influence their electro-optical properties. The goal of this chapter is to investigate the role of intermolecular interactions on the electro-optical properties of conjugated molecules. To this end, we study the changes in the electronic, optical and structural properties of the molecular crystals induced by application of high pressure. We achieve this by a combined experimental[1] and theoretical investigation consisting of the following steps:

(i) Experimental determination of the pressure-dependent lattice constants by X-ray diffraction measurements.

(ii) Refinement of internal structural parameters such as the molecular orientation from the diffraction patterns if allowed for by the quality of the spectra.

(iii) Minimization of the total energy within DFT for a given set of lattice parameters by optimizing all internal structural degrees of freedom, involving (a) molecular orientation as well as (b) bond lengths and angles.

[1]The work presented in this chapter is part of a joint research project with the Institute for Solid State Physics of the University of Technology, Graz. The measurements at HASYLAB (Hamburg, Germany) have been conducted by G. Heimel, M. Oehzelt, and R. Resel from the University of Technology, and by K. Weinmeier and myself from the University of Graz.

(iv) Determination of the electronic band structure for the fully relaxed crystal structures in terms of Kohn-Sham energies.

(v) Computation of the optical properties in the independent quasi-particle approximation for the optimized geometries.

The organization of this chapter follows the prescription given above, exemplified for two prototypical conjugated molecular crystals, namely, biphenyl (2P) and *para*-terphenyl (3P). We note that some of the results presented in this chapter have already been discussed in the publications appended to this thesis. We will refer to those articles with [P–1], [P–2], ... according to the List of Papers given on page 161.

8.2 Structural Properties

8.2.1 Lattice Constants

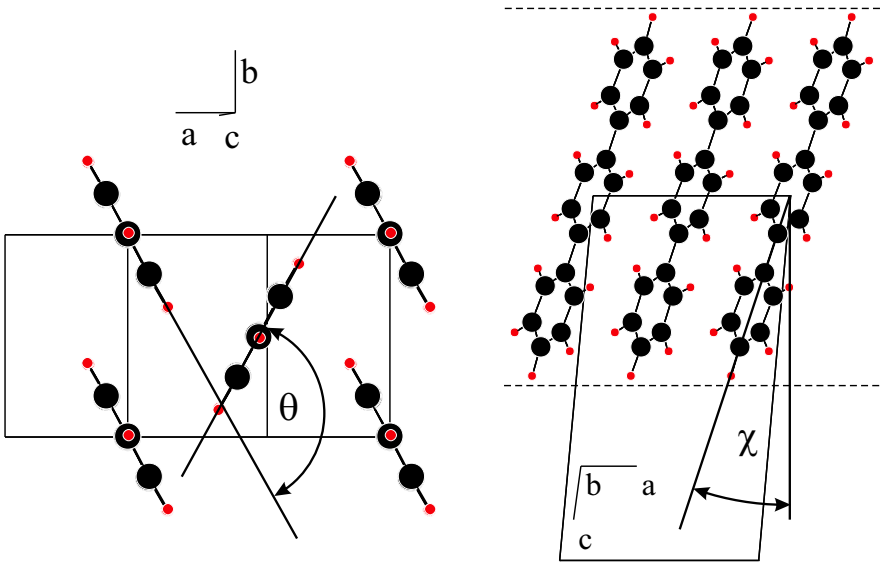

Figure 8.1: The crystal structure of oligo-phenylenes exemplified for 3P. The left panel is a projection perpendicular to the molecular layers showing the herring-bone angle θ, whereas the right panel is a side-view of such a layer displaying the definition of the setting angle χ.

At room temperature and ambient pressure, biphenyl (2P), $C_{12}H_{10}$ and *para*-terphenyl (3P), $C_{18}H_{14}$, both crystallize in a monoclinic crystal structure with the space group $P2_1/a$ [107, 108]. This structure represents the so-called *herring-bone* arrangement which is very common for (almost) all planar rod-like molecules.

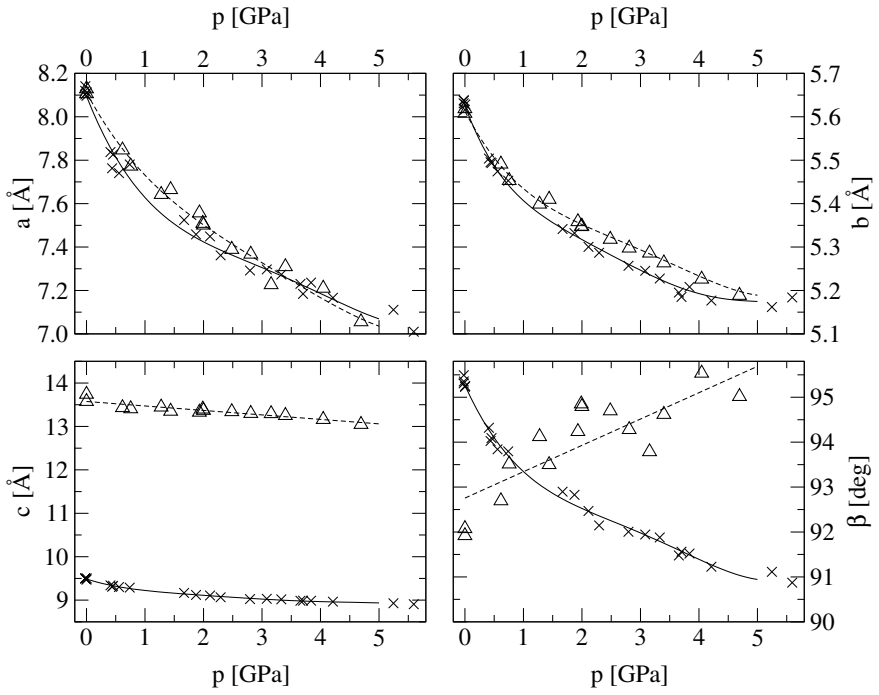

Figure 8.2: The lattice constants a, b, c and the monoclinic angle β of 2P (crosses) and 3P (triangles) as a function of pressure. The data has been extracted from X-ray diffraction experiments under pressure. The full (dashed) lines are polynomial fits to the 2P (3P) data according to Table 8.1.

The oligo-phenylene molecules form layers aligned parallel to the ab plane. The normal vectors of the molecular planes of the two inequivalent molecules enclose the herring-bone angle θ, and the molecular axis is at an angle χ with respect to the c^* axis. The molecular arrangement and the definition of the two angles θ and χ is also illustrated in Figure (8.1).

The pressure dependent lattice parameters of 2P and 3P are determined from X-ray diffraction experiments. These measurements have been performed by energy dispersive scattering at the beam-line F3 at HASYLAB, Germany. Crystalline 2P and 3P powder has been enclosed in a diamond anvil cell, the applied pressure is determined by using sodium chloride as a pressure calibrant. The diffraction pattern is measured in steps of approximately 0.5 GPa up to a maximum pressure of 6 GPa, where two experimental series are carried out for each material. An example for such a diffraction pattern of 3P can be found in [P–7]. By fitting the diffraction patterns to the $P2_1/a$ space group, the lattice parameters a, b, c and the monoclinic angle β are obtained. Unfortunately, the low energy resolution of the spectra did not allow for a Rietveld refinement of the internal structural parameters such as the molecular orientation. The results are displayed in Fig. (8.2). We have also parameterized the pressure dependence of the lattice constants in

Table 8.1: Parameterization of the pressure dependence of the lattice constants for 2P and 3P valid for pressures below 5 GPa. The experimental data for a, b, c and β is fitted to a polynomial expansion according to $d(p) = \sum_n d_n p^n$, where p denotes the pressure in GPa and d is any of the lattice parameters a, b, c or β.

			2P	
	a [Å]	b [Å]	c [Å]	β [deg]
d_0	8.095	5.626	9.487	95.3
d_1	−0.679	−0.364	−0.440	−2.9
d_2	0.261	0.205	0.251	1.2
$d_3 \times 10^{-2}$	−5.203	−7.051	−9.043	26.3
$d_4 \times 10^{-2}$	0.376	1.170	1.605	2.1
$d_5 \times 10^{-3}$	0.0	−0.721	−1.074	0.0
			3P	
	a [Å]	b [Å]	c [Å]	β [deg]
d_0	8.112	5.613	13.575	92.8
d_1	−0.504	−0.261	−0.103	0.6
d_2	0.151	0.104	0.0	0.0
$d_3 \times 10^{-2}$	−3.050	−2.309	0.0	0.0
$d_4 \times 10^{-3}$	2.369	1.867	0.0	0.0

terms of polynomial fits, which are listed in Table 8.1. The strongest effect is found on a, which reduces by 1 Å for both 2P and 3P upon going from ambient pressure to 5 GPa. The equivalent changes on b and c are smaller by roughly a factor of 2. Whereas the monoclinic angle β decreases by 4° in 2P, it increases by approximately 3° in 3P. It might be surprising that the monoclinic angle β shows an opposite behavior for 2P and 3P, in particular when looking at the similarities in the pressure dependence of a, b and c. We point out that also in the series of oligo-phenylenes at *ambient* pressure there is no clear trend of β as a function of oligomer length. This is because β depends very sensitively on the details of the interlayer packing, and is therefore not a smooth function of oligomer length. This might also explain the opposite sign in the slope of the pressure dependence of β in 2P and 3P, respectively.

The pressure dependence of the unit cell volume which evidently follows from the pressure dependence of the lattice parameters can be used to determine the bulk modulus B of the materials, according to

$$B = -V \frac{\partial p}{\partial V}, \tag{8.1}$$

where V is the volume and p denotes the pressure. Figure (8.3) shows the measured pressure of 2P and 3P versus the unit cell volume. In addition to the data

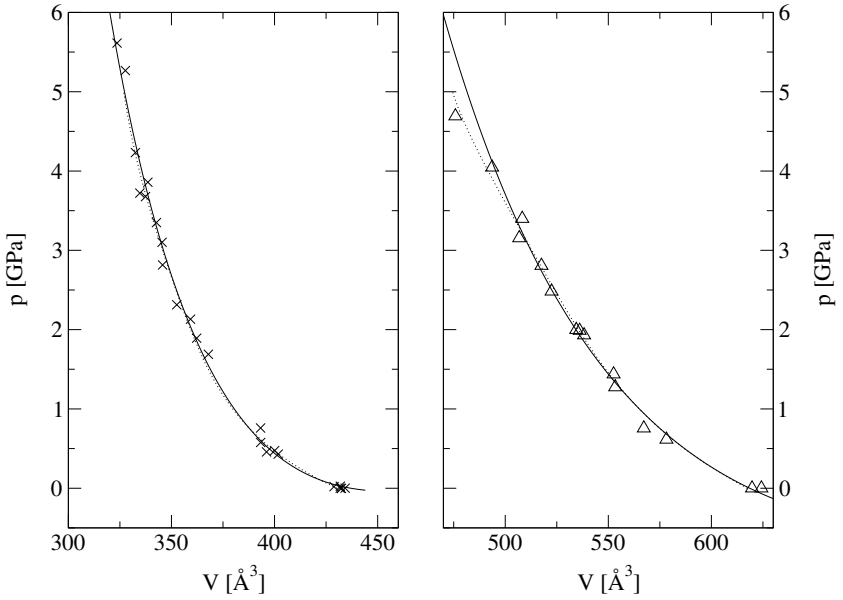

Figure 8.3: Pressure p as a function of unit cell volume V for 2P (left panel) and 3P (right panel). Symbols correspond to the measured data, while the full lines represent the best fit according to the equation of state (8.2). The dotted lines follow from the polynomial fits for the lattice parameters according to Table 8.1.

points (symbols) two different fits are displayed. The dashed lines are obtained by calculating the unit cell volume using the polynomial expansions of the lattice parameters as listed in Table 8.1, whereas the full lines are fits according to an equation of state as suggested by Birch [109]

$$\begin{aligned} p(V) &= \frac{3}{8}B_0(3B'-16)\left(\frac{V_0}{V}\right)^{\frac{5}{3}} - \frac{3}{4}B_0(3B'-14)\left(\frac{V_0}{V}\right)^{\frac{7}{3}} \\ &+ 9B_0(B'-4)\left(\frac{V_0}{V}\right)^{3}. \end{aligned} \tag{8.2}$$

Here, B_0 denotes the bulk modulus at zero pressure, B' its pressure derivative, and V_0 the unit cell volume at ambient pressure. The best fit to the data points for 2P (3P) yields $V_0 = 435.8\,(618.6)$ Å^3 , $B_0 = 2.4\,(7.7)$ GPa, and $B' = 24.1\,(8.1)$. Using Eq. (8.2) it is straight forward to compute the bulk modulus as a function of pressure according to the definition (8.1). The results (full lines) are displayed in Fig. (8.4) together with data from the literature (circles) [106]. In addition to the fit according to the equation of state (8.2), we have also included the bulk modulus as obtained from a simple polynomial fit of the lattice constants (dotted line). We notice that the latter fit produces unphysical oscillations of the bulk modulus as a function of pressure. On the other hand, the bulk modulus calculated from the equation of state agrees well with the previously measured data.

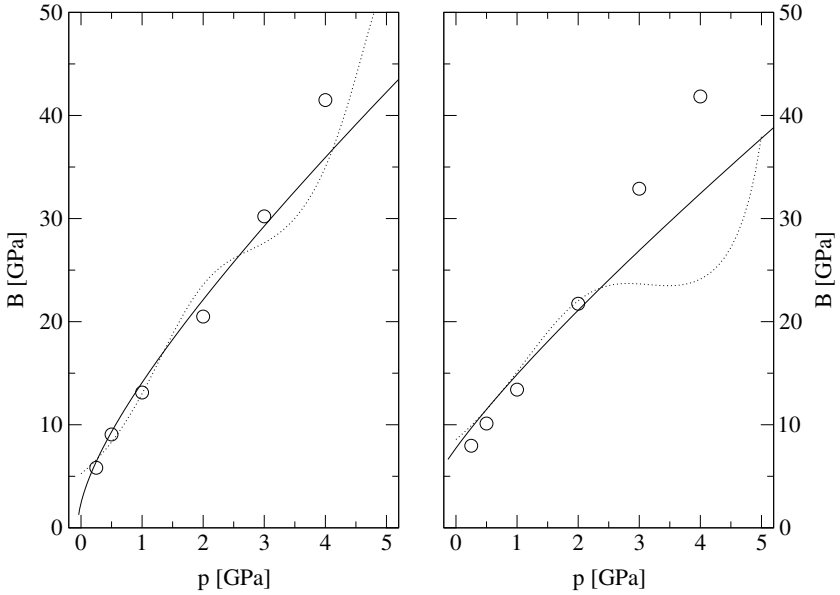

Figure 8.4: The bulk modulus B versus pressure p for 2P (left panel) and 3P (right panel). The full and dotted lines, respectively, follow from the experimental volume dependence through a fit according to the equation of state (8.2) and a polynomial fit. The symbols are experimental data taken from [106].

The discrepancies at higher pressures are within the experimental error bars. So far we have looked only at *external* structural parameters, such as the lattice parameters or the volume, but we do not know yet how the *internal* structure, determined by the molecular orientation, and the bond lengths and angles, is modified under pressure. Since it is not possible to refine these properties from the 2P and 3P diffraction patterns, we will compute the molecular orientation and geometry by total energy minimizations.

8.2.2 Molecular Arrangement and Bond Lengths

In order to reduce the number of required basis functions, all calculations presented in this and the subsequent sections have been performed with the APW+lo basis set of the WIEN97 code as discussed in Chapter 5. We have used the following parameters during the self-consistency cycles for all 2P and 3P computations. The muffin-tin radii of C and H, respectively, have been set to 1.29 and 0.75 Bohr, and an $RK_{\max}$ value of 3.0 has been used. For the C atom, this amounts to a value of 5.2 for $RK_{\max}(C)$. The summations over the BZ have been carried out by using 12 **k** points and utilizing the tetrahedron method. If not stated differently, we have treated exchange and correlation effects by a GGA potential due to Perdew and Wang [110].

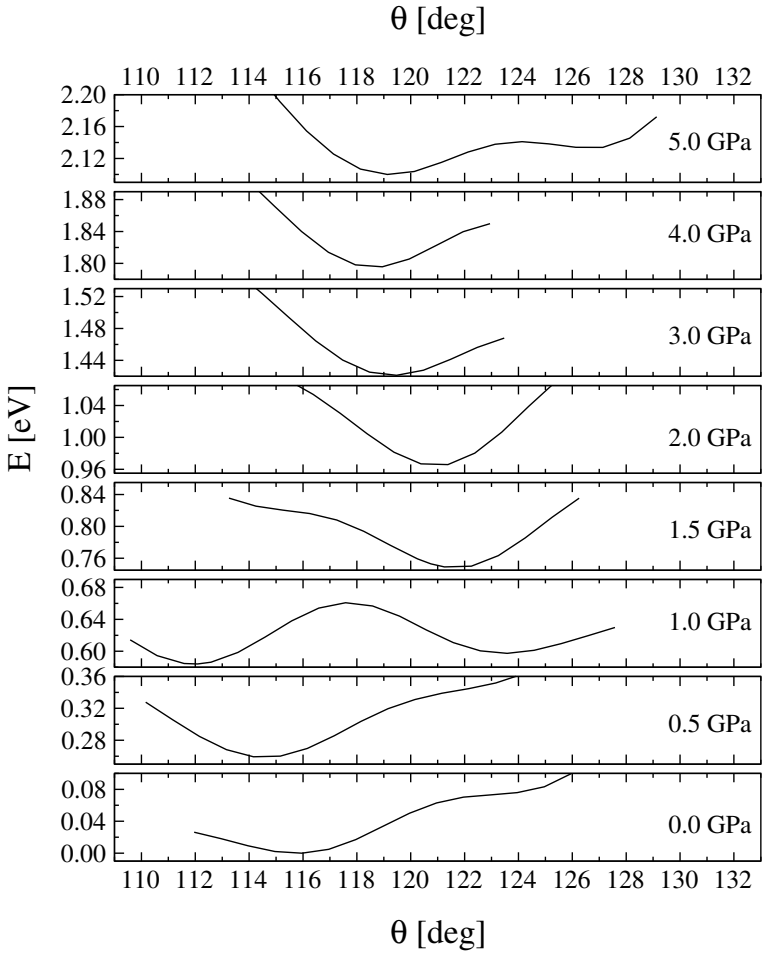

Figure 8.5: Total Energies E in 2P as a function of the herring-bone angle θ for a number of pressure points. The origin of the energy scale has been shifted to the energy minimum of the 2P crystal structure at 0 GPa.

The optimum molecular geometry can be obtained by simply minimizing the forces acting on the nuclei, thereby also optimizing the total energy. However, such a scheme only works well for the *intra*-molecular structure, that is for the bond lengths and angles, while it is not practicable for a determination of the molecule's *orientation* within the unit cell. Therefore, we optimize the bond lengths and angles in a first step by utilizing the atomic forces, where the molecules are forced to be planar due to symmetry. The planarity of the molecules is, however, no real restriction for the pressure region we are interested in here, since we have shown that the application of a moderate pressure of roughly 0.5 GPa is sufficient to planarize the molecules [P–2]. In a second step, we minimize the total energy of the crystal with respect to the molecular orientation for *fixed* bond lengths and angles. To this end, we define two angles describing the molec-

Table 8.2: Calculated herring-bone angle θ and setting angle χ of biphenyl (2P) and terphenyl (3P) as a function of pressure. In addition, the zero pressure values as obtained from single crystal structure resolutions (exp.) for 2P [107] and 3P [108] are given.

	2P		3P	
p [GPa]	θ [deg]	χ [deg]	θ [deg]	χ [deg]
0.0	116.0	15.7	91.3	17.6
0.5	114.2	18.7		
1.0	112.1	17.2	114.0	18.7
1.5	121.3	18.2		
2.0	121.4	18.0	121.1	18.3
3.0	119.5	17.8	120.0	18.7
4.0	119.0	19.6	127.8	19.6
5.0	119.1	19.1	125.1	19.7
exp.	112.5	17.1	111.6	17.6

ular orientation. The herring-bone angle θ is the angle between the two normal vectors of the molecular planes of the two inequivalent molecules, whereas the setting angle χ is given as the angle between the molecular axis and the normal to the ab plane (Fig. 8.1). Note that the molecular axis has been found to lie in the ab plane for 2P and 3P in the investigated pressure range, therefore 2 parameters are sufficient in order to determine the orientation of the molecule. The optimum orientation is obtained by finding the energy minimum of the 2-dimensional energy surface $E = E(\theta, \chi)$. Figure (8.5) shows the total energy of 2P as a function of the herring-bone angle θ for a number of pressure points between 0 and 5 GPa. We see that the optimum θ is no continuous function of pressure due to the double well structure of $E(\theta)$, as can be seen, for instance, at 1.0 GPa. Below this pressure the minimum is in the left potential well, whereas at higher pressures the optimum θ lies at the right part of the double well. The optimized molecular orientations of 2P and 3P given by θ and χ together with experimental values for ambient pressure are listed in Table 8.2. As a function of pressure, the herring-bone angle θ shows the strongest dependence. We find more planar configurations at higher pressures for 2P as well as for 3P in accordance with the large change in the lattice parameter a. While there is a more or less monotonous change for 3P, there is a jump in the herring-bone angle θ due to the double well structure of the energy surface (see Fig. 8.5). The setting angle χ is increased by only 3° and 2° up to 5 GPa for 2P and 3P, respectively. It should be noted that our calculations fail to reproduce the experimental zero pressure data taken from the single crystal solutions [107, 108], in particular the herring-bone angle θ for 3P can not be provided correctly by our calculations. For the follow-

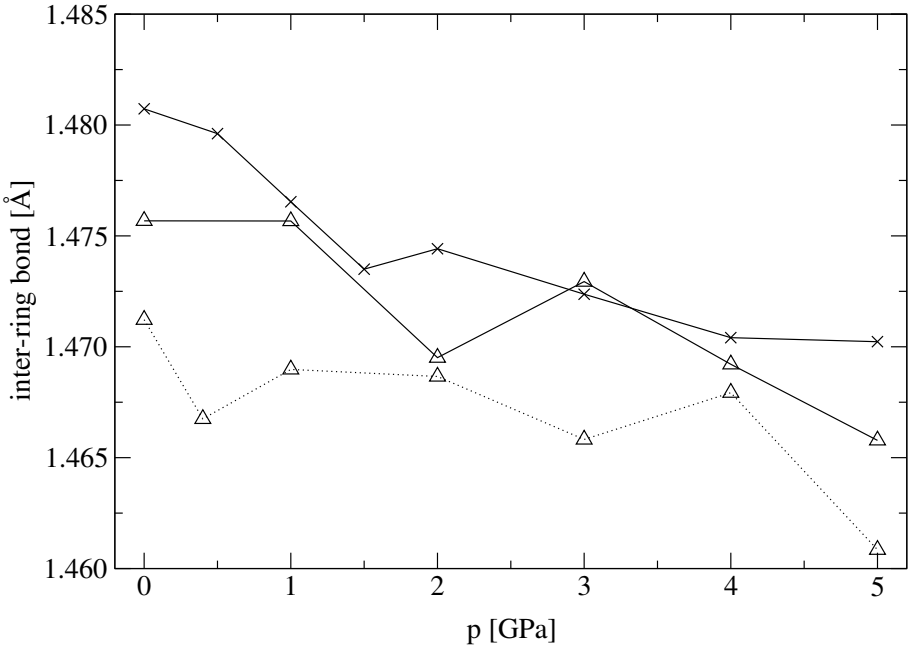

Figure 8.6: The calculated inter-ring bond length of 2P (crosses) and 3P (triangles) as a function of pressure. Data points connected with full lines (dashed lines) have been obtained by using a GGA (LDA) potential.

ing two reasons we believe that our results for θ and χ are still relevant. First, similar calculations for a molecular crystal of anthracene in the same pressure region have shown that the predicted changes in the molecular orientation agree well with experimental data [P–10]. Second, we think that the GGA we have used for the exchange-correlation potential produces an over-binding effect which results in the fact that the pressure scale given in Table 8.2 appears to be shifted by roughly 1 GPa. That is, the computed molecular orientation at 1 GPa agrees quite well with the experimental one at ambient pressure. Moreover, we note that the GGA potential is no improvement upon the LDA in this respect, and the LDA yields about the same molecular orientation as the GGA does [P–10].

Subsequent to the optimization of the molecular orientation, the internal molecular geometry (bond lengths and angles) is relaxed once again by making use of the atomic forces. We find, for instance, the length of the molecule defined by the end-hydrogens changes by noticeable 0.05 (0.09) Å for 2P (3P) when increasing the pressure from 0 to 5 GPa. This effect can be understood in terms of the rather soft inter-ring bonds as can be seen from a plot of the inter-ring bond length over pressure in Figure 8.6. Note, however, that the change in the layer thickness (compare Figure 8.1) given by $c \times \sin\beta$ is 0.52 (0.59) Å for 2P (3P), thus roughly an order of magnitude larger than the change in the length of the molecule. Consequently, the reduction of the layer thickness is mainly due to a

closer packing of the layers.

8.2.3 Total Energies and Bulk Moduli

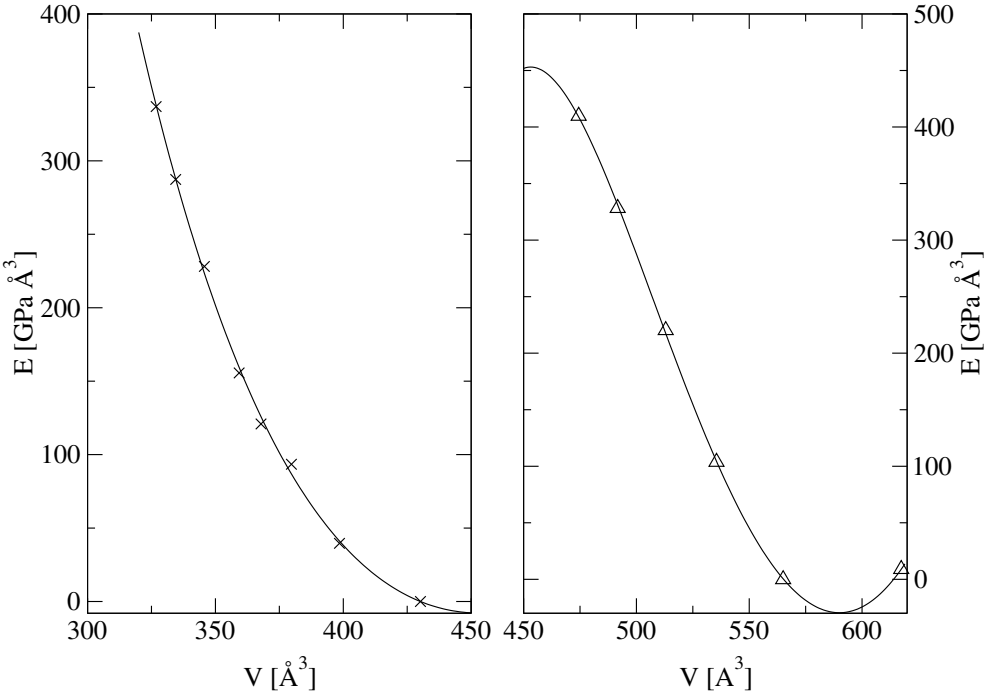

Figure 8.7: The total energy E of 2P (left) and 3P (right) over the volume V. Symbols correspond to the calculated values, whereas the lines are fits according to the equation of state (8.3). The origin of the energy scale has been shifted to the total energy at ambient pressure.

As a result of the geometry optimization for 2P and 3P presented in the previous section, we have available the total energies of the completely relaxed structures as a function of unit cell volume. This data can be utilized to obtain a theoretical value for the bulk modulus. To this end, we make a least squares fit of the calculated total energies E as a function of volume V to a form proposed by Birch [109]

$$E(V) = E_0 + \frac{9}{8} B_0 V_0 \left[\left(\frac{V_0}{V} \right)^{2/3} - 1 \right]^2 + \frac{9}{16} B_0 V_0 (B_0' - 4) \left[\left(\frac{V_0}{V} \right)^{2/3} - 1 \right]^3 . \quad (8.3)$$

Here, B_0 and V_0, respectively, denote the zero pressure bulk modulus and unit cell volume, and B_0' is the pressure derivative of the bulk modulus. The form of Eq. (8.3) is a third order expansion of the total energy [109], which has been

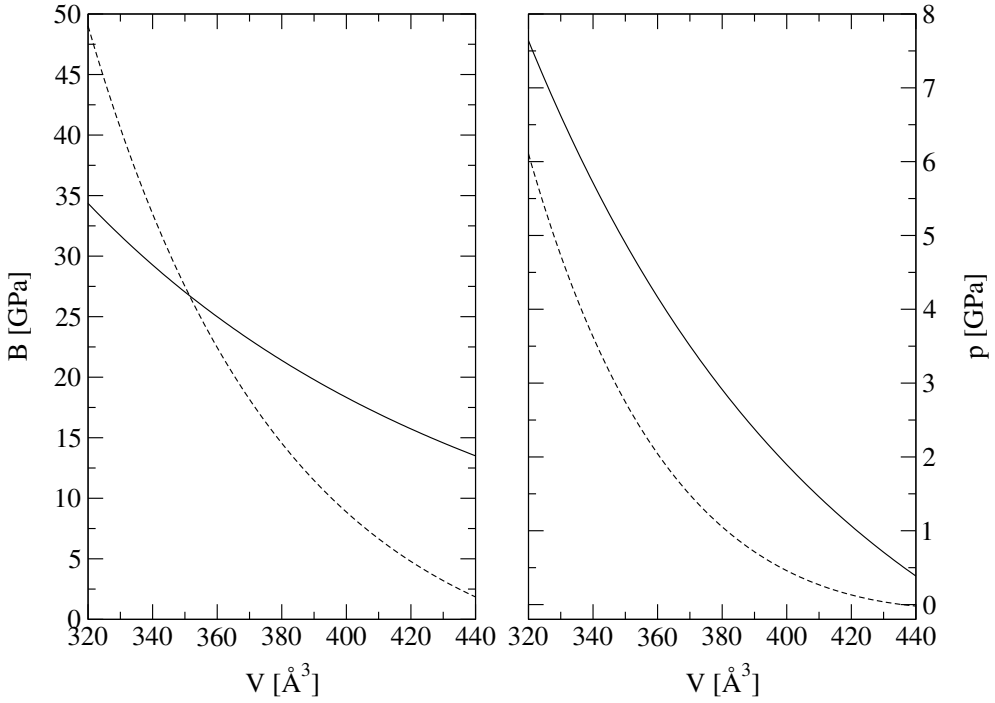

Figure 8.8: Comparison between experimental and theoretical results for the bulk modulus B (left) and the pressure p (right) as a function of the unit cell volume of 2P. The full lines are the theoretical results following from a fit of the calculated total energies using the equation of state, whereas the dashed lines are experimental data resulting from the measured volume under pressure.

proven to yield successful results for a majority of calculations. Fig. (8.7) displays the total energies of 2P and 3P versus unit cell volume as resulting from the complete relaxation of all internal structural parameters. The least squares fit to the data according to the equation of state (8.3) yields for 2P: $V_0 = 453.4$ Å^3, $B_0 = 12.2$ GPa, and $B_0' = 3.46$, whereas the fit does not produce reasonable values in the case of 3P. In Figure (8.8) we compare the computed bulk modulus for 2P with corresponding experimental values as obtained in Sec. 8.2.1. We notice, for instance, that the calculations overestimate the experimental bulk modulus at ambient pressure, while at 5 GPa the computations yield a too small value. We will discuss these findings in more detail in the last section of this chapter.

8.3 The Electronic Structure

The electronic band structures of oligo-phenylene molecular crystals at *ambient* pressure have already been discussed in some detail in previous publications [96, 111]. We have depicted the band structures and densities of states (DOS) for

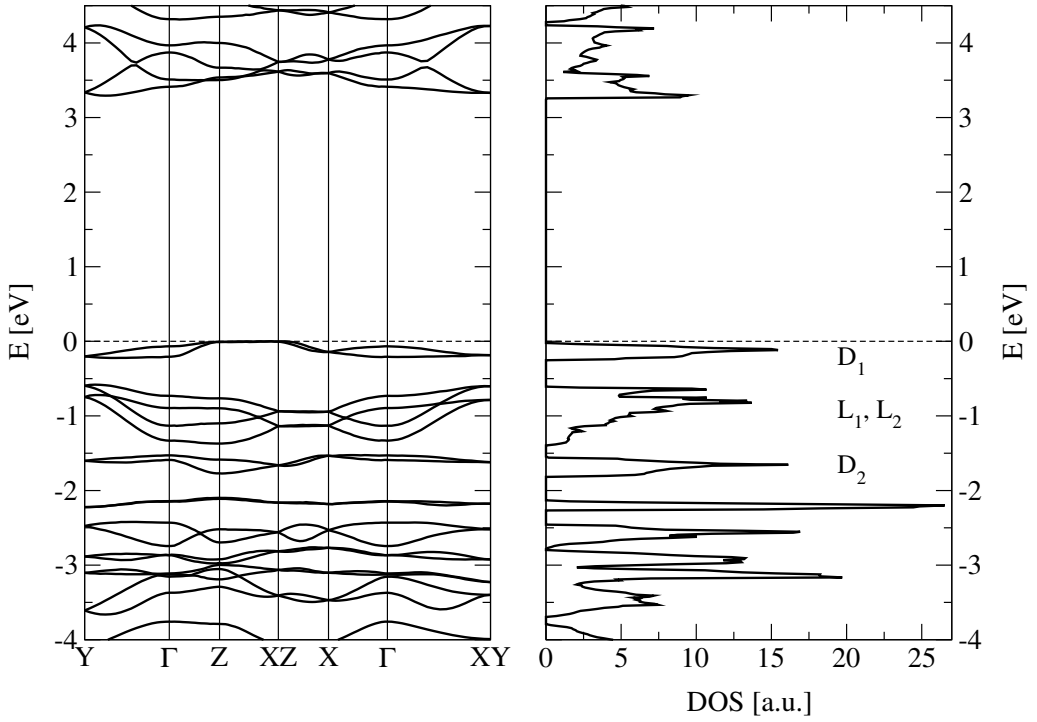

Figure 8.9: The electronic band structure (left) and the density of states (right) of 2P at ambient pressure. The energetic position of the localized (L) and de-localized (D) valence π bands is indicated.

2P at ambient pressure and at 5 GPa in Figures (8.9) and (8.10), respectively. The analogous plots for 3P have already been presented in [P–9]. All band structures are resulting from the Kohn-Sham energies and the band gap has not been corrected by including a scissors operator shift.

We observe a linear reduction of the band gap for 2P (3P) from 3.25 (2.71) eV with a pressure coefficient of -50 (-40) meV/GPa. The top valence bands and bottom conduction bands can be attributed to wave functions de-localized over the whole molecule, especially over the C atoms along the long molecular axis, while the lower lying valence bands and higher lying conduction bands are strongly localized on the off-axis C atoms of the molecule. The energetic positions of these *de-localized* (D_1 and D_2) and *localized* (L_1 and L_2) valence bands are indicated in Figure (8.9). The band dispersion is much weaker for the de-localized bands than it is for the localized ones.[2] This is due to the fact that in the herring-bone structure the localized wave functions get geometrically closer to those of the neighboring molecule than the de-localized ones do.

In order to further illustrate these circumstances we have depicted the wave

[2]Remember that the term de-localized refers to the wave function *within* one molecule, whereas the band dispersion is determined by the overlap *between* two neighboring molecules.

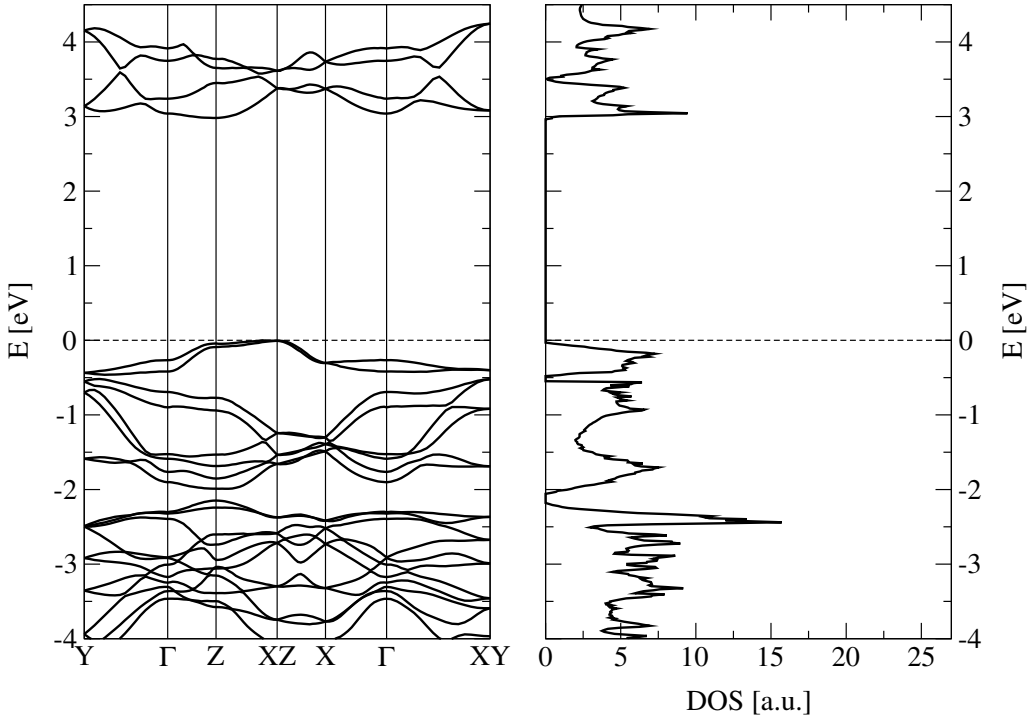

Figure 8.10: The electronic band structure (left) and the density of states (right) of 2P at 5 GPa.

functions of a de-localized and a localized valence state in a plane perpendicular to the molecular axis in Figure (8.11). Note that we have used the same scale for both types of wave functions. While the electron is more or less restricted to one molecule in the de-localized state, there is considerable overlap of the orbitals between neighboring molecules in the localized state. We think that the latter states are responsible for the formation of the herring-bone pattern, since the herring-bone arrangement maximizes the overlap of a π orbital at one molecule with corresponding π orbitals at the neighboring two molecules. On the other hand, the de-localized states which determine the transport and the low energy optical properties are little influenced by the crystalline environment. Therefore, we expect the oligo-phenylenes to exhibit poor carrier mobilities and to show similar optical properties as isolated molecules.

Similarly, we can understand that pressure affects the localized states more strongly than the de-localized ones. This can be seen from the comparison of Figures (8.9) and (8.10) for 2P and from [P–9] for 3P. Upon increasing the pressure from 0 to 5 GPa, the band width of the top valence bands grows from 0.23 to 0.45 eV for 2P, and from 0.20 to 0.32 eV for 3P, respectively, on the other hand the localized states' band width increases from 0.8 (1.0) to 1.5 (1.6) eV for 2P (3P). Concerning the lowest unoccupied bands we observe an interesting effect

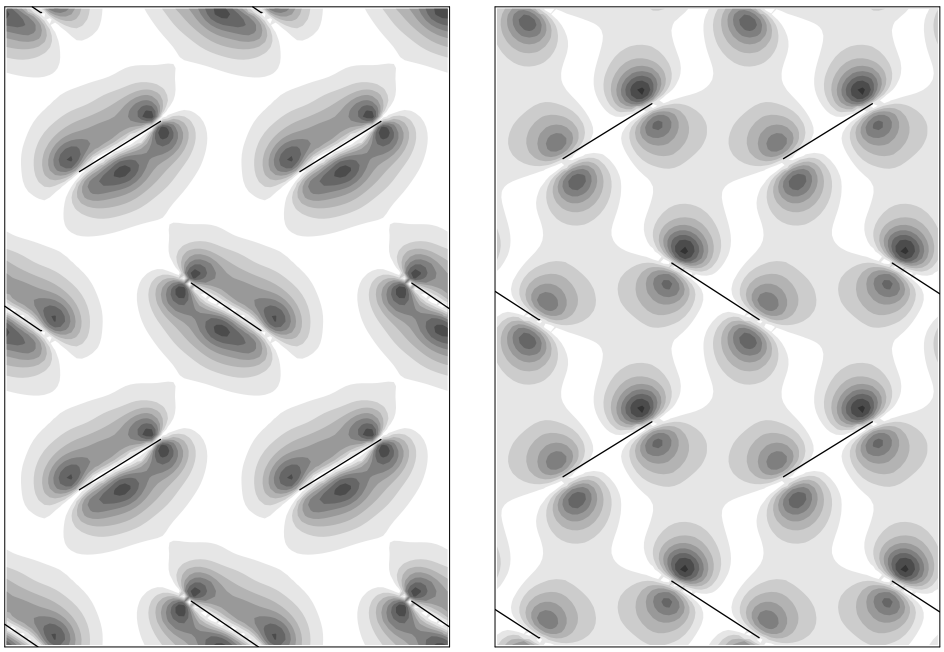

Figure 8.11: The absolute value of the wave functions of the de-localized (left) and localized (right) valence bands in a plane parallel to the *ab* plane. The projections of the molecules are indicated as lines in order to illustrate the herring-bone arrangement of the molecules.

under applied pressure. While at ambient pressure the lowest lying conduction band is of de-localized character, the localized state shifts below the former at higher pressures, and becomes the lowest conduction band. This is true for 2P as well as for 3P. This may result in a considerable increase of the electron mobility of oligo-phenylene crystals under pressure. Generally, the band dispersion perpendicular to the long molecular axis is much stronger than it is parallel to the molecules. Thus, the intermolecular interaction is much stronger within one layer than it is between layers.

8.4 Optical Properties

We have calculated the imaginary part of the DF in the independent quasi-particle approximation according to Eq. (4.50). The optimized crystal structures of 2P and 3P as a function of pressure, as presented in Section 8.2.2, serve as input for the computation of the Kohn-Sham energies and transition matrix elements. For the summation over the BZ in Eq. (4.50) we use the tetrahedron method and a grid of 1120 **k** points. The results for 2P at 0 and 5 GPa are displayed in

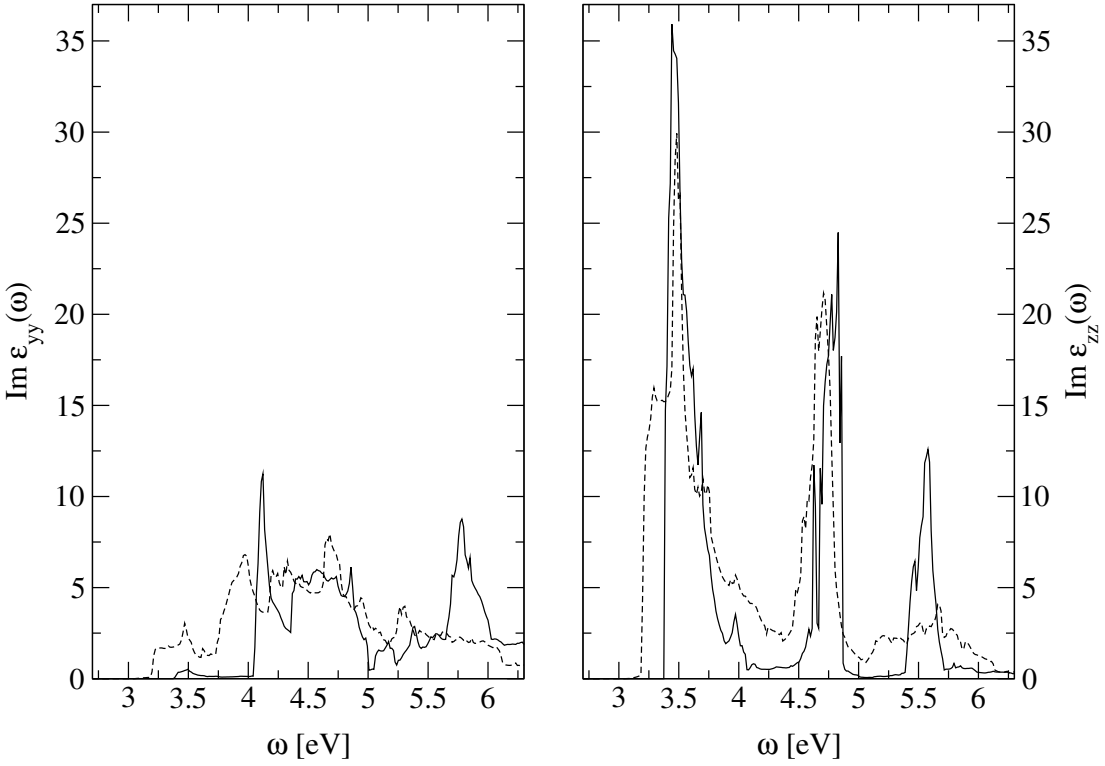

Figure 8.12: The dielectric function of 2P at 0 (full lines) and 5 (dashed lines) GPa. The left and right panels, respectively, display the yy and zz components of the imaginary part of $\epsilon(\omega)$, where the yy (zz) axis is perpendicular (parallel) to the molecular axis.

Figure (8.12), whereas the 3P spectra have already been discussed in [P–9]. Note that we did not include a scissors shift in the results displayed in Figure (8.12). The left panel shows the yy components of the imaginary part of the DF for 0 and 5 GPa, whereas the right panel displays their zz components. Because the molecular axis lies in the ac plane and is approximately parallel to the c axis, we notice that the yy (zz) component describes absorption processes for light polarized perpendicular (parallel) to the molecular axis. A more detailed explanation of how to obtain the absorption coefficient from the dielectric tensor is given in [96].

The strong zz-polarized, lowest energy absorption feature is formed by transitions from de-localized to de-localized bands. The transitions involving localized bands and de-localized states, on the other hand, are yy-polarized. The general pressure effect on the dielectric function is (i) a broadening due to increased band dispersions, and (ii) a red shift due to (symmetric) band broadening of both valence and conduction bands. Both effects are clearly observed in Figure (8.12). The red shift of the absorption is much more pronounced on the yy-component

(0.7 eV) as compared to the zz component (0.2 eV) since the localized bands involved in the yy polarized transition are far more sensitive to the pressure induced increase in intermolecular interaction. Similar findings have been made for 3P in [P–9]. It is interesting to check whether the observed red shifts in the absorption are due to changes of the molecular geometry (*intra*-molecular) or due to the enhanced *inter*-molecular interactions. To this end, we have performed single molecule calculations[3] for the 2P and 3P molecules extracted from the fully optimized crystal structures [P–9]. By this we obtain optical transition energies versus pressure for isolated molecules having the bond lengths and angles as in the corresponding crystalline environment but *without* including intermolecular effects. We find that the pressure induced changes on these transition energies are negligibly small both for 2P and 3P [P–9]. From this we conclude that the pressure effect seen in Figure (8.12) is purely intermolecular, while the pressure induced changes on the internal molecular geometry do not significantly alter the optical response of the system.

8.5 Discussion and Outlook

In this chapter, we have presented the pressure dependent lattice parameters of 2P and 3P up to 5 GPa as resulting from diffraction measurements at a synchrotron beam-line at HASYLAB, Germany. These serve as input for total energy and atomic force calculations. We have used the new APW+lo basis set implemented in the WIEN97 code, which has proven to save computer time [90]. The internal molecular geometry as well as the orientation of the molecules within the unit cell follow from the minimization of the total energies and atomic forces. The dominating effects under pressure are (i) an increase of the herring-bone angle resulting in a more planar arrangement of the molecules, and (ii) a reduction of the inter-ring bond length thereby enhancing the π-conjugation of the molecules. Unfortunately, we can not directly compare these theoretical predictions to experiment, since the poor quality of the diffraction patterns did not allow for a Rietveld refinement of the internal structural parameters. We have, however, confidence in our results since similar calculations for anthracene molecular crystals under pressure have proven to describe the molecular orientation correctly [P–10].

As a second result, we have determined the bulk modulus both experimentally as well as theoretically. While the experimental values agree well with previously measured data, the computations for 2P, for instance, considerably overestimate the bulk modulus at ambient pressure, and yield 25% too small values at 5 GPa. One is lead to the conclusion that this failure is due to the wrong long-range behavior of the exchange-correlation functionals in the local density or in the

[3]These computations have been performed by Georg Heimel using the GAUSSIAN98 code.

generalized gradient approximations. In particular, both the LDA and the GGA do not contain van der Waals interactions, though the over-binding effect of the LDA and – to a less extent – the GGA partly compensates for the missing dispersion forces. We believe that the LDA as well as the GGA are accurate enough in order to describe the optimized structure but that the bulk modulus, given by the second derivative of the total energy, is more sensitive to the details of the exchange-correlation (xc) potential and therefore requires a more sophisticated xc-functional. We think, however, that we have to dismiss the picture of *pure* van-der-Waals-crystals, which has been discussed in the literature for oligo-phenylenes as well as for other molecular crystals, such as oligo-thiophenes or polyacenes. This is evidenced, on the one hand, by the good agreement of structural parameters obtained with the LDA and GGA when compared to experiment [P–10], and, on the other hand, by the considerable band dispersions found in the band structures. In fact, we believe the bonding character of this overlap to be – at least partly – responsible for the formation of the herring-bone structure.

Concerning the optical properties discussed in this chapter, we find a red shift and a broadening of the transitions under pressure. Analysis shows that these effects are of purely inter-molecular origin, and changes in the molecular geometry are of less importance in the high pressure regime up to 5 GPa. This is somewhat opposite to what has been found for the low pressure region up to say 0.5 GPa, where the planarization of the oligo-phenylene molecules is the most dominating effect seen in the optical absorption [P–2]. It would of course be highly interesting to compare our results for the dielectric function under pressure to experimental results. These measurements are currently under progress and we are looking forward to them since a comparison with experimental results could decide whether the pressure effects on the DF can be understood within the independent quasi-particle approach used in this chapter, or electron-hole correlations are important. Nevertheless, we plan for the future to investigate the excitonic structure also for these molecular crystals, in order to determine such quantities as excitonic binding energies or singlet-triplet splittings as a function of pressure.

Appendix A

Mathematical Tools

A.1 Fourier Series Conventions of Lattice Periodic Functions

A.1.1 Local Functions

Consider a function $f(\mathbf{r})$ which has the lattice periodicity of the crystal, such as the electron density or the crystal potential

$$f(\mathbf{r}+\mathbf{R}) = f(\mathbf{r}), \tag{A.1}$$

where $\mathbf{R}$ denotes any direct lattice vector. Then, the function f may be expanded in the Fourier series

$$f(\mathbf{r}) = \frac{1}{\Omega}\sum_{\mathbf{G}} f_{\mathbf{G}} e^{i\mathbf{G}\mathbf{r}}, \tag{A.2}$$

with the Fourier coefficients given by

$$f_{\mathbf{G}} = \int_{\Omega} \mathrm{d}^3 r f(\mathbf{r}) e^{-i\mathbf{G}\mathbf{r}}. \tag{A.3}$$

The summation runs over the reciprocal lattice vectors $\mathbf{G}$, and the integration is over the crystal volume Ω. If the function f, however, does not have the periodicity of the lattice, such as an external perturbation, we have to include a sum over the a vector $\mathbf{q}$ from the first Brillouin zone, and write the Fourier expansion of f in the way

$$f(\mathbf{r}) = \frac{1}{\Omega}\sum_{\mathbf{q}}^{\mathrm{BZ}}\sum_{\mathbf{G}} f_{\mathbf{G}}(\mathbf{q}) e^{i(\mathbf{q}+\mathbf{G})\mathbf{r}} \tag{A.4}$$

$$f_{\mathbf{G}}(\mathbf{q}) = \int_{\Omega} \mathrm{d}^3 r f(\mathbf{r}) e^{-i(\mathbf{q}+\mathbf{G})\mathbf{r}}. \tag{A.5}$$

A.1.2 Nonlocal Functions

Response functions for crystalline systems are in general non-local functions of $\mathbf{r}$ and $\mathbf{r}'$ that are invariant, if *both* space variables are translated by a direct lattice vector $\mathbf{R}$, thus

$$f(\mathbf{r}+\mathbf{R},\mathbf{r}'+\mathbf{R}) = f(\mathbf{r},\mathbf{r}'). \tag{A.6}$$

We use the following convention for the Fourier expansions of functions $f(\mathbf{r},\mathbf{r}')$ with the property (A.6)

$$f(\mathbf{r},\mathbf{r}') = \frac{1}{\Omega}\sum_{\mathbf{q}}^{\mathrm{BZ}}\sum_{\mathbf{G}\mathbf{G}'} e^{i(\mathbf{q}+\mathbf{G})\mathbf{r}} f_{\mathbf{G}\mathbf{G}'}(\mathbf{q}) e^{-i(\mathbf{q}+\mathbf{G}')\mathbf{r}'} \tag{A.7}$$

$$f_{\mathbf{G}\mathbf{G}'}(\mathbf{q}) = \frac{1}{\Omega}\int_\Omega \mathrm{d}^3r \int_\Omega \mathrm{d}^3r' e^{-i(\mathbf{q}+\mathbf{G})\mathbf{r}} f(\mathbf{r},\mathbf{r}') e^{-i(\mathbf{q}+\mathbf{G}')\mathbf{r}'}. \tag{A.8}$$

The quantity $f_{\mathbf{G}\mathbf{G}'}(\mathbf{q})$ for a given $\mathbf{q}$ from the first Brillouin zone can be interpreted as a matrix where the matrix indices are reciprocal lattice vectors $\mathbf{G}$ and $\mathbf{G}'$.

A.2 Crystal Lattice Integrals and Summations

In this section, some useful integrals over the crystal volume or unit cell, and some relations involving summations over lattice vectors will be given.

$$\int_\Omega \mathrm{d}^3r e^{i\mathbf{q}\mathbf{r}} = \Omega\,\delta_{\mathbf{q},\mathbf{0}} \tag{A.9}$$

$$\int_{\Omega_0} \mathrm{d}^3r e^{i\mathbf{G}\mathbf{r}} = \Omega_0\,\delta_{\mathbf{G},\mathbf{0}}. \tag{A.10}$$

Here, Ω and Ω_0, respectively, denote the crystal and the unit cell volume, and $\mathbf{q}$ and $\mathbf{G}$ are vectors from the first Brillouin zone, and reciprocal lattice vectors, respectively. The summation over direct lattice vectors $\mathbf{R}$ of the plane wave $e^{i\mathbf{q}\mathbf{R}}$ is given by

$$\sum_{\mathbf{R}} e^{i\mathbf{q}\mathbf{R}} = \frac{\Omega}{\Omega_0}\sum_{\mathbf{G}} \delta_{\mathbf{q},\mathbf{G}}, \tag{A.11}$$

where the factor Ω/Ω_0 is just the number of unit cells in the crystal. Note that the summation over $\mathbf{G}$ is only non-zero if $\mathbf{q}$ is equal to zero, provided that $\mathbf{q}$ is from the first Brillouin zone.

A.3 Inversion of a Block Matrix

A matrix M has the block structure

$$M = \begin{pmatrix} A & P \\ Q & R \end{pmatrix}. \tag{A.12}$$

Provided that A and R are non-singular matrices, the inverse matrix M^{-1} is given by

$$M^{-1} = \begin{pmatrix} W & X \\ Y & Z \end{pmatrix}, \tag{A.13}$$

where the matrices W, X Y and Z are determined by the following set of equations

$$\begin{aligned} W &= (A - PR^{-1}Q)^{-1} && \text{(A.14)} \\ X &= -WPR^{-1} && \text{(A.15)} \\ Y &= -R^{-1}QW && \text{(A.16)} \\ Z &= R^{-1} + YW^{-1}X. && \text{(A.17)} \end{aligned}$$

In the special case where the matrix Q is zero we obtain a much simplified structure of the inverse matrix M^{-1} given by

$$M^{-1} = \begin{pmatrix} A^{-1} & -A^{-1}PR^{-1} \\ 0 & R^{-1} \end{pmatrix}. \tag{A.18}$$

Appendix B

Computational Details

B.1 Convergence of Electron-Hole Matrix Elements

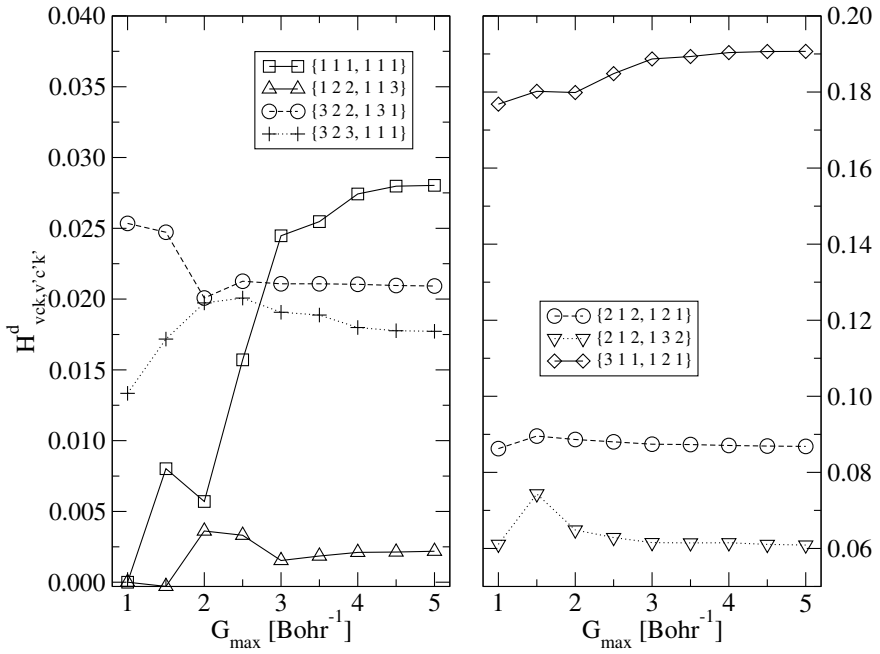

Figure B.1: The convergence of the electron-hole interaction matrix elements for LiF with respect to $G_{\max}$.

This section supplements Sec. 6.4.3 where we have discussed the dependence of the electron-hole matrix elements $H^{dir}_{vc\mathbf{k},v'c'\mathbf{k}'}$ on the cut-off parameters $\mathbf{G}_{\max}$ and $RK_{\max}$. There we have presented the convergence properties for Si. For

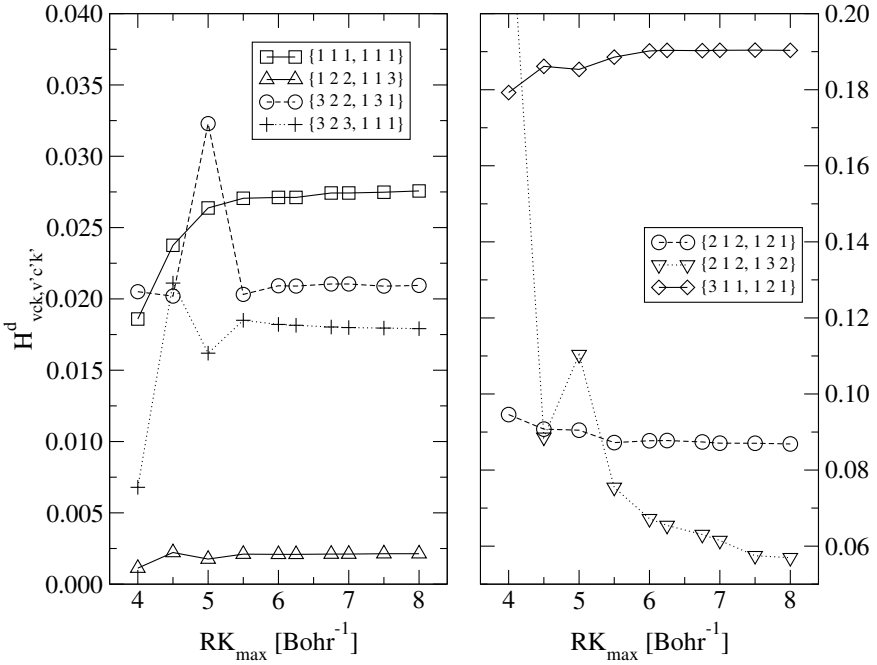

Figure B.2: The convergence of the electron-hole interaction matrix elements for LiF with respect to $RK_{\max}$.

completeness we also give the corresponding convergence test for LiF as well as for PA. For LiF, Figs. (B.1) and (B.2) display the dependence of some selected elements of $H^{dir}_{vc\mathbf{k},v'c'\mathbf{k}'}$ on $\mathbf{G}_{\max}$ and $RK_{\max}$, respectively. The analogous results for PA are presented in Figs. (B.3) and (B.4).

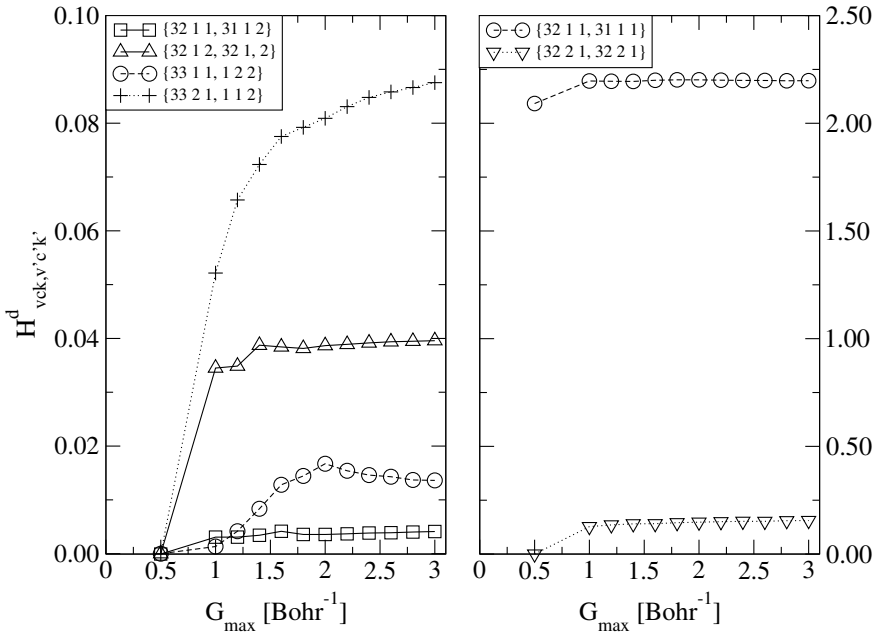

Figure B.3: The convergence of the electron-hole interaction matrix elements for PA with respect to $G_{\max}$.

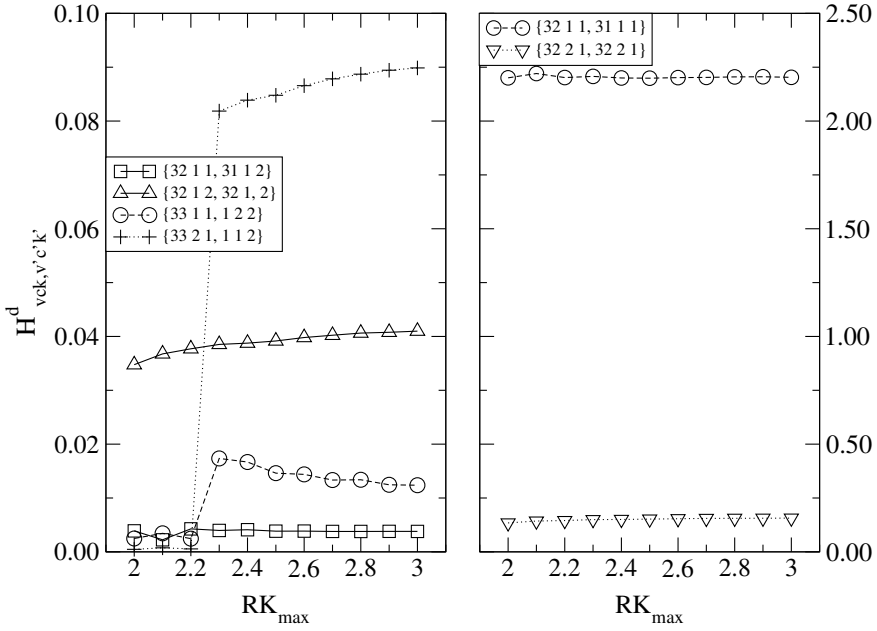

Figure B.4: The convergence of the electron-hole interaction matrix elements for PA with respect to $RK_{\max}$.

B.2 Convergence of the Macroscopic DF

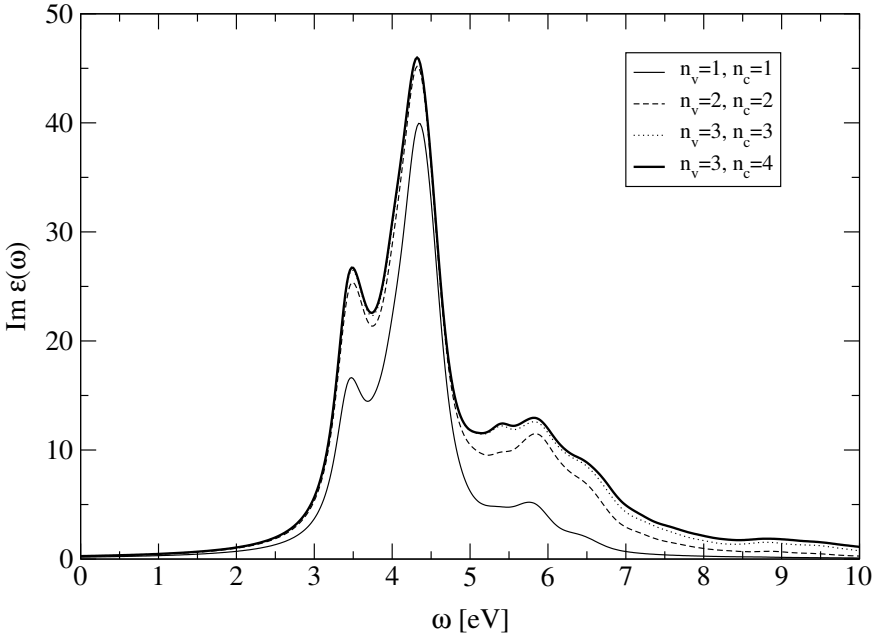

Figure B.5: The convergence of the dielectric function of Si with respect to the number of valence bands N_v and conduction bands N_c included in the exciton description. The number of $\mathbf{k}$ points was set to 512.

This section supplements Sec. 6.4.4 where we have checked the convergence of the macroscopic DF $\epsilon_M(\omega)$ resulting from the solution of the BSE with respect to the number of valence and conduction bands N_v and N_c, and the size of the $\mathbf{k}$ grid $N_\mathbf{k}$. The results obtained for the insulator LiF have already been shown in Figs. (6.12) and (6.13). Here we present the convergence tests for Si and PA, respectively. The influence of the number of bands N_v and N_c included in the exciton description can be seen from Figs. (B.5) and (B.6) for Si and PA. For these calculations we have used $\mathbf{k}$ meshes of $N_\mathbf{k} = 8 \times 8 \times 8$ and $N_\mathbf{k} = 1 \times 1 \times 64$, respectively. The dependence of $\epsilon_M(\omega)$ for Si on the $\mathbf{k}$ grid, on the other hand, is shown in Fig. (B.7).

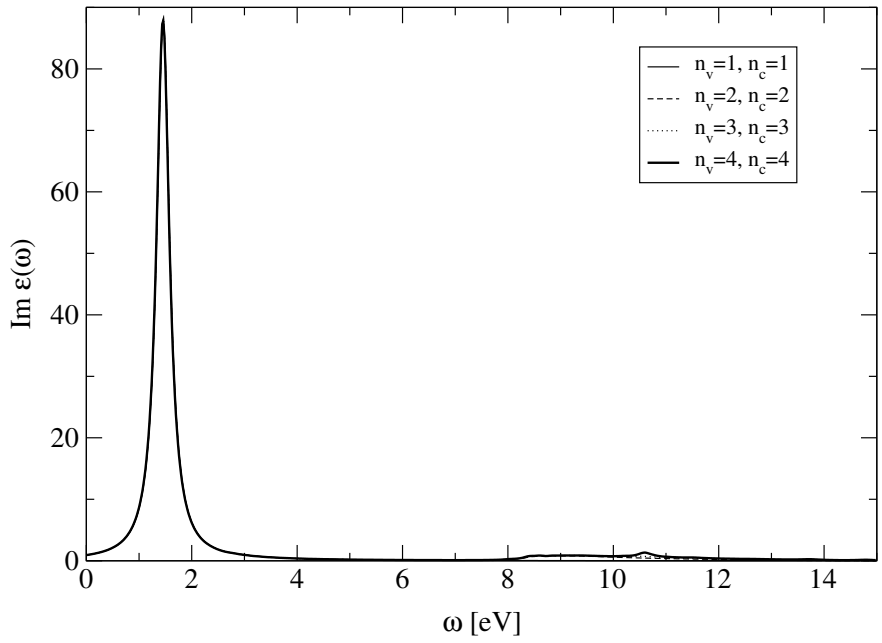

Figure B.6: The convergence of the dielectric function of PA with respect to the number of valence bands N_v and conduction bands N_c included in the exciton description. The number of **k** points was set to 32.

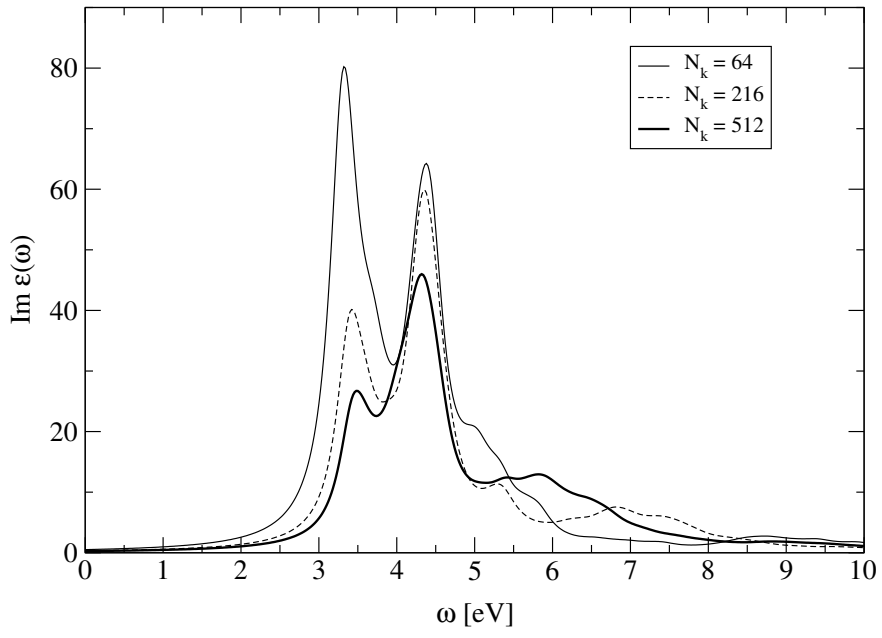

Figure B.7: The convergence of the dielectric function of Si with respect to the number of **k** points $N_{\mathbf{k}}$ used for the evaluation of the electron-hole interaction. The number of valence and conduction bands was set to 3 and 4, respectively.

B.3 Interpolation of the e-h-Kernel

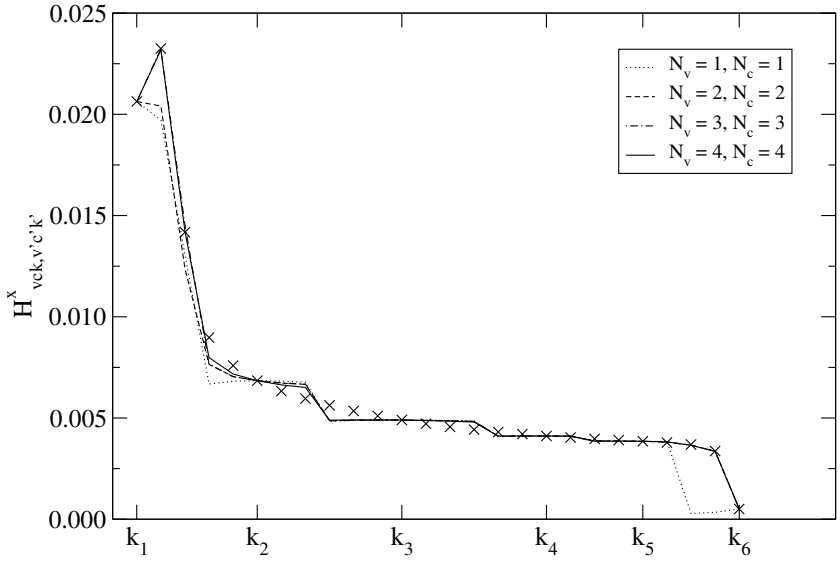

Figure B.8: Interpolation of exchange-matrix elements H^x in Si. Crosses (lines) denote the exact (interpolated) values, where N_v (N_c) is the number of valence (conduction) bands included in the expansion of wave functions. The vectors indicated at the x axis have been used as sampling points, for the interpolation. All vectors are along the [111] direction, and $\mathbf{k}_1 = \{\frac{1}{500}, \frac{3}{500}, \frac{5}{500}\}$ and $\mathbf{k}_6 = \{\frac{251}{500}, \frac{253}{500}, \frac{255}{500}\}$.

In Section 6.3.6 we have seen how we can interpolate the electron-hole interaction matrix elements from a coarse grid, which we denote by $\{\tilde{\mathbf{k}}, \tilde{\mathbf{k}}'\}$, to a denser mesh $\{\mathbf{k}, \mathbf{k}'\}$. By expanding the Bloch periodic parts of the wave functions at $\mathbf{k}$ and $\mathbf{k}'$ in terms of those at $\tilde{\mathbf{k}}$ and $\tilde{\mathbf{k}}'$, respectively, we were able to derive expressions (6.88–6.90) for the direct and exchange parts of the electron-hole kernel. Here, we will demonstrate the application of the these interpolation formulas for Si and PA. For Si, we have fixed one $\mathbf{k}$ point at $\mathbf{k} = \{\frac{1}{500}, \frac{3}{500}, \frac{5}{500}\}$ and varied the second vector $\mathbf{k}'$ starting from $\mathbf{k}' = \mathbf{k}$ to the zone boundary along the [111] direction. The *exact* results for the matrix elements $H^x_{vc\mathbf{k},v'c'\mathbf{k}'}$ and $C_{vc\mathbf{k},v'c'\mathbf{k}'}$ are given by the crosses in Figs. (B.8) and (B.9), where we have chosen both v and v' as the top valence, and c and c' as the lowest conduction bands, respectively. In addition to the exact results, we have plotted the *interpolated* values according to Eqs. (6.89) and (6.90). The four curves correspond to taking into account 1, 2, 3 or 4 conduction and valence bands in the expansion of the wave functions. The $\mathbf{k}$ vectors denoted at the x axis of the plot have been used as sampling points for the interpolation. Consequently, the exact and the interpolated values coincide at these points. We notice that the interpolation is clearly improved if more bands are included in the expansion of the wave functions though some aspects of the interpolation remain rather unsatisfactory. For instance, the interpolation

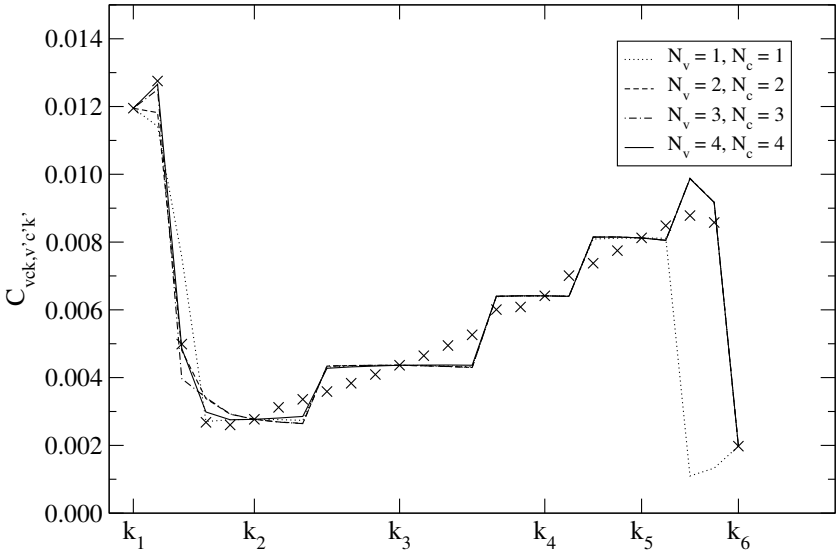

Figure B.9: Same as in Fig (B.8) but for the direct interaction matrix elements $C_{vc\mathbf{k},v'c'\mathbf{k}'}$.

fails to reproduce the slope of the exact matrix elements $C_{vc\mathbf{k},v'c'\mathbf{k}'}$ depicted in Fig. (B.9). This result is somewhat surprising because the steep changes in the matrix elements are very well described by the interpolation scheme.

We have also tested our interpolation scheme on an isolated polyacetylene chain. The results for the exchange matrix elements $H^x_{vc\mathbf{k},v'c'\mathbf{k}'}$ and the direct term $C_{vc\mathbf{k},v'c'\mathbf{k}'}$ are displayed in Figs. (B.10) and (B.11). First of all we notice, that there is almost no improvement in the interpolated values if more than 2 valence and conduction bands are taken into account. In order to describe the sudden change in the matrix elements between vectors $\mathbf{k}_3$ and $\mathbf{k}_4$, which is due to a band crossing, it is sufficient to include the bands that are involved in the crossing. However, the interpolation scheme does not correctly describe the details of the matrix elements, in particular the exchange matrix elements in the vicinity of the Z point $\mathbf{k}_5$. While the exact values are more or less constant, the interpolation is strongly decreasing. Moreover, this failure is not improved upon taking into account more valence and conduction bands. We think that the reason for these shortcomings is the following: In our interpolation scheme we expand the Bloch periodic part of a *valence* state at a given reciprocal vector only in terms of *valence* states of a neighboring $\mathbf{k}$ vector as done in [83]. However, in the vicinity of the band gap, in particular if it is quite small, we ought to include also *conduction* states in the expansion of the considered valence band. That means that each of the summations in Eqs. (6.88)–(6.90) should run over all valence *and* conduction states, which are used in the electron-hole treatment. Consequently, we would require for all matrix elements not only the combinations $\{vc\mathbf{k}, v'c'\mathbf{k}'\}$

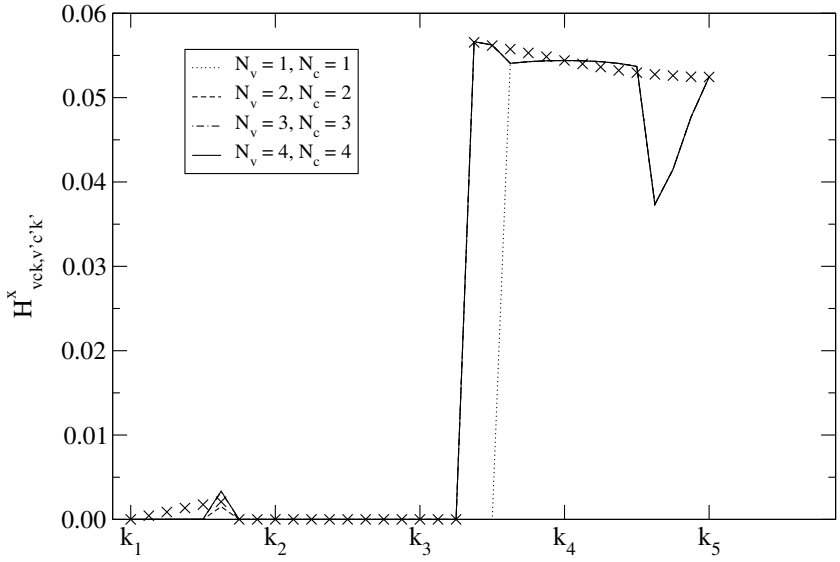

Figure B.10: Interpolation of exchange-matrix elements H^x in PA. Crosses (lines) denote the exact (interpolated) values, where N_v (N_c) is the number of valence (conduction) bands included in the expansion of wave functions. The vectors indicated at the x axis have been used as sampling points, for the interpolation. All vectors are along the [001] direction, and $\mathbf{k}_1 = \{0, 0, 0\}$ and $\mathbf{k}_5 = \{0, 0, \frac{1}{2}\}$.

but the full matrix $\{nm\mathbf{k}, n'm'\mathbf{k}'\}$, where n and m denote any valence or conduction states. We did, however, not yet extend our interpolation scheme in the manner described above, thereby proving the explanation for the unsatisfactory interpolation displayed in Figs. (B.10) and (B.11). In summary, the interpolation scheme as described in Sec. (6.3.6) has not turned out to be as satisfying as we expected and therefore has not been used for the calculations presented in this thesis. Future work, however, should be directed towards an implementation of the modifications motivated above, because a *working* interpolation scheme contains an enormous potential for saving computer time, which in turn is vital if larger systems are of interest.

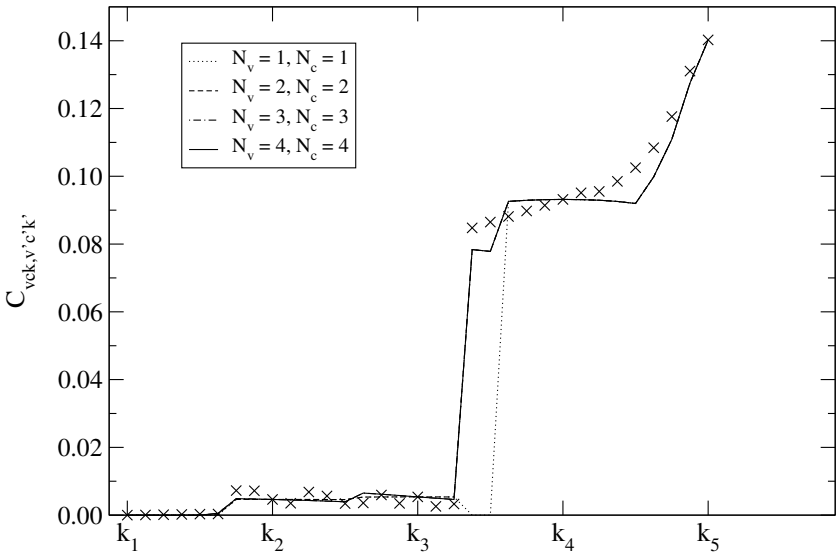

Figure B.11: Same as in Fig (B.10) but for the direct interaction matrix elements $C_{vc\mathbf{k},v'c'\mathbf{k}'}$.

Acknowledgments

First of all, I am most grateful to my supervisor Claudia Ambrosch-Draxl who has encouraged my studies in many different ways during the past years. Not only did she support me in scientific issues, but Claudia also managed to create this warm and relaxed atmosphere which turned working in her group into an enjoyable experience.

I am indebted to Ulrich Hohenester not only for carefully examining this thesis, but also for his ability to find meaningful physical interpretations behind the sometimes complicated formalism.

I want to thank my co-workers from the University of Technology Graz, Roland Resel, Egbert Zojer, and Martin Oehzelt for the encouraging discussions and for providing the indispensable experimental data. I am particularly grateful to Georg Heimel for discussing new ideas, for helping me to interpret the results, and, last but not least, for having fun – even at HASYLAB.[1]

I also want to express my gratitude to Jorge Sofo who has given me some insight into the interesting question of how to obtain excited-state properties from density functional theory. Moreover did his lecture form the basis of the presentation given in Chapter 3.

I am extremely thankful to Georg Madsen and his co-workers from the University of Technology Wien for providing me with a pre-release of their APW+lo version of the WIEN97 code. It really helped a lot in saving computer time. I also would like to acknowledge Uwe Birkenheuer who has left his wave-function plotting utility to me. The – as I think – very nice pictures of exciton wave functions are due to his program.

This work would have been much harder without the help of Timo Thonhauser who was always willing to pay attention to my coding problems, and also has never stopped answering my LaTeX questions. Equally important, however, was our common preference for fine single malt whiskey.

I am also thankful to Florian Ladstätder who has a non-negligible part in the success of this work. He might not be aware of the fact that he called my

[1] The meaning of this last comment should be clear to everyone who has spent a week or so at this rather tedious place.

attention to some crucial errors in my computer program. Moreover is Florian the creator of those legendary chocolate cakes that play an – some say *the* – essential role in our video nights.

I also would like to thank all the other group members, Kerstin Weinmeier, Jürgen Spitaler, Heinrich Auer, and Eugene Sherman since they too can be held responsible for the nice atmosphere in our group. The list of names must, however, be completed by those of two former group members, namely Pavol Dudešek and Robert Kouba. They introduced me to the mysteries of the WIEN97 program, and some parts of my computer program lean on earlier works of Pavol.

This work would have not been possible without the financial support from the *Österreichische Akademie der Wissenschaften* in the form their *Doktorandenstipendium*. This scholarship made it possible for me to concentrate on physics rather than on raising various sources of financial support.

And last, but not least, I would like to say thank you to my parents for their steady support during all the years of my studies.

Peter Puschnig
Graz, January 2002

List of Figures

3.1 Dyson's equation 22
3.2 The Bethe-Salpeter Equation 25
3.3 The electron-hole interaction kernel in the GW approximation . . 27

5.1 Definition of the interstitial and spheres region 58

6.1 Convergence of Im$\epsilon_{\mathbf{GG'}}(\mathbf{q},\omega)$ of Si with respect to $RK_{\max}$ and $l_{\max}$. 84
6.2 The imaginary part of the head of the dielectric matrix for Si. . . 85
6.3 The imaginary part of the head of the dielectric matrix for PA. . . 86
6.4 Si, convergence of $\epsilon_{\mathbf{GG}}(\mathbf{q})$ with respect to the number of $\mathbf{k}$ points 87
6.5 LiF, convergence of $\epsilon_{\mathbf{GG}}(\mathbf{q})$ with respect to the number of $\mathbf{k}$ points 88
6.6 PA, convergence of $\epsilon_{\mathbf{GG}}(\mathbf{q})$ with respect to the number of $\mathbf{k}$ points 89
6.7 Si, convergence of $\epsilon_{\mathbf{GG}}(\mathbf{q})$ with respect to $E_{\max}$ 90
6.8 LiF, convergence of $\epsilon_{\mathbf{GG}}(\mathbf{q})$ with respect to $E_{\max}$ 91
6.9 PA, convergence of $\epsilon_{\mathbf{GG}}(\mathbf{q})$ with respect to $E_{\max}$ 92
6.10 Convergence of the e-h kernel with respect to $G_{\max}$ for Si 93
6.11 Convergence of the e-h kernel with respect to $RK_{\max}$ for Si 93
6.12 Convergence of the DF of LiF with respect to the number of bands 94
6.13 Convergence of the DF of LiF with respect to the number of $\mathbf{k}$'s . 94

7.1 The DF of Si in the RPA compared to literature data 96
7.2 The dielectric function of Si as obtained from the BSE. 97
7.3 Joint density of states for Si. 98
7.4 Comparison of the DF of Si including e-h correlations with literature data 99
7.5 The DF of LiF in the RPA compared to literature data 101
7.6 The dielectric function of LiF as obtained from the BSE. 102
7.7 Comparison of the DF of LiF including e-h correlations with literature data 103
7.8 The exciton wave function of LiF in the (010) plane. 104
7.9 The exciton wave function of LiF along [101] and [100]. 105
7.10 The dielectric function of isolated trans-polyacetylene 106
7.11 Exciton wave functions of isolated polyacetylene chain 107

7.12 Electronic band structure of crystalline poly-acetylene 109
7.13 The RPA spectrum of crystalline poly-acetylene 110
7.14 The DF of crystalline PA including e-h correlations 111
7.15 The exciton wave function of crystalline PA 112

8.1 The crystal structure of oligo-phenylenes 116
8.2 The lattice constants of 2P and 3P as a function of pressure . . . 117
8.3 Pressure as a function of unit cell volume for 2P and 3P 119
8.4 The bulk modulus versus pressure for 2P and 3P 120
8.5 Total energies in 2P as a function of the herring-bone angle 121
8.6 The inter-ring bond length of 2P and 3P as a function of pressure 123
8.7 The total energy of 2P and 3P as a function of volume 124
8.8 Comparison between experimental and theoretical results for the bulk modulus 125
8.9 The electronic structure of 2P at ambient pressure 126
8.10 The electronic structure of 2P at 5 GPa 127
8.11 The wave functions of the de-localized and localized valence bands 128
8.12 The dielectric function of 2P at 0 and 5 GPa 129

B.1 Convergence of the e-h kernel with respect to $G_{\max}$ for LiF 137
B.2 Convergence of the e-h kernel with respect to $RK_{\max}$ for LiF . . . 138
B.3 Convergence of the e-h kernel with respect to $G_{\max}$ for PA 139
B.4 Convergence of the e-h kernel with respect to $RK_{\max}$ for PA . . . 139
B.5 Convergence of the DF of Si with respect to the number of bands 140
B.6 Convergence of the DF of PA with respect to the number of bands 141
B.7 Convergence of the DF of Si with respect to the number of $\mathbf{k}$ points 141
B.8 Interpolation of exchange-matrix elements H^x in Si 142
B.9 Interpolation of direct interaction matrix elements C in Si 143
B.10 Interpolation of exchange-matrix elements H^x in PA 144
B.11 Interpolation of direct interaction matrix elements C in PA 145

List of Tables

8.1 Pressure dependence of lattice constants for 2P and 3P 118
8.2 Calculated herring-bone angle and setting angle of 2P and 3P . . 122

Mathematical Symbols and Abbreviations

$A^{\lambda}_{vc\mathbf{k}}$	electron-hole coupling coefficients
c	conduction band index
Δ	scissors operator shift
ϵ	microscopic dielectric matrix
$\epsilon_M(\omega)$	macroscopic dielectric function
$\varepsilon_{v\mathbf{k}}$, $\varepsilon_{c\mathbf{k}}$	Kohn-Sham valence and conduction energies
$E_{v\mathbf{k}}$, $E_{c\mathbf{k}}$	quasi-particle valence and conduction energies
E^{λ}	exciton energies
$G(1,2)$	one-particle Green's function
$\mathbf{G}, \mathbf{K}$	reciprocal lattice vectors
$H^{e}_{vc\mathbf{k},v'c'\mathbf{k}'}$	electron-hole interaction matrix elements
$\mathbf{k}$, $\mathbf{q}$	vectors within the first Brillouin zone
$L(1,1',2,2')$	two-particle correlation function
P	complete polarization
$\hat{P}$	irreducible polarization
$\hat{P}^0$	irreducible polarization in the RPA
$\phi_{\mathbf{k}+\mathbf{G}}(\mathbf{r})$	LAPW basis function
$\Phi^{\lambda}(\mathbf{r}_e, \mathbf{r}_h)$	exciton wave function
$\mathbf{r}$	position vector
$\mathbf{R}$	direct lattice vector
v	valence band index
$v(\mathbf{r}, \mathbf{r}')$, $v_{\mathbf{q}}$	Coulomb potential
W	screened Coulomb interaction
$\Sigma(1,2)$	self energy
$\psi_{v\mathbf{k}}$, $\psi_{c\mathbf{k}}$	Kohn-Sham valence and conduction orbitals
Ξ	electron-hole interaction kernel
ω	frequency
Ω	crystal volume
Ω_0	unit cell volume

2P, 3P	biphenyl, terphenyl
APW	augmented plane-wave
APW+lo	augmented plane-wave plus local orbital
BSE	Bethe-Salpeter equation
BZ	Brillouin zone
CI	configuration interaction
DF	dielectric function
DFT	density functional theory
GGA	generalized gradient approximation
GW	Green's function G times screened interaction W
IBZ	irreducible Brillouin zone
KS	Kohn–Sham
LAPW	linearized augmented plane–wave
LCAO	linear combination of atomic orbitals
LDA	local density approximation
LO	local orbital
MT	muffin tin
OS	oscillator strength
PA	polyacetylene
QP	quasi particle
RPA	random phase approximation
SCF	self–consistent field
TD-DFT	time-dependent density functional theory
XC	exchange-correlation

Bibliography

[1] C. K. Chiang, C. R. Fincher, Y. W. Park, A. J. Heeger, H. Shirakawa, E. J. Louis, S. C. Gau, A. G. MacDiarmid, *Phys. Rev. Lett.* **39**, 1098 (1977).

[2] C. W. Tang, S. A. VanSlyke, *Appl. Phys. Lett.* **51**, 913 (1987).

[3] J. H. Burroughes, D. D. C. Bradley, A. R. Brown, R. N. Marks, K. Mackay, R. H. Friend, P. L. Burn, A. Kraft, A. B. Holmes, *Nature* **347**, 539 (1990).

[4] D. Braun, A. J. Heeger, *Appl. Phys. Lett.* **58**, 1982 (1991).

[5] G. Grem, G. Leditzky, B. Ullrich, G. Leising, *Adv. Mat.* **4**, 36 (1992).

[6] R. H. Friend, R. W. Gymer, A. B. Holmes, J. H. Burroughes, R. N. Marks, C. Taliani, D. D. C. Bradley, D. A. D. Santos, J. L. Bredas, M. Lögdlund, W. R. Salaneck, *Nature* **397**, 121 (1999).

[7] N. S. Sariciftci, L. Smilowitz, A. J. Heeger, F. Wudl, *Science* **258**, 1474 (1992).

[8] J. J. M. Halls, C. A. Walsh, N. C. Greenham, E. A. Marseglia, R. H. Friend, S. C. Moratti, A. B. Holmes, *Nature* **376**, 498 (1995).

[9] F. Garnier, G. Horowitz, X. Peng, D. Fichou, *Adv. Mat.* **2**, 592 (1990).

[10] F. Garnier, R. Hajlaoui, A. Yassar, P. Srivastava, *Science* **265**, 1684 (1994).

[11] A. Dodabalapur, L. Torsi, H. E. Katz, *Science* **268**, 270 (1995).

[12] J. H. Schön, C. Kloc, E. Bucher, B. Batlogg, *Nature* **403**, 408 (2000).

[13] J. H. Schön, S. Berg, C. Kloc, B. Batlogg, *Science* **287**, 1022 (2000).

[14] J. H. Schön, C. Kloc, R. C. Haddon, B. Batlogg, *Science* **288**, 656 (2000).

[15] J. H. Schön, C. Kloc, B. Batlogg, *Nature* **406**, 702 (2000).

[16] J. H. Schön, C. Kloc, A. Dodabalapur, B. Batlogg, *Science* **289**, 599 (2000).

[17] J. H. Schön, C. Kloc, B. Batlogg, *Science* **288**, 2338 (2000).

[18] P. Hohenberg, W. Kohn, *Phys. Rev.* **136**, B864 (1964).

[19] W. Kohn, L. J. Sham, *Phys. Rev.* **140**, A1133 (1965).

[20] R. O. Jones, O. Gunnarsson, *Rev. Mod. Phys.* **61**, 689 (1989).

[21] W. Kohn, *Rev. Mod. Phys.* **71**, 1253 (1999).

[22] L. J. Sham, T. M. Rice, *Phys. Rev.* **144**, 708 (1966).

[23] W. Hanke, L. J. Sham, *Phys. Rev. B* **12**, 4501 (1975).

[24] W. Hanke, *Adv. Phys.* **27**, 287 (1978).

[25] W. Hanke, L. J. Sham, *Phys. Rev. Lett.* **43**, 387 (1979).

[26] W. Hanke, L. J. Sham, *Phys. Rev. B* **21**, 4656 (1980).

[27] G. Strinati, *Phys. Rev. Lett.* **49**, 1519 (1982).

[28] G. Strinati, *Phys. Rev. B* **29**, 5718 (1984).

[29] S. Albrecht, G. Onida, L. Reining, *Phys. Rev. B* **55**, 10278 (1997).

[30] S. Albrecht, L. Reining, R. Del Sole, G. Onida, *Phys. Rev. Lett.* **80**, 4510 (1998).

[31] L. X. Benedict, E. L. Shirley, R. B. Bohn, *Phys. Rev. Lett.* **80**, 4514 (1998).

[32] M. Rohlfing, S. G. Louie, *Phys. Rev. Lett.* **81**, 2312 (1998).

[33] M. Rohlfing, S. G. Louie, *Phys. Rev. Lett.* **82**, 1959 (1999).

[34] J.-W. van der Horst, P. A. Bobbert, M. A. J. Michels, G. Brocks, P. J. Kelly, *Phys. Rev. Lett.* **83**, 4413 (1999).

[35] B. Arnaud, M. Alouani, *Phys. Rev. B* **63**, 085208 (2001).

[36] O. K. Andersen, *Phys. Rev. B* **12**, 3060 (1975).

[37] P. Blaha, K. Schwarz, J. Luitz, *WIEN97, A Full Potential Linearized Augmented Plane Wave Package for Calculating Crystal Properties*, (Karlheinz Schwarz, Technische Universität Wien, Vienna, 1999). ISBN 3–9501031–0–4.

[38] A. Ruini, F. Rossi, U. Hohenester, E. Molinari, R. B. Capaz, M. J. Caldas, *Synth. Met.* **119**, 257 (2001).

[39] J.-W. van der Horst, P. A. Bobbert, P. H. L. de Jong, M. A. J. Michels, G. Brocks, P. J. Kelly, *Phys. Rev. B* **61**, 15817 (2000).

[40] L. Hedin, *Phys. Rev.* **139**, A796 (1965).

[41] L. Hedin, S. Lundquist, *Solid State Physics*, vol. 23, (Academic, New York, 1969).

[42] S. L. Adler, *Phys. Rev.* **126**, 413 (1962).

[43] N. Wiser, *Phys. Rev.* **129**, 62 (1963).

[44] W. Kohn, *Proceedings of the International School of Physics, Enrico Fermi* **Course LXXXIX**, 4 (1985).

[45] M. Levy, *Phys. Rev. A* **26**, 1200 (1982).

[46] D. M. Ceperly, *Phys. Rev. B* **18**, 3126 (1978).

[47] D. M. Ceperly, B. J. Alder, *Phys. Rev. Lett.* **45**, 566 (1980).

[48] J. Harris, R. O. Jones, *J. of Phys. F* **4**, 1170 (1974).

[49] D. C. Langreth, J. P. Perdew, *Sol. State Comm.* **17**, 1425 (1975).

[50] O. Gunnarsson, B. I. Lundqvist, *Phys. Rev. B* **13**, 4274 (1976).

[51] J. P. Perdew, K. Burke, M. Enzerhof, *Phys. Rev. Lett.* **77**, 3865 (1996).

[52] J. F. Janak, *Phys. Rev. B* **18**, 7165 (1978).

[53] J. P. Perdew, R. G. Parr, M. Levy, J. L. Balduz, *Phys. Rev. Lett.* **49**, 1691 (1982).

[54] J. P. Perdew, M. Levy, *Phys. Rev. Lett.* **51**, 1884 (1983).

[55] L. J. Sham, M. Schlüter, *Phys. Rev. Lett.* **51**, 1888 (1983).

[56] M. S. Hybertson, S. G. Louie, *Phys. Rev. Lett.* **55**, 1418 (1986).

[57] M. S. Hybertson, S. G. Louie, *Phys. Rev. B* **34**, 5390 (1986).

[58] R. W. Godby, M. Schlüter, L. J. Sham, *Phys. Rev. Lett.* **56**, 2415 (1986).

[59] R. W. Godby, M. Schlüter, L. J. Sham, *Phys. Rev. B* **37**, 10159 (1988).

[60] E. Runge, E. K. U. Gross, *Phys. Rev. Lett.* **52**, 997 (1984).

[61] M. Petersilka, U. J. Gossmann, E. K. U. Gross, *Phys. Rev. Lett.* **76**, 1212 (1996).

[62] I. V. Tokatly, O. Pankratov, *Phys. Rev. Lett.* **86**, 2078 (2001).

[63] R. M. Dreizler, E. K. U. Gross, *Density Functional Theory*, (Springer Verlag, Berlin, 1990).

[64] K. Burke, E. K. U. Gross. A guided tour of time-dependent density functional theory. In *Density Functionals: Theory and Applications* (1998), D. Joubert, Ed., Springer, Berlin.

[65] A. L. Fetter, H. D. Walecka, *Quantum Theory of Many-Particle Systems*, (McGraw-Hill, 1971).

[66] G. Baym, L. P. Kadanoff, *Phys. Rev.* **124**, 287 (1961).

[67] G. Baym, *Phys. Rev.* **127**, 1391 (1961).

[68] J. Schwinger, *Proc. Natl. Acad. Sci. U.S.* **37**, 452 (1951).

[69] P. Martin, J. Schwinger, *Phys. Rev.* **115**, 1342 (1959).

[70] H. Ehrenreich, M. H. Cohen, *Phys. Rev.* **115**, 786 (1959).

[71] F. Wooten, *Optical Properties of Solids*, (Academic Press, New York and London, 1972).

[72] J. Lindhard, *Mat.-fys. Meddr.* **28**, 8 (1954).

[73] V. Ambegaokar, W. Kohn, *Phys. Rev.* **117**, 423 (1960).

[74] R. Del Sole, E. Fiorino, *Phys. Rev. B* **29**, 4631 (1984).

[75] P. Nozieres, D. Pines, *Phys. Rev.* **109**, 741 (1958).

[76] P. Nozieres, D. Pines, *Phys. Rev.* **109**, 762 (1958).

[77] P. Nozieres, D. Pines, *Phys. Rev.* **109**, 1062 (1958).

[78] Z. H. Levine, D. C. Allen, *Phys. Rev. Lett.* **63**, 1719 (1989).

[79] Z. H. Levine, D. C. Allen, *Phys. Rev. B* **43**, 4187 (1991).

[80] R. Del Sole, R. Girlanda, *Phys. Rev. B* **48**, 11789 (1993).

[81] M. S. Hybertson, S. G. Louie, *Phys. Rev. B* **35**, 5585 (1987).

[82] W. Kohn, *Phys. Rev.* **110**, 851 (1958).

[83] M. Rohlfing, S. G. Louie, *Phys. Rev. B* **62**, 4927 (2000).

[84] B. Arnaud, Ph. D. thesis, Universite Louis Pasteur, Strasbourg/France, (December 2000).

[85] F. Bechstedt, K. Tenelsen, B. Adolph, R. Del Sole, *Phys. Rev. Lett.* **78**, 1528 (1997).

[86] J. C. Slater, *Phys. Rev.* **51**, 846 (1937).

[87] P. I. Sorantin, Ph. D. thesis, Technische Universität Wien, Vienna, (May 1990).

[88] D. J. Singh, *Planewaves, Pseudopotentials and the LAPW Method*, (Kluwer Academic Publishers, Boston/Dordrecht/London, 1994). ISBN 0–7923–9412–7.

[89] P. Dufek, Ph. D. thesis, Technische Universität Wien, Wien/Austria, (1994).

[90] E. Sjöstedt, L. Nordström, D. J. Singh, *Sol. State Comm.* **114**, 15 (2000).

[91] R. Kouba, master thesis, Karl–Franzens–Universität, Graz/Austria, (1995).

[92] B. Kohler, S. Wilke, M. Scheffler, R. Kouba, C. Ambrosch-Draxl, *Comp. Phys. Commun.* **94**, 31 (1996).

[93] R. Abt, Ph. D. thesis, Karl–Franzens–Universität, Graz/Austria, (May 1997).

[94] G. Lehmann, M. Taut, *Phys. Stat. Sol.* **54**, 469 (1972).

[95] P. E. Blöchl, O. Jepsen, O. K. Andersen, *Phys. Rev. B* **49**, 16223 (1994).

[96] P. Puschnig, master thesis, Karl–Franzens–Universität, Graz/Austria, (March 1999).

[97] M. Wagner, *Gruppentheoretische Methoden in der Physik*, (Vieweg, Braunschweig/Wiesbaden, 1998).

[98] D. E. Aspnes, A. A. Studna, *Phys. Rev. B* **27**, 985 (1983).

[99] P. Lautenschlager, M. Garriga, L. Viña, M. Cardona, *Phys. Rev. B* **36**, 4821 (1987).

[100] C. S. Wang, B. M. Klein, *Phys. Rev. B* **24**, 3417 (1981).

[101] L. X. Benedict, E. L. Shirley, R. B. Bohn, *Phys. Rev. B* **57**, R9385 (1998).

[102] S. G. Louie, J. R. Chelikowsky, M. L. Cohen, *Phys. Rev. Lett.* **34**, 155 (1975).

[103] D. M. Roessler, W. C. Walker, *J. Opt. Soc. Am.* **57**, 835 (1967).

[104] P. Vogl, D. K. Campbell, *Phys. Rev. B* **41**, 12797 (1990).

[105] P. Vogl, D. K. Campbell, *Phys. Rev. Lett.* **62**, 2012 (1989).

[106] Landolt-Boernstein, *Zahlenwerte und Funktionen aus Physik, Chemie, Astronomie, Geophysik und Technik*, vol. 2, (Springer, Berlin, 1957).

[107] G.-P. Charbonneau, Y. Delugeard, *Acta Cryst. B* **33**, 1586 (1977).

[108] H. M. Rietveld, E. N. Maslen, C. J. B. Clews, *Acta Cryst. B* **26**, 693 (1970).

[109] F. Birch, *J. Geophys. Res.* **83**, 1257 (1978).

[110] J. P. Perdew, Y. Wang, *Phys. Rev. B* **45**, 13244 (1992).

[111] P. Puschnig, C. Ambrosch-Draxl, *Phys. Rev. B* **60**, 7891 (1999).

List of Papers

This list comprises a number of publications that have been written during the development of this thesis. They are all concerned with the electronic, optical and structural properties of oligophenyls under pressure. Thus, they can be viewed as a supplement to the results presented in Chapter 8.

[P–1] S. Yang, W. Graupner, S. Guha, P. Puschnig, C. Martin, H.R. Chandrasekhar, M. Chandrasekhar, G. Leising, and C. Ambrosch-Draxl, "Geometry-Dependent Electronic Properties of Highly Fluorescent Conjugated Molecules", *Phys. Rev. Lett.* **85**, 2388 (2000).

[P–2] P. Puschnig, G. Heimel, E. Zojer, R. Resel, G. Leising, M. Kriechbaum, C. Ambrosch-Draxl, and W. Graupner, "Pressure studies on the intermolecular interactions in biphenyl", *Synth. Met.* **116**, 327 (2001).

[P–3] G. Heimel, P. Puschnig, Q. Cai, C. Martin, E. Zojer, W. Graupner, M. Chandrasekhar, H.R. Chandrasekhar, C. Ambrosch-Draxl, G. Leising, "High pressure studies on the structural conformation of oligophenylenes", *Synth. Met.* **116**, 163 (2001).

[P–4] C. Ambrosch-Draxl, P. Puschnig, E. Zojer, and G. Leising, "Doping effects on the electronic and structural properties of poly(para-phenylene) investigated from first principles", *Synth. Met.* **119**, 211 (2001).

[P–5] P. Puschnig and C. Ambrosch-Draxl, "Ab-initio study on the intermolecular interactions in polythiophene", *Synth. Met.* **119**, 245 (2001).

[P–6] G. Heimel, Q. Cai, C. Martin, P. Puschnig, W. Graupner, C. Ambrosch-Draxl, M. Chandrasekhar, and G. Leising, "On the structure of oligophenyls", *Synth. Met.* **119**, 371 (2001).

[P–7] G. Heimel, E. Zojer, R. Resel, P. Puschnig, K. Weinmeier, C. Ambrosch-Draxl, "Structural properties of conjugated molecular crystals under high pressure", *SPIE Proc.* (in print).

[P–8] K. Weinmeier, P. Puschnig, C. Ambrosch-Draxl, G. Heimel, E. Zojer, and R. Resel, "High pressure studies of poly-aromatic molecular crystals: optical and electronic properties from first principles", *SPIE Proc.* (in print).

[P–9] P. Puschnig, G. Heimel, K. Weinmeier, R. Resel, and C. Ambrosch-Draxl, "High pressure studies on the optical and electronic properties of para-terphenyl", *High Pressure Research* (in print).

[P–10] M. Oehzelt, K. Weinmeier, G. Heimel, P. Puschnig, R. Resel, C. Ambrosch-Draxl, F. Porsch, and A. Nakayama, "Structural properties of anthracene under high pressure", *High Pressure Research* (in print).